

Mechanical reliability and oxygen permeation of $\text{Ce}_{0.8}\text{Gd}_{0.2}\text{O}_{2-\delta}\text{-FeCo}_2\text{O}_4$ dual phase membranes

Fanlin Zeng

Energie & Umwelt / Energy & Environment

Band / Volume 529

ISBN 978-3-95806-527-7

UNIVERSITY
OF TWENTE.

 **JÜLICH**
Forschungszentrum

Forschungszentrum Jülich GmbH
Institut für Energie- und Klimaforschung
Werkstoffstruktur und -eigenschaften (IEK-2)

Mechanical reliability and oxygen permeation of $\text{Ce}_{0.8}\text{Gd}_{0.2}\text{O}_{2-\delta}$ - FeCo_2O_4 dual phase membranes

Fanlin Zeng

Schriften des Forschungszentrums Jülich
Reihe Energie & Umwelt / Energy & Environment

Band / Volume 529

ISSN 1866-1793

ISBN 978-3-95806-527-7

Bibliografische Information der Deutschen Nationalbibliothek.
Die Deutsche Nationalbibliothek verzeichnet diese Publikation in der
Deutschen Nationalbibliografie; detaillierte Bibliografische Daten
sind im Internet über <http://dnb.d-nb.de> abrufbar.

Herausgeber und Vertrieb: Forschungszentrum Jülich GmbH
Zentralbibliothek, Verlag
52425 Jülich
Tel.: +49 2461 61-5368
Fax: +49 2461 61-6103
zb-publikation@fz-juelich.de
www.fz-juelich.de/zb

Umschlaggestaltung: Grafische Medien, Forschungszentrum Jülich GmbH

Druck: Grafische Medien, Forschungszentrum Jülich GmbH

Copyright: Forschungszentrum Jülich 2021

Schriften des Forschungszentrums Jülich
Reihe Energie & Umwelt / Energy & Environment, Band / Volume 529

Diss. Univ. Twente, 2021

ISSN 1866-1793
ISBN 978-3-95806-527-7

Vollständig frei verfügbar über das Publikationsportal des Forschungszentrums Jülich (JuSER)
unter www.fz-juelich.de/zb/openaccess.



This is an Open Access publication distributed under the terms of the [Creative Commons Attribution License 4.0](https://creativecommons.org/licenses/by/4.0/), which permits unrestricted use, distribution, and reproduction in any medium, provided the original work is properly cited.

Content

SUMMARY

SAMENVATTING

1 Introduction.....	1
1.1 Energy consumption	2
1.2 Carbon capture technologies.....	4
1.3 Oxygen transport membranes.....	5
1.3.1 Mechanism of oxygen transport	6
1.3.2 Membrane materials.....	8
1.4 Scope of the thesis.....	12
2 Phase and microstructural characterizations for $\text{Ce}_{0.8}\text{Gd}_{0.2}\text{O}_{2-\delta}$ - FeCo_2O_4 dual phase oxygen transport membranes	21
2.1 Introduction	22
2.2 Experimental.....	23
2.3 Results and discussion	28
2.3.1 Microstructure characterization	28
2.3.2 Phase characterization	31
2.3.3 Effect of microstructure parameters on ambipolar conductivity	34
2.4 Conclusions	38
Appendix A2.....	43

3 Mechanical reliability of $\text{Ce}_{0.8}\text{Gd}_{0.2}\text{O}_{2-\delta}\text{-FeCo}_2\text{O}_4$ dual phase membranes synthesized by one-step solid-state reaction 47

 3.1 Introduction 48

 3.2 Experimental 50

 3.3 Results and discussion 55

 3.3.1 Phase constituents and microstructure 55

 3.3.2 Residual stress 60

 3.3.3 Mechanical properties 63

 3.3.4 Subcritical crack growth and Weibull analysis 66

 3.3.5 Fractography 69

 3.3.6 Reliability and lifetime analysis 75

 3.4 Conclusions 78

 Appendix A3 86

4 Optimization of sintering conditions for improved microstructural and mechanical properties of dense $\text{Ce}_{0.8}\text{Gd}_{0.2}\text{O}_{2-\delta}\text{-FeCo}_2\text{O}_4$ oxygen transport membranes 93

 4.1 Introduction 94

 4.2 Experimental 96

 4.3 Results and discussion 99

 4.3.1 Characterization of phase transformations 99

 4.3.2 Microstructural investigations 101

 4.3.3 Mechanical properties 104

 4.4 Conclusions 109

 Appendix A4 117

5 Micro-mechanical characterization of $\text{Ce}_{0.8}\text{Gd}_{0.2}\text{O}_{2-\delta}\text{-FeCo}_2\text{O}_4$ dual phase oxygen transport membranes	121
5.1 Introduction	122
5.2 Experimental	123
5.3 Results and discussion	125
5.3.1 Phase and microstructure characterizations	125
5.3.2 Mechanical properties	129
5.4 Conclusions	134
Appendix A5	139
6 Residual stress and mechanical strength of $\text{Ce}_{0.8}\text{Gd}_{0.2}\text{O}_{2-\delta}\text{-FeCo}_2\text{O}_4$ dual phase oxygen transport membranes	141
6.1 Introduction	142
6.2 Experimental	144
6.3 Results and discussion	148
6.3.1 Microstructure	148
6.3.2 Lattice constants	150
6.3.3 Residual stress	152
6.3.4 Fracture strength and fractography	158
6.4 Conclusions	163
Appendix A6	170

7 Enhancing oxygen permeation of solid-state reactive sintered $\text{Ce}_{0.8}\text{Gd}_{0.2}\text{O}_{2-\delta}\text{-FeCo}_2\text{O}_4$ composite by optimizing the powder preparation method	175
7.1 Introduction	176
7.2 Experimental	180
7.3 Results and discussion	183
7.3.1 Powder characteristics	183
7.3.2 Phase and microstructure characterizations	188
7.3.3 Oxygen permeation	193
7.4 Conclusions	204
Appendix A7	209
8 Reflections and perspectives	215
8.1 Introduction	216
8.2 Powder preparation	216
8.2.1 Powder composition	216
8.2.2 Powder synthesis methods	217
8.3 Sintering profiles	219
8.4 Mechanical stability after long-term operation	220
8.5 Conclusions	221

Acknowledgements

About the author

SUMMARY

Dual phase oxygen transport membranes, consisting of ionic and electronic conducting phases, exhibit great potential in high-purity oxygen generation due to their high stability under harsh application atmospheres. Oxygen-ion conductive fluorite oxides (e.g. $\text{Ce}_{0.8}\text{Gd}_{0.2}\text{O}_{2-\delta}$) and electron conductive spinel phases (e.g. FeCo_2O_4) are promising material candidates for such a dual phase oxygen transport membrane. Mechanical properties (e.g. elastic modulus, hardness, strength and subcritical crack growth behaviour) and oxygen permeation of the membrane are important parameters regarding reliability for future applications. These parameters have close relationships with composition and microstructural characteristics, like grain size, phase distribution and defects (e.g. microcracks). However, these relationships are currently not fully understood. Therefore, in this thesis, the influence of composition, grain size and microstructural defects on mechanical properties are investigated for $\text{Ce}_{0.8}\text{Gd}_{0.2}\text{O}_{2-\delta}$ - FeCo_2O_4 membranes. Milling procedures during powder fabrication and ceramic sintering profiles are optimized to overcome the formation of unfavorable microstructural defects. Furthermore, the effects of grain size and phase distribution on oxygen permeation are discussed for a 85 wt% $\text{Ce}_{0.8}\text{Gd}_{0.2}\text{O}_{2-\delta}$ -15 wt% FeCo_2O_4 membrane.

Chapter 1 of this thesis presents currently known potential applications and basic concepts of oxygen transport membranes (e.g. mechanism of oxygen transport and material candidates). Promising prospects for dual phase oxygen transport membranes are reflected, in particular those for the $\text{Ce}_{0.8}\text{Gd}_{0.2}\text{O}_{2-\delta}$ - FeCo_2O_4 composites.

Chapter 2 reports on investigations and quantifications of phase compositions and microstructural features including volume fractions, grain sizes, and contiguity for the different phases in $z\text{Ce}_{0.8}\text{Gd}_{0.2}\text{O}_{2-\delta}$ -(1-z) FeCo_2O_4 ($z = 50, 60, 70, 85$ or 90 wt%) composites. The characterizations reveal a multi-phase system containing Ce_1 -

$x\text{Gd}_x\text{O}_{2-\delta}$ ($x \approx 0.1$), and $\text{Fe}_y\text{Co}_{3-y}\text{O}_4$ ($0.2 < y < 1.2$), CoO and $\text{Gd}_{0.85}\text{Ce}_{0.15}\text{Fe}_{0.75}\text{Co}_{0.25}\text{O}_3$ phases in the membranes. A novel model is derived to calculate the ambipolar conductivity using the quantified phase constituents and microstructural features. These calculations results indicate that, if the grain sizes of all phases in the composites are identical, a 85 wt% $\text{Ce}_{0.8}\text{Gd}_{0.2}\text{O}_{2-\delta}$ -15 wt% FeCo_2O_4 composite exhibits the highest ambipolar conductivity. Besides, both experimental data and calculated results indicate a rather poor ambipolar conductivity of the membrane containing a significant amount of large grains.

The mechanical limits regarding application in particular strength and lifetime are presented in **Chapter 3** for $z\text{Ce}_{0.8}\text{Gd}_{0.2}\text{O}_{2-\delta}$ -(1- z) FeCo_2O_4 ($z = 50$ or 85 wt%) composites containing a significant amount of large grains. In general, the fracture strengths of as-sintered membranes are reduced by the presence of tensile residual stresses and microcracks. In particular, for the 85 wt% $\text{Ce}_{0.8}\text{Gd}_{0.2}\text{O}_{2-\delta}$ -15 wt% FeCo_2O_4 composite, after an operation time of 10 years, the failure stress, inducing a failure probability of 1 %, significantly decreases from ~ 48 MPa to ~ 2 MPa, which appears to be a result of tensile residual stresses and microcracks.

To improve the mechanical properties and ambipolar conductivity, the grain size of the membranes is reduced by starting with smaller initial particle sizes of the powder mixtures. These powder mixtures with reduced particle sizes are subsequently used to sinter $\text{Ce}_{0.8}\text{Gd}_{0.2}\text{O}_{2-\delta}$ - FeCo_2O_4 composites that are further investigated as outlined in **Chapters 4-7**.

Studies of the effects of sintering profiles on microstructural and mechanical characteristics of 85 wt% $\text{Ce}_{0.8}\text{Gd}_{0.2}\text{O}_{2-\delta}$ -15 wt% FeCo_2O_4 composite are presented in **Chapter 4**. The results indicate that the optimal sintering temperature appears to be 1200 °C with a holding time of 10 h, since the microstructure sintered at this temperature possesses a density exceeding 99 %, relatively small grains and small surface defects, which contributes to a high average flexural strength of approximately 266 MPa. This optimal sintering profile is further applied to sinter the $\text{Ce}_{0.8}\text{Gd}_{0.2}\text{O}_{2-\delta}$ - FeCo_2O_4 composites as described in **Chapters 5-7**.

Chapter 5 reports the elastic modulus and hardness of $z\text{Ce}_{0.8}\text{Gd}_{0.2}\text{O}_{2-\delta}-(1-z)\text{FeCo}_2\text{O}_4$ ($z = 50, 60, 70, 85$ or 90 wt%) composites as well as of the individual phases in these membranes. The mechanical properties were determined by nanoindentation tests at room temperature. It unveils that the magnitude of the elastic moduli of the different phases is in the order $\text{Gd}_{0.9}\text{Ce}_{0.1}\text{Fe}_{0.8}\text{Co}_{0.2}\text{O}_3 > \text{Ce}_{1-x}\text{Gd}_x\text{O}_{2-\delta} \approx \text{Fe}_x\text{Co}_{3-x}\text{O}_4 > \text{CoO}$, and difference in hardness values are also in the same order. The average elastic modulus and hardness of the composites are in the ranges of $\sim 214\text{-}223$ GPa, and $\sim 10.5\text{-}11.5$ GPa, respectively. The elastic modulus of the composites marginally decreases with increasing iron cobalt spinel content, while the hardness values of the composites are affected to a slightly stronger extent by porosity rather than by the compositional variation. Any compositional effect appears to diminish above a porosity of around 1%.

Chapter 6 focuses on fracture strength and its relationship to residual stresses of $z\text{Ce}_{0.8}\text{Gd}_{0.2}\text{O}_{2-\delta}-(1-z)\text{FeCo}_2\text{O}_4$ ($z = 50, 70$ or 85 wt%) composites. The strength was determined by ring-on-ring bending tests, and the residual stress and residual stress gradient were derived from X-ray diffraction (based on the $\sin^2 \psi$ method) and the indentation method. The results reveal that the strength of composites increase with decreasing spinel content. The low fracture strength of the composites with high spinel content is attributed to tensile residual stress gradients and microcracks at the surface. It is found that for 50 wt% $\text{Ce}_{0.8}\text{Gd}_{0.2}\text{O}_{2-\delta}$ -50 wt% FeCo_2O_4 composite, the residual tensile stress decreases when a dwelling step at 850 °C for 100 h is applied after sintering. However, it is proposed to limit the spinel content to a nominal value of 15 wt% in order to eliminate the residual tensile stress and thereby yielding a material of high mechanical strength.

In **Chapter 7** oxygen permeances are discussed for 85 wt% $\text{Ce}_{0.8}\text{Gd}_{0.2}\text{O}_{2-\delta}$ -15 wt% FeCo_2O_4 membranes with three different microstructures. The first membrane has a small average grain size (~ 0.4 μm) and a homogeneous distribution of the two phases, while the second membrane has bigger grains and a less homogeneous phase distribution. The results indicate that the membrane with a fine and homogeneous

microstructure exhibits higher oxygen permeance ($\sim 1.7 \times 10^{-8} \text{ mol}\cdot\text{cm}^2\cdot\text{s}^{-1}$ at $\sim 900 \text{ }^\circ\text{C}$, measured for a bare membrane with a thickness of $\sim 0.96 \text{ mm}$) than a membrane with larger grains due to good connections between ionic/electronic conducting phase and large triple phase boundaries (TPBs) at the surface. Finally, a dry powder mixing method is introduced to prepare the third membrane. This membrane has a unique microstructure with relative straight paths for ionic and electronic conduction, resulting in significantly improved oxygen permeance ($\sim 2.7 \times 10^{-8} \text{ mol}\cdot\text{cm}^2\cdot\text{s}^{-1}$ at $\sim 900 \text{ }^\circ\text{C}$, measured for a surface-activated membrane with a thickness of $\sim 0.96 \text{ mm}$), if compared with the other two membranes after the limiting effect from surface exchange is overcome by a $\sim 10 \text{ }\mu\text{m}$ porous $\text{La}_{0.58}\text{Sr}_{0.4}\text{Co}_{0.2}\text{Fe}_{0.8}\text{O}_{3-\delta}$ layers.

Finally, **Chapter 8** reflects the overall findings, and give perspectives for future research. It is reflected that the membranes with a high iron cobalt spinel content suffer from low mechanical strength due to the existence of microcracks and residual tensile stresses. A crack-free microstructure with only small surface defects and small grain size is obtained for 85 wt% $\text{Ce}_{0.8}\text{Gd}_{0.2}\text{O}_{2-\delta}$ -15 wt% FeCo_2O_4 membrane using the optimized powder preparation procedure and sintering profile. This microstructure exhibits significantly improved strength and oxygen permeation. Future improvements in oxygen permeation without compromising mechanical strength can be realized by further reducing the grain size without inducing microstructural defects like microcracks and pore agglomerates. It is recommended to use nano-sized powder mixtures and/or apply a two-step sintering profile. Besides, it is necessary to investigate the mechanical stability of the membrane after a long-term operation.

SAMENVATTING

Keramische zuurstof-selectieve membranen, die uit een separate ionen- en elektronen-geleidende fase bestaan, bieden interessante mogelijkheden voor het verkrijgen van zuurstof met hoge zuiverheid, terwijl deze materialen een hoge mechanische en chemische stabiliteit vertonen onder extreme omstandigheden. In dit proefschrift worden de mechanische eigenschappen (bijv. elasticiteitsmodulus, hardheid, sterkte en sub-kritische scheurgroei) en de zuurstofpermeatie beschreven van composietmaterialen die bestaan uit het zuurstofionen geleidende fluoriet $\text{Ce}_{0.8}\text{Gd}_{0.2}\text{O}_{2-\delta}$ en het elektronen geleidende spinel FeCo_2O_4 . De relatie is onderzocht tussen deze parameters en de microstructuur van het membraan, zoals keramische korrelgrootte, kristal fase verdeling en grootte/grootteverdeling van eventueel aanwezige microscheurtjes. De maalprocedures tijdens de fabricage van de keramische poeders alsmede het temperatuur programma tijdens sinteren van het keramisch membraan zijn geoptimaliseerd om de vorming van defecten in het materiaal tegen te gaan. Daarnaast wordt in dit proefschrift ingegaan op de effecten van keramische korrelgrootte en kristal fase verdeling op de zuurstof permeatie door het membraan. Met de resultaten van dit onderzoek is het keramisch fabricageproces zodanig aangepast, dat een membraan is verkregen met optimale mechanische en zuurstoftransport eigenschappen.

Hoofdstuk 1 van dit proefschrift geeft de stand van zaken weer voor potentiële toepassingen van deze 100 % zuurstof-selectieve membranen. Daarnaast wordt het zuurstoftransport mechanisme behandeld. Tevens wordt ingegaan op de mogelijkheden van verschillende veelbelovende tweefasen zuurstoftransport membranen met in het bijzonder de $\text{Ce}_{0.8}\text{Gd}_{0.2}\text{O}_{2-\delta}$ - FeCo_2O_4 composieten: Het materiaal waar in dit proefschrift aandacht aan wordt besteed.

In **hoofdstuk 2** worden de volume fracties, korrelgroottes en contiguiteit van de verschillende fasen gekwantificeerd voor composieten met als algemene samenstelling: $z\text{Ce}_{0.8}\text{Gd}_{0.2}\text{O}_{2-\delta}-(1-z)\text{FeCo}_2\text{O}_4$ ($z = 50, 60, 70, 85$ of 90 gew. %). Al deze composieten bestaan uit meerdere kristalfasen; nl: $\text{Ce}_{1-x}\text{Gd}_x\text{O}_{2-\delta}$ ($x \approx 0.1$), $\text{Fe}_y\text{Co}_{3-y}\text{O}_4$ ($0.2 < y < 1.2$), CoO en $\text{Gd}_{0.85}\text{Ce}_{0.15}\text{Fe}_{0.75}\text{Co}_{0.25}\text{O}_3$. Daarnaast wordt, aan de hand van de resultaten in dit hoofdstuk, een model gepresenteerd voor het berekenen van de ambipolaire geleiding van deze materialen. De resultaten van deze berekening tonen aan dat een composiet, bestaande uit 85 gew. % $\text{Ce}_{0.8}\text{Gd}_{0.2}\text{O}_{2-\delta}$ en 15 gew. % FeCo_2O_4 , de hoogste ambipolaire geleiding vertoont, indien de korrelgroottes van alle fasen in het materiaal identiek zijn. Daarnaast tonen zowel de experimentele als berekende resultaten aan, dat een membraan met aanzienlijk aantal grote korrels een slecht ambipolaire geleiding vertoont.

De maximale mechanische belasting, gerelateerd met sterkte en levensduur voor het toepassen van $z\text{Ce}_{0.8}\text{Gd}_{0.2}\text{O}_{2-\delta}-(1-z)\text{FeCo}_2\text{O}_4$ ($z = 50$ of 85 gew. %) composieten met een aanzienlijk aantal grote korrels is beschreven in **hoofdstuk 3**. In het algemeen neemt de breuksterkte van de membranen af door de aanwezigheid, na sinteren, van resterende trekspanningen en microscheurtjes. Met name voor het 85 gew. % $\text{Ce}_{0.8}\text{Gd}_{0.2}\text{O}_{2-\delta}$ - 15 gew. % FeCo_2O_4 composiet is aangetoond dat de faalspanning, uitgaande van een faalkans van 1 %, sterk afneemt van ~ 48 MPa naar ~ 2 MPa na een gebruiksperiode van 10 jaar. Dit is vooral een gevolg van de aanwezigheid van resterende trekspanningen en microscheurtjes.

Om de mechanische eigenschappen en de ambipolaire geleiding van deze materialen te verbeteren moet de korrelgrootte van de membranen worden verkleind. Dit kan worden gerealiseerd door uit te gaan van kleinere deeltjesgroottes van de uitgangspoeders. Gesinterde $\text{Ce}_{0.8}\text{Gd}_{0.2}\text{O}_{2-\delta}$ - FeCo_2O_4 composieten, uitgaande van deze fijnkorrelige poedermengsels, worden verder onderzocht in de **hoofdstukken 4-7**.

Hoofdstuk 4 behandelt het effect van verschillende sinterprofielen op de microstructurele en mechanische karakteristieken van het 85 gew. % $\text{Ce}_{0.8}\text{Gd}_{0.2}\text{O}_{2-\delta}$

en 15 gew. % FeCo_2O_4 composiet materiaal. De resultaten tonen aan dat het optimale sinterprofiel 1200 °C is met een verblijftijd van 10 uur bij deze temperatuur. Op deze manier wordt een relatieve dichtheid van ruim 99 % verkregen met relatief kleine keramische korrelgroottes en relatief weinig defecten aan het oppervalk. Deze microstructuur resulteert in een hoge buigsterkte van 266 MPa. Dit optimale sinterprofiel wordt verder toegepast in de **hoofdstukken 5-7** voor het sinteren van $\text{Ce}_{0.8}\text{Gd}_{0.2}\text{O}_{2-\delta}$ - FeCo_2O_4 composieten.

Hoofdstuk 5 gaat in op de elasticiteitsmodulus en hardheid van $z\text{Ce}_{0.8}\text{Gd}_{0.2}\text{O}_{2-\delta}$ -(1-z) FeCo_2O_4 ($z = 50, 60, 70, 85$ of 90 gew. %) composieten, inclusief die van de afzonderlijke kristalfasen in deze membranen. Deze mechanische eigenschappen zijn bepaald aan de hand van nano-indentatie metingen bij kamertemperatuur. De resultaten tonen aan dat zowel de elasticiteitsmodulus als de hardheid van de verschillende fasen afneemt in de volgorde: $\text{Gd}_{0.9}\text{Ce}_{0.1}\text{Fe}_{0.8}\text{Co}_{0.2}\text{O}_3 > \text{Ce}_{1-x}\text{Gd}_x\text{O}_{2-\delta} \approx \text{Fe}_x\text{Co}_{3-x}\text{O}_4 > \text{CoO}$. De gemiddelde elasticiteitsmodulus en hardheid waarden van de verschillende composieten zijn respectievelijk in de orde grootte ~ 214 - 223 GPa en ~ 10.5 - 11.5 GPa. De elasticiteitsmodulus neemt marginaal af met een toenemende concentratie van de ijzer-kobalt spinel fase in het composiet. De hardheid wordt in iets sterkere mate beïnvloed door de porositeit dan door de (chemische) samenstelling van de composieten. Daarnaast kan geconcludeerd worden dat voor alle composieten met een porositeit van meer dan 1 % de porositeit een sterker effect heeft op elasticiteitsmodulus en hardheid dan de chemische samenstelling.

De relatie tussen breuksterkte en de restspanningen na het sinteren van $z\text{Ce}_{0.8}\text{Gd}_{0.2}\text{O}_{2-\delta}$ -(1-z) FeCo_2O_4 ($z = 50, 70$ of 85 gew. %) keramische materialen wordt behandeld in **hoofdstuk 6**. De breuksterktes zijn bepaald aan de hand van ring-op-ring buigtesten, terwijl de waarden voor restspanning en restspanningsgradiënt verkregen zijn door analyse van Röntgen diffractie (gebaseerd op de $\sin^2 \psi$ methode) en indenter metingen. De resultaten tonen aan dat de sterkte van de composieten toeneemt met afnemende concentratie van de spinel fase. De lage breuksterkte voor de composieten met hoge spinel concentratie kan worden toegeschreven aan de

aanwezigheid van trekspanningsgradiënten en microscheurtjes aan het oppervlak van het materiaal. Daarnaast is aangetoond dat voor $\text{Ce}_{0.8}\text{Gd}_{0.2}\text{O}_{2-\delta}$ -50 gew. % FeCo_2O_4 composieten de aanwezige trekspanning in het materiaal afneemt als na het sinteren het materiaal gedurende 100 uur bij 850 °C wordt gehouden. Tenslotte wordt in dit hoofdstuk voorgesteld om een nominale concentratie van 15 gew. % van het spinel in het composiet te hebben om de resterende trekspanningen te elimineren en daarbij een materiaal te hebben met een hoge mechanische sterkte.

In **hoofdstuk 7** wordt de zuurstof permeatie beschreven van 85 gew. % $\text{Ce}_{0.8}\text{Gd}_{0.2}\text{O}_{2-\delta}$ -15 gew. % FeCo_2O_4 membranen met drie verschillende microstructuren. Het eerste membraan heeft een kleine gemiddelde korrelgrootte ($\sim 0.4 \mu\text{m}$) en een homogene verdeling van de fasen terwijl het tweede membraan grotere korrels heeft en een minder homogene verdeling van de fasen. De resultaten tonen aan dat het membraan met een fijnkorrelige en homogene microstructuur een hogere zuurstof permeatie vertoont van $1.7 \times 10^{-8} \text{ mol}\cdot\text{cm}^2\cdot\text{s}^{-1}$ bij $\sim 900 \text{ }^\circ\text{C}$, gemeten aan een gesinterd membraan met een dikte van $\sim 0.96 \text{ mm}$. Deze hogere zuurstof permeatie in vergelijking met het grofkorrelige, inhomogene membraan wordt toegeschreven aan een betere hechting tussen de ionogene en elektronen geleidende fasen in het keramiek en daarnaast een grotere drie-fase grenslijn concentratie aan het oppervlak. Tenslotte wordt in dit hoofdstuk een derde type membraan beschreven, welke gemaakt door uit te gaan van het droog mengen van de uitgangspoeder. Het resulterende membraan heeft een unieke microstructuur met relatief rechte transport paden door het membraan voor zuurstof ionen en elektronen, wat resulteert in een duidelijke verbetering van de zuurstof permeatie ($2.7 \times 10^{-8} \text{ mol}\cdot\text{cm}^2\cdot\text{s}^{-1}$ bij $\sim 900 \text{ }^\circ\text{C}$, gemeten aan een oppervlakte geactiveerd membraan met een totale dikte van $\sim 0.96 \text{ mm}$) in vergelijking met de andere twee membranen, nadat de limitering door de zuurstof uitwisselingsreactie aan het oppervlakte is overwonnen door het aanbrengen van een $10 \mu\text{m}$ oppervlakte-actieve poreuze $\text{La}_{0.58}\text{Sr}_{0.4}\text{Co}_{0.2}\text{Fe}_{0.8}\text{O}_{3-\delta}$ laag.

Tenslotte geeft **hoofdstuk 8** een evaluatie van de resultaten en bevindingen weer, die in dit proefschrift zijn gepresenteerd, plus suggesties voor verder onderzoek op

dit gebied. Aangetoond is dat membranen met een hoge concentratie van de ijzer-kobalt spinel fase een lage mechanische sterke hebben vanwege de aanwezigheid van microscheurtjes en resterende restspanningen. Een keramische microstructuur zonder microscheurtjes met slechts een klein aantal oppervlakte defecten en kleine korrelgroottes kan verkregen worden voor een 85 gew. % $\text{Ce}_{0.8}\text{Gd}_{0.2}\text{O}_{2-\delta}$ -15 gew. % FeCo_2O_4 membraan, waarbij gebruik gemaakt wordt van de optimale poeder bereidingsprocedure in samenhang met het optimale sinterprofiel. Deze microstructuur vertoont een duidelijk verbeterde sterkte en zuurstof permeatie. Verdere verbetering in de zuurstofpermeatie, zonder compromissen te sluiten met betrekking tot mechanische sterkte, kan worden gerealiseerd door verdere reductie van de keramische korrelgrootte zonder dat er defecten in de keramische microstructuur ontstaan, zoals microscheurtjes en het agglomereren van poriën. Om deze microstructuur te realiseren wordt aanbevolen om poedermengsels te gebruiken met nanokristallijne deeltjesgrootte en tijdens het sinteren een twee-staps temperatuur programma te gebruiken. Als laatste moet nog aangegeven worden dat verder onderzoek noodzakelijk is naar de mechanische stabiliteit van het membraan na een lange periode van in bedrijfstelling.

CHAPTER 1

Introduction

1.1 Energy consumption

The global energy demand has increased substantially in a concurrent trend with modern society development [1]. Between 2018 and 2050, global energy demand is expected to rise by almost 50 percent [2], as presented in Figure 1.1. To satisfy this growing demand, upsurges of fossil fuels (oil, coal, petroleum and natural gas) production have appeared successively over the past few decades, while the energy conversion by other sources is growing slowly, as exemplified in Figure 1.2 for United States [3]. It is predicted that fossil fuels will continue to play an important role in meeting global energy needs in the coming decades [2,4], as indicated in Figure 1.3. Fossil fuels are projected to continue to account for no less than 70 percent of total world energy consumption until 2050, although consumption of renewable energy is rising [2].

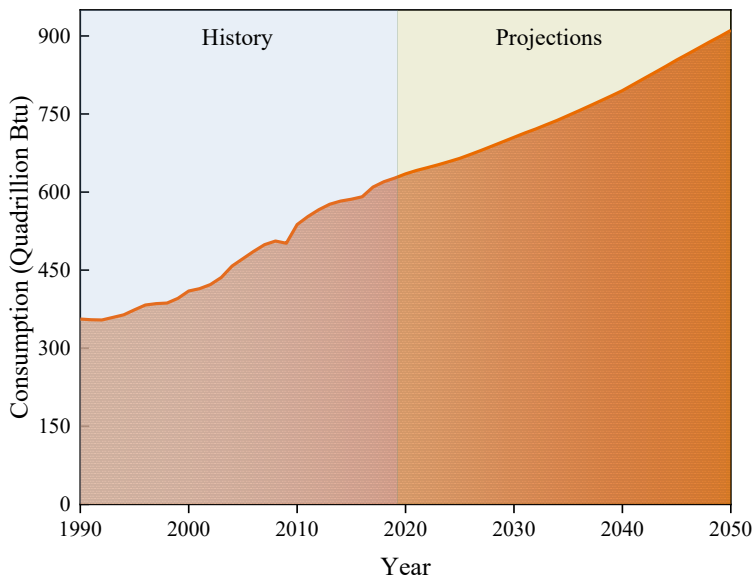


Figure 1.1 Total world energy consumption. Data adapted from U.S. Energy Information Administration [2].

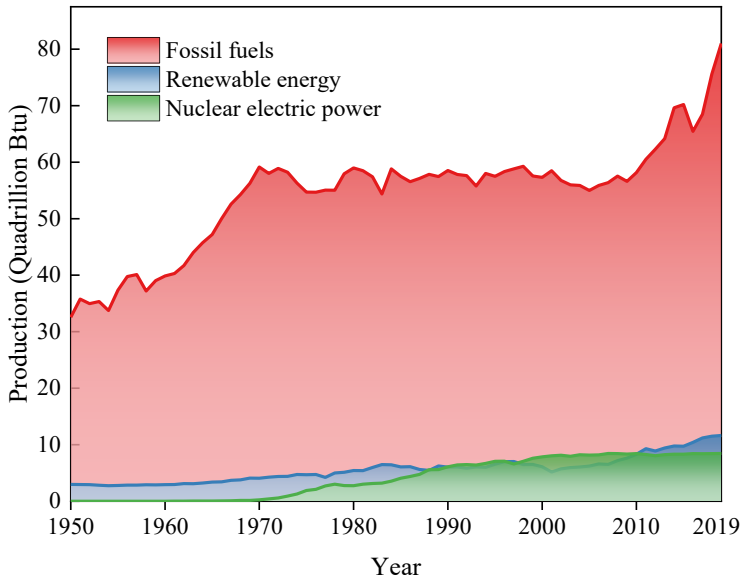


Figure 1.2 Primary energy production in the United States. Data adapted from U.S. Energy Information Administration [3].

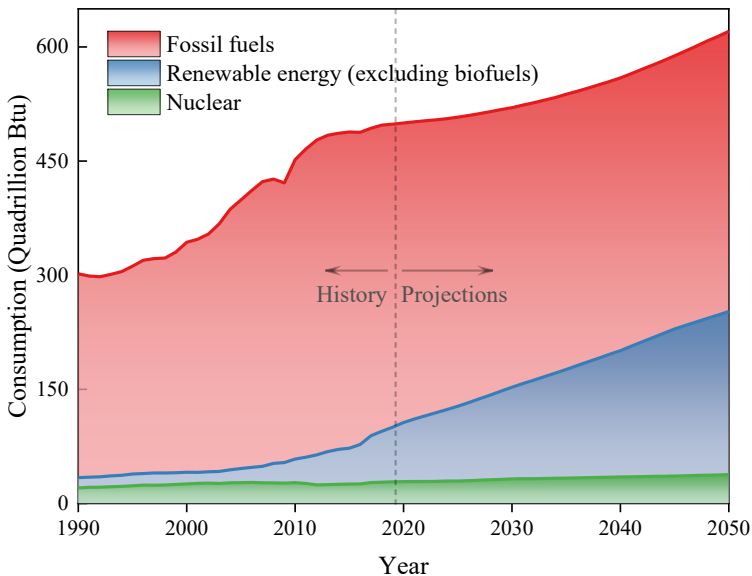


Figure 1.3 World energy consumption from different energy sources. Data adapted from U.S. Energy Information Administration [2].

However, the continuous usage of a vast amount of fossil fuels rapidly increases the carbon dioxide (CO₂) concentration in the atmosphere [1,5], which is commonly recognized as a critical cause of global warming [6]. The environmental problems associated with increasing CO₂ emissions lead to a growing concern from the global community. Agreements such as the Kyoto Protocol [7] and the Paris Agreement [8] were signed by many countries as common efforts to reduce the emissions of greenhouse gases and slow the pace of global warming. It is very crucial to develop technologies to minimize the CO₂ emissions from the usage of fossil fuels.

1.2 Carbon capture technologies

Carbon capture technologies have been developed to reduce CO₂ emissions from processes based on burning of fossil fuels. The carbon capture technologies are mainly based on three different implementation schemes: post-combustion, pre-combustion and oxyfuel combustion [9].

In the post-combustion scheme, CO₂ is captured from the exhaust gases resulting from fuel combustion with air. This route can easily be retrofitted into existing plants, but the capture efficiency is significantly challenged by the low CO₂ content in combustion flue gas [10], which is caused by a significant volume of nitrogen (~ 79 vol%) from the air, used for combustion [11]. The energy penalty and the associated costs are elevated in order to achieve a CO₂ concentration above 95.5 % for transport and storage [12]. It was estimated that the utilization of post-combustion in gas and coal-fired plants would increase the cost of electricity by 32 % and 65 %, respectively [13].

By contrast, in the oxyfuel combustion scheme, the combustion of fuel is conducted in almost pure oxygen instead of air. The exhaust gases possess a rather high concentration of CO₂ (over 80 %) and a low nitrogen content, which simplifies the subsequent CO₂ purification and separation processes [12]. The oxyfuel technique can be regarded as a modified post-combustion, and is technically feasible if a large quantity of high purity oxygen is continuously supplied [11]. The major part of the

efficiency losses within the oxyfuel combustion process is due to the need of an oxygen feed [14].

In the pre-combustion scheme, CO₂ is separated and captured from a gas mixture of H₂ and CO₂ with high CO₂ concentration (>20 %) [12]. The gas mixture results from the reaction between steam and syngas (mainly CO and H₂). The syngas can be obtained by partial oxidization of coal or hydrocarbon fuels (e.g. CH₄), where a pure stream of oxygen is needed. With a more moderate energy penalty of 10 %, the pre-combustion capture tends to have a broad potential [12]. However, deploying facilities for pre-combustion capture requires very high capital investments [12].

In general, if oxygen can be produced by economic processes, the oxyfuel combustion scheme is more promising to realize economical capture of CO₂.

1.3 Oxygen transport membranes

Ceramic oxygen-ion transport membranes are very attractive materials due to their capability to enhance the efficiency of pure oxygen production. Substantial economic and environmental benefits can be attained by applying ceramic oxygen-ion transport membranes in carbon capture technologies [9].

Large-scale oxygen production is currently relying on the cryogenic air separation process, in which air is firstly compressed, then liquefied at very low temperatures (approximately -185 °C), and distillation is carried out to remove oxygen from the air [15]. This process is very effective: it can be controlled precisely by adjustments of pressure and temperature [15]. However, due to the use of electromotive-driven equipment to compress the air, a substantial energy penalty is incurred [16]. In addition, the costs of investment in a cryogenic distillation unit is high and may account for more than 30 % of the total costs of investment [17]. Therefore, the cryogenic air separation process is typically costly and is not an economical process for CO₂ capture through the oxyfuel combustion scheme.

To lower capital costs and energy consumption for pure oxygen production, a high-temperature membrane air separation technology can be implemented using dense mixed ionic-electronic conductive ceramic membranes as key components, which possess a 100 % selectivity regarding O_2 [18]. The oxygen permeation through the membrane initiates when two sides of the membrane experience different oxygen partial pressures at high temperatures. The mechanism of oxygen transport and membrane materials are introduced in section 1.3.1 and 1.3.2, respectively.

1.3.1 Mechanism of oxygen transport

When an oxygen partial pressure (P_{O_2}) gradient is imposed across the membrane at elevated temperatures (typically in the range of 700-1000 °C), the oxygen permeation process starts with three main steps: gas-solid interfacial exchange at the membrane surface exposed to high oxygen partial pressure (P'_{O_2}), ambipolar diffusion of charged carriers through the bulk of the oxygen transport membrane and gas-solid interfacial exchange at the membrane surface exposed to low oxygen partial pressure (P''_{O_2}).

The gas-solid interfacial exchange process is also known as surface exchange. For surface exchange at the membrane surface, exposed to high oxygen partial pressure, multiple steps take place: oxygen adsorption, oxygen dissociation, incorporation of dissociated oxygen ions into the membrane lattice and catching electrons, which can be written as equation (1.1) using the Kröger-Vink notation [19]. Correspondingly, the reversed form of equation (1.1) can represent surface exchange at the membrane surface exposed to low oxygen partial pressure, as shown in equation (1.2).



where subscripts O_o , V_o and h represents an oxygen ion occupying an oxygen lattice site, an oxygen vacancy and an electron hole, respectively. And superscripts \times and \cdot denote an electroneutral state and one positive effective charge, respectively.

When oxygen ions and electrons are regarded as charge carriers and the diffusion paths of oxygen ions are not addressed, the overall reactions related to oxygen exchange at two sides can be simplified as equation (1.3) and equation (1.4), respectively [19].



The ambipolar diffusion of charge carriers through the bulk is schematically illustrated in Figure 1.4. The oxygen ions and electrons resulted from equation (1.3) and (1.4), respectively, pass through the bulk of the membrane in opposite directions (see Figure 1.4). Oxygen ions diffuse either through oxygen vacancies or oxygen interstitial sites [19].

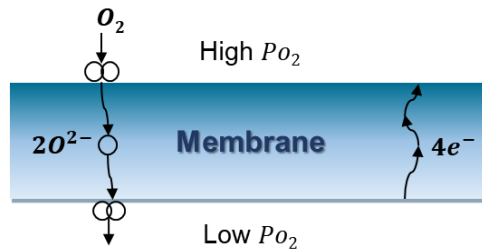


Figure 1.4 Schematics representing oxygen transport processes through a mixed ionic-electronic conductive ceramic membrane when charge carriers are considered to be oxygen ions and electrons.

The overall oxygen transport process is limited by the slowest step. If bulk diffusion is the only rate-limiting step, the oxygen permeation flux through the membrane can be described by the Wagner equation [20, 21]:

$$J_{O_2} = -\frac{R \cdot T}{16 \cdot F^2 \cdot L} \cdot \int_{\ln P'_{O_2}}^{\ln P''_{O_2}} \sigma_{amb} \cdot \ln P_{O_2} \quad (1.5)$$

where T is the temperature, R the gas constant, L the thickness of the membrane, F the Faraday constant, σ_{amb} is the ambipolar conductivity.

When the limiting effects from surface exchange are not negligible, the oxygen permeation flux is reduced according to [20]:

$$J_{O_2} = -\frac{1}{1 + \frac{2L_c}{L}} \cdot \frac{R \cdot T}{16 \cdot F^2 \cdot L} \cdot \int_{\ln P'_{O_2}}^{\ln P''_{O_2}} \sigma_{amb} \cdot \ln P_{O_2} \quad (1.6)$$

where L_c is a characteristic thickness, defined as being the thickness where the resistances from bulk diffusion and surface exchange are equal [22]. When $L_c \ll L$, the limiting effect from surface exchange is negligible, hence, bulk diffusion is the major rate-limiting step, and equation (1.6) can be simplified leading to equation (1.5). However, when L is in the vicinity of L_c , the limiting effects from surface exchange are non-negligible [20].

1.3.2 Membrane materials

According to the phase constituents used for the realization of ambipolar diffusion of oxygen ions and electrons, the membrane materials can be classified into two groups: single phase membranes and dual phase membranes [23], as illustrated in Figure 1.5. The single phase membranes rely on one phase to realize mixed ionic-electronic conductivity (see Figure 1.5(a)), while the dual phase membranes utilizes two kinds of phases to obtain mixed ionic-electronic conductivity (see Figure 1.5(b)); each kind of phase contributes either to ionic or electronic conductivity.

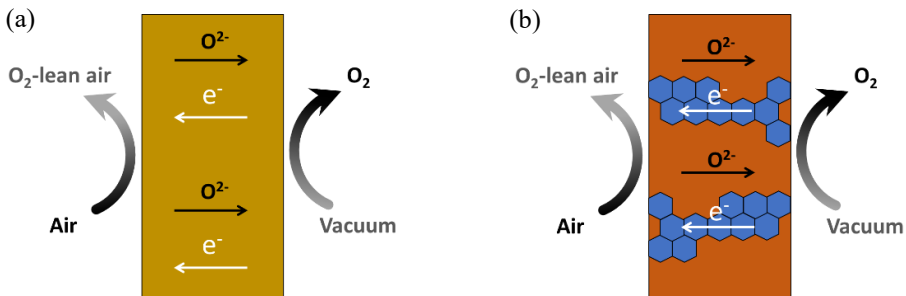


Figure 1.5 Schematics representing (a) single phase membrane and (b) dual phase membrane for oxygen permeation. In (b), the hexagons represent the electronic conducting phase, which is surrounded by the ionic conducting phase.

Single phase membranes

Single phase membranes, exhibiting high oxygen flux are typically made of ceramics with the perovskite structure. An ideal perovskite structure is a cubic symmetry with a formula of ABO_3 , in which A, B and O are the larger cations, smaller cation and oxygen anion, respectively. A can be either a rare earth metal, an alkali metal or an alkaline earth metal, locating at the corners surrounded by twelve equidistant oxygen ions [24], as schematically displayed in Figure 1.6(a). B is typically a transition metal or rare earth metal at the centre of the cube, forming an octahedral with six neighboring oxygen ions [24]. As an alternative representation, Figure 1.6(b) provides a view of the cubic structure with A cations at the centre and B cations at the corner [24].

To allow oxygen ion conductivity, it is necessary to introduce oxygen vacancies by partial substitution of original cations at the A-site by another cation with a lower oxidation state than the initial one [25]. On the other hand, the B-site usually contains cations with variable valences, e.g. Fe and Co, which introduces high electronic or hole conduction. Typical perovskite materials with A and B-site doping are $Ba_{0.5}Sr_{0.5}Co_{0.8}Fe_{0.2}O_{3-\delta}$ (BSCF) and $La_{0.6}Sr_{0.4}Co_{0.2}Fe_{0.8}O_{3-\delta}$ (LSCF), which have been studied intensively for application as oxygen transport materials due to the exceptional oxygen permeability [26-34]. However, the BSCF membrane suffers from poor structural stability at intermediate temperature due to the growth of the hexagonal phase, which already leads to a 50 % decrease in oxygen permeability after 240 h of operation at 750 °C [35]. Besides, BSCF and LSCF membranes are prone to irreversible material deterioration on exposure to CO_2 and/or SO_2 under a chemical potential gradient at elevated temperatures [36-43]. For example, the oxygen flux of the BSCF membrane decreases to zero within several minutes when exposed to CO_2 due to carbonating reactions [36, 41]. Irreversible decomposition was reported for the LSCF membrane after SO_2 exposure [38]. Consequently, these high oxygen permeable perovskite materials are not suitable for application in carbon capture technologies.

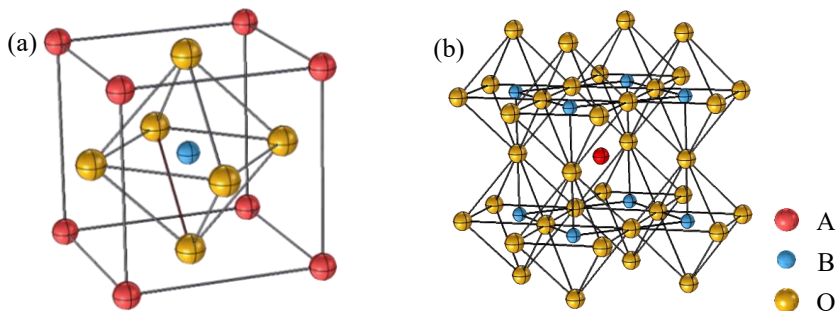


Figure 1.6 Schematic views of ideal cubic perovskite structures (ABO_3) with individual centres of (a) A cation and (b) B cation.

Dual phase membranes

Dual phase membranes consist of an oxygen conducting phase (or phases) and an electron conducting phase (or phases), which are responsible for conducting oxygen ions and electrons, respectively (see Figure 1.5(b)). Oxides with a fluorite structure, e.g. gadolinium- or samarium-doped ceria, and yttria-stabilized zirconia, are often selected as the ion-conducting phase for these dual phase membranes because of their high ionic conductivity as well as their high chemical stability in an acidic atmosphere [44-46]. The high ionic conductivities of fluorite oxides are benefiting from oxygen vacancies generated by doping. In case of $Ce_{1-x}Gd_xO_{2-\delta}$ ($x = 0.1$ or 0.2), as examples, oxygen vacancies are created by the substitution of Ce in CeO_2 by Gd according to [47]:



where subscripts Ce and O represents the Ce and O site within the fluorite lattice, respectively. Superscripts \times , $'$, and $''$ denote an electroneutral state, one negative effective charge, and two positive effective charges, respectively. The introduction of oxygen vacancies expands the lattice, which is known as a chemical expansion [48].

The electron conducting phase should ideally possess a stability as good as the typical ionic conducting phases, i.e. fluorite oxides. Besides, it should be thermally

and chemically compatible with the ionic conducting phase. Spinel oxides, e.g. $\text{Fe}_x\text{Co}_{3-x}\text{O}_4$ ($x = 1$ or 2), NiFe_2O_4 , and $\text{Mn}_{1.5}\text{Co}_{1.5}\text{O}_4$, have attracted considerable attention as suitable electronic conducting phases combined with fluorite oxides to form robust high-performance dual phase membranes [49-53]. For example, 60 wt% $\text{Ce}_{0.9}\text{Gd}_{0.1}\text{O}_{2-\delta}$ -40 wt% NiFe_2O_4 membranes experienced no decline of the oxygen permeation flux within a 100 h operation using CO_2 as sweep gas [54]. Furthermore, 40 vol% $\text{Ce}_{0.8}\text{Tb}_{0.2}\text{O}_{2-\delta}$ -60 vol% NiFe_2O_4 membrane remained stable in wet SO_2 and CO_2 containing gas at 800 °C for 170 h [55], and its oxygen flux was reported to even increase after 76 h permeation test using CO_2 as sweep gas [55].

Overall, the key advantage of a dual phase membrane over a perovskite membrane is the high stability under acidic atmospheres (e.g. CO_2 and SO_2).

Promising material candidates for carbon capture

Dual phase membranes are supposed to have more potential for oxyfuel applications than perovskite membranes. A promising material candidate, developed specifically for oxyfuel combustion, is the $\text{Ce}_{0.8}\text{Gd}_{0.2}\text{O}_{2-\delta}$ - FeCo_2O_4 membrane, which mainly consists of a $\text{Ce}_{1-x}\text{Gd}_x\text{O}_{2-\delta}$ ($0 < x < 0.2$) (CGO) fluorite phase as the ion conducting phase, as well as a $\text{Fe}_y\text{Co}_{3-y}\text{O}_4$ ($0 < y < 2$) (FCO) spinel phase and a $\text{Gd}_{0.85}\text{Ce}_{0.15}\text{Fe}_{0.75}\text{Co}_{0.25}\text{O}_3$ (GCFCO) perovskite phase as the electron conducting phases [49]. The composition 85 wt% $\text{Ce}_{0.8}\text{Gd}_{0.2}\text{O}_{2-\delta}$ -15 wt% FeCo_2O_4 possesses high tolerance over 200 h operation in CO_2 - and SO_2 -containing gas mixtures at 850 °C under an oxygen partial pressure gradient [50]. To reduce cost from carbon capture, it is necessary to develop facile, efficient and economical synthesis methods to prepare membrane components with high and reliable mechanical and chemical performance. Hence, solid-state reaction plus sintering in a single-step thermal process (i.e. solid-state reactive sintering) appears to be a very attractive method for scaling up the production of oxygen transport membranes [56].

1.4 Scope of the thesis

This thesis includes a concise framework of studies on $\text{Ce}_{0.8}\text{Gd}_{0.2}\text{O}_{2-\delta}\text{-FeCo}_2\text{O}_4$ dual phase membranes prepared by solid-state reactive sintering using $\text{Ce}_{0.8}\text{Gd}_{0.2}\text{O}_{2-\delta}$, Co_3O_4 and Fe_2O_3 as raw materials. The main aim of the work is to enhance mechanical reliability and oxygen permeation of $\text{Ce}_{0.8}\text{Gd}_{0.2}\text{O}_{2-\delta}\text{-FeCo}_2\text{O}_4$ dual phase membranes by optimizing the powder preparation method, which affects phase constituents and microstructural characteristics (i.e. density, grain sizes, phase distributions and defects/microcracks) of the sintered membranes. The powder mixtures used for solid-state reactive sintering are prepared by different mixing and milling procedures to tune the particle size and homogeneity. The microstructural characteristics and phase constituents of the sintered membranes are analyzed in detail, and their influences on mechanical reliability (i.e. residual stress, mechanical properties, subcritical crack growth, and lifetime prediction) and chemical performance characteristics regarding ionic/electronic conductivity and oxygen permeation are discussed.

Detailed characterizations and quantifications regarding phase constituents and microstructural features for $\text{Ce}_{0.8}\text{Gd}_{0.2}\text{O}_{2-\delta}\text{-FeCo}_2\text{O}_4$ dual phase membranes are presented in **Chapter 2**. All aspects including phase constituents, phase volume fraction, grain size, and phase contiguity are discussed, as well as the relation between these microstructure features and chemical properties. Besides, a novel model is utilized to assess the evolution of the ambipolar conductivity with respect to phase constituents and microstructural features.

In **Chapter 3**, the mechanical properties and subcritical crack growth behaviour of the synthesized $\text{Ce}_{0.8}\text{Gd}_{0.2}\text{O}_{2-\delta}\text{-FeCo}_2\text{O}_4$ dual phase membranes are characterized based on mechanical testing results from Vickers indentations and ring-on-ring tests using different loading rates. The objective is to assess the limits in mechanical application in particular regarding reliability and lifetime. Mechanical properties, including elastic modulus, hardness, fracture toughness and fracture strength are assessed at room temperature, and their relationships with the composition, residual

stress and microstructural characteristics, like grain size and microcrack size/concentration, are discussed. The subcritical crack growth behaviour and the failure probability are analyzed based on fracture stress data obtained at different loading rates, and based on the lifetime under static stress. The associated effects of composition, residual stress and microcracks are discussed.

The $\text{Ce}_{0.8}\text{Gd}_{0.2}\text{O}_{2-\delta}\text{-FeCo}_2\text{O}_4$ dual phase membranes investigated in **Chapter 2** and **Chapter 3** are further improved regarding mechanical and chemical performance by optimizing particle sizes and homogeneities of initial powder mixtures. The improved membranes are the research focus in **Chapters 4-7**.

The effects of sintering profiles on the microstructural and mechanical characteristics of 85 wt% $\text{Ce}_{0.8}\text{Gd}_{0.2}\text{O}_{2-\delta}$ -15 wt% FeCo_2O_4 membrane prepared by using optimized powder mixtures are investigated in **Chapter 4**. The phase interaction temperatures as determined by high-temperature X-ray diffraction are selected as sintering temperatures to assess the effect of the phase interactions on microstructural characteristics. The relations between the mechanical properties and the microstructural changes are discussed, and finally, an optimal sintering temperature is proposed, and applied to sinter the $\text{Ce}_{0.8}\text{Gd}_{0.2}\text{O}_{2-\delta}\text{-FeCo}_2\text{O}_4$ dual phase membranes to be investigated in **Chapters 5-7**.

In **Chapter 5**, micro-mechanical properties (elastic modulus and hardness) of $\text{Ce}_{0.8}\text{Gd}_{0.2}\text{O}_{2-\delta}\text{-FeCo}_2\text{O}_4$ dual phase membranes prepared by the optimized powder mixtures are characterized via indentation testing at room temperature. In order to reveal contributions of the mechanical properties of individual phases to the mechanical properties of the composites, the grain sizes of individual phases in composites are optimized for the mechanical properties assessment of individual phases via targeted indentation testing. The relationships between mechanical properties of the composites and compositional variations as well as porosities are discussed.

As the membranes need to provide sufficient mechanical strength to realize long-term reliable operation, **Chapter 6** focuses on the characterization of fracture strength and residual stresses, as well as the development of thermal processing steps to alleviate detrimental residual stresses (tensile stresses), for $\text{Ce}_{0.8}\text{Gd}_{0.2}\text{O}_{2-\delta}$ - FeCo_2O_4 dual phase membranes prepared by optimized powder mixtures. Investigations are focused on the typical aspects that challenge the fracture behaviour, including composition and microstructural defects, as well as residual stress and residual stress gradient, which are derived from X-ray diffraction (based on the $\sin^2 \psi$ method) and the indentation method. The relation between fracture strength and residual stress is discussed according to fractography analysis for membranes fractured with different surface positions that experience different residual stress states after sintering.

Chapter 7 compares microstructural characteristics and oxygen permeation performance of a 85 wt% $\text{Ce}_{0.8}\text{Gd}_{0.2}\text{O}_{2-\delta}$ -15 wt% FeCo_2O_4 membrane prepared by the unoptimized and optimized powder mixtures. The effect of milling procedures on particle sizes of the raw materials and powder mixtures are analyzed in detail. In comparison to the traditional ball-milling method, a facile but effective dry mixing method is developed to prepare inhomogeneous powder mixtures. The microstructural characteristics and phase constituents of all sintered membranes are analyzed in detail, and their influence on oxygen permeation performance is discussed.

Finally, **Chapter 8** reflects on the importance of the overall findings, and provides recommendations for future research.

References

- [1] M.A. Abdelkareem, K. Elsaid, T. Wilberforce, M. Kamil, E.T. Sayed, A. Olabi, Environmental aspects of fuel cells: A review, *Science of the Total Environment* 752 (2021) 141803.
- [2] Monthly energy review, US Energy Information Administration (EIA), Washington, DC, USA, 2020.
- [3] L. Capuano, International energy outlook 2020 (IEO2020), US Energy Information Administration (EIA), Washington, DC, USA, 2020.
- [4] N. Abas, A. Kalair, N. Khan, Review of fossil fuels and future energy technologies, *Futures* 69 (2015) 31-49.
- [5] M.D. Leonard, E.E. Michaelides, D.N. Michaelides, Energy storage needs for the substitution of fossil fuel power plants with renewables, *Renewable Energy* 145 (2020) 951-962.
- [6] V. Ramanathan, Y. Feng, Air pollution, greenhouse gases and climate change: Global and regional perspectives, *Atmospheric Environment* 43(1) (2009) 37-50.
- [7] S. Oberthür, H.E. Ott, *The Kyoto Protocol: international climate policy for the 21st century*, Springer Science & Business Media 1999.
- [8] P. Agreement, Paris agreement, HeinOnline, p. 2017.
- [9] R. Kneer, D. Toporov, M. Förster, D. Christ, C. Broeckmann, E. Pfaff, M. Zwick, S. Engels, M. Modigell, OXYCOAL-AC: Towards an integrated coal-fired power plant process with ion transport membrane-based oxygen supply, *Energy & Environmental Science* 3(2) (2010) 198-207.
- [10] D.Y.C. Leung, G. Caramanna, M.M. Maroto-Valer, An overview of current status of carbon dioxide capture and storage technologies, *Renewable and Sustainable Energy Reviews* 39 (2014) 426-443.
- [11] B.J.P. Buhre, L.K. Elliott, C.D. Sheng, R.P. Gupta, T.F. Wall, Oxy-fuel combustion technology for coal-fired power generation, *Progress in Energy and Combustion Science* 31(4) (2005) 283-307.
- [12] A.A. Olajire, CO₂ capture and separation technologies for end-of-pipe applications-a review, *Energy* 35(6) (2010) 2610-2628.

- [13] M. Kanniche, R. Gros-Bonnivard, P. Jaud, J. Valle-Marcos, J.-M. Amann, C. Bouallou, Pre-combustion, post-combustion and oxy-combustion in thermal power plant for CO₂ capture, *Applied Thermal Engineering* 30(1) (2010) 53-62.
- [14] I. Pfaff, A. Kather, Comparative thermodynamic analysis and integration issues of CCS steam power plants based on oxy-combustion with cryogenic or membrane based air separation, *Energy Procedia* 1(1) (2009) 495-502.
- [15] B. Moghtaderi, Application of chemical looping concept for air separation at high temperatures, *Energy & Fuels* 24(1) (2010) 190-198.
- [16] J. Dou, E. Krzystowczyk, A. Mishra, X. Liu, F. Li, Perovskite Promoted Mixed Cobalt–Iron Oxides for Enhanced Chemical Looping Air Separation, *ACS Sustainable Chemistry & Engineering* 6(11) (2018) 15528-15540.
- [17] Y. Zeng, S. Tamhankar, N. Ramprasad, F. Fitch, D. Acharya, R. Wolf, A novel cyclic process for synthesis gas production, *Chemical Engineering Science* 58(3-6) (2003) 577-582.
- [18] X. Zhu, W. Yang, *Mixed conducting ceramic membranes*, Springer, 2017.
- [19] X. Zhu, W. Yang, *Introduction to Mixed Ionic-Electronic Conducting Membranes, Mixed Conducting Ceramic Membranes*, Springer 2017, pp. 1-10.
- [20] J.H. Joo, G.S. Park, C.-Y. Yoo, J.H. Yu, Contribution of the surface exchange kinetics to the oxygen transport properties in Gd_{0.1}Ce_{0.9}O_{2-δ}-La_{0.6}Sr_{0.4}Co_{0.2}Fe_{0.8}O_{3-δ} dual-phase membrane, *Solid State Ionics* 253 (2013) 64-69.
- [21] F. Zeng, J. Malzbender, S. Baumann, M. Krüger, L. Winnubst, O. Guillon, W.A. Meulenber, Phase and microstructural characterizations for Ce_{0.8}Gd_{0.2}O_{2-δ}-FeCo₂O₄ dual phase oxygen transport membranes, *Journal of the European Ceramic Society* 40(15) (2020) 5646-5652.
- [22] C. Li, W. Li, J.J. Chew, S. Liu, X. Zhu, J. Sunarso, Rate determining step in SDC-SSAF dual-phase oxygen permeation membrane, *Journal of Membrane Science* 573 (2019) 628-638.
- [23] X. Zhu, W. Yang, *Mixed conducting ceramic membranes*, Springer-Verlag, Berlin, Germany, 2017.
- [24] W. Zhou, R. Ran, Z. Shao, Progress in understanding and development of Ba_{0.5}Sr_{0.5}Co_{0.8}Fe_{0.2}O_{3-δ}-based cathodes for intermediate-temperature solid-oxide fuel cells: a review, *Journal of Power Sources* 192(2) (2009) 231-246.

- [25] K. Zhang, J. Sunarso, Z. Shao, W. Zhou, C. Sun, S. Wang, S. Liu, Research progress and materials selection guidelines on mixed conducting perovskite-type ceramic membranes for oxygen production, *RSC Advances* 1(9) (2011) 1661-1676.
- [26] S. Baumann, J. Serra, M. Lobera, S. Escolástico, F. Schulze-Küppers, W.A. Meulenberg, Ultrahigh oxygen permeation flux through supported $\text{Ba}_{0.5}\text{Sr}_{0.5}\text{Co}_{0.8}\text{Fe}_{0.2}\text{O}_{3-\delta}$ membranes, *Journal of Membrane Science* 377(1-2) (2011) 198-205.
- [27] Z. Shao, W. Yang, Y. Cong, H. Dong, J. Tong, G. Xiong, Investigation of the permeation behavior and stability of a $\text{Ba}_{0.5}\text{Sr}_{0.5}\text{Co}_{0.8}\text{Fe}_{0.2}\text{O}_{3-\delta}$ oxygen membrane, *Journal of Membrane Science* 172(1-2) (2000) 177-188.
- [28] Z. Shao, G. Xiong, H. Dong, W. Yang, L. Lin, Synthesis, oxygen permeation study and membrane performance of a $\text{Ba}_{0.5}\text{Sr}_{0.5}\text{Co}_{0.8}\text{Fe}_{0.2}\text{O}_{3-\delta}$ oxygen-permeable dense ceramic reactor for partial oxidation of methane to syngas, *Separation and Purification Technology* 25(1-3) (2001) 97-116.
- [29] H. Wang, Y. Cong, W. Yang, Oxygen permeation study in a tubular $\text{Ba}_{0.5}\text{Sr}_{0.5}\text{Co}_{0.8}\text{Fe}_{0.2}\text{O}_{3-\delta}$ oxygen permeable membrane, *Journal of Membrane Science* 210(2) (2002) 259-271.
- [30] J.M. Serra, J. Garcia-Fayos, S. Baumann, F. Schulze-Küppers, W.A. Meulenberg, Oxygen permeation through tape-cast asymmetric all- $\text{La}_{0.6}\text{Sr}_{0.4}\text{Co}_{0.2}\text{Fe}_{0.8}\text{O}_{3-\delta}$ membranes, *Journal of Membrane Science* 447 (2013) 297-305.
- [31] J.A. Lane, S.J. Benson, D. Waller, J.A. Kilner, Oxygen transport in $\text{La}_{0.6}\text{Sr}_{0.4}\text{Co}_{0.2}\text{Fe}_{0.8}\text{O}_{3-\delta}$, *Solid State Ionics* 121(1-4) (1999) 201-208.
- [32] X. Tan, Z. Wang, H. Liu, S. Liu, Enhancement of oxygen permeation through $\text{La}_{0.6}\text{Sr}_{0.4}\text{Co}_{0.2}\text{Fe}_{0.8}\text{O}_{3-\delta}$ hollow fibre membranes by surface modifications, *Journal of Membrane Science* 324(1-2) (2008) 128-135.
- [33] X. Tan, K. Li, Modeling of air separation in a LSCF hollow-fiber membrane module, *AIChE Journal* 48(7) (2002) 1469-1477.
- [34] Y. Teraoka, H.-M. Zhang, S. Furukawa, N. Yamazoe, Oxygen permeation through perovskite-type oxides, *Chemistry Letters* 14(11) (1985) 1743-1746.
- [35] K. Efimov, Q. Xu, A. Feldhoff, Transmission electron microscopy study of $\text{Ba}_{0.5}\text{Sr}_{0.5}\text{Co}_{0.8}\text{Fe}_{0.2}\text{O}_{3-\delta}$ perovskite decomposition at intermediate temperatures, *Chemistry of Materials* 22(21) (2010) 5866-5875.

- [36] M. Arnold, H. Wang, A. Feldhoff, Influence of CO₂ on the oxygen permeation performance and the microstructure of perovskite-type (Ba_{0.5}Sr_{0.5})(Co_{0.8}Fe_{0.2})O_{3-δ} membranes, *Journal of Membrane Science* 293(1-2) (2007) 44-52.
- [37] A. Waindich, A. Möbius, M. Müller, Corrosion of Ba_{1-x}Sr_xCo_{1-y}Fe_yO_{3-δ} and La_{0.3}Ba_{0.7}Co_{0.2}Fe_{0.8}O_{3-δ} materials for oxygen separating membranes under Oxycoal conditions, *Journal of Membrane Science* 337(1-2) (2009) 182-187.
- [38] J. Gao, L. Li, Z. Yin, J. Zhang, S. Lu, X. Tan, Poisoning effect of SO₂ on the oxygen permeation behavior of La_{0.6}Sr_{0.4}Co_{0.2}Fe_{0.8}O_{3-δ} perovskite hollow fiber membranes, *Journal of Membrane Science* 455 (2014) 341-348.
- [39] T. Ramirez-Reina, J.L. Santos, N. García-Moncada, S. Ivanova, J.A. Odriozola, Development of Robust Mixed-Conducting Membranes with High Permeability and Stability, *Perovskites and Related Mixed Oxides* (2016) 719-738.
- [40] S. Engels, T. Markus, M. Modiggell, L. Singheiser, Oxygen permeation and stability investigations on MIEC membrane materials under operating conditions for power plant processes, *Journal of Membrane Science* 370(1-2) (2011) 58-69.
- [41] M. Schulz, R. Kriegel, A. Kämpfer, Assessment of CO₂ stability and oxygen flux of oxygen permeable membranes, *Journal of Membrane Science* 378(1-2) (2011) 10-17.
- [42] X. Tan, N. Liu, B. Meng, J. Sunarso, K. Zhang, S. Liu, Oxygen permeation behavior of La_{0.6}Sr_{0.4}Co_{0.8}Fe_{0.2}O₃ hollow fibre membranes with highly concentrated CO₂ exposure, *Journal of Membrane Science* 389 (2012) 216-222.
- [43] S.J. Benson, D. Waller, J.A. Kilner, Degradation of La_{0.6}Sr_{0.4}Fe_{0.8}Co_{0.2}O_{3-δ} in Carbon Dioxide and Water Atmospheres, *Journal of the Electrochemical Society* 146(4) (1999) 1305.
- [44] J.H. Joo, K.S. Yun, C.-Y. Yoo, J.H. Yu, Novel oxygen transport membranes with tunable segmented structures, *Journal of Materials Chemistry A* 2(22) (2014) 8174-8178.
- [45] K. Zhang, Z. Shao, C. Li, S. Liu, Novel CO₂-tolerant ion-transporting ceramic membranes with an external short circuit for oxygen separation at intermediate temperatures, *Energy & Environmental Science* 5(1) (2012) 5257-5264.
- [46] K.S. Yun, C.-Y. Yoo, S.-G. Yoon, J.H. Yu, J.H. Joo, Chemically and thermo-mechanically stable LSM-YSZ segmented oxygen permeable ceramic membrane, *Journal of Membrane Science* 486 (2015) 222-228.

- [47] M. Mogensen, T. Lindegaard, U.R. Hansen, G. Mogensen, Physical properties of mixed conductor solid oxide fuel cell anodes of doped CeO_2 , *Journal of the Electrochemical Society* 141(8) (1994) 2122.
- [48] K.L. Duncan, Y. Wang, S.R. Bishop, F. Ebrahimi, E.D. Wachsman, Role of point defects in the physical properties of fluorite oxides, *Journal of the American Ceramic Society* 89(10) (2006) 3162-3166.
- [49] M. Ramasamy, E. Persoon, S. Baumann, M. Schroeder, F. Schulze-Küppers, D. Görtz, R. Bhave, M. Bram, W.A. Meulenber, Structural and chemical stability of high performance $\text{Ce}_{0.8}\text{Gd}_{0.2}\text{O}_{2-\delta}$ - FeCo_2O_4 dual phase oxygen transport membranes, *Journal of Membrane Science* 544 (2017) 278-286.
- [50] Y. Lin, S. Fang, D. Su, K.S. Brinkman, F. Chen, Enhancing grain boundary ionic conductivity in mixed ionic-electronic conductors, *Nature communications* 6 (2015) 6824.
- [51] J. Garcia-Fayos, M. Balaguer, J.M. Serra, Dual-Phase Oxygen Transport Membranes for Stable Operation in Environments Containing Carbon Dioxide and Sulfur Dioxide, *ChemSusChem* 8(24) (2015) 4242-4249.
- [52] H. Luo, H. Jiang, T. Klande, F. Liang, Z. Cao, H. Wang, J. Caro, Rapid glycine-nitrate combustion synthesis of the CO_2 -stable dual phase membrane $40\text{Mn}_{1.5}\text{Co}_{1.5}\text{O}_{4-\delta}$ - $60\text{Ce}_{0.9}\text{Pr}_{0.1}\text{O}_{2-\delta}$ for CO_2 capture via an oxy-fuel process, *Journal of Membrane Science* 423-424 (2012) 450-458.
- [53] C. Zhang, J. Sunarso, S. Liu, Designing CO_2 -resistant oxygen-selective mixed ionic-electronic conducting membranes: guidelines, recent advances, and forward directions, *Chemical Society Reviews* 46(10) (2017) 2941-3005.
- [54] H. Luo, K. Efimov, H. Jiang, A. Feldhoff, H. Wang, J. Caro, CO_2 -stable and cobalt-free dual-phase membrane for oxygen separation, *Angewandte Chemie International Edition* 50(3) (2011) 759-763.
- [55] M. Balaguer, J. García-Fayos, C. Solís, J.M. Serra, Fast oxygen separation through SO_2 - and CO_2 -stable dual-phase membrane based on NiFe_2O_4 - $\text{Ce}_{0.8}\text{Tb}_{0.2}\text{O}_{2-\delta}$, *Chemistry of Materials* 25(24) (2013) 4986-4993.
- [56] J. Zhu, G. Zhang, G. Liu, Z. Liu, W. Jin, N. Xu, Perovskite hollow fibers with precisely controlled cation stoichiometry via one-step thermal processing, *Advanced Materials* 29(18) (2017) 1606377.

CHAPTER 2

Phase and microstructural characterizations for $\text{Ce}_{0.8}\text{Gd}_{0.2}\text{O}_{2-\delta}\text{-FeCo}_2\text{O}_4$ dual phase oxygen transport membranes

Abstract

Dual phase oxygen transport membranes were prepared via solid state reaction at 1200 °C. The sintered membranes were characterized via X-ray diffraction, back scattered electron microscopy and electron backscatter diffraction, and associated with image analysis and calculations to quantify phase compositions and microstructural features including volume fractions, grain sizes, and contiguity. The characterizations reveal a multi-phase system containing $\text{Ce}_{1-x}\text{Gd}_x\text{O}_{2-\delta}$ ($x \approx 0.1$) (CGO10), and $\text{Fe}_y\text{Co}_{3-y}\text{O}_4$ ($0.2 < y < 1.2$) (FCO), CoO and $\text{Gd}_{0.85}\text{Ce}_{0.15}\text{Fe}_{0.75}\text{Co}_{0.25}\text{O}_3$ (GCFCO) in the sintered membranes. In addition, a novel model is utilized to assess the evolution of the ambipolar conductivity with respect to microstructural features. Both experimental and calculated results indicate that if the grain sizes of all phases in the composites are similar, the optimal ambipolar conductivity is reached with a volume ratio of ionic conducting phase to electronic conducting phase close to 4:1. Meanwhile, the GCFCO phase dominates the effective electronic conductivity.

This chapter has been published as: F. Zeng, J. Malzbender, S. Baumann, M. Krüger, L. Winnubst, O. Guillon, W.A. Meulenber, Phase and microstructural characterizations for $\text{Ce}_{0.8}\text{Gd}_{0.2}\text{O}_{2-\delta}\text{-FeCo}_2\text{O}_4$ dual phase oxygen transport membranes, *Journal of the European Ceramic Society* 40(15) (2020) 5646-5652.

DOI: 10.1016/j.jeurceramsoc.2020.06.035.

2.1 Introduction

Mixed ionic-electronic conducting (MIEC) membranes provide, due to their almost 100% selectivity with respect to oxygen, high efficiency in terms of pure oxygen separation [1], oxyfuel coal combustion [2] and petro-chemical processes [3]. Typical perovskite-type single phase MIEC membranes, such as $\text{Ba}_{0.5}\text{Sr}_{0.5}\text{Co}_{0.8}\text{Fe}_{0.2}\text{O}_{3-\delta}$ [4] and $\text{La}_{0.6}\text{Sr}_{0.4}\text{Co}_{0.2}\text{Fe}_{0.8}\text{O}_{3-\delta}$ [5], achieve high oxygen fluxes but suffer from carbonation or sulfating reaction induced phase instabilities at elevated temperature on exposure to CO_2 or SO_2 [6, 7].

Dual phase oxygen transport membranes become recently the focus of scientific studies. They consist of separate ionic and electronic conducting phases, and exhibit good chemical stability under flue gas conditions [8]. Their oxygen permeability can be optimized by either selecting high performance and stable individual conducting phases, and/or tailoring microstructural factors like phase volume fraction, grain size, and spatial distribution of the phases [9-11]. The selection of conducting materials permits flexibility since plenty of ionic and electronic conducting phases have been developed and tested regarding their individual performance [12-15].

However, microstructural aspects are more challenging since their influence on properties are not fully understood. For example, it has been suggested for dual phase oxygen transport membranes that a minor phase should possess a volume fraction above 30% to form percolation to obtain high ambipolar conductivity and oxygen permeability [1]. Besides, the grain size of the minor phase was recommended to be smaller or equal to that of the matrix phase [9, 11, 16]. However, for dual phase oxygen transport membrane with a minor phase volume of less than 30%, good oxygen permeability was also reported, such as for 80 vol% $\text{Ce}_{0.8}\text{Sm}_{0.2}\text{O}_{2-\delta}$ -20 vol.% $\text{PrBaCo}_2\text{O}_{5+\delta}$ with a fiber-shaped electronic conductive skeleton [17], and for 81.5 vol% $\text{Ce}_{0.8}\text{Gd}_{0.2}\text{O}_{2-\delta}$ -18.5 vol% FeCo_2O_4 with a multi-phase system consisting of the $\text{Ce}_{1-x}\text{Gd}_x\text{O}_{2-\delta}$ ($0 < x < 0.2$) (CGO) fluorite phase, the $\text{Fe}_y\text{Co}_{3-y}\text{O}_4$ ($0 < y < 2$) (FCO) spinel phase, the CoO rock salt phase, and the $\text{Gd}_{0.85}\text{Ce}_{0.15}\text{Fe}_{0.75}\text{Co}_{0.25}\text{O}_3$ (GCFCO) perovskite phase [8].

Based on the realization of the complex but important microstructures of dual phase oxygen transport membranes, the microstructural characterization, quantification, and optimization are essential as the initial step, especially for dual phase oxygen transport membranes that involve phase interactions. Hence, the current work reports on a detailed characterization and quantification regarding phase constituents and microstructural features for $\text{Ce}_{0.8}\text{Gd}_{0.2}\text{O}_{2-\delta}\text{-FeCo}_2\text{O}_4$ composites. All aspects including phase constituents, phase volume fraction, grain size, and phase contiguity are discussed, as well as the relation between these microstructure features and chemical properties.

2.2 Experimental

Powder mixtures of $\text{Ce}_{0.8}\text{Gd}_{0.2}\text{O}_{2-\delta}$ (CGO20) (Treibacher Industrie AG, 99 %), Co_3O_4 (Merck, 99 %) and Fe_2O_3 (Merck, 99 %) (the mole ratio of $\text{Co}_3\text{O}_4/\text{Fe}_2\text{O}_3$ was fixed at 4:3 to form FeCo_2O_4 (FC2O) spinel) were inserted into a polyethylene bottle with ethanol and 5 mm diameter zirconia balls, and ball milled on a roller bench for 3 days. The mass ratio of powder-ball-ethanol was set to be 1:2:3. After milling, the powders were dried at 75 °C for 3 days, then they were uniaxially pressed into disc shapes with a pressure of 20 MPa and sintered at 1200 °C for 10 h in air to obtain dense composites [18]. Each sintered composite was ground and polished to a mirror finish for characterizations of crystal structure and microstructure. The sintered composites were abbreviated as CF. Finally, five CF composites, abbreviated as 50CF, 60CF, 70CF, 85CF and 90CF, were synthesized via powder mixtures with weight fractions of CGO20 equal to 50 wt%, 60 wt%, 70 wt%, 85 wt% and 90 wt%, respectively. It should be noted, that the amount and chemical composition of each phase in the sintered membranes might be different from the nominal ones in the starting powder mixtures due to phase interactions.

Crystal structures were determined via X-ray diffraction (XRD) (Empyrean, Malvern Panalytical Ltd) equipped with a Cu long fine focus tube, Bragg-Brentano^{HD} mirror, PIXcel3D detector. Crystal structure analysis and associated phase

quantifications were carried out by Rietveld refinement using the software TOPAS 6 (Bruker AXS GmbH) with crystal structure data from the Inorganic Crystal Structure Database (ICSD) (FIZ Karlsruhe GmbH) as references. Microstructures were characterized via backscattered electron images and color-coded phase maps captured from data obtained by back scattered electron microscopy (BSEM) (Merlin, Carl Zeiss Microscopy Ltd) and electron backscatter diffraction (EBSD) (NordlysNano, Oxford Instruments Ltd), respectively. Accordingly, microstructure aspects including grain sizes, and area fractions of the different phases, were deduced via image analysis by the HKL Channel 5 software packages. The volume fraction was regarded to be equal to the area fraction for each phase in a random section through each composite [19]. The porosity of the sintered membrane was deduced from the area fraction of pores based on analysis of at least three BSEM pictures via ImageJ software.

The ambipolar conductivity (σ_{amb}) is defined as a function of partial conductivity of the ionic and electronic conducting phases within the membrane composites [20, 21]:

$$\sigma_{amb} = \frac{\sigma_{p,i} \cdot \sigma_{p,e}}{\sigma_{p,i} + \sigma_{p,e}} \quad (2.1)$$

where $\sigma_{p,i}$ and $\sigma_{p,e}$ represent the partial ionic and electronic conductivity, respectively.

The sum of $\sigma_{p,i}$ and $\sigma_{p,e}$ equals to the total conductivity (σ_t) [20]:

$$\sigma_t = \sigma_{p,i} + \sigma_{p,e} \quad (2.2)$$

The ionic transport number (t_i) and electronic transport number (t_e) are defined by equation (2.3) and (2.4), respectively [20-23]:

$$t_i = \frac{\sigma_{p,i}}{\sigma_t} \quad (2.3)$$

$$t_e = \frac{\sigma_{p,e}}{\sigma_t} \quad (2.4)$$

The sum of t_i and t_e always equals to unity to maintain electroneutrality [24].

A novel model is proposed here to estimate the effect of microstructural characteristics (e.g. volume fraction and grain size) on ambipolar conductivity. The microstructure of a randomly distributed dual phase oxygen transport composite can be disassembled into an equivalent structure containing three portions: effective ionic conducting portion (*I*), effective electronic conducting portion (*II*) and insulated portion (*III*), as illustrated by schematic diagrams in Figure 2.1. The effective ionic/electronic conducting portion is a continuous medium (see Figure 2.1(b)), and assumed to provide the effective ionic/electronic transport paths, and the insulated portion is not contributive to the conductivity. The volume fraction of the effective ionic/electronic conducting portion is then defined as effective volume fraction of ionic/electronic conducting phases. If ionic/electronic conducting phases in the composites possess pure ionic/electronic conductivity, and there are no frictional interactions during ionic and electronic diffusion, the partial conductivity at an equilibrium state under a given temperature and oxygen partial pressure gradient is predicted to be proportional to the effective volume fraction. And the proportionality factor is approximated as intrinsic ionic/electronic conductivity of the ionic/electronic conducting phase in a form of a dense single phase material, as presented by equation (2.5) and (2.6):

$$\sigma_{p,i} = \sigma_i \cdot V_{eff,i} \quad (2.5)$$

$$\sigma_{p,e} = \sigma_e \cdot V_{eff,e} \quad (2.6)$$

where σ_i and σ_e are the intrinsic ionic conductivity of the ionic conducting phase and the intrinsic electronic conductivity of the electronic conducting phase, respectively, while $V_{eff,i}$ and $V_{eff,e}$ are effective volume fraction of the ionic and electronic conducting phases within the composite, respectively. As can be seen in Figure 2.1(b), the volume of each conducting phase disassembled into continuous and insulated portions, hence, the cumulated effective volume fraction of the ionic/electronic conducting phase is practically always less than the total volume fraction of ionic/electronic conducting phase.

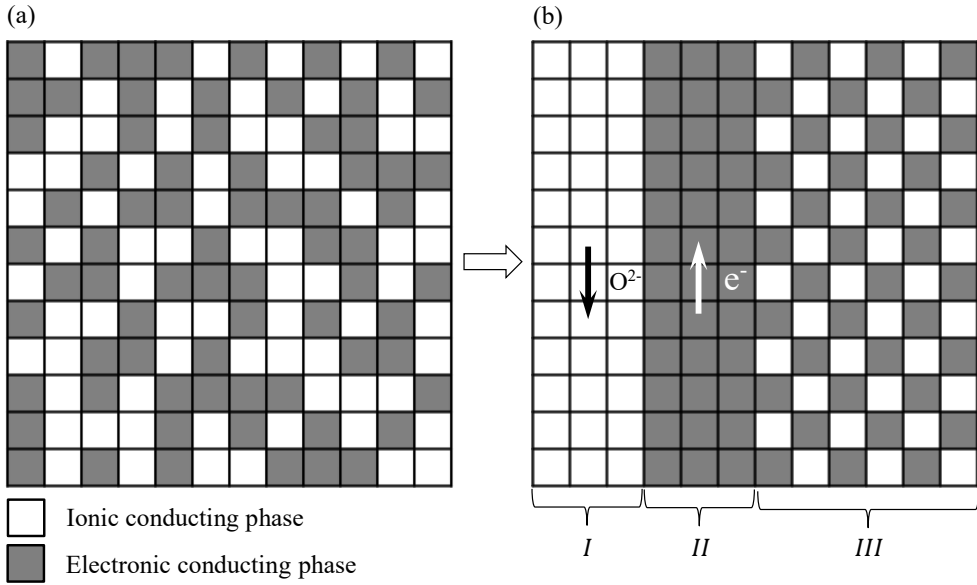


Figure 2.1 Schematic diagrams represent (a) microstructure of a randomly distributed dual phase oxygen transport membrane, and (b) equivalently disassembled structure of (a) (reproduced from [25]). (*I*, *II* and *III* are effective ionic conducting portion, effective electronic conducting portion and insulated portion assuming that transport can only take place across edges and not across corners, respectively)

The effective volume fraction defined here is equivalent to the parameter reported as continuous volume fraction [25], and it was also reported that the continuous volume fraction of one phase within a dual phase material is equal to the product of the contiguity and the total volume fraction of this phase [26]. Hence, the effective volume fractions of ionic and electronic conducting phases are calculated by equation (2.7) and (2.8), respectively:

$$V_{eff,i} = C_i \cdot V_i \quad (2.7)$$

$$V_{eff,e} = C_e \cdot V_e \quad (2.8)$$

where V_i and V_e are the total volume fractions of ionic and electronic phases, respectively, and C_i and C_e denote the contiguities of the ionic and electronic phases, respectively.

The contiguity of a phase within a dual phase material is expressed as the fraction of the total interconnected surface area of this phase shared with particles of the same phase [27], and it is correlated with the total volume fractions and the grain size ratio of two phases within the dual phase material, as indicated by the following equations [25, 27]:

$$C_i = \frac{V_i \cdot R}{V_i \cdot R + V_e} \quad (2.9)$$

$$C_i + C_e = 1 \quad (2.10)$$

$$V_i + V_e = 1 \quad (2.11)$$

$$R = \frac{d_e}{d_i} \quad (2.12)$$

where C , V , d , and R are contiguity, volume fraction, grain size and grain size ratio of electronic phase to ionic phase, respectively, and subscript i and e represent ionic and electronic phase, respectively.

Combining relations from equation (2.5)-(2.12), equation (2.1) can be expressed as:

$$\sigma_{amb} = \frac{V_i^2 \cdot R \cdot \sigma_i \cdot (1 - V_i)^2 \cdot \sigma_e}{V_i^2 \cdot R \cdot \sigma_i + (1 - V_i)^2 \cdot \sigma_e} \cdot \frac{1}{1 + (R - 1) \cdot V_i} \quad (2.13)$$

Equation (13) provides estimations of effects of microstructural and intrinsic properties on ambipolar conductivity. In case the R value equals 1, equation (2.13) simplifies to:

$$\sigma_{amb} = \frac{V_i^2 \cdot \sigma_i \cdot (1 - V_i)^2 \cdot \sigma_e}{V_i^2 \cdot \sigma_i + (1 - V_i)^2 \cdot \sigma_e} \quad (2.14)$$

With known σ_i and σ_e , the influence of the volume ratio on ambipolar conductivity can be assessed by equation (2.14) for dual phase composite membranes.

2.3 Results and discussion

2.3.1 Microstructure characterization

The microstructures of CF composites were investigated via BSEM and EBSD. An example for 50CF is presented in Figure 2.2, which demonstrates the coexistence of CGO fluorite, FCO spinel, GdFeO₃-type perovskite, and CoO rock salt phase. The formula of GdFeO₃-type perovskite has been reported to be Gd_{0.85}Ce_{0.15}Fe_{0.75}Co_{0.25}O₃ (GCFCO) [8, 28]. FCO possesses a rather uneven grain size, being coarsely distributed among CGO. Each sample has a density that exceeds 99 % (Table A2.1).

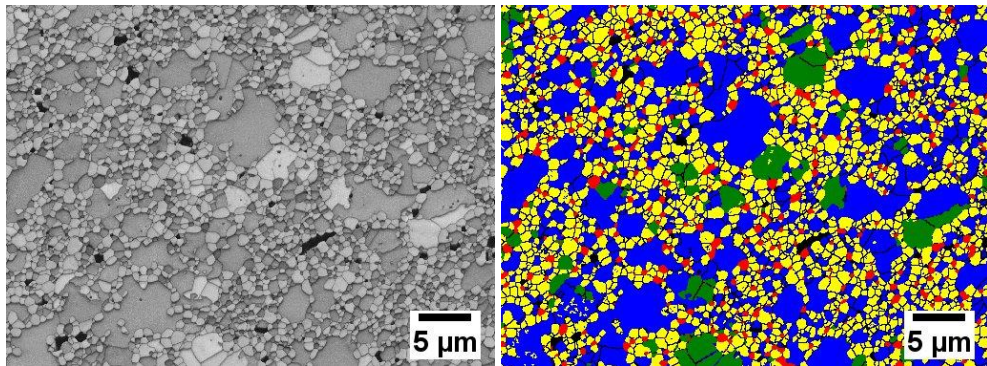


Figure 2.2 Microstructure investigation via BSEM (left) and EBSD phase mapping (right) on 50CF. (the yellow, red, blue and green phase are CGO, GCFCO, FCO and CoO, respectively)

The volume fraction of each phase was obtained from EBSD phase mapping results, which can be seen in Table 2.1. As expected, the volume fraction of CGO in the sintered composites increases with the increasing weight ratio of CGO20 to FC20 in the starting powder mixture. Besides, a relatively considerable amount of GCFCO perovskite is characterized, and the maximum GCFCO perovskite content exists for 85CF. All composites except 90CF possess a high-temperature stable CoO phase, which remains at room temperature as a result of uncompleted oxidization [18]. In addition, normalized volume fractions of ionic and electronic conducting phases are also calculated, regarding CGO as ionic conducting phase and FCO, CoO and

GCFCO phase as electronic conducting phases, since FCO, CoO and GCFCO phase are electronic conductive phases with negligible ionic conductivity [29].

Table 2.1 Volume fractions of the different phases in the CF composites sintered at 1200 °C.

Composite	CGO as ionic conducting phase (vol%)	Electronic conducting phase			
		FCO (vol%)	GCFCO (vol%)	CoO (vol%)	Sum (vol%)
50CF	40.4	43.0	5.4	11.2	59.6
60CF	52.3	32.2	7.3	8.2	47.7
70CF	66.2	21.0	8.3	4.5	33.8
85CF	80.1	9.0	10.0	0.9	19.9
90CF	93.6	3.4	3.0	0	6.4

Grain sizes were also deduced from the EBSD measurements and results are presented in Table A2.2. The grain sizes of CGO and GCFCO are $\sim 0.6 \mu\text{m}$ and $\sim 0.5 \mu\text{m}$, respectively. They are almost the same and rather similar among all composites, while grain sizes of the FCO and CoO phases decrease slightly with increasing CGO content and possess large standard deviations.

Since the limited number of characterized FCO and CoO grains might induce large inaccuracy in the grain size calculations (Table A2.2), an image analysis based method was conducted via ImageJ software for comparison, but average grain sizes of FCO and CoO grains were merged into one value in the calculation as FCO and CoO can hardly be separated via thresholding in backscattered electron images. Based on the rather good detection of a large number of black FCO and CoO grains (see Figure A2.1), the obtained average grain sizes of FCO and CoO, as shown in Table 2.2, are slightly larger than the ones measured via EBSD, meanwhile, they

show a bimodal distribution profile with a second peak at a large grain size of $\sim 3 \mu\text{m}$ (Figure A2.2), which leads to large uncertainties in the determination of the average grain sizes. The calculated average R values of the CF composites, as given in Table 2.3, vary between 1 and 2 with rather large deviations ($\sim 90\%$).

Table 2.2 Average grain size of FCO and CoO as obtained via an image analysis method.

Composite \ Parameter	Number of grains	Average grain size (μm)
50CF	2525	1.2 ± 0.9
60CF	2539	1.0 ± 0.8
70CF	2276	0.9 ± 0.6
85CF	1106	0.8 ± 0.6
90CF	709	0.8 ± 0.6

Table 2.3 Calculated average R values for the CF composites.

Composite	Average R
50CF	1.7 ± 1.5
60CF	1.3 ± 1.2
70CF	1.3 ± 1.1
85CF	1.2 ± 1.0
90CF	1.1 ± 1.0

According to the characterized volume fractions and average grain sizes, contiguities of ionic and electronic conducting phases were calculated using equations (2.9)-(2.12). The contiguity of electronic conducting phases is lower than that of ionic

conducting phase, and monotonously decreases with increasing volume fraction of ionic conducting phase, as shown in Figure 2.3, but the reduced R contributes slightly to an improvement of the contiguity of the electronic conducting phases. For a phase within a dual phase composite, higher contiguity and higher volume fraction indicates a larger continuous volume and less tendency of insulation (as can be seen by equation (2.7) and (2.8)), and hence a better percolation and will further improve the conductivity.

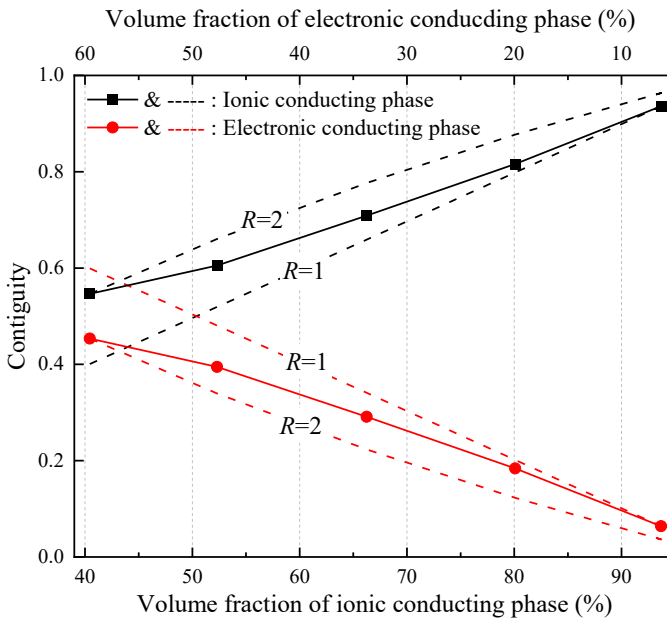


Figure 2.3 Contiguities of ionic and electronic conducting phases in the CF composites with solid lines as actual value and dotted lines corresponding to simulated value with associated R shown for each line.

2.3.2 Phase characterization

The phase constituents of CF composites were investigated via XRD. The XRD patterns (Figure A2.3) reveal a multi-phase system that is similar to the one investigated by EBSD (see Figure 2.2). For 50CF, 60CF and 70CF, four phases are identified: Gd-doped ceria fluorite (CGO), cobalt iron spinel (FCO), GCFCO

perovskite and CoO rock salt. But for 85CF, CoO can be hardly found and quantified by XRD due to its limited amount as revealed in Table 2.1. And for 90CF, it seems that diffraction patterns of CoO instead of FCO can be fitted. However, according to the volume fractions obtained from EBSD investigations (see Table 2.1), CoO does not appear in 90CF. Hence, diffraction patterns of FCO are fitted for 90CF to derive weight fractions. It is not possible to match any kind of cobalt iron spinel in the ICSD, which confirms the coexistence of FCO spinels with variations of the cobalt to iron ratio. The lattice parameters of CGO and GCFCO are almost identical among the composites (Table A2.3), which indicates a similar composition in the respective phase in each composite.

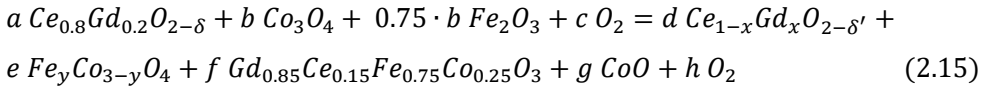
The weight fraction of each phase was deduced from the XRD data. As shown in Table 2.4, the characterized CGO content in each sintered composite is lower than the nominal CGO20 content in the respective starting powder mixture due to phase interactions between CGO20 and FC2O. The tendency regarding the weight fraction of each phase as a function of nominal CGO20 content in the starting powder is identical in terms of the volume fraction as shown in Table 2.1.

Table 2.4 Weight fractions of the different phases in the CF composites sintered at 1200 °C.

Composite	Nominal composition		Composition after sintering at 1200 °C			
	CGO20 (wt%)	FC2O (wt%)	CGO (wt%)	FCO (wt%)	GCFCO (wt%)	CoO (wt%)
50CF	50	50	40.2	41.9	8.5	9.4
60CF	60	40	47.7	34.8	10.7	6.8
70CF	70	30	59.0	25.2	10.9	4.9
85CF	85	15	70.9	14.5	14.6	0
90CF	90	10	83.5	4.2	12.3	0

The formation of the GCFCO perovskite consumes Gd from CGO20 as well as Fe and Co from FC2O. The phase reaction is presented in equation (2.15).

Since the ionic conductivity of Gd-doped cerium oxide depends on the Gd content [30, 31], and the electronic conductivity of cobalt iron oxide is a result of the ratio of Fe to Co [32], it is necessary to determine the stoichiometry of Gd, i.e. x , in the Gd-doped cerium oxide and the one of Fe, i.e. y , in the cobalt iron spinel formed in the sintered composites. Hence, x and y were calculated by equation (2.16) & (2.17) and (2.18) & (2.19), respectively. The parameters a and b were known inputs, and the f and g were deduced from the characterized weight fraction from the XRD patterns (Table 2.4).



$$0.8 \cdot a = (1 - x) \cdot d + 0.15 \cdot f \quad (2.16)$$

$$0.2 \cdot a = d \cdot x + 0.85 \cdot f \quad (2.17)$$

$$3 \cdot b = e \cdot (3 - y) + 0.25 \cdot g \quad (2.18)$$

$$1.5 \cdot b = e \cdot y + 0.75 \cdot f \quad (2.19)$$

where a , b , d , e , f , g are stoichiometric coefficients of $Ce_{0.8}Gd_{0.2}O_{2-\delta}$ (CGO20), Co_3O_4 , Fe_2O_3 , $Ce_{1-x}Gd_xO_{2-\delta'}$ (CGO), $Fe_yCo_{3-y}O_4$ (FCO), $Gd_{0.85}Ce_{0.15}Fe_{0.75}Co_{0.25}O_3$ (GCFCO) and CoO phases, respectively. The parameters c and h are stoichiometric coefficients of O_2 . The subscripts δ and δ' refer to the oxygen non-stoichiometry.

The calculated results are presented in Table 2.5. The average CGO in the CF composites can be characterized as $Ce_{0.9}Gd_{0.1}O_{2-\delta'}$ (CGO10) since the average stoichiometry of Gd in CGO is close to 0.1 and almost independent of CGO content in the CF composites. The stoichiometry of Fe in FCO, however, varies between ~ 0.2 -1.2. It should be noted, that there is a small amount of CoO in 85CF, which is not capable to be quantified by XRD, but it induces limited errors in the derived y value of 85CF. Thus, it can be concluded that the formation of the GCFCO phase consumes maximally about 50 % of the Gd in CGO20 with sufficient stoichiometry

of Fe. But it should be pointed out that among different grains the stoichiometry might locally deviate from the average value.

Table 2.5 Calculated average in x $Ce_{1-x}Gd_xO_{2-\delta}$ (CGO) and y in $Fe_yCo_{3-y}O_4$ (FCO).

Composite	x	y
50CF	0.12	1.18
60CF	0.11	1.10
70CF	0.12	1.04
85CF	0.12	0.47
90CF	0.13	0.24

2.3.3 Effect of microstructure parameters on ambipolar conductivity

The oxygen permeation through the membrane is controlled by both oxygen surface exchange and ambipolar bulk diffusion of oxygen ions and electrons [1]. When the surface exchange is rather fast compared to the bulk diffusion, the ambipolar conductivity is dominating [1], and this ambipolar conductivity can then be predicted by equations (2.13) or (2.14) with consideration of the influence from microstructure aspects, such as volume fraction, grain size and contiguity.

Since the studied composites contained two main electronic conducting phases, i.e. GCFCO and $Fe_yCo_{3-y}O_4$ ($0.2 < y < 1.2$), but only one ionic conducting phase, i.e. CGO (can be estimated as CGO10), calculations of the ambipolar conductivity via equation (2.14) were performed for three assumed dual phase composites with an R value equals to 1. One of the assumed composites consists of CGO10 and GCFCO, abbreviated as CGO10&GCFCO, the other one contains CGO10 and $FeCo_2O_4$, named as CGO10&FC2O, and the last one composes of CGO10 and Co_3O_4 , denoted as CGO10& Co_3O_4 . The ambipolar conductivities of the CF composites are expected to be higher than that of CGO10&GCFCO but lower than that of CGO10&FC2O

and CGO10&Co₃O₄. CoO is not considered here because CoO is only stable at a temperature above 950 °C [33], below which CoO tends to be gradually oxidized into spinel with time.

The O₂ permeation conditions for the calculations of ambipolar conductivities were set to be at a temperature of 800 °C, and the atmospheres of two sides of the membrane were selected to be air and Ar, respectively. Necessary inputs for equation (2.14) include the volume fractions and intrinsic conductivities of ionic and electronic conducting phases under the selected calculation conditions. Although FCO segregation and reduction were investigated at the surfaces of the CF materials in the temperature range of ~ 700-1000 °C with an air/Ar gradient, phase structures and compositions in the bulk of the CF materials are rather stable [8]. Hence, the volume fractions of ionic/electronic conducting phases under the selected O₂ permeation conditions are considered as approximately the same as the investigated ones at room temperature. Meanwhile, the electronic conductivity of GCFCO and FCO for the calculation of ambipolar conductivity is estimated to be the same as the one in air at 800 °C, as listed in Table 2.6. Since the stoichiometry of Fe in FCO varies between 0.2 and 1.2 (see Table 2.5), the lower and upper bound for electronic conductivity of FCO are assumed to be equal to the electronic conductivity of Co₃O₄ and FC2O, respectively. Besides, although CGO10 exhibits electronic conductivity in addition to ionic conductivity under low oxygen partial pressure [34], it was reported for CGO10 that in Ar atmosphere (~ 10⁻⁵ atm) and at a temperature of 800 °C, the total conductivity is almost equal to the ionic conductivity [30]. In the O₂ permeation test, Ar is used as a sweep gas, which is continuously enriched in oxygen and, thus, the low oxygen partial pressure is fairly above 10⁻⁵ atm, which indicates that the experimental conditions can hardly be sufficient to reduce Ce⁴⁺ to Ce³⁺ and, hence does not significantly induce small polarons in CGO10. Therefore, for the calculation of ambipolar conductivity, CGO10 is regarded as a pure ionic conducting phase with an ionic conductivity estimated to be the same as the one measured in air at 800 °C as shown in Table 2.6.

Table 2.6 Ionic and electronic conductivity of the different phases at 800 °C in air.

Phase	Conductivity (S/cm)		Reference	
	σ_i	σ_e		
$\text{Ce}_{0.9}\text{Gd}_{0.1}\text{O}_{2-\delta}$	0.075	-	[30, 31]	
$\text{Gd}_{0.85}\text{Ce}_{0.15}\text{Fe}_{0.75}\text{Co}_{0.25}\text{O}_3$	-	2.56	[8]	
$\text{Fe}_y\text{Co}_{3-y}\text{O}_4$ ($0.2 < y < 1.2$)	lower bound: Co_3O_4	-	6.7	[36, 37]
	upper bound: FeCo_2O_4	-	19.8	[8]

Accordingly, the ambipolar conductivity was calculated as a function of volume fraction of ionic/electronic conducting phase as presented in Figure 2.4. Meanwhile, the experimental ambipolar conductivities of 60CF, 85CF, and 90CF were also shown in Figure 2.4. These experimental values were deduced via equation (2.20) based on oxygen permeation results at 800 °C that have been reported for the CF composites with a verified R value close to 1 [8, 29, 35]:

$$\sigma_{amb} = \frac{16 \cdot L \cdot F^2 \cdot j_{O_2}}{R' \cdot T} / \ln \frac{p_{O_2}^{feed}}{p_{O_2}^{sweep}} \quad (2.20)$$

where j_{O_2} is the oxygen flux, L the thickness of the membrane, T the temperature, R' the gas constant, F the Faraday constant, and the $p_{O_2}^{feed}$ and $p_{O_2}^{sweep}$ are the oxygen partial pressures at the feed and sweep side, respectively.

The calculated curves (see Figure 2.4) indicate that the maximum σ_{amb} improves when CGO10 partners with an electronic conducting phase with higher electronic conductivity, meanwhile more CGO10 content is necessary to achieve the maximum σ_{amb} . The maximum σ_{amb} for CGO10&GCFCO, CGO10& Co_3O_4 , and CGO10&FC2O appears when CGO10 is ~ 76 vol%, ~ 82 vol%, and ~ 87 vol%,

respectively. The composite with ~ 87 vol% CGO10 and ~ 13 vol% FC2O possesses the highest σ_{amb} among the ones calculated for all composites.

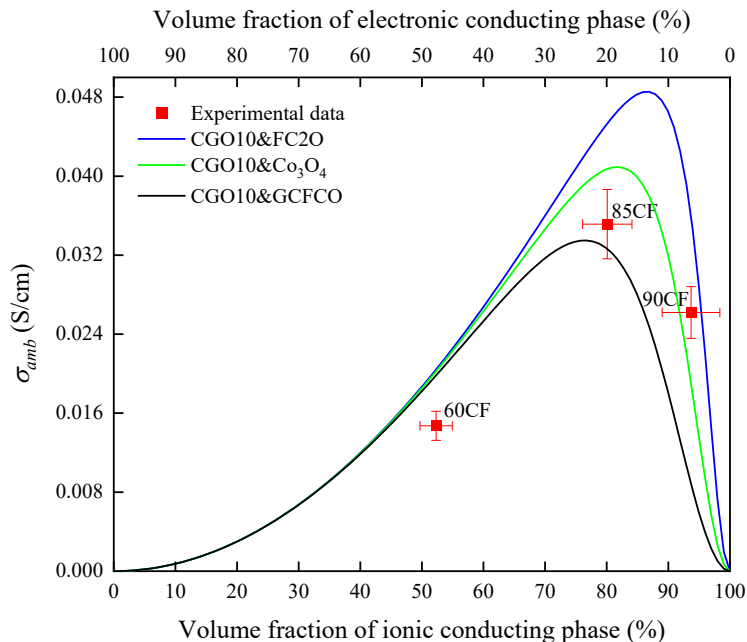


Figure 2.4 Ambipolar conductivity as a function of volume fraction of ionic/electronic conducting phase when $R = 1$.

In contrast to calculation results, the experimental σ_{amb} of the CF composites, except 60CF, are located between the calculated σ_{amb} of CGO10&GCFCO and CGO10&FC2O. The experimental σ_{amb} of 90CF is located slightly above the calculated σ_{amb} of CGO10&Co₃O₄, it could be owing to the fact that the FCO spinel in 90CF possesses a small amount of Fe (see Table 2.5), and exhibits a higher electronic conductivity than that of Co₃O₄ [32]. Furthermore, the highest experimental σ_{amb} of the CF composites is lower than the calculated ones of CGO10&Co₃O₄ and CGO10&FC2O, but rather close to the one of CGO10&GCFCO. This infers that GCFCO is dominating the effective electronic conductivity in the CF composites with the highest σ_{amb} , i.e. 85CF, among all the electronic conducting phases. However, according to the study on 60 vol% Ce_{0.8}Gd_{0.2}O_{2- δ} -40 vol%

Fe_2CoO_4 composite [38], the newly formed perovskites are completely isolated. With similar phase constituents, 85CF is expected to form also a poorly connected GCFCO. Therefore, the effective electronic conductivity of 85CF relies on the electronic conductive network formed by GCFCO and FCO, and is determined by the component with the lowest electronic conductivity, i.e. GCFCO [29].

For 85CF with an R value larger than 1 as shown in this study, the σ_{amb} was determined to be ~ 0.021 S/cm at 800 °C as derived via equation (2.20) on the basis of reported oxygen permeation results [18]. It is much lower than the σ_{amb} of 85CF with R being close to 1, since the larger FCO grains cannot bridge the GCFCO grains as good as the small FCO grains can do this. Therefore, future improvement of the performance will rely on the reduction of the grain size of FCO.

2.4 Conclusions

Phase and microstructure characterizations were carried out for the CF composites prepared via solid state reaction. It reveals the formations of $\text{Ce}_{1-x}\text{Gd}_x\text{O}_{2-\delta}$ ($x \approx 0.1$), $\text{Fe}_y\text{Co}_{3-y}\text{O}_4$ ($0.2 < y < 1.2$), CoO and a newly formed perovskite phase - $\text{Gd}_{0.85}\text{Ce}_{0.15}\text{Fe}_{0.75}\text{Co}_{0.25}\text{O}_3$. Meanwhile, the grain size ratio of electronic conducting phases (i.e. FCO, CoO and GCFCO) to ionic conducting phase (i.e. CGO10) is between 1 and 2 with a large standard deviation, since grain sizes of FCO and CoO are rather large and uneven.

New equations are proposed to assess the evolution of ambipolar conductivity as a function of the volume fractions and grain size ratio of the two phases. When R is close to 1, the measured σ_{amb} of 85CF and 90CF are located between the calculated ones of CGO10&FC2O and CGO10&GCFCO. Furthermore, the measured highest ambipolar conductivity for the CF composites is achieved for 85CF with ~ 80 vol% CGO10, it is much close to the calculated one for CGO10&GCFCO with ~ 76 vol% CGO10; Thus, the GCFCO dominates the effective electronic conductivity in the electronic conductive network formed by FCO and GCFCO in the bulk of 85CF in

the oxygen permeation process. Furthermore, small FCO grains contribute to bridging the GCFCO gains and improving the ambipolar conductivity.

Overall, the new material combination provides the basis of a viable high-performance oxygen-separation membrane at least for applications with oxidizing atmospheres, such as oxy-combustion processes. Although the stability of the spinel phase is rather limited in low oxygen partial pressure, e.g. membrane reactors, this phase is partly transformed into the chemically more stable perovskite during sintering. Therefore, the solid state reactive sintering approach paves the way to further material development covering a wide range of applications. Nevertheless, specific stability testing in targeted application conditions is mandatory for any kind of material because long term stability is key to success for proving novel technologies such as membrane reactors.

References

- [1] X. Zhu, W. Yang, Mixed conducting ceramic membranes, Springer-Verlag, Berlin, Germany, 2017.
- [2] H. Stadler, F. Beggel, M. Habermehl, B. Persigehl, R. Kneer, M. Modigell, P. Jeschke, Oxyfuel coal combustion by efficient integration of oxygen transport membranes, *International Journal of Greenhouse Gas Control* 5(1) (2011) 7-15.
- [3] Z. Cao, H. Jiang, H. Luo, S. Baumann, W.A. Meulenber, J. Assmann, L. Mleczko, Y. Liu, J. Caro, Natural gas to fuels and chemicals: improved methane aromatization in an oxygen-permeable membrane reactor, *Angewandte Chemie International Edition* 52(51) (2013) 13794-13797.
- [4] S. Baumann, J. Serra, M. Lobera, S. Escolástico, F. Schulze-Küppers, W. Meulenber, Ultrahigh oxygen permeation flux through supported $\text{Ba}_{0.5}\text{Sr}_{0.5}\text{Co}_{0.8}\text{Fe}_{0.2}\text{O}_{3-\delta}$ membranes, *Journal of Membrane Science* 377(1-2) (2011) 198-205.
- [5] J.M. Serra, J. Garcia-Fayos, S. Baumann, F. Schulze-Küppers, W. Meulenber, Oxygen permeation through tape-cast asymmetric all- $\text{La}_{0.6}\text{Sr}_{0.4}\text{Co}_{0.2}\text{Fe}_{0.8}\text{O}_{3-\delta}$ membranes, *Journal of membrane science* 447 (2013) 297-305.

- [6] M. Arnold, H. Wang, A. Feldhoff, Influence of CO₂ on the oxygen permeation performance and the microstructure of perovskite-type (Ba_{0.5}Sr_{0.5})(Co_{0.8}Fe_{0.2})O_{3-δ} membranes, *Journal of Membrane Science* 293(1-2) (2007) 44-52.
- [7] A. Waindich, A. Möbius, M. Müller, Corrosion of Ba_{1-x}Sr_xCo_{1-y}FeyO_{3-δ} and La_{0.3}Ba_{0.7}Co_{0.2}Fe_{0.8}O_{3-δ} materials for oxygen separating membranes under Oxycoal conditions, *Journal of Membrane Science* 337(1-2) (2009) 182-187.
- [8] M. Ramasamy, E. Persoon, S. Baumann, M. Schroeder, F. Schulze-Küppers, D. Görtz, R. Bhave, M. Bram, W. Meulenber, Structural and chemical stability of high performance Ce_{0.8}Gd_{0.2}O_{2-δ}-FeCo₂O₄ dual phase oxygen transport membranes, *Journal of Membrane Science* 544 (2017) 278-286.
- [9] X. Zhu, H. Wang, W. Yang, Relationship between homogeneity and oxygen permeability of composite membranes, *Journal of Membrane Science* 309(1-2) (2008) 120-127.
- [10] H. Luo, H. Jiang, K. Efimov, J. Caro, H. Wang, Influence of the preparation methods on the microstructure and oxygen permeability of a CO₂-stable dual phase membrane, *AIChE Journal* 57(10) (2011) 2738-2745.
- [11] Q. Li, X. Zhu, Y. He, Y. Cong, W. Yang, Effects of sintering temperature on properties of dual-phase oxygen permeable membranes, *Journal of membrane science* 367(1-2) (2011) 134-140.
- [12] B.C. Steele, Ceramic ion conducting membranes, *Current Opinion in Solid State Materials Science* 1(5) (1996) 684-691.
- [13] V. Kharton, A. Kovalevsky, A. Viskup, A. Shaula, F. Figueiredo, E. Naumovich, F. Marques, Oxygen transport in Ce_{0.8}Gd_{0.2}O_{2-δ}-based composite membranes, *Solid State Ionics* 160(3-4) (2003) 247-258.
- [14] A. Petric, H. Ling, Electrical Conductivity and Thermal Expansion of Spinel at Elevated Temperatures, *Journal of the American Ceramic Society* 90(5) (2007) 1515-1520.
- [15] E. Verwey, P. Haayman, F. Romeijn, Physical properties and cation arrangement of oxides with spinel structures II. Electronic conductivity, *The Journal of Chemical Physics* 15(4) (1947) 181-187.
- [16] H. Li, X. Zhu, Y. Liu, W. Wang, W. Yang, Comparative investigation of dual-phase membranes containing cobalt and iron-based mixed conducting perovskite for oxygen permeation, *Journal of membrane science* 462 (2014) 170-177.
- [17] T. Chen, H. Zhao, Z. Xie, J. Wang, Y. Lu, N. Xu, Ce_{0.8}Sm_{0.2}O_{2-δ}-PrBaCo₂O_{5+δ} dual-phase membrane: Novel preparation and improved oxygen permeability, *Journal of Power Sources* 223 (2013) 289-292.

- [18] M. Ramasamy, Dual phase oxygen transport membrane for efficient oxyfuel combustion, PhD thesis, Bochum University, Bochum, Germany, 2016.
- [19] A.J. Schwartz, M. Kumar, B.L. Adams, D.P. Field, Electron backscatter diffraction in materials science, Springer, Livermore, USA, 2009.
- [20] S.G. Patrício, E.I. Papaioannou, B.M. Ray, I.S. Metcalfe, F.M.B. Marques, Composite CO₂ separation membranes: Insights on kinetics and stability, *Journal of Membrane Science* 541 (2017) 253-261.
- [21] F.M.B. Marques, S.G. Patrício, E. Muccillo, R. Muccillo, On the model performance of composite CO₂ separation membranes, *Electrochimica Acta* 210 (2016) 87-95.
- [22] E. Vøllestad, H. Zhu, R.J. Kee, Interpretation of defect and gas-phase fluxes through mixed-conducting ceramics using Nernst-Planck-Poisson and integral formulations, *Journal of The Electrochemical Society* 161(1) (2014) F114-F124.
- [23] X. Tan, S. Liu, K. Li, R. Hughes, Theoretical analysis of ion permeation through mixed conducting membranes and its application to dehydrogenation reactions, *Solid State Ionics* 138(1-2) (2000) 149-159.
- [24] K. Li, Ceramic membranes for separation and reaction, John Wiley & Sons, London, United Kingdom, 2007.
- [25] Z. Fan, A. Miodownik, P. Tsakirooulos, Microstructural characterisation of two phase materials, *Materials science technology* 9(12) (1993) 1094-1100.
- [26] H.-C. Lee, J. Gurland, Hardness and deformation of cemented tungsten carbide, *Materials science and engineering* 33(1) (1978) 125-133.
- [27] J. Gurland, The measurement of grain contiguity in two-phase alloys, *Transactions of the Metallurgical Society of AIME* 212 (1958) 452-455.
- [28] F. Zeng, J. Malzbender, S. Baumann, F. Schulze-Küppers, M. Krüger, A. Nijmeijer, O. Guillon, W.A. Meulenber, Micro-mechanical characterization of Ce_{0.8}Gd_{0.2}O_{2-δ}-FeCo₂O₄ dual phase oxygen transport membranes, *Advanced Engineering Materials* (2020) 1901558.
- [29] M. Ramasamy, S. Baumann, A. Opitz, R. Iskandar, J. Mayer, D. Udomsilp, U. Breuer, M. Bram, Phase Interaction and Distribution in Mixed Ionic Electronic Conducting Ceria-Spinel Composites, *Advances in Solid Oxide Fuel Cells Electronic Ceramics II: Ceramic Engineering Science Proceedings*, 37(3) (2017) 99-112.
- [30] S. Wang, T. Kobayashi, M. Dokiya, T. Hashimoto, Electrical and ionic conductivity of Gd-doped ceria, *Journal of The Electrochemical Society* 147(10) (2000) 3606-3609.

- [31] J.H. Joo, G.S. Park, C.-Y. Yoo, J.H. Yu, Contribution of the surface exchange kinetics to the oxygen transport properties in $\text{Gd}_{0.1}\text{Ce}_{0.9}\text{O}_{2-\delta}\text{-La}_{0.6}\text{Sr}_{0.4}\text{Co}_{0.2}\text{Fe}_{0.8}\text{O}_{3-\delta}$ dual-phase membrane, *Solid State Ionics* 253 (2013) 64-69.
- [32] T. Kiefer, Entwicklung neuer Schutz-und Kontaktierungsschichten für Hochtemperatur-Brennstoffzellen, PhD thesis, Ruhr-Universität Bochum, Bochum, Germany, 2008.
- [33] P.J. Murray, J.W. Linnett, Mössbauer studies in the spinel system $\text{Co}_x\text{Fe}_{3-x}\text{O}_4$, *Journal of Physics and Chemistry of Solids* 37(6) (1976) 619-624.
- [34] S.-H. Park, H.-I. Yoo, Defect-chemical role of Mn in Gd-doped CeO_2 , *Solid State Ionics* 176(15-16) (2005) 1485-1490.
- [35] M. Ramasamy, S. Baumann, J. Palisaitis, F. Schulze-Küppers, M. Balaguer, D. Kim, W.A. Meulenber, J. Mayer, R. Bhawe, O. Guillon, Influence of Microstructure and Surface Activation of Dual-Phase Membrane $\text{Ce}_{0.8}\text{Gd}_{0.2}\text{O}_{2-\delta}\text{-FeCo}_2\text{O}_4$ on Oxygen Permeation, *Journal of the American Ceramic Society* 99(1) (2016) 349-355.
- [36] E.M. Garcia, The electrochemical behavior of cobalt electrodeposits on 430 stainless steel as solid oxide fuel cell interconnect, *Surface and Coatings Technology* 235 (2013) 10-14.
- [37] Y. Ji, J.A. Kilner, M.F. Carolan, Electrical conductivity and oxygen transfer in gadolinia-doped ceria (CGO)- $\text{Co}_3\text{O}_{4-\delta}$ composites, *Journal of the European Ceramic Society* 24(14) (2004) 3613-3616.
- [38] W.M. Harris, K.S. Brinkman, Y. Lin, D. Su, A.P. Cocco, A. Nakajo, M.B. DeGostin, Y.-c.K. Chen-Wiegart, J. Wang, F. Chen, Characterization of 3D interconnected microstructural network in mixed ionic and electronic conducting ceramic composites, *Nanoscale* 6(9) (2014) 4480-4485.

Appendix A2

Table A2.1 Porosities of the CF composites via image analysis.

Composites	Porosity (%)
50CF	0.5 ± 0.2
60CF	0.9 ± 0.2
70CF	0.9 ± 0.3
85CF	0.4 ± 0.2
90CF	0.3 ± 0.2

Table A2.2 Grain sizes of the CF composites via EBSD.

Quantification Composites	Grain numbers				Grain size (μm)			
	CGO	FCO	GCFCO	CoO	CGO	FCO	GCFCO	CoO
50CF	3348	1051	584	257	0.6 ± 0.2	0.9 ± 0.8	0.5 ± 0.2	1.0 ± 0.7
60CF	3656	791	769	220	0.7 ± 0.2	0.9 ± 0.8	0.5 ± 0.2	1.0 ± 0.6
70CF	2639	423	638	106	0.6 ± 0.3	0.7 ± 0.7	0.4 ± 0.2	0.7 ± 0.5
85CF	4025	342	763	48	0.6 ± 0.2	0.5 ± 0.4	0.5 ± 0.2	0.5 ± 0.3
90CF	4534	112	286	-	0.6 ± 0.3	0.6 ± 0.5	0.4 ± 0.1	-

Table A2.3 Lattice parameters of respective phases in the CF composites.

Phase Compositions	CGO fluorite		GCFCO perovskite	
	a(Å)	a(Å)	b(Å)	c(Å)
50CF	5.42	5.34	5.62	7.66
60CF	5.42	5.34	5.62	7.66
70CF	5.42	5.34	5.61	7.66
85CF	5.42	5.34	5.61	7.65
90CF	5.42	5.34	5.62	7.64

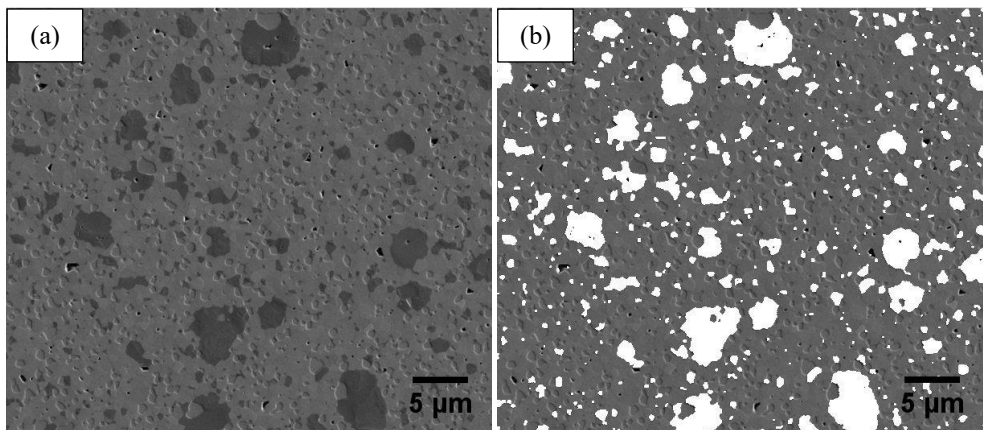


Figure A2.1 Detection of (b) FCO and CoO from (a) SEM of 85CF.

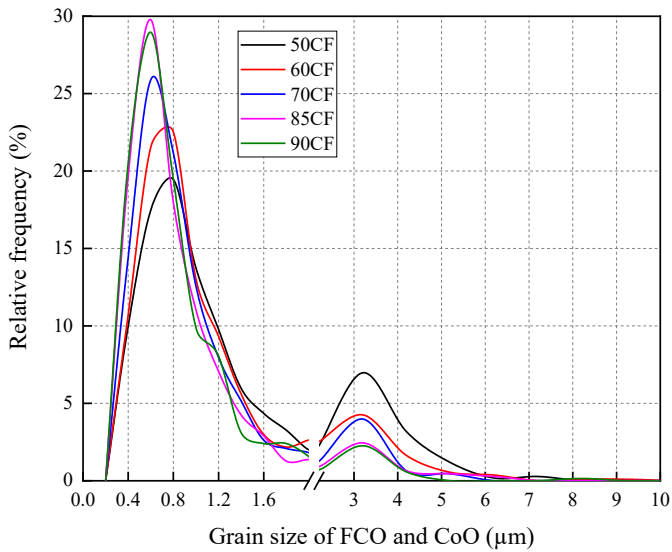


Figure A2.2 Grain size distributions of FCO and CoO.

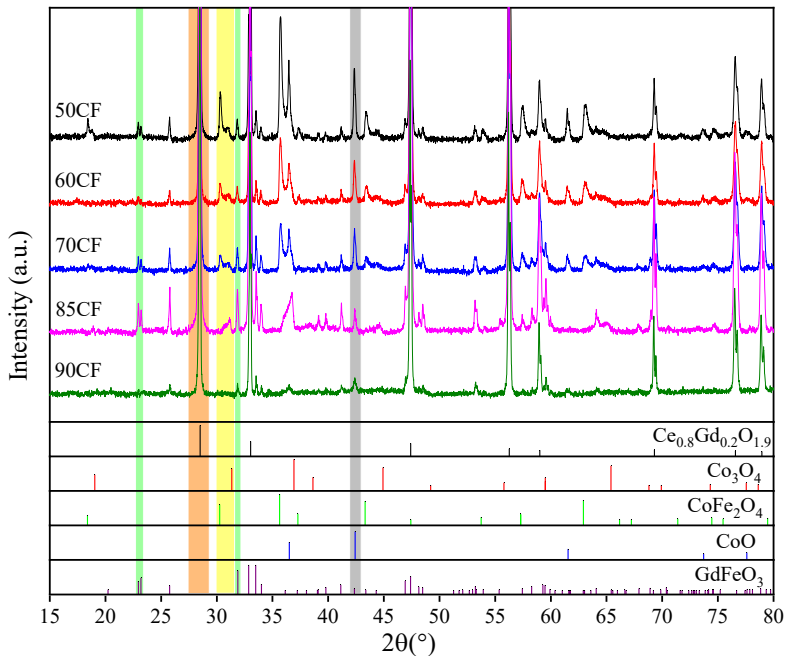


Figure A2.3 XRD patterns of the CF composites after sintering at 1200 °C (non-overlapped peaks highlighted as orange, yellow, green and grey can be matched as CGO fluorite, FCO spinel, GCFCO perovskite and CoO rock salt, respectively).

CHAPTER 3

Mechanical reliability of Ce_{0.8}Gd_{0.2}O_{2-δ}-FeCo₂O₄ dual phase membranes synthesized by one-step solid-state reaction

Abstract

Ce_{0.8}Gd_{0.2}O_{2-δ}-FeCo₂O₄ composites are attractive candidate materials for high-purity oxygen generation providing robust chemical stability. Aiming for future industrial applications, a feasible solid-state reaction process with one thermal processing step was used to synthesize 50 wt% Ce_{0.8}Gd_{0.2}O_{2-δ}-50 wt% FeCo₂O₄ and 85 wt% Ce_{0.8}Gd_{0.2}O_{2-δ}-15 wt% FeCo₂O₄ composites. Mechanical reliabilities of the sintered membranes were assessed based on the characterized mechanical properties and subcritical crack growth behaviour. In general, the fracture strengths of as-sintered membranes were reduced by tensile residual stresses and microcracks. In particular, the enhanced subcritical crack growth behaviour, which leads to limited stress tolerance and high failure probability after a 10-years operation, was evaluated in more detail. Further materials and processing improvements are needed to eliminate the tensile stress and microcracks to warrant a long-term reliable operation of the composites.

This chapter has been published as: F. Zeng, J. Malzbender, S. Baumann, W. Zhou, M. Ziegner, A. Nijmeijer, O. Guillon, R. Schwaiger, W.A. Meulenberg, Mechanical reliability of Ce_{0.8}Gd_{0.2}O_{2-δ}-FeCo₂O₄ dual phase membranes synthesized by one-step solid-state reaction, Journal of the American Ceramic Society (2020).

DOI: 10.1111/jace.17583.

3.1 Introduction

Environmentally friendly and efficient processes for energy generation and conversion are of great importance [1]. Among the solutions for CO₂ capture technologies to reduce greenhouse gas emissions, ceramic oxygen transport membranes represent key components [2], due to their almost 100 % selectivity to oxygen [3]. Moreover, oxygen transport membranes have the capability to improve the efficiency of other industrial processes, such as production of pure oxygen [4-6], petro-chemical processes [7-11], and oxy-combustion [12-14].

Ceramic perovskites, such as Ba_{0.5}Sr_{0.5}Co_{0.8}Fe_{0.2}O_{3-δ} [15], and La_{0.6}Sr_{0.4}Co_{0.2}Fe_{0.8}O_{3-δ} [16], are the most popular material candidates due to their high oxygen permeation fluxes. But practical applications of these single phase perovskite membranes are limited due to their degradation in atmospheres containing CO₂ and SO₂ [17-24]. Such a stability limitation can be overcome by the development of dual phase membrane materials, which consist of two separate phases responsible for ionic and electronic conduction, respectively [25-33].

Ce_{1-x}Gd_xO_{2-δ} ($x = 0.1$ or 0.2) is often used as the ion-conducting phase because of its high ionic conductivity (~ 0.075 - 0.1 S·cm⁻¹) [34-37] and chemical stability [25-27, 29, 31, 33, 37-41]. The high ionic conductivity of Ce_{1-x}Gd_xO_{2-δ} ($x = 0.1$ or 0.2) has been attributed to oxygen vacancies created by the substitution of Ce in CeO₂ by Gd according to [42]:



where subscripts *Ce* and *O* represents the *Ce* and *O* site within the CGO lattice, respectively. And superscripts \times , $'$, and $\cdot\cdot$ denote an electroneutral state, one negative effective charge, and two positive effective charges, respectively. The introduction of oxygen vacancies expands the lattice, which is known as chemical expansion [43].

A suitable electron-conducting phase for $\text{Ce}_{1-x}\text{Gd}_x\text{O}_{2-\delta}$ ($x = 0.1$ or 0.2)-based dual phase membranes should have a comparable conductivity to achieve high ambipolar conductivity [3], and similar thermal expansion coefficients to avoid formation of large residual stress and microcracks [39]. In addition to excellent electronic conductivities ($\sim 0.85\text{-}19 \text{ S}\cdot\text{cm}^{-1}$) that are adjustable by Fe content [25, 37, 44, 45], $\text{Fe}_x\text{Co}_{3-x}\text{O}_4$ ($0 < x < 3$) spinels have appropriate thermal expansion coefficients that are close to the thermal expansion coefficient of $\text{Ce}_{1-x}\text{Gd}_x\text{O}_{2-\delta}$ ($x = 0.1$ or 0.2) ($\sim 12 \times 10^{-6} \text{ K}^{-1}$) [44, 46, 47]. Furthermore, $\text{Fe}_x\text{Co}_{3-x}\text{O}_4$ ($0 < x < 3$) spinels can serve as sintering agents for $\text{Ce}_{1-x}\text{Gd}_x\text{O}_{2-\delta}$ ($x = 0.1$ or 0.2) to reduce the sintering temperature and increase the density of the material [36, 47].

$\text{Ce}_{0.8}\text{Gd}_{0.2}\text{O}_{2-\delta}\text{-FeCo}_2\text{O}_4$ composites synthesized by a Pechini process, as typical examples, were revealed to possess a crack-free microstructure with high density ($\sim 97\%$) after sintering at 1200°C [48]. The optimal nominal composition with the highest oxygen permeation flux and best chemical stability against CO_2 and SO_2 was reported to be $85 \text{ wt}\% \text{ Ce}_{0.8}\text{Gd}_{0.2}\text{O}_{2-\delta}\text{-}15 \text{ wt}\% \text{ FeCo}_2\text{O}_4$ [25].

Aiming toward future scaling-up of dual phase membranes for industrial applications, mechanical behaviour and robustness, in addition to chemical performance and stability, are of critical importance to warrant long-term safe operation [7, 20]. Only a limited number of reports focused on the mechanical properties of dual phase membranes [49-53], reporting values for, e.g. elastic modulus, hardness, fracture strength and fracture toughness. The subcritical crack growth behaviour of dual phase membranes, though, has not yet been studied. In fact, long-term mechanical reliability of ceramic materials only allows limited subcritical crack growth [54-57], since a fast degradation of fracture strength with increasing service time can be expected for ceramics that are susceptible to subcritical crack growth [55]. Such dependence of strength on service time can be predicted utilizing a lifetime assessing model based on failure probability analysis, i.e. Weibull analysis, and parameterized subcritical crack growth behaviour [58].

In this work, we are comparing the mechanical reliability of $\text{Ce}_{0.8}\text{Gd}_{0.2}\text{O}_{2-\delta}$ - FeCo_2O_4 composites with two different compositions. One composite is 85 wt% $\text{Ce}_{0.8}\text{Gd}_{0.2}\text{O}_{2-\delta}$ -15 wt% FeCo_2O_4 , which has great potential due to its excellent chemical stability and good oxygen permeance [25]. For comparison, a fairly different composite 50 wt% $\text{Ce}_{0.8}\text{Gd}_{0.2}\text{O}_{2-\delta}$ -50 wt% FeCo_2O_4 was prepared to reveal the potential effect of the compositional differences. Mechanical properties, including elastic modulus, hardness, fracture toughness and fracture strength, were assessed at room temperature, and their relationships with the phase structure, residual stress and the microstructural characteristics are discussed. The subcritical crack growth behaviour, failure probability and lifetime under static stress are analyzed based on fracture stress data obtained by ring-on-ring tests at different loading rates.

3.2 Experimental

A solid-state reaction process with one-step thermal processing, as a very promising technique for scaling-up manufacturing process [13], was utilized to synthesize $\text{Ce}_{0.8}\text{Gd}_{0.2}\text{O}_{2-\delta}$ - FeCo_2O_4 composites. $\text{Ce}_{0.8}\text{Gd}_{0.2}\text{O}_{1.9}$ (Treibacher Industrie AG, 99 %) (CGO), Co_3O_4 (Alfa Aesar, 99.7 %) and Fe_2O_3 (Sigma-Aldrich, 99 %) powders (the Co/Fe mole ratio fixed at a value of two to obtain a nominal FeCo_2O_4) were mixed in a plastic bottle, and ball milled with ethanol and 5 mm (diameter) zirconia balls for 3 days. The weight ratio of powder-ball-ethanol was set to be 1:2:3. The milled powder mixtures were then dried and pressed into pellets using a pressure of 50 MPa. The pellets were sintered in air at 1200 °C for 10 h. A slow cooling rate of 0.5 K/min was applied for the cooling step from 900 °C and 800 °C to facilitate the oxidation of CoO rock salt phase [59]. The heating/cooling rate for other temperature range was 3 K/min. Two composites were sintered, and they will be referred to as 50CF and 85CF corresponding to weight ratios of $\text{Ce}_{0.8}\text{Gd}_{0.2}\text{O}_{2-\delta}$ to FeCo_2O_4 being equal to 50:50 and 85:15 in the starting powder mixtures, respectively.

To reveal possible variations of phase structure, microstructure and associated mechanical properties across the sintered pellets, we investigated the as-sintered

surface, the sub-surface, as well as the bulk material. The sub-surface and the bulk material were exposed using two different surface preparation procedures. The as-sintered surface without any surface preparation serves as a reference and will be referred to as “surface”. The first polishing procedure included five polishing steps on the as-sintered pellet surfaces to obtain a mirror-finished surface exposing the sub-surface material. Particle sizes of the diamond pastes used during polishing were reduced in every polishing step from 15 μm to 6 μm , then to 3 μm , and finally to 1 μm . The final step was conducted using 50 nm colloidal silica suspension. The polishing time for each step was ~ 1 h to remove the defects and scratches from the preceding step. A thickness of approximately 30 μm was removed after finishing the five polishing steps, hence, the obtained surface will be referred to as “sub-surface”.

The second procedure included additional grinding steps before polishing to reveal the bulk material. The surfaces of the as-sintered pellets were first ground using SiO_2 -sandpaper with grit sizes ascending from 400 to 1200, and then polished with the same steps as the ones used for the first procedure. Potential residual stress induced by grinding was removed by the fine polishing steps [60]. These combined grinding and polishing steps removed a thickness of approximately 0.3 mm. The obtained surfaces are expected to represent the bulk of the material and will be referred to as “bulk”.

The crystal structure at the surface and in the bulk of the sintered composites was characterized by X-ray diffraction (XRD) (Empyrean, Malvern Panalytical Ltd). The instrument was equipped with a Cu long fine focus tube (40 kV / 40 mA), Bragg-Brentano^{HD} mirror (divergence = 0.4°), and PIXcel3D detector (1D-mode, active length = 3.35° , 255 channels).

The residual stress (σ_r) of the surface and the sub-surface of the sintered composites were determined by XRD based on the $\sin^2 \psi$ method assuming an equibiaxial stress state [61]. Such a method is most appropriate for cubic phases with isotropic elastic constants [61]. Hence, the residual stresses were only determined for CGO and FCO

phases. Lattice spacing (d) of crystal planes (311) of CGO, crystal plane (440) of FCO and crystal plane (220) of CoO were derived based on the diffraction peaks obtained at different angles (ψ). The diffraction peaks at high 2θ positions ($> 85^\circ$) were recorded to enable sufficient intensity for analysis using a Philips MRD Pro diffractometer with Cr- K_α (35 kV / 50 mA) radiation. For a homogeneous stress state, the lattice spacing is approximately linearly proportional to $\sin^2 \psi$. The residual stress (σ_r) was calculated by [61]:

$$\sigma_r = \frac{E}{\nu + 1} \cdot \frac{1}{d_{\psi_0}} \cdot \frac{\partial d_\psi}{\partial \sin^2 \psi} \quad (3.2)$$

where E and ν are elastic modulus and Poisson's ratio, and d_{ψ_0} is the lattice spacing in a stress-free sample; d_ψ is the lattice spacing at an angle ψ . The E values for CGO, FCO and CoO were 229 GPa, 209 GPa and 193 MPa, respectively [53]. The ν was assumed to be 0.3, which is a typical value for ceramics [62].

Microstructures of surface, sub-surface and bulk of the sintered composites were investigated by scanning electron microscopy (SEM) (Merlin, Carl Zeiss Microscopy, Oberkochen, Germany) and back scattered electron microscopy (BSEM) (Merlin, Carl Zeiss Microscopy, Oberkochen, Germany). The porosity was estimated as the area fraction of the pores.

Fracture stresses and associated average fracture strengths of the as-sintered composites were determined from data obtained by ring-on-ring tests operated with an electromechanical testing machine (Instron 1362, Lebow Ltd) following the general procedure outlined in ASTM C1499-05 [63]. Loading rings and support rings with diameters of 3.43 and 9.99 mm, respectively, were used. The pellet surface in contact with the support ring was the tensile surface during loading. Four different stress rates, i.e. 20 MPa/s, 2 MPa/s, 0.2 MPa/s, and 0.02 MPa/s were applied for each as-sintered composite. Due to the limited number of specimens, only five 50CF pellets were tested at each loading condition. Ten 85CF pellets were tested at a loading rate of 20 MPa/s, while only five 85CF pellets were tested at each of the

other loading rates. The individual fracture stress (σ_f) and elastic modulus (E) were derived by equation (3.3) [63] and equation (3.4) [56], respectively.

$$\sigma_f = \frac{3F}{2\pi \cdot t^2} \cdot \left[(1 - \nu) \cdot \frac{r_s^2 - r_l^2}{2r_p^2} + (1 + \nu) \cdot \ln \frac{r_s}{r_l} \right] \quad (3.3)$$

$$E = \frac{3(1 - \nu^2) \cdot r_l^2 \cdot \Delta F}{2\pi \cdot \Delta f \cdot t^3} \cdot \left[\frac{r_s^2}{r_l^2} - 1 - \ln \frac{r_s}{r_l} + \frac{1}{2} \cdot \left(\frac{1 - \nu}{1 + \nu} \right) \cdot \left(\frac{r_s^2 - r_l^2}{r_p^2} \right) \cdot \frac{r_s^2}{r_l^2} \right] \quad (3.4)$$

where F is the fracture force, ΔF and Δf are load and displacement interval of the linear part (from F to 50 % F) in a load-displacement curve, respectively. r is the radius, t is the thickness, subscripts s , l , and p denote the support ring, loading ring, and the tested pellet, respectively. The elastic modulus was determined from ring-on-ring tests at the highest loading rate, i.e. 20 MPa/s, since the load-displacement curve at low loading rate might be nonlinear due to potential subcritical crack growth (SCG).

Five ground and polished 50CF pellets were also tested, respectively, by ring-on-ring tests to determine the elastic modulus and fracture stress of the bulk materials at a loading rate of 20 MPa/s.

The effect of loading rate on strength was described by the parameterized subcritical crack growth (SCG) behaviour, which was assessed by [64]:

$$\log \sigma_0 = \frac{1}{n + 1} \cdot \log \dot{\sigma} + \log D \quad (3.5)$$

where $\dot{\sigma}$, n , and D are loading rate, SCG exponent, and SCG constant, respectively. σ_0 is the characteristic strength, and defined as fracture stress with a failure probability (P_f) of ~ 63 %. The SCG exponent and constant were derived by linear regression method based on equation A3.1-A3.6.

The relation of σ_0 and P_f was described by a two-parameter Weibull distribution [65]:

$$P_f = 1 - \exp \left[- \left(\frac{\sigma_f}{\sigma_0} \right)^m \right] \quad (3.6)$$

where m is the Weibull modulus. m and σ_0 were derived with the corresponding 90 % confidence intervals by linear regression method based on equation A3.7&A3.8.

To predict a lifetime under a static load, the σ_0 measured under dynamic load was firstly converted to equivalent stress (σ_{1s}) that causes failure in 1 s with a probability of $\sim 63.2\%$ under static load by [58]:

$$\sigma_{1s} = \sigma_0 \cdot \left(\frac{\sigma_0}{\dot{\sigma} \cdot (n + 1)} \right)^{\frac{1}{n}} \quad (3.7)$$

The characteristic strengths at different lifetimes were correlated according to the relationship [58]:

$$\frac{t_2}{t_1} = \left(\frac{\sigma_1}{\sigma_2} \right)^n \quad (3.8)$$

where $\sigma_i (i = 1,2)$ denotes the characteristic strength for a lifetime $t_i (i = 1,2)$.

Thus, the characteristic strength (σ_t) at a given lifetime (t) was derived by combing equation (3.7) and (3.8):

$$\sigma_t = \sigma_0 \cdot \left(\frac{\sigma_0}{\dot{\sigma} \cdot t \cdot (n + 1)} \right)^{\frac{1}{n}} \quad (3.9)$$

In the case that n has an infinite value, the corresponding σ_t was estimated to be equal to σ_0 .

For deriving uncertainties of σ_t , equation (3.9) was plotted as a 3D surface with n and σ_0 as independent variables and σ_t as a dependent variable using OriginPro software [66]. The n value changed between the lower and upper uncertainty limits. And σ_0 varied within 90 % confidence interval. Thereby, the maximum and minimum σ_t value were obtained from the plotted 3D surface, and defined as the upper and lower uncertainty limits of σ_t , respectively.

A strength-probability-time (SPT) diagram was constructed to express the relationship between stress, failure probability and lifetime [54-56, 58]. Since low Weibull modulus and low characteristic strength indicate high failure probabilities

at low stresses, the lower uncertainty limit of an SPT line at a given lifetime (t) was obtained using the lower confidence bound of Weibull modulus (m) and the lower uncertainty limit of characteristic strength (σ_t). Correspondingly, the upper uncertainty limit of an SPT line at a given lifetime (t) was derived by using the upper confidence bound of Weibull modulus and the upper uncertainty limit of characteristic strength (σ_t). Therefore, the uncertainty of each SCG was derived with the consideration of uncertainties of n and 90 % confidence intervals of m and σ_0 .

To clarify fracture modes and fracture origins, the fracture surfaces were investigated by BSEM. The size of flaws as the likely or apparent fracture origins were measured, and compared with the estimated critical flaw size that leads to failure using [67]:

$$\sqrt{C} = \frac{K_{IC}}{Y \cdot \sigma} \quad (3.10)$$

where C , K_{IC} , Y , and σ are fracture origin size, fracture toughness, stress intensity factor, and stress at the fracture origin, respectively. For a surface flaw as a fracture origin, the C is equal to the depth of the flaw [68]. The Y value is approximately $1.12\sqrt{\pi}$ for a half-penny shaped crack [57, 69]. The σ is practically identical to the fracture stress of the sample that only experiences the external stress applied during the strength measurement.

The fracture toughness (K_{IC}) and hardness (H) were determined for the polished pellet using the conventional Vickers indentation method [70]. Detailed experimental procedures and equations for derivations of K_{IC} and H can be found in our previous publication [71].

3.3 Results and discussion

3.3.1 Phase constituents and microstructure

EBSM measurements were only carried out at the bulk to verify the phase constituents of the sintered composites, since the as-sintered surfaces do not yield

reliable results due to their uneven topography. As illustrated in Figure 3.1, four phases are revealed: CGO fluorite, FCO spinel, CoO rock salt, and GdFeO₃-type perovskite. The composition of GdFeO₃-type perovskite was reported as Gd_{0.85}Ce_{0.15}Fe_{0.75}Co_{0.25}O₃ (GCFCO) [48, 72]. However, the CoO rock salt phase, being a result of uncomplete oxidization [72], is only observed in the 50CF composite.

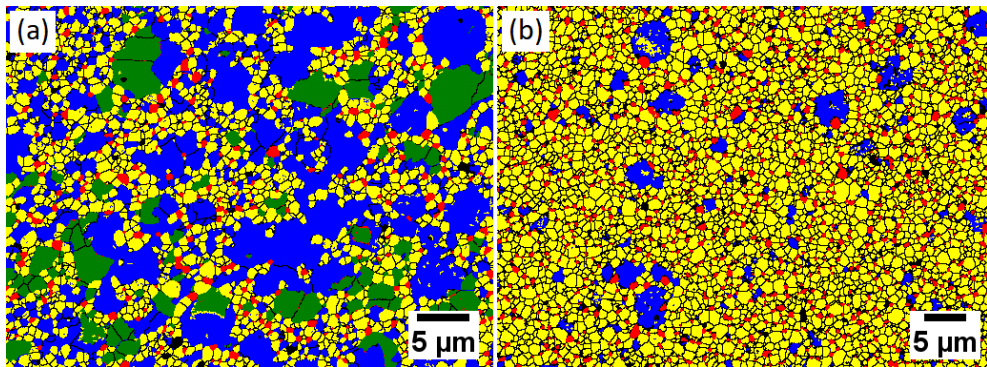


Figure 3.1 EBSD phase maps of the bulk of (a) 50CF and (b) 85CF. CGO, GCFCO, FCO, and CoO appear as yellow, red, blue, and green, respectively. In both (a) and (b), the pores can clearly be distinguished as black spots. The dark lines represent the grain or phase boundaries.

The porosity of each sintered composite is less than 1 % (see Figure 3.2, Figure 3.3 and Figure A3.1). No obvious microcracks are found in the bulk of both composites (see Figure A3.1), while a considerable amount of long microcracks ($\sim 10\text{-}30\ \mu\text{m}$) exists at the surface of 50CF (see Figure 3.2(a,b)). Such long microcracks were not found at the surface of 85CF (see Figure 3.2(c)). The sub-surfaces of 50CF and 85CF exhibit traces of relatively short microcracks ($\sim 4\ \mu\text{m}$), as verified in Figure 3.3. The sub-surface microcracks in 50CF might be linked to surface microcracks or even be an extension of surface microcracks. Overall the mechanism leading to the microcracks is unclear. A possible cause of the microcracks can be internal stress generated by the potential difference in chemical expansion of some localized CGO grains or the difference in the thermal expansion coefficients of different phases.

Nevertheless, these observations indicate that microcracks exist in a shallow sub-surface region of the sintered pellets. Such microcracks are expected to reduce the mechanical strength, and also influence the SCG behaviours.

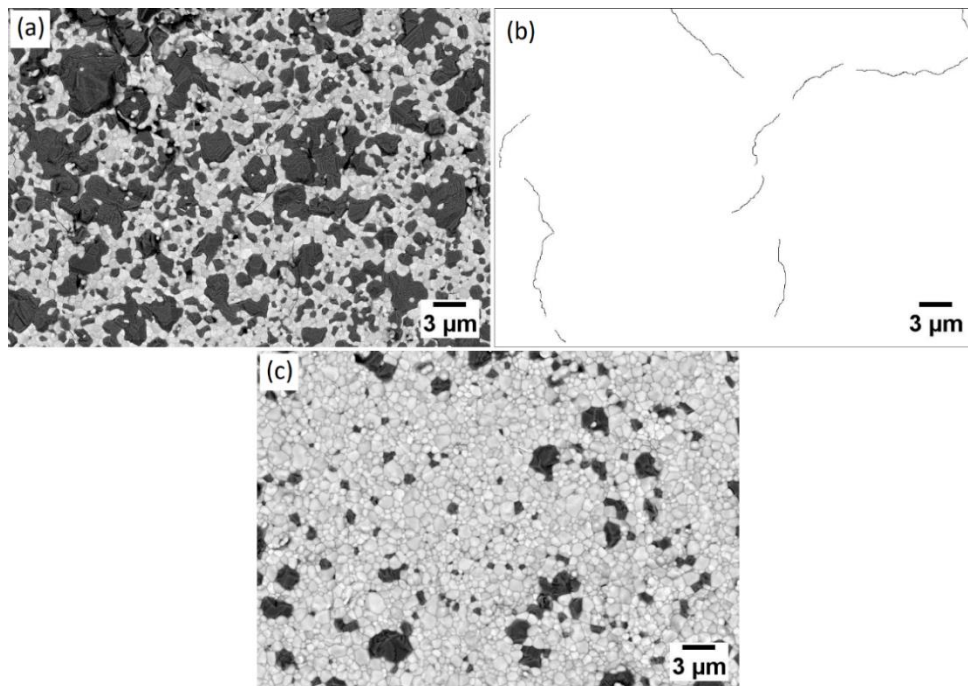


Figure 3.2 Surfaces of the as-sintered (a) 50CF and (c) 85CF. (b) shows a sketch of the microcracks shown in (a). The FCO and CoO grains appear as in dark-grey, while the CGO and GCFCO grains are shown as lighter shades of grey.

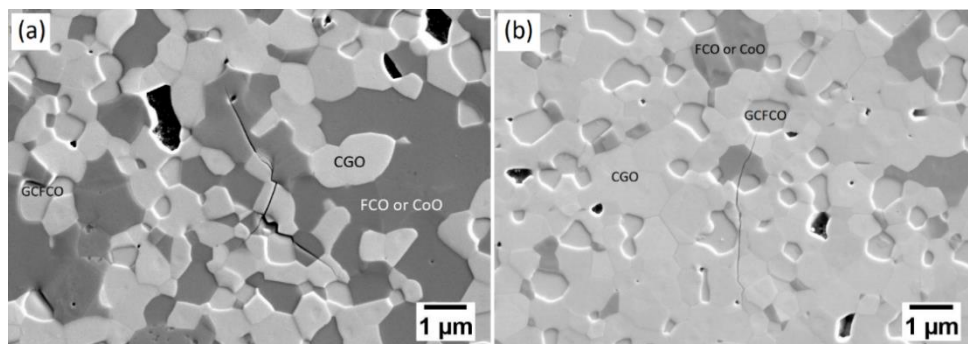


Figure 3.3 Microcracks in the sub-surface regions of (a) 50CF and (b) 85CF.

To compare the amount of each phase across the sintered pellets in more detail, both surface and bulk of the composites were characterized by XRD. As presented in Figure 3.4, 85CF shows no significant differences in phase amounts at the surface and bulk, while 50CF possesses a slightly higher amount of FCO in the bulk. CoO seems to appear only in 50CF, and the CoO in the bulk is around double that at the surface. Since the penetration depth of X-rays increases with the incident angle during measurement, and is on average greater than a few microns [73, 74], the XRD investigation at the surface is expected to reveal crystal information also of the sub-surface material. Thus, the amount of CoO detected at the surface might, in fact, include some amount of sub-surface CoO. The surface skin layer possibly contains no CoO since the excess oxygen in air should oxidize CoO into Co_3O_4 gradually while the temperature decreases from ~ 1200 K [59].

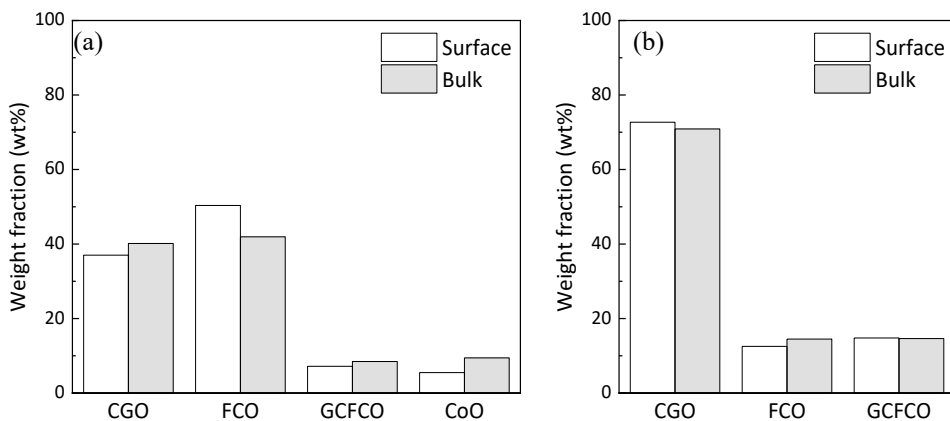


Figure 3.4 Phase quantifications of (a) 50CF and (b) 85CF in the bulk and at the surface.

For pure CoO, the oxidation of the surface layer can be described by equation (3.11) [75], and the bulk is oxidized according to equation (3.12) [75]. The continuous oxidation of CoO in the bulk relies on the transport of ionized cations and electrons to the surface layer, where the reaction described by equation (3.11) takes place [76].



where subscript i means “ionized”.

For the dual phase material studied here, the ionized Co cations and electrons cannot be transported easily to the surface due to a shortage of diffusion paths, and some portions of the CoO in the bulk is expected to remain unoxidized. However, no CoO could be found in the bulk of 85CF after cooling (see Figure 3.1(b)). It is unlikely that all CoO grains are well connected to form continuous paths for transporting the ionized Co cations and electrons from bulk to surface in 85CF. Hence, it implies that the reaction of equation (3.11) is still possible to happen at heterophase boundaries in the bulk. Since CGO shows the ability to dissociate oxygen according to equation (3.13) [43], reaction (3.11) may happen at CGO/CoO interfaces, which is supported by the occurrence of an O-deficient layer surrounding the isolated spinel phase [46]. Since the ability of CGO to dissociate oxygen is limited, continuous reactions in equations (3.11) and (3.12) rely on the supplement of oxygen ions diffused from the surface through free paths formed by CGO. The unoxidized CoO in the bulk of 50CF is an implication of insufficient supplement of oxygen ions due to a shortage of CGO free paths.



The lattice constants of CGO and GCFCO were derived from the XRD data, while it was not possible to obtain a value for the lattice constant of FCO due to the variation of the cobalt-to-iron ratios [53]. The formation of GCFCO consumes Gd from the $Ce_{0.8}Gd_{0.2}O_{1.9}$ in the initial powder mixtures, and reverses the reaction equilibrium in equation (3.1), which results in a reduction of oxygen vacancies and leads to a shrinkage of the CGO lattice. Such a reaction can easily reach a balance at the sintering temperature, i.e. 1200 °C, because of the fast diffusion. The content of formed GCFCO remains stable upon cooling [71]. Since the average Gd content in GCFCO was reported as almost constant [48, 53], a similar amount of GCFCO in the surface and the bulk (Figure 3.4) implies that the total consumed Gd amount from $Ce_{0.8}Gd_{0.2}O_{1.9}$ is the same. In other words, the Gd content left in CGO is the same in the surface and the bulk, and, hence, the lattice constants of CGO should not be

different. However, the lattice constant of CGO in the bulk is slightly higher than the one in the surface for both composites, as shown in Figure 3.5. The lattice constants of GCFCO and CoO, though, are almost identical in the bulk and the surface (Table A3.1). A possible reason might be that the oxygen vacancies produced according to equation (3.13) during the cooling process are partially balanced by the oxygen ions that are transported from the surface through free paths. This means that part of the CGO in the bulk contains additional oxygen vacancies, and hence, has a larger lattice constant. Nevertheless, these hypotheses need further validation, which is out of the scope of this work.

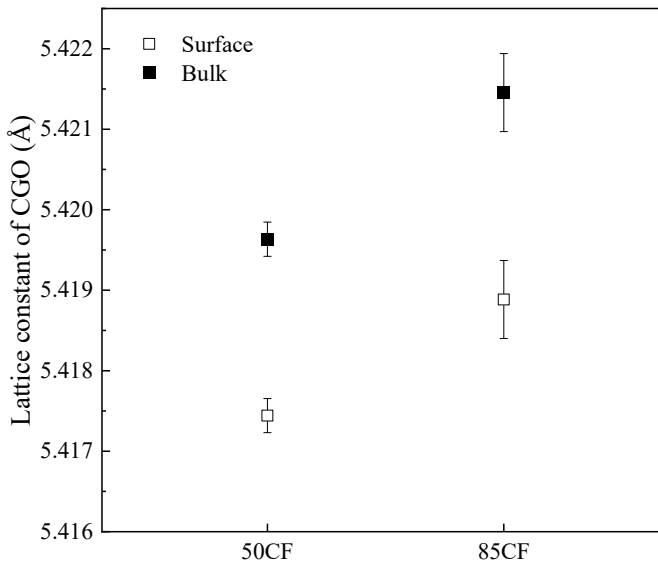


Figure 3.5 Lattice constants of CGO of surface and bulk regions of the sintered composites.

3.3.2 Residual stress

A similar thermal expansion coefficient ($\sim 12 \times 10^{-6} \text{ K}^{-1}$) has been reported for FCO and CGO [44, 46, 47], as well as for GdFeO_3 [77] and $\text{Gd}_{0.8}\text{Sr}_{0.2}\text{FeO}_{3-\delta}$ [78], whose perovskite crystal structures are similar to the one of GCFCO. Therefore, no significant thermal-mismatch-induced residual stress is anticipated in the sintered composites. However, a chemically induced residual stress can be expected in the

sintered composites following the hypotheses state above (see Figure 3.5). The surface is, thus, expected to be under tensile stress since the lattice shrinkage during cooling is larger in the surface than in the bulk.

The residual stresses of CGO, FCO and CoO in the surface of each as-sintered composite were determined by XRD, respectively. Linear dependences of $\sin^2 \psi$ on d were obtained for CGO, FCO and CoO, as exemplified for 50CF in Figure 3.6. The calculated residual stress values are listed in Table 3.1, showing that CGO, FCO and CoO experience tensile residual stresses. Since GCFCO is randomly distributed and surrounded by the majority phases, i.e. CGO and FCO, the stress state in GCFCO is expected to be the same as the one of CGO and FCO. Hence, the whole surface is under tensile stress. For 85CF, only the Bragg reflections of CGO provide enough intensity to be used for residual stress determination. Besides, the broadening and overlapping of FCO diffractions peaks at high 2θ positions, due to the variation of Co-to-Fe ratio, make it difficult to determine the peak position and peak shift for residual stress analysis for FCO.

To detect a potential residual stress gradient, the residual stresses of CGO, FCO and CoO were also determined in the sub-surface of each composite, as shown in Figure 3.6 for 50CF. The lattice spacing is almost independent of $\sin^2 \psi$ for the sub-surface CGO and CoO, which indicates a stress-free state. By contrast, a nonlinear change of the lattice spacing with increasing $\sin^2 \psi$ is obtained for the sub-surface FCO, which is an indication of a mixed stress state resulting in an average stress value close to 0 [61]. In fact, a compressive stress state is expected in the sub-surface, which should counterbalance the tensile surface stresses. However, it is difficult to conclude on any residual stress state for the sub-surface according to Figure 3.6. A low magnitude of the sub-surface stress can result from a thin stressed surface layer since the sum of all stresses should be zero.

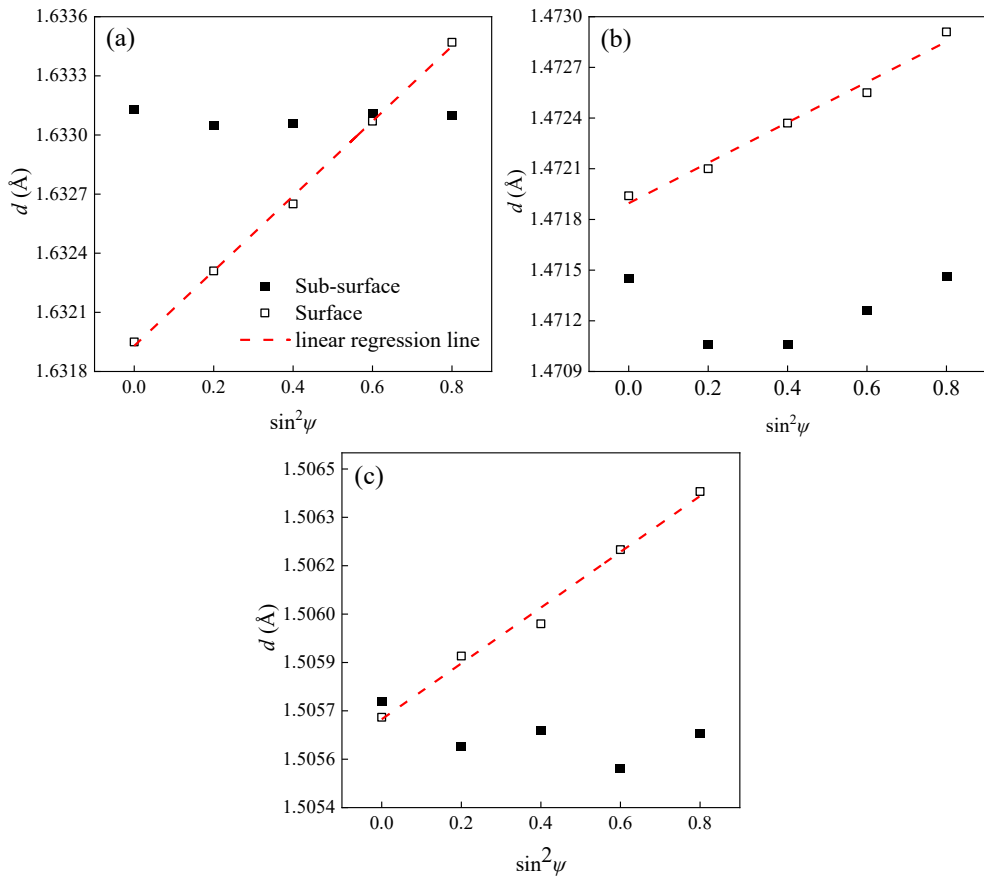


Figure 3.6 Dependence of d on $\sin^2\psi$ values for 50CF: (a) (311) plane in CGO, (b) (440) plane in FCO and (c) (220) plane in CoO. (The legends in (a) are also applied to (b) and (c)).

Table 3.1 Residual stress in CGO, FCO and CoO in the surfaces of the sintered composites determined by XRD.

Composite	Residual stress (MPa)		
	CGO	FCO	CoO
50CF	205 ± 4	130 ± 11	85 ± 5
85CF	94 ± 9	-	×

-: Not detectable due to low intensity

×: Phase does not exist

Nevertheless, it should be noted that the residual stress determined by XRD represents an average residual stress value of a layer consisting of materials in and below the surface tested by XRD due to the penetration depth of X-rays (as mentioned in the previous section) [74].

3.3.3 Mechanical properties

The E and σ_f values of the as-sintered composites derived from the ring-on-ring test data at the highest loading rate of 20 MPa/s, are shown in Table 3.2. The average E values, to which all phases and undulations in the composite contribute, of the two composites are similar within the limits of experimental uncertainty. The E values for 50CF and 85CF with rather small grains ($< 1 \mu\text{m}$) were determined by nanoindentation tests at a load of 150 mN, and reported to be ~ 215 GPa and ~ 223 GPa, respectively [53]. These values are higher than the ones shown in Table 3.2, while it is not unexpected that nanoindentation tests yield higher E values than macroscopic techniques [79].

Table 3.2 Elastic modulus and average fracture stress of the as-sintered composites measured at a loading rate of 20 MPa/s.

Composite	E (GPa)	σ_f (MPa)
50CF	197 ± 12	105 ± 18
85CF	191 ± 34	134 ± 34

The average σ_f values show only a minor dependency on composition when the uncertainties are considered (see Table 3.2). Hence, differences in residual stress and potential microcrack effects on strength are not reflected in differences between the σ_f values of the two as-sintered composites.

Thus, ring-on-ring tests with the same loading rate were conducted for 50CF after surface layer removal with the bulk surface representing the tensile surface. Based on the microstructural investigations and residual stress analysis, the bulk surface

was free of both microcracks (see Figure A3.1 (a)) and residual stress (see Figure 3.6). The derived E and σ_f values are presented in Figure 3.7. It unveils that the E values measured for bulk and initial surface are almost identical considering the uncertainties, while the σ_f value obtained for the bulk material is clearly higher than the one measured for the initial surface. The tensile residual stress and microcracks tend to reduce the fracture stress as expected. Hence, the mechanical properties of the bulk can be regarded as the intrinsic strength of the composite due to the absence of a surface layer with residual stress and microcracks. The agreement of the values for the initial surfaces of the two different composites appears in this context to be only coincidental since the 85CF was not affected to the same extent by residual stress and microcracks.

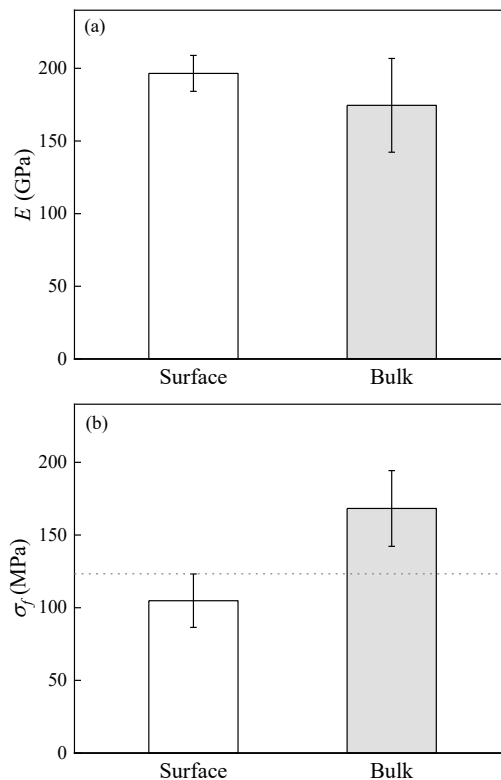


Figure 3.7 Elastic modulus (a) and fracture stress (b) of 50CF measured at surface and bulk with a loading rate of 20 MPa/s.

Hence, H and K_{IC} values were measured only for the bulk of sintered composites to obtain intrinsic values without effects of residual stress and microcracks. As given in Table 3.3, when the inherent experimental uncertainties are considered, the H and K_{IC} values do not show a strong dependence on the applied loads, and the K_{IC} values are almost independent of composition, while the hardness of 85CF is higher than the hardness of 50CF. The difference in hardness can be attributed to a compositional effect since the porosity difference of the two composites is rather small (see Figure 3.2, Figure 3.3 and Figure A3.1). Since the H value of CGO and FCO phase are similar [53], the compositional effect on hardness can be reflected by the amount of CoO phase, which shows a low hardness of ~ 6 GPa [53], and is only detected in 50CF (see Figure 3.4(a)). Thus, a higher hardness value for 85CF can be expected in agreement with the experimental results. By contrast, the 50CF and 85CF with rather small grains ($< 1 \mu\text{m}$) were reported to possess a similar H of ~ 12 GPa [53], which was determined by nanoindentation tests at a load of 150 mN. The reported values did not show a dependence on composition and are higher than the H values shown in Table 3.3. Such differences can be explained in two aspects. On the one hand, the reported 50CF only possesses a very small amount of CoO, which has a small grain size ($< 1 \mu\text{m}$) and is rather inhomogeneously distributed. Hence, the degradation effect of CoO on H is expected to be smaller and harder to be revealed for the reported 50CF than for the 50CF studied here. On the other hand, the higher H value for the reported composites can be attributed to some grain boundary strengthening effect, as well as potential indentation size effect [62].

Table 3.3 Mechanical properties of the sintered composites.

Composite	H (GPa)		K_{IC} (MPa·m ^{0.5})	
	1 N	5N	1 N	5N
50CF	8.1 ± 0.3	8.8 ± 0.2	0.88 ± 0.11	0.93 ± 0.11
85CF	9.8 ± 0.6	9.9 ± 0.3	0.78 ± 0.12	0.85 ± 0.08

The indentation cracks generated at a load of 5 N (see Figure A3.2) reveal a similar crack propagation pattern for the two composites. The cracks appear to predominantly propagate through the grains with no typical preferred paths towards or bypassing any phase constituent or grain boundary. Crack deflections in dual phase membrane composites were reported to be strongly affected by a variation of residual stress states that appears between the phase constituents [49]. Hence, the observed undeflected cracks are implications of stress-free states (or rather small stresses) for phase constituents in the bulk of the composites, which agrees with the conclusions presented in the previous sections.

3.3.4 Subcritical crack growth and Weibull analysis

Although it seems like an effective way to improve the strength of the pellet shape sample by removing the layer with residual stress and microcracks, it is not practical to do so for a membrane component with a large dimension or in a case of nonplanar shape, especially for tubular membrane components. Hence, the evaluation of subcritical crack growth (SCG) behaviour, Weibull distribution and lifetime will still be based on fracture stress data measured for as-sintered composites.

The SCG behaviours of the as-sintered composites are assessed by plotting fracture stresses as a function of loading rate, as shown in Figure 3.8. For 50CF, fracture stresses do not appear to change significantly with loading rate. By contrast, for 85CF, fracture stresses appear to increase with loading rate. A rather strong increase of the fracture stresses is observed when the loading rate increases from 0.2 MPa/s to 2 MPa/s. The SCG parameters were then deduced by linear regression according to equation (S7). A steep slope of the linear regression line suggests high sensitivity to SCG, and leads to a small n value (note n is proportional to the reciprocal of the slope).

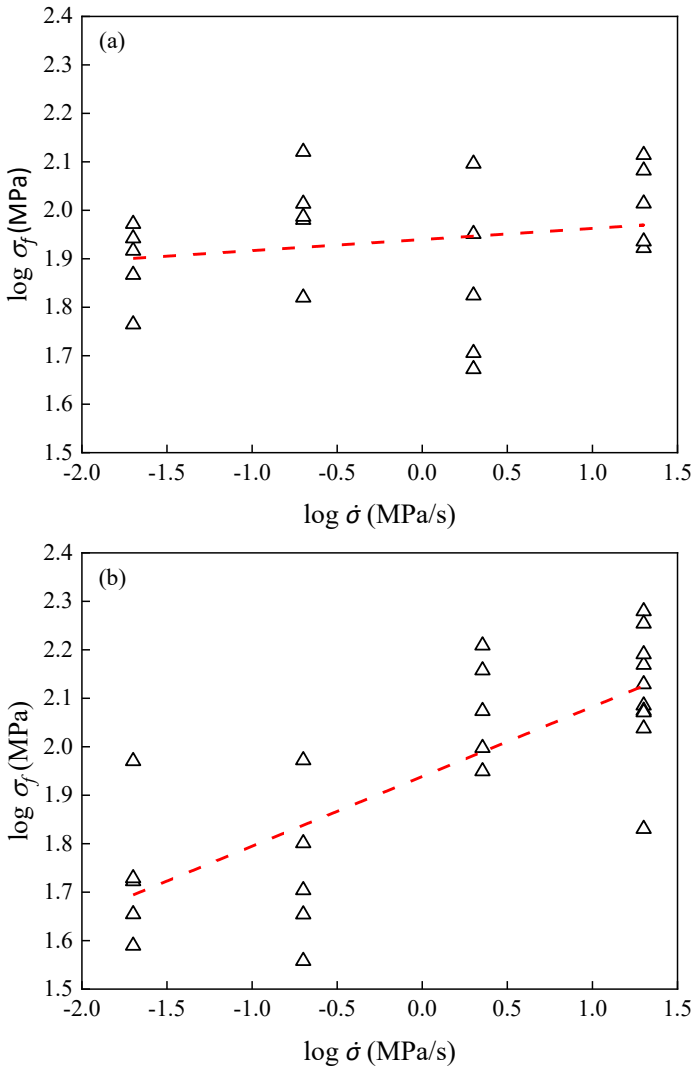


Figure 3.8 Fracture stress as a function of the loading rate for (a) 50CF and (b) 85CF. The red dotted lines are the linear regression fits.

The calculated SCG parameters are presented in Table 3.4. The D values are identical for the two composites, while the n value of 50CF is much higher than the one of 85CF. And the confidence interval of n value is narrower for 85CF than for 50CF. Although the mathematical analysis determined a minimum slope with a negative value for 50CF, it is realistic to consider that the minimum slope is close to

zero and n is infinity since no defect healing effect can happen during mechanical loading [56]. The infinite upper confidence bound of n value for 50CF implies that there is no SCG. The n value of 50CF is close to that of the popular dense perovskite oxygen transport membranes, i.e. $\text{Ba}_{0.5}\text{Sr}_{0.5}\text{Co}_{0.8}\text{Fe}_{0.2}\text{O}_{3-\delta}$ ($n \approx 40$) [56] and $\text{La}_{0.58}\text{Sr}_{0.4}\text{Co}_{0.2}\text{Fe}_{0.8}\text{O}_{3-\delta}$ ($n \approx 49$) [56], which indicates no pronounced SCG behaviour. The n value of 85CF is lower than that of soda-lime glasses ($n \sim 11-18$), which is known to be prone to static fatigue [80]. Therefore, it can be concluded that 85CF is more susceptible to SCG than 50CF. Since the two composites were tested under the same environment, such a distinguishable SCG behaviour might be induced by compositional and microstructural variations.

Table 3.4 SCG exponent (n) and SCG constant (D) with upper and low uncertainty limits.

Composite	n	D
50CF	$43^{+\infty}_{-20}$	87^{+6}_6
85CF	6^{+1}_{-1}	87^{+6}_6

Weibull analysis was then conducted for all fracture stresses of the as-sintered composites. For 85CF, the fracture strength data obtained at the highest loading rate, i.e. 20 MPa/s were used to minimize the effect of SCG on Weibull analysis. For 50CF, the fracture strength data from all loading rates were combined to increase the data quantity and improve the feasibility for Weibull analysis since they possess low variations at different loading rates due to the limited SCG effect (see Figure 3.8(a)). The Weibull distributions of fracture stresses can be well described by a linear relationship in the log representation, as presented in Figure A3.3.

The derived Weibull parameters are listed in Table 3.5. The m values of the two composites are similar, and lower than that of the popular dense perovskite oxygen transport membrane - $\text{Ba}_{0.5}\text{Sr}_{0.5}\text{Co}_{0.8}\text{Fe}_{0.2}\text{O}_{3-\delta}$ ($\sim 8-10$ [54, 81]). The low m value

indicates rather larger failure probabilities for comparably low stresses. 85CF and 50CF have a more pronounced difference in characteristic strength than in average strength at 20 MPa/s. The σ_0 value of 85CF is higher than that of 50CF considering the confidence intervals. Hence, it is concluded that 85CF is mechanically more robust than 50CF against instant failure.

Table 3.5 Weibull modulus (m) and characteristic strength (σ_0) obtained by a linear regression method. (Numbers in brackets refer to the 90 % confidence intervals)

Composite	m	σ_0 (MPa)
50CF	4.1 [3.8-4.4]	99 [96-101]
85CF	4.1 [3.5-4.6]	148 [141-155]

3.3.5 Fractography

The fracture surfaces were investigated by SEM to determine the fracture mode. For both composites, the fracture path developed mainly in a transgranular mode (see Figure A3.4), which agrees with the previous observations based on indentation cracks in section 3.4.

The investigation of fracture origins was carried out for the samples that failed at the lowest stresses at 20 MPa/s and 0.02 MPa/s, respectively. Besides, for 85CF fractured at 20 MPa/s, since the lowest strength value is much lower than the other ones that concentrate tightly (see Figure 3.8(b)), the fracture origins of the sample with the second-lowest strength were also investigated as representatives for the majority case. The largest flaws close to the fracture position were determined to be the likely fracture origins followed by rather long fracture lines. In general, all fracture origins appear to be located at the tensile surface, as highlighted in Figure 3.9 and Figure 3.10. However, they are clearly different for the two composites.

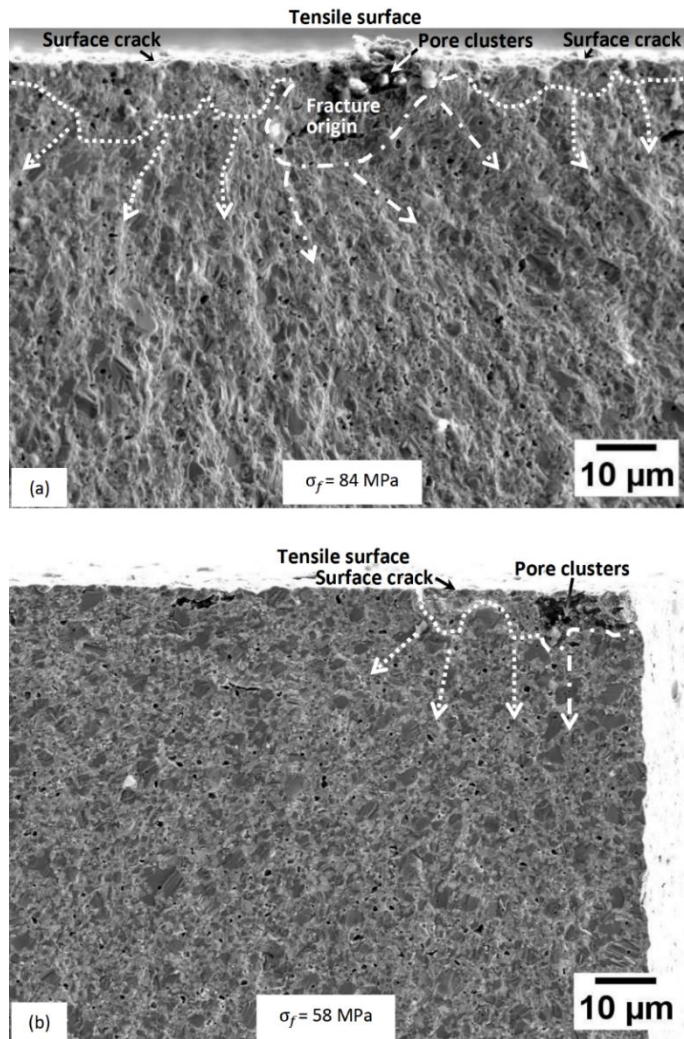


Figure 3.9 Likely fracture origins of as-sintered 50CF fractured at (a) 20 MPa/s and (b) 0.02 MPa/s. The dotted and dash-dotted lines represent boundaries of surface cracks and pore clusters, respectively, as possible fracture origins. The fracture lines for each type of fracture origin are indicated by the arrows.

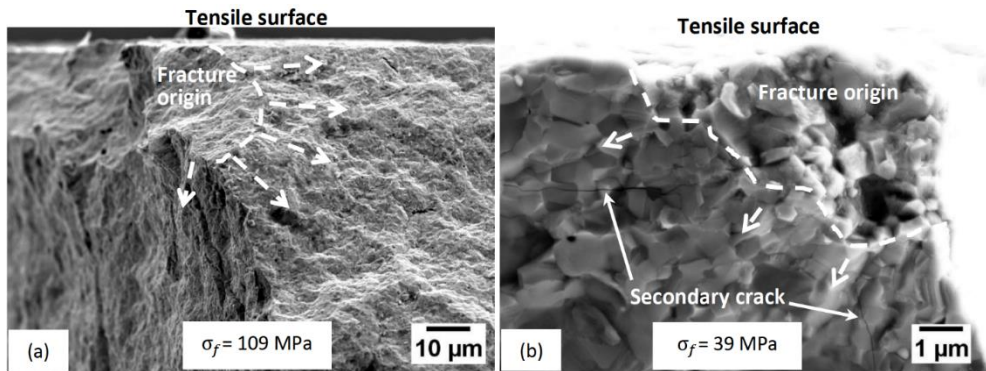


Figure 3.10 Likely fracture origins of 85CF fractured at (a) 20 MPa/s and (b) 0.02 MPa/s. The dashed lines represent the likely boundaries of fracture origins. The fracture lines are indicated by the dashed arrows.

For as-sintered 50CF failed at 20 MPa/s and 0.02 MPa/s, the pore clusters and microcracks at surface likely interacted with each other and appear to have contributed together to initiating the fracture (see Figure 3.9).

For the ground and polished 50CF, only one type of flaw appears to be the fracture origin due to the absence of long microcracks (see Figure A3.5). Although a small surface flaw, as shown in Figure A3.5(b), seems to initiate the crack proportions, the sample has apparently failed at the large flaw ($\sim 20 \mu\text{m}$) highlighted in Figure A3.5(a) indicated by the long extension of fracture lines.

For as-sintered 85CF, it is hard to determine where the fracture has started for the sample with the lowest fracture strength of 68 MPa at 20 MPa/s. Several surface-located flaws appear to develop rather long fracture lines (see Figure A3.6(a)). The largest one is around $\sim 20 \mu\text{m}$ (see Figure A3.6(b)). By contrast, for the sample with the second-lowest fracture strength of 109 MPa at 20 MPa/s, a more distinct surface-located flaw can be characterized to be the likely origin (see Figure 3.10(a)). Similarly, for the samples with the lowest fracture strength at 0.02 MPa/s, rather discernible surface-located flaws can also be characterized as the likely fracture origins (see Figure 3.10(b)), the sizes of which are much smaller than those observed

for the samples fractured at 20 MPa/s. In addition, secondary cracks are found surrounding the fracture origins (see Figure 3.10(b)), which, though, do not appear to have developed to a critical size. These secondary cracks could be a result of slow crack propagation, and might have interacted with the sub-surface short microcracks (see Figure 3.3).

The sizes of the fracture origin were measured and compared with the values estimated by equation (10). For the ground and polished 50CF, the total σ value at the fracture origins can be regarded as equal to the fracture stress due to the absence of residual stresses (see Figure 3.6). Hence, the size of the fracture origin shown in Figure A3.5(a) was calculated to be $\sim 12 \mu\text{m}$, which is close to the measured value ($\sim 19 \mu\text{m}$) considering the uncertainties induced by measurement and Y value.

For the sample experiencing tensile residual stress at the surface, it is necessary to consider how the tensile residual stress (see Table 3.1) contributes to the total σ value around the fracture origin. As an approximation, the σ value is calculated as the sum of the fracture stress of the sample and the residual stress around the fracture origin, i.e. $\sigma = \sigma_f + \sigma_r$. Although it was shown that the tensile stress decreased gradually from surface to a certain depth ($< 30 \mu\text{m}$) in bulk, the tensile stress at a given depth around the fracture origin cannot be determined. Hence, the σ_r value for correction of σ value is assumed to be between 0 (stress-free) and the maximum tensile stress value, i.e. the tensile stress value in CGO (see Table 3.1). Thereby, a lower and an upper limit of C are calculated to represent the fracture origin size of a sample with and without tensile residual stress, respectively. The measured C should not be smaller than the lower limit value of the estimated C since average residual stress around the fracture origin is expected to be lower than the maximum tensile stress at surface. The degradation effect of tensile residual stress on fracture stress is expected to be stronger for smaller fracture origins due to the higher tensile residual stress value.

As given in Table 3.6, the fracture stress of the sample does not show a clear dependence on fracture origin size due to the effect of tensile residual stress. For

large fracture origins ($\approx 20 \mu\text{m}$), the measured C is in the vicinity of the upper limit of the estimated C , which implies a limit contribution of tensile residual stress. For small fracture origins ($< 10 \mu\text{m}$), the measured C is much lower than the upper limit of the estimated C , which emphasizes the contribution of tensile residual stress.

Table 3.6 Comparison of the estimated and measured fracture origin sizes for the as-sintered composites.

Composite	Loading rate (MPa/s)	σ (MPa)		C -estimated (μm)		C -measured (μm)
		Lower limit: σ_f	Upper limit: $\sigma_f + \max \sigma_r$	Lower limit	Upper limit	
50CF	0.02	58	263	3	58	9
	20	84	289	2	28	22
85CF	0.02	39	133	11	123	5
	20	109	203	5	16	19

The measured size of small fracture origin in 50CF is larger than the lower limit value of the estimated C as expected. This observation indicates that the average residual stress around the fracture origin is tensile and slightly lower than the maximum tensile stress at the surface, although uncertainties in the size of the fracture origin need to be considered.

However, the measured size of the small fracture origin in 85CF is even lower than the lower limit value of the estimated C . It cannot be concluded for 85CF that the residual stress around the fracture origin is compressive since the size of the fracture origin is smaller than the thickness of the tensile stress surface layer determined by XRD due to the relatively large penetration depth of X-ray at high incidence angles [74]. Hence, the fracture origin shown in Figure 3.10(b) for 85CF was under tensile stress. Since the small fracture origin appears in the sample fractured at a low loading

rate, the unexpected small fracture origin size could be explained by the relatively strong SCG behaviour, but again uncertainties in fracture origin determination can bias the result.

Under dynamic loading conditions, the stress intensity (K) at the fracture origin increases gradually with increasing applied stress to the critical value ($= K_{IC}$) due to the increase of stress value and flaw size (If SCG occurs). The measured C value can be the initial size of the flaw where SCG begins, while the C value estimated by equation (10) represents the final size of the flaw that leads to failure. Hence, the measured flaw size, i.e. the apparent fracture origin size, can only be regarded as the initial size of the fracture origin when SCG occurs.

Figure 3.11 shows schematics that suggest the process of SCG for 85CF. The SCG initiates from a flaw, while microcracks surrounding the flaw have a certain probability to extend. We would also like to point out that the size of the flaw and microcracks are comparable (see Figure 3.3(b) and Figure 3.10(b)). They can grow and interact or merge, and finally reach a critical size leading to failure. At a medium loading rate, low stresses, which permit SCG, last for a short time; the sample experiences a moderate SCG (see Figure 3.11(b)). By contrast, an enhanced SCG occurs at a low loading rate since the sample stays at low stress values for a long time, during which the initial small flaw and the sub-surface microcracks grow simultaneously and merge to form flaws with large sizes (see Figure 3.11(c)); the critical stress intensity, at which the sample finally fails, tends to reach at a comparably low stress value. However, such a fracture process is not likely to happen in 50CF, which is less sensitive to SCG effects as the failure is determined by surface-located flaws and microcracks (see Figure 3.2(b) and Figure 3.9) that are much larger than sub-surface microcracks (see Figure 3.3(a)) and cannot permit stable crack growth.

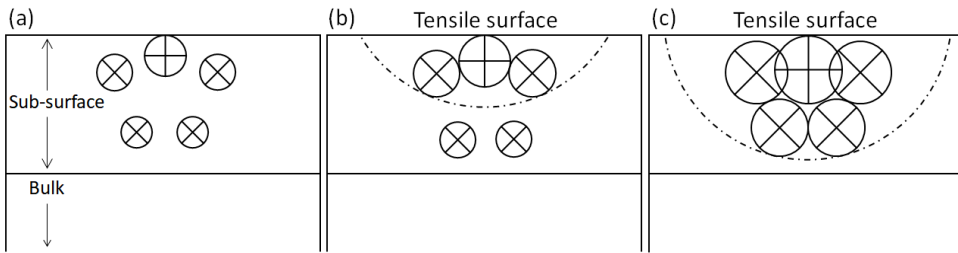


Figure 3.11 Schematics illustrating the interactions of a surface-located flaw (\oplus) and sub-surface microcracks (\otimes) in the sample fractured after SCG: (a) initial state of the sample, (b) sample fractured after a moderate SCG, and (c) sample fractured after an enhanced SCG. Dash-dotted lines represent the sizes where the sample failure is expected, referred to as boundaries of fracture origins.

3.3.6 Reliability and lifetime analysis

With the obtained Weibull and SCG parameters, SPT diagrams were constructed for three lifetimes, i.e. 1 s, 1 month, and 10 years. The 3D surface plots for deriving uncertainties of σ_t ($t = 1$ s, 1 month and 10 years), indicate that the σ_t changes monotonously as a function of n and σ_0 (see Figure A3.7 and Figure A3.8). In the 3D surface plots, the n and σ_0 varies within the range shown in Table 3.4 and Table 3.5, respectively. Hence, extreme values, i.e. the upper and lower uncertainty limit of σ_t , appear at the corresponding vertices of the 3D surfaces. For 50CF, the upper uncertainty limits of σ_t were estimated to be equal to σ_0 since the upper uncertainty limit of n is infinity.

The SPT lines with uncertainty intervals are illustrated in Figure 3.12. The slope of each line is equal to the Weibull modulus, m value. A higher m value suggests rather low failure probabilities for low static stress, although all m values reported here are overall rather low. Each line is shifted parallelly to the right when the time of operation increases, which means smaller stress induces the same failure probability and predicting a decrease of mechanical reliability with increasing time of operation. The shifting interval between two neighboring times of operation increases with n

value. Thus, the degradation of mechanical reliability with time of operation is faster with a lower n value.

The static failure stress values are higher for the SPT line on the right than the one on the left for equal failure probabilities. Hence, 85CF appears mechanically a bit more reliable than 50CF for instant failure within 1 s considering the uncertainties (see Figure 3.12(a)). When the time of operation increases to 1 month, the SPT line of 85CF shifts a much larger distance than the one of 50CF (see Figure 3.12(b)). The SPT line continues to shift to the left when the time of operation increases from 1 month to 10 years, but the shifting distances are rather small (see Figure 3.12(c)). The uncertainty intervals of the SPT lines of the two composites do not overlap at 1 month and 10 years (see Figure 3.12(b)&(c)). Thus, 85CF appears significantly less reliable than 50CF for long-term (e.g. 10 years) operation. Such a large degradation of mechanical reliability for 85CF is accompanied by the rather small n value (Table 3.4), which provokes the large shift of the SPT line from right to left when the time of operation increases from 1 s to 10 years.

Table 3.7 lists static failure stresses for a failure probability of 1 %. For instant failure within 1 s, the critical stress value is slightly higher for 85CF than for 50CF considering the uncertainties of the experiments. However, when for a lifetime that increases from 1 s to 10 years, the failure stress of 85CF is reduced significantly, while the failure stress of 50CF only decreases slightly. These results indicate that the mechanical reliability of 85CF is not sufficient for long-term operation. Further improvements are needed to optimize the SCG behaviour to obtain an improved n value.

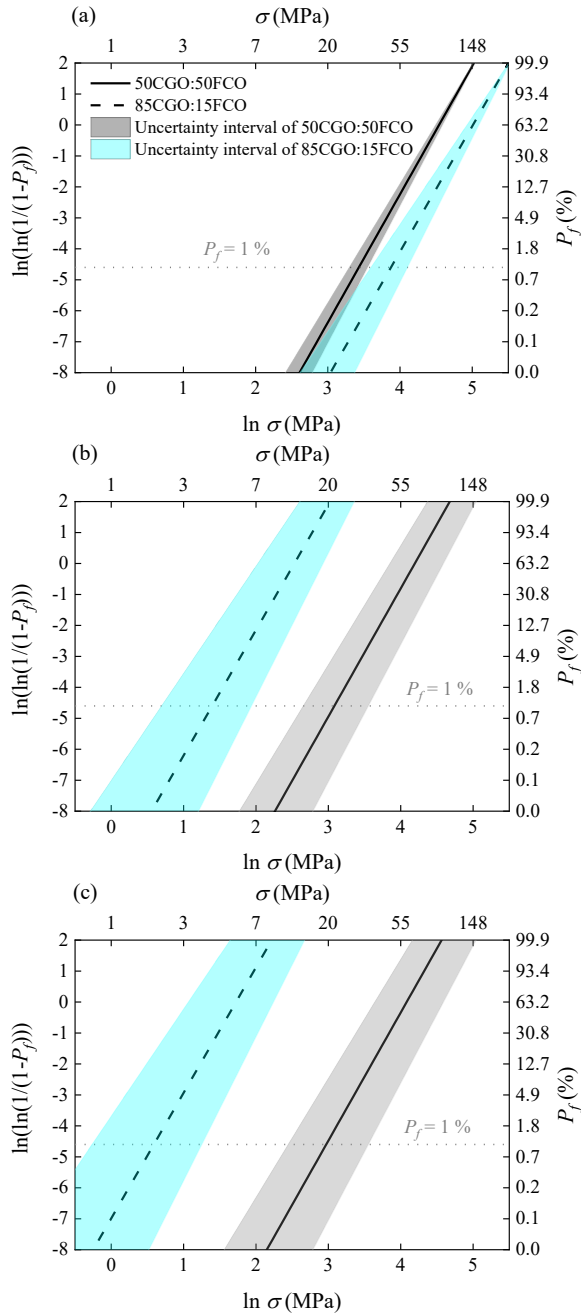


Figure 3.12 Prediction of failure probability as a function of static stress for different times of operation: (a) 1 s, (b) 1 month and (c) 10 years. (The legends in (a) are also applied to (b) and (c)).

Table 3.7 Failure stresses inducing a failure probability of 1 %.

Composite	Lifetime	Failure stress (MPa)
50CF	1 s	31^{+4}_{-4}
	1 month	22^{+13}_{-8}
	10 years	20^{+15}_{-8}
85CF	1 s	48^{+12}_{-12}
	1 month	4^{+3}_{-2}
	10 years	2^{+2}_{-1}

3.4 Conclusions

Dual phase composite membranes were prepared by a one-step solid-state reaction process from powder mixtures with two different weight ratios of CGO to FCO, i.e. 50:50, 85:15. With an objective to access the mechanical limits regarding application in particular reliability and lifetime, the mechanical properties and SCG behaviour of the synthesized membranes were characterized based on mechanical testing results from Vickers indentations and ring-on-ring tests with different loading rates. The associated effects of composition, residual stress and microcracks were discussed.

50CF and 85CF have similar mechanical properties, i.e. elastic modulus and fracture toughness, while 85CF shows a more pronounced SCG behaviour than 50CF. At a high loading rate (20 MPa/s), the average fracture strength is only slightly lower for 50CF than for 85CF, although 50CF exhibited long microcracks and high tensile residual stress. Nevertheless, the degradation effects of long microcracks and tensile residual stress are corroborated by a pronounced improvement of the average strength for 50CF, which exhibited surfaces free of microcrack and no tensile residual stress. When the loading rate decreased to 0.02 MPa/s, the strength of 50CF remained almost constant, while the strength of 85CF was significantly reduced,

which resulted in a higher failure probability and a reduction of the stress tolerance after a service time of 10 years.

The one-step processing of 85CF needs to be improved to avoid the fast strength degradation caused by the tensile residual stresses and microcracks observed in our research work. A reduction of the grain size and/or optimized sintering profiles might provide new directions to explore, which we will pursue in our future work.

References

- [1] A.M. Omer, Energy, environment and sustainable development, *Renewable and Sustainable Energy Reviews* 12(9) (2008) 2265-2300.
- [2] J. Kotowicz, T. Chmielniak, K. Janusz-Szymańska, The influence of membrane CO₂ separation on the efficiency of a coal-fired power plant, *Energy* 35(2) (2010) 841-850.
- [3] X. Zhu, W. Yang, *Mixed conducting ceramic membranes*, Springer-Verlag, Berlin, Germany, 2017.
- [4] P. Niehoff, F. Schulze-Kueppers, S. Baumann, W.A. Meulenberg, O. Guillon, R. Vassen, Fabrication of laboratory-scale planar oxygen separation membrane modules, *American Ceramic Society Bulletin* 94(1) (2015) 28-31.
- [5] K. Zhang, J. Sunarso, Z. Shao, W. Zhou, C. Sun, S. Wang, S. Liu, Research progress and materials selection guidelines on mixed conducting perovskite-type ceramic membranes for oxygen production, *RSC Advances* 1(9) (2011) 1661-1676.
- [6] H. Wang, S. Werth, T. Schiestel, J. Caro, Perovskite hollow-fiber membranes for the production of oxygen-enriched air, *Angewandte Chemie International Edition* 44(42) (2005) 6906-6909.
- [7] P.-M. Geffroy, J. Fouletier, N. Richet, T. Chartier, Rational selection of MIEC materials in energy production processes, *Chemical Engineering Science* 87 (2013) 408-433.
- [8] C. Karakaya, R.J. Kee, Progress in the direct catalytic conversion of methane to fuels and chemicals, *Progress in Energy and Combustion Science* 55 (2016) 60-97.
- [9] H. Jiang, H. Wang, S. Werth, T. Schiestel, J. Caro, Simultaneous Production of Hydrogen and Synthesis Gas by Combining Water Splitting with Partial Oxidation of Methane in a Hollow-Fiber Membrane Reactor, *Angewandte Chemie International Edition* 47(48) (2008) 9341-9344.

- [10] H.J. Bouwmeester, Dense ceramic membranes for methane conversion, *Catalysis Today* 82(1-4) (2003) 141-150.
- [11] X. Dong, W. Jin, N. Xu, K. Li, Dense ceramic catalytic membranes and membrane reactors for energy and environmental applications, *Chemical Communications* 47(39) (2011) 10886-10902.
- [12] H. Stadler, F. Beggel, M. Habermehl, B. Persigehl, R. Kneer, M. Modigell, P. Jeschke, Oxyfuel coal combustion by efficient integration of oxygen transport membranes, *International Journal of Greenhouse Gas Control* 5(1) (2011) 7-15.
- [13] M. Ramasamy, Dual phase oxygen transport membrane for efficient oxyfuel combustion, PhD thesis, Bochum University, Bochum, Germany, 2016.
- [14] X. Zhu, H. Liu, Y. Cong, W. Yang, Novel dual-phase membranes for CO₂ capture via an oxyfuel route, *Chemical Communications* 48(2) (2012) 251-253.
- [15] S. Baumann, J. Serra, M. Lobera, S. Escolástico, F. Schulze-Küppers, W.A. Meulenber, Ultrahigh oxygen permeation flux through supported Ba_{0.5}Sr_{0.5}Co_{0.8}Fe_{0.2}O_{3-δ} membranes, *Journal of Membrane Science* 377(1-2) (2011) 198-205.
- [16] J.M. Serra, J. Garcia-Fayos, S. Baumann, F. Schulze-Küppers, W.A. Meulenber, Oxygen permeation through tape-cast asymmetric all-La_{0.6}Sr_{0.4}Co_{0.2}Fe_{0.8}O_{3-δ} membranes, *Journal of Membrane Science* 447 (2013) 297-305.
- [17] M. Arnold, H. Wang, A. Feldhoff, Influence of CO₂ on the oxygen permeation performance and the microstructure of perovskite-type (Ba_{0.5}Sr_{0.5})(Co_{0.8}Fe_{0.2})O_{3-δ} membranes, *Journal of Membrane Science* 293(1-2) (2007) 44-52.
- [18] A. Waindich, A. Möbius, M. Müller, Corrosion of Ba_{1-x}Sr_xCo_{1-y}Fe_yO_{3-δ} and La_{0.3}Ba_{0.7}Co_{0.2}Fe_{0.8}O_{3-δ} materials for oxygen separating membranes under Oxycoal conditions, *Journal of Membrane Science* 337(1-2) (2009) 182-187.
- [19] J. Gao, L. Li, Z. Yin, J. Zhang, S. Lu, X. Tan, Poisoning effect of SO₂ on the oxygen permeation behavior of La_{0.6}Sr_{0.4}Co_{0.2}Fe_{0.8}O_{3-δ} perovskite hollow fiber membranes, *Journal of Membrane Science* 455 (2014) 341-348.
- [20] T. Ramirez-Reina, J.L. Santos, N. García-Moncada, S. Ivanova, J.A. Odriozola, Development of Robust Mixed-Conducting Membranes with High Permeability and Stability, *Perovskites and Related Mixed Oxides* (2016) 719-738.
- [21] S. Engels, T. Markus, M. Modigell, L. Singheiser, Oxygen permeation and stability investigations on MIEC membrane materials under operating conditions for power plant processes, *Journal of Membrane Science* 370(1-2) (2011) 58-69.

- [22] M. Schulz, R. Kriegel, A. Kämpfer, Assessment of CO₂ stability and oxygen flux of oxygen permeable membranes, *Journal of Membrane Science* 378(1-2) (2011) 10-17.
- [23] X. Tan, N. Liu, B. Meng, J. Sunarso, K. Zhang, S. Liu, Oxygen permeation behavior of La_{0.6}Sr_{0.4}Co_{0.8}Fe_{0.2}O₃ hollow fibre membranes with highly concentrated CO₂ exposure, *Journal of Membrane Science* 389 (2012) 216-222.
- [24] S.J. Benson, D. Waller, J.A. Kilner, Degradation of La_{0.6}Sr_{0.4}Fe_{0.8}Co_{0.2}O_{3-δ} in Carbon Dioxide and Water Atmospheres, *Journal of the Electrochemical Society* 146(4) (1999) 1305.
- [25] M. Ramasamy, E. Persoon, S. Baumann, M. Schroeder, F. Schulze-Küppers, D. Görtz, R. Bhave, M. Bram, W.A. Meulenber, Structural and chemical stability of high performance Ce_{0.8}Gd_{0.2}O_{2-δ}-FeCo₂O₄ dual phase oxygen transport membranes, *Journal of Membrane Science* 544 (2017) 278-286.
- [26] H. Luo, K. Efimov, H. Jiang, A. Feldhoff, H. Wang, J. Caro, CO₂-stable and cobalt-free dual-phase membrane for oxygen separation, *Angewandte Chemie International Edition* 50(3) (2011) 759-763.
- [27] H. Luo, H. Jiang, K. Efimov, F. Liang, H. Wang, J.r. Caro, CO₂-tolerant oxygen-permeable Fe₂O₃-Ce_{0.9}Gd_{0.1}O_{2-δ} dual phase membranes, *Industrial & Engineering Chemistry Research* 50(23) (2011) 13508-13517.
- [28] Z. Wang, W. Sun, Z. Zhu, T. Liu, W. Liu, A novel cobalt-free, CO₂-stable, and reduction-tolerant dual-phase oxygen-permeable membrane, *ACS applied materials & interfaces* 5(21) (2013) 11038-11043.
- [29] H. Cheng, N. Zhang, X. Xiong, X. Lu, H. Zhao, S. Li, Z. Zhou, Synthesis, Oxygen Permeation, and CO₂-Tolerance Properties of Ce_{0.8}Gd_{0.2}O_{2-δ}-Ba_{0.95}La_{0.05}Fe_{1-x}Nb_xO_{3-δ} Dual-Phase Membranes, *ACS Sustainable Chemistry & Engineering* 3(9) (2015) 1982-1992.
- [30] X. Zhu, Y. Liu, Y. Cong, W. Yang, Ce_{0.85}Sm_{0.15}O_{1.925}-Sm_{0.6}Sr_{0.4}Al_{0.3}Fe_{0.7}O₃ dual-phase membranes: One-pot synthesis and stability in a CO₂ atmosphere, *Solid State Ionics* 253 (2013) 57-63.
- [31] B. Wang, J. Yi, L. Winnubst, C. Chen, Stability and oxygen permeation behavior of Ce_{0.8}Sm_{0.2}O_{2-δ}-La_{0.8}Sr_{0.2}CrO_{3-δ} composite membrane under large oxygen partial pressure gradients, *Journal of Membrane Science* 286(1-2) (2006) 22-25.
- [32] S. Guo, Z. Liu, J. Zhu, X. Jiang, Z. Song, W. Jin, Highly oxygen-permeable and CO₂-stable Ce_{0.8}Sm_{0.2}O_{2-δ}-SrCo_{0.9}Nb_{0.1}O_{3-δ} dual-phase membrane for oxygen separation, *Fuel Processing Technology* 154 (2016) 19-26.

- [33] S.K. Kim, M.J. Shin, J. Rufner, K. van Benthem, J.H. Yu, S. Kim, $\text{Sr}_{0.95}\text{Fe}_{0.5}\text{Co}_{0.5}\text{O}_{3-\delta}$ - $\text{Ce}_{0.9}\text{Gd}_{0.1}\text{O}_{2-\delta}$ dual-phase membrane: Oxygen permeability, phase stability, and chemical compatibility, *Journal of Membrane Science* 462 (2014) 153-159.
- [34] S. Wang, T. Kobayashi, M. Dokiya, T. Hashimoto, Electrical and ionic conductivity of Gd-doped ceria, *Journal of the Electrochemical Society* 147(10) (2000) 3606-3609.
- [35] J.H. Joo, G.S. Park, C.-Y. Yoo, J.H. Yu, Contribution of the surface exchange kinetics to the oxygen transport properties in $\text{Gd}_{0.1}\text{Ce}_{0.9}\text{O}_{2-\delta}$ - $\text{La}_{0.6}\text{Sr}_{0.4}\text{Co}_{0.2}\text{Fe}_{0.8}\text{O}_{3-\delta}$ dual-phase membrane, *Solid State Ionics* 253 (2013) 64-69.
- [36] H. Takamura, M. Kawai, K. Okumura, A. Kamegawa, M. Okada, Preparation and oxygen permeability of Gd-doped ceria and spinel-type ferrite composites, *MRS Online Proceedings Library Archive* 756 (2002).
- [37] Y. Ji, J.A. Kilner, M.F. Carolan, Electrical conductivity and oxygen transfer in gadolinia-doped ceria (CGO)- $\text{Co}_3\text{O}_{4-\delta}$ composites, *Journal of the European Ceramic Society* 24(14) (2004) 3613-3616.
- [38] V. Kharton, A. Kovalevsky, A. Viskup, A. Shaula, F. Figueiredo, E. Naumovich, F. Marques, Oxygen transport in $\text{Ce}_{0.8}\text{Gd}_{0.2}\text{O}_{2-\delta}$ -based composite membranes, *Solid State Ionics* 160(3-4) (2003) 247-258.
- [39] A.J. Samson, M. Søgaaard, P.V. Hendriksen, (Ce,Gd) $\text{O}_{2-\delta}$ -based dual phase membranes for oxygen separation, *Journal of Membrane Science* 470 (2014) 178-188.
- [40] V.V. Kharton, A.V. Kovalevsky, A.P. Viskup, F.M. Figueiredo, A.A. Yaremchenko, E.N. Naumovich, F.M.B. Marques, Oxygen Permeability of $\text{Ce}_{0.8}\text{Gd}_{0.2}\text{O}_{2-\delta}$ - $\text{La}_{0.7}\text{Sr}_{0.3}\text{MnO}_{3-\delta}$ Composite Membranes, *Journal of the Electrochemical Society* 147(7) (2000) 2814-2821.
- [41] U. Nigge, H.D. Wiemhöfer, E.W.J. Römer, H.J.M. Bouwmeester, T.R. Schulte, Composites of $\text{Ce}_{0.8}\text{Gd}_{0.2}\text{O}_{1.9}$ and $\text{Gd}_{0.7}\text{Ca}_{0.3}\text{CoO}_{3-\delta}$ as oxygen permeable membranes for exhaust gas sensors, *Solid State Ionics* 146(1-2) (2002) 163-174.
- [42] M. Mogensen, T. Lindegaard, U.R. Hansen, G. Mogensen, Physical properties of mixed conductor solid oxide fuel cell anodes of doped CeO_2 , *Journal of the Electrochemical Society* 141(8) (1994) 2122.
- [43] K.L. Duncan, Y. Wang, S.R. Bishop, F. Ebrahimi, E.D. Wachsman, Role of point defects in the physical properties of fluorite oxides, *Journal of the American Ceramic Society* 89(10) (2006) 3162-3166.
- [44] T. Kiefer, Entwicklung neuer Schutz- und Kontaktierungsschichten für Hochtemperatur-Brennstoffzellen, PhD thesis, Ruhr-Universität Bochum, Bochum, Germany, 2008.

- [45] Z.H. Bi, J.H. Zhu, J.L. Batey, CoFe₂O₄ spinel protection coating thermally converted from the electroplated Co-Fe alloy for solid oxide fuel cell interconnect application, *Journal of Power Sources* 195(11) (2010) 3605-3611.
- [46] M. Ramasamy, S. Baumann, J. Palisaitis, F. Schulze-Küppers, M. Balaguer, D. Kim, W.A. Meulenber, J. Mayer, R. Bhawe, O. Guillon, Influence of Microstructure and Surface Activation of Dual-Phase Membrane Ce_{0.8}Gd_{0.2}O_{2-δ}-FeCo₂O₄ on Oxygen Permeation, *Journal of the American Ceramic Society* 99(1) (2016) 349-355.
- [47] E.Y. Pikalova, A.N. Demina, A.K. Demin, A.A. Murashkina, V.E. Sopernikov, N.O. Esina, Effect of doping with Co₂O₃, TiO₂, Fe₂O₃, and Mn₂O₃ on the properties of Ce_{0.8}Gd_{0.2}O_{2-δ}, *Inorganic Materials* 43(7) (2007) 735-742.
- [48] M. Ramasamy, S. Baumann, A. Opitz, R. Iskandar, J. Mayer, D. Udomsilp, U. Breuer, M. Bram, Phase Interaction and Distribution in Mixed Ionic Electronic Conducting Ceria-Spinel Composites, *Advances in Solid Oxide Fuel Cells Electronic Ceramics II: Ceramic Engineering Science Proceedings* 37(3) (2017) 99-112.
- [49] S. Kim, S.H. Kim, K.S. Lee, J.H. Yu, Y.-H. Seong, I.S. Han, Mechanical properties of LSCF (La_{0.6}Sr_{0.4}Co_{0.2}Fe_{0.8}O_{3-δ})-GDC (Ce_{0.9}Gd_{0.1}O_{2-δ}) for oxygen transport membranes, *Ceramics International* 43(2) (2017) 1916-1921.
- [50] T. Nithyanantham, S. Biswas, N. Nagendra, S. Bandopadhyay, Studies on mechanical behavior of LSFT-CGO dual-phase membranes at elevated temperatures in ambient air and slightly reducing environments, *Ceramics International* 40(6) (2014) 7783-7790.
- [51] S. Lia, W. Jin, N. Xu, J. Shi, Mechanical strength, and oxygen and electronic transport properties of SrCo_{0.4}Fe_{0.6}O_{3-δ}-YSZ membranes, *Journal of Membrane Science* 186(2) (2001) 195-204.
- [52] K. Raju, S. Kim, C.J. Hyung, J.H. Yu, Y.-H. Seong, S.-H. Kim, I.-S. Han, Optimal sintering temperature for Ce_{0.9}Gd_{0.1}O_{2-δ}-La_{0.6}Sr_{0.4}Co_{0.2}Fe_{0.8}O_{3-δ} composites evaluated through their microstructural, mechanical and elastic properties, *Ceramics International* 45(1) (2019) 1460-1463.
- [53] F. Zeng, J. Malzbender, S. Baumann, F. Schulze-Küppers, M. Krüger, A. Nijmeijer, O. Guillon, W.A. Meulenber, Micromechanical Characterization of Ce_{0.8}Gd_{0.2}O_{2-δ}-FeCo₂O₄ Dual Phase Oxygen Transport Membranes, *Advanced Engineering Materials* 22(6) (2020) 1901558.
- [54] G. Pećanac, S. Baumann, J. Malzbender, Mechanical properties and lifetime predictions for Ba_{0.5}Sr_{0.5}Co_{0.8}Fe_{0.2}O_{3-δ} membrane material, *Journal of Membrane Science* 385 (2011) 263-268.

- [55] L. Wang, R. Dou, G. Wang, Y. Li, M. Bai, D. Hall, Y. Chen, Subcritical crack growth behavior of a perovskite-structured $\text{Ba}_{0.5}\text{Sr}_{0.5}\text{Co}_{0.8}\text{Fe}_{0.2}\text{O}_{3-\delta}$ oxygen transport membrane, *International Journal of Applied Ceramic Technology* 15(1) (2018) 63-73.
- [56] G. Pećanac, S. Foghmoes, M. Lipińska-Chwałek, S. Baumann, T. Beck, J. Malzbender, Strength degradation and failure limits of dense and porous ceramic membrane materials, *Journal of the European Ceramic Society* 33(13-14) (2013) 2689-2698.
- [57] R.O. Silva, J. Malzbender, F. Schulze-Küppers, S. Baumann, O. Guillon, Mechanical properties and lifetime predictions of dense $\text{SrTi}_{1-x}\text{Fe}_x\text{O}_{3-\delta}$ ($x = 0.25, 0.35, 0.5$), *Journal of the European Ceramic Society* 37(7) (2017) 2629-2636.
- [58] M. Barsoum, *Fundamentals of ceramics*, Taylor & Francis, New York, USA, 2019.
- [59] P.J. Murray, J.W. Linnett, Mössbauer studies in the spinel system $\text{Co}_x\text{Fe}_{3-x}\text{O}_4$, *Journal of Physics and Chemistry of Solids* 37(6) (1976) 619-624.
- [60] Y. Zheng, J.M. Vieira, F.J. Oliveira, J.P. Davim, P. Brogueira, Relationship between flexural strength and surface roughness for hot-pressed Si_3N_4 self-reinforced ceramics, *Journal of the European Ceramic Society* 20(9) (2000) 1345-1353.
- [61] M.E. Fitzpatrick, A.T. Fry, P. Holdway, F.A. Kandil, J. Shackleton, L. Suominen, Determination of residual stresses by X-ray diffraction, National Physical Laboratory, Teddington, UK, 2005.
- [62] A. Atkinson, A. Selcuk, Mechanical behaviour of ceramic oxygen ion-conducting membranes, *Solid State Ionics* 134(1-2) (2000) 59-66.
- [63] ASTM, C1499-05: Standard test method for monotonic equibiaxial flexural strength of advanced ceramics at ambient temperature, ASTM International, West Conshohocken, PA, 2003.
- [64] ASTM, C1368-18: Standard test method for determination of slow crack growth parameters of advanced ceramics by constant stress-rate strength testing at ambient temperature, ASTM International, West Conshohocken, PA, 2018.
- [65] ASTM, C1239-13: Standard practice for reporting uniaxial strength data and estimating weibull distribution parameters for advanced ceramics, ASTM International, West Conshohocken, PA, 2013.
- [66] Origin(Pro), Version 2020, OriginLab Corporation, Northampton, MA, USA, 2020.
- [67] C. Krautgasser, R. Bermejo, P. Supancic, R. Danzer, Influence of the scatter of strength and of measurement uncertainties on the determination of the subcritical crack growth exponent in ceramics and glasses, *Journal of the European Ceramic Society* 37(4) (2017) 1873-1878.

- [68] ASTM, C1322-15: Standard practice for fractography and characterization of fracture origins in advanced ceramics, ASTM International, West Conshohocken, PA, 2010.
- [69] R. Bermejo, P. Supancic, C. Krautgasser, R. Morrell, R. Danzer, Subcritical crack growth in low temperature co-fired ceramics under biaxial loading, *Engineering Fracture Mechanics* 100 (2013) 108-121.
- [70] G.R. Anstis, P. Chantikul, B.R. Lawn, D.B. Marshall, A critical evaluation of indentation techniques for measuring fracture toughness: I, direct crack measurements, *Journal of the American Ceramic Society* 64(9) (1981) 533-538.
- [71] F. Zeng, J. Malzbender, S. Baumann, A. Nijmeijer, L. Winnubst, M. Ziegner, O. Guillon, R. Schwaiger, W.A. Meulenberg, Optimization of sintering conditions for improved microstructural and mechanical properties of dense $\text{Ce}_{0.8}\text{Gd}_{0.2}\text{O}_{2-\delta}\text{-FeCo}_2\text{O}_4$ oxygen transport membranes, *Journal of the European Ceramic Society* 41(1) (2021) 509-516.
- [72] F. Zeng, J. Malzbender, S. Baumann, M. Krüger, L. Winnubst, O. Guillon, W.A. Meulenberg, Phase and microstructural characterizations for $\text{Ce}_{0.8}\text{Gd}_{0.2}\text{O}_{2-\delta}\text{-FeCo}_2\text{O}_4$ dual phase oxygen transport membranes, *Journal of the European Ceramic Society* 40(15) (2020) 5646-5652.
- [73] K. Raju, S. Kim, J.H. Yu, S.-H. Kim, Y.-H. Seong, I.-S. Han, Rietveld refinement and estimation of residual stress in GDC-LSCF oxygen transport membrane ceramic composites, *Ceramics International* 44(9) (2018) 10293-10298.
- [74] M. Bouroushian, T. Kosanovic, Characterization of thin films by low incidence X-ray diffraction, *Cryst. Struct. Theory Appl* 1(3) (2012) 35-39.
- [75] M. Żyła, G. Smoła, A. Knapik, J. Rysz, M. Sitarz, Z. Grzesik, The formation of the Co_3O_4 cobalt oxide within CoO substrate, *Corrosion Science* 112 (2016) 536-541.
- [76] A. Kaczmarek, Z. Grzesik, S. Mrowec, On the defect structure and transport properties of Co_3O_4 spinel oxide, *High Temperature Materials and Processes* 31(4-5) (2012) 371-379.
- [77] K. Orlinski, R. Diduszko, M. Kopcewicz, D.A. Pawlak, The influence of chromium substitution on crystal structure and shift of Néel transition in $\text{GdFe}_{1-x}\text{Cr}_x\text{O}_3$ mixed oxides, *Journal of Thermal Analysis and Calorimetry* 127(1) (2017) 181-187.
- [78] C.R. Dyck, R.C. Peterson, Z.B. Yu, V.D. Krstic, Crystal structure, thermal expansion and electrical conductivity of dual-phase $\text{Gd}_{0.8}\text{Sr}_{0.2}\text{Co}_{1-y}\text{Fe}_y\text{O}_{3-\delta}$ ($0 \leq y \leq 1.0$), *Solid State Ionics* 176(1-2) (2005) 103-108.
- [79] E. Wachtel, I. Lubomirsky, The elastic modulus of pure and doped ceria, *Scripta Materialia* 65(2) (2011) 112-117.

[80] S.R. Choi, J.A. Salem, F.A. Holland, Estimation of Slow Crack Growth Parameters for Constant Stress-Rate Test Data of Advanced Ceramics and Glass by the Individual Data and Arithmetic Mean Methods. NASA TM-107369, 1997, NASA Technical Memorandum (2002).

[81] L. Wang, R. Dou, G. Wang, Y. Li, M. Bai, D. Hall, Y. Chen, Fracture strength and Weibull analysis of $\text{Ba}_{0.5}\text{Sr}_{0.5}\text{Co}_{0.8}\text{Fe}_{0.2}\text{O}_{3-\delta}$ oxygen transport membranes evaluated by biaxial and uniaxial bending tests, *Materials Science and Engineering: A* 670 (2016) 292-299.

Appendix A3

1. Determination of SCG exponent and constant by linear regression

The linear regression was performed for equation (5) using the OriginPro software [1], where the slope (α) and interception (β) with respective standard deviations (δ) were also obtained. The SCG exponent and constant were calculated by equations (A3.1) and (A3.2), respectively.

$$n = \frac{1}{\alpha} - 1 \quad (\text{A3.1})$$

$$D = 10^{\beta} \quad (\text{A3.2})$$

And the lower (l) and upper (u) uncertainty limits of for n , and D were calculated according to equation (A3.3) and (A3.6).

$$n_l = \frac{1}{\alpha + \delta_{\alpha}} - 1 \quad (\text{A3.3})$$

$$n_u = \frac{1}{\alpha - \delta_{\alpha}} - 1 \quad (\text{A3.4})$$

$$D_l = 10^{\beta - \delta_{\beta}} \quad (\text{A3.5})$$

$$D_u = 10^{\beta + \delta_{\beta}} \quad (\text{A3.6})$$

2. Determination of Weibull modulus and characteristic strength by linear regression

Weibull modulus and characteristic strength (σ_0) with the corresponding 90% confidence intervals were derived by linear regression method based on equation A3.7 [2]:

$$\ln\left(\ln\frac{1}{1-P_f}\right) = m \cdot \ln\sigma_f - m \cdot \ln\sigma_0 \quad (A3.7)$$

The obtained σ_f values were ranked in ascending order, and P_f value assigned to each σ_f value was estimated using [3].

$$P_f = \frac{I - 0.5}{N} \quad (A3.8)$$

where I is the I th datum of the ranked σ_f values, N the total number of the σ_f values.

3. Lattice constants

Table A3.1 Lattice constants of GCFCO and CoO at surface and bulk.

Composite	Inspecting position	GCFCO			CoO
		a (Å)	b (Å)	c (Å)	a (Å)
50CF	Surface	5.338	5.614	7.652	4.263
	Bulk	5.339	5.615	7.657	4.262
85CF	Surface	5.336	5.608	7.652	-
	Bulk	5.336	5.611	7.653	-

4. Microstructures investigated at the bulk of the sintered composites

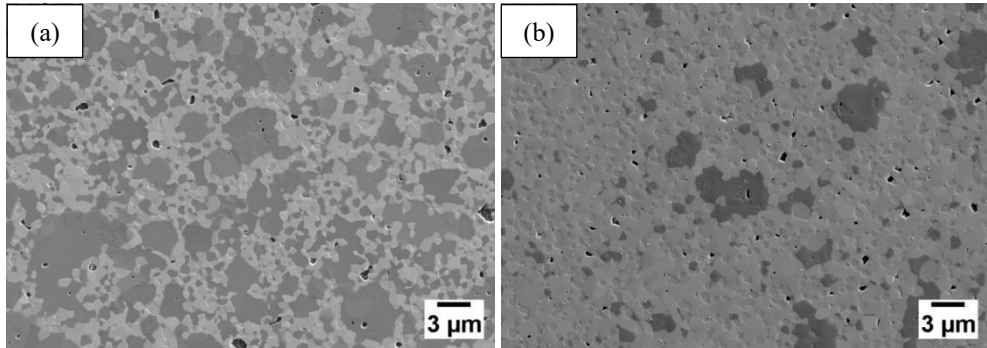


Figure A3.1 Bulk of (a) 50CF and (b) 85CF. (Note that few silica particles from the polishing suspension are remaining in (b) after polishing).

5. Indentation cracks

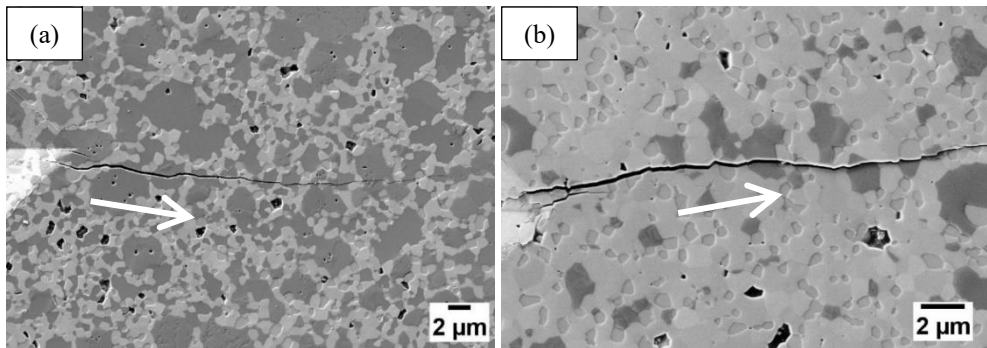


Figure A3.2 Indentation cracks on (a) 50CF and (b) 85CF with a load of 5 N. (Arrows indicate the propagating directions of cracks)

6. Weibull distributions of fracture stress

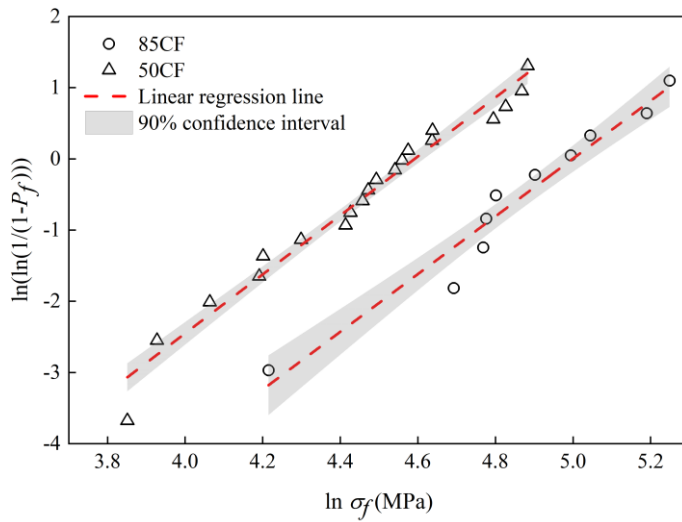


Figure A3.3 Weibull distributions of fracture stresses of the two composites.

7. Fracture surface

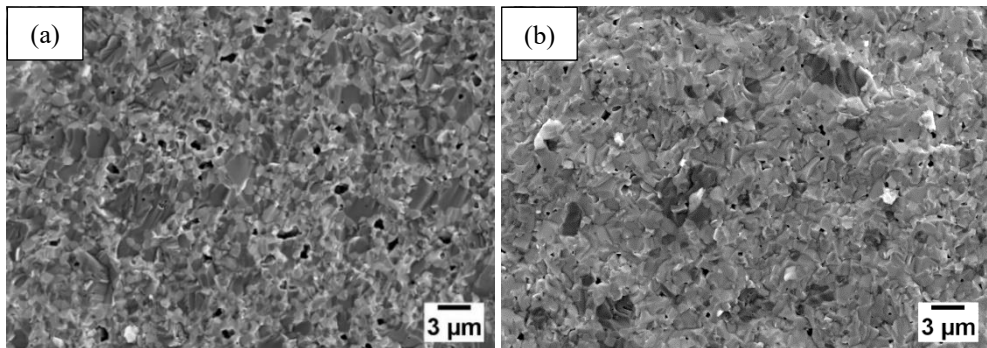


Figure A3.4 Fracture surface of (a) 50CF and (b) 85CF.

8. Likely fracture origins

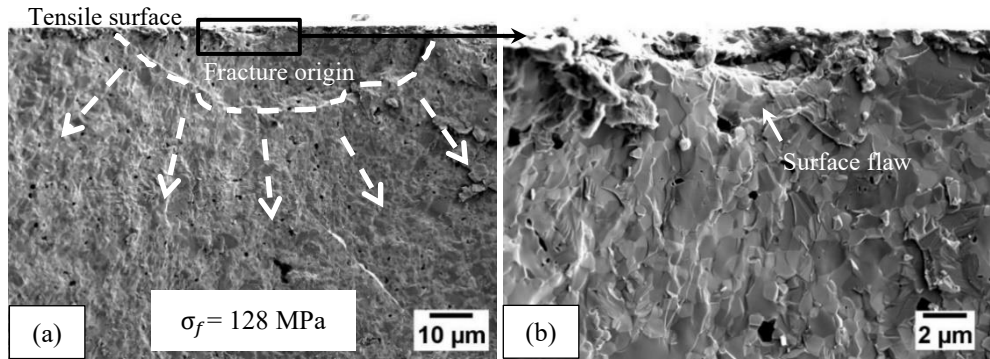


Figure A3.5 Likely fracture origins of the ground and polished 50CF fractured at a loading rate of 20 MPa/s: (b) is the zoom view of the framed area in (a). The dashed lines represent the likely boundaries of fracture origins. The fracture lines are indicated by the dashed arrows.

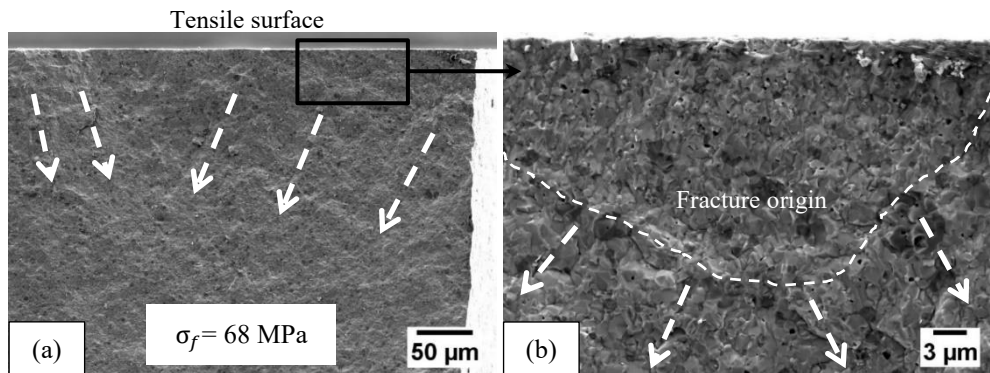


Figure A3.6 Likely fracture origins of 85CF fractured at 20 MPa/s. (b) is the zoom view of the framed area in (a). The dashed lines represent the likely boundaries of fracture origins. The fracture lines are indicated by the dashed arrows.

9. 3D surfaces for deriving uncertainties of characteristic strength

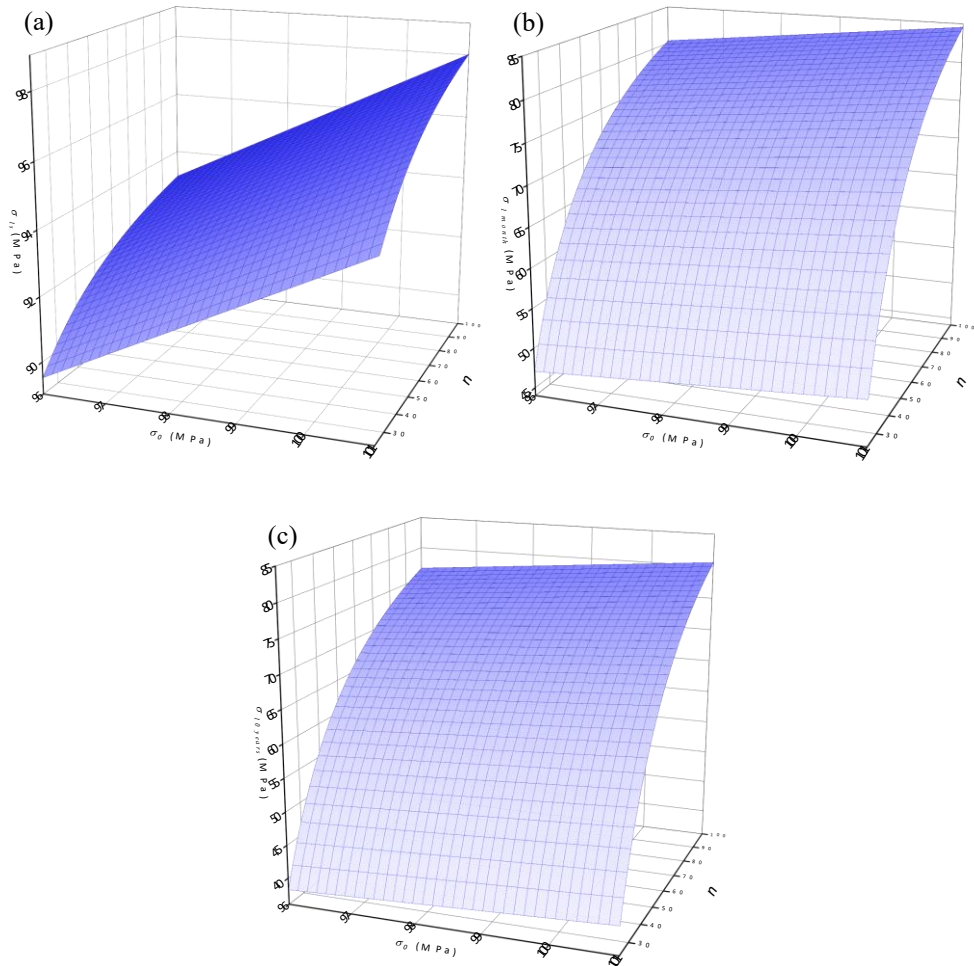


Figure A3.7 The 3D surfaces for deriving uncertainties of characteristic strength of 50CF at (a) 1 s, (b) 1 month, and (c) 10 years.

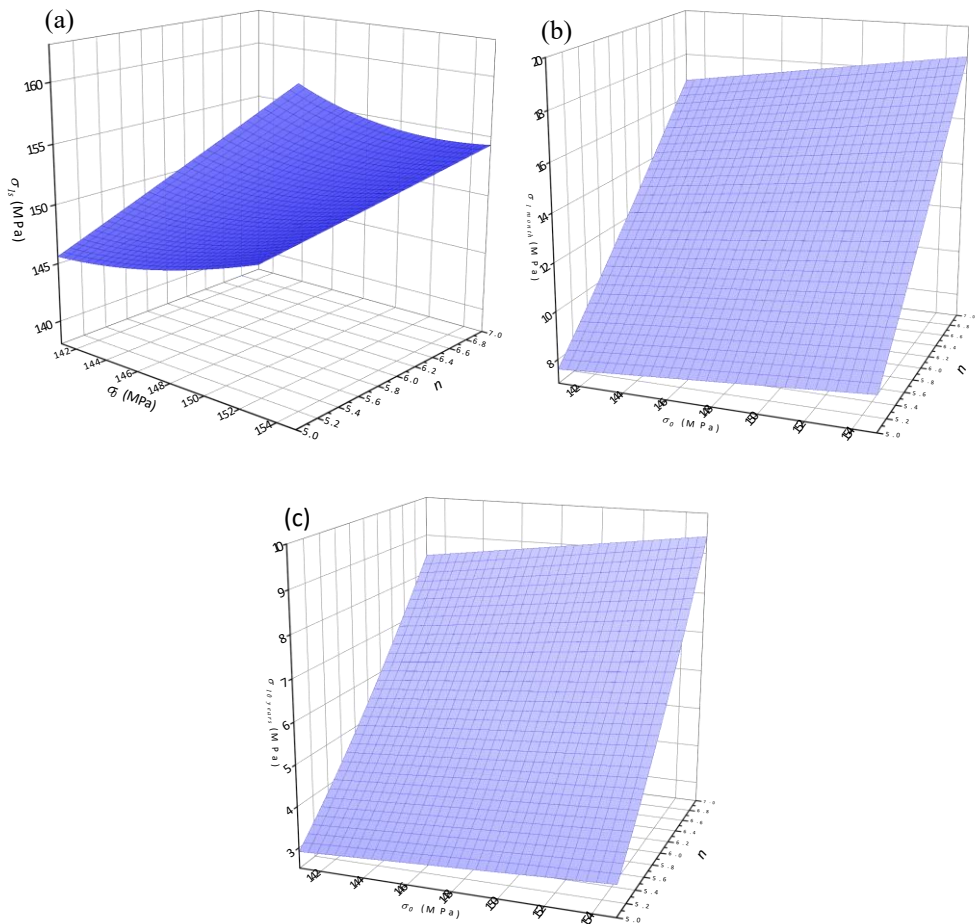


Figure A3.8 The 3D surfaces for deriving uncertainties of characteristic strength of 85CF at (a) 1 s, (b) 1 month, and (c) 10 years.

10. References

- [1] Origin(Pro), Version 2020, OriginLab Corporation, Northampton, MA, USA, 2020.
- [2] Quinn JB, Quinn GD. A practical and systematic review of Weibull statistics for reporting strengths of dental materials. *Dental Materials* 26(2) (2010) 135-147.
- [3] ASTM, C1239-13: Standard practice for reporting uniaxial strength data and estimating weibull distribution parameters for advanced ceramics, ASTM International, West Conshohocken, PA, 2013.

CHAPTER 4

Optimization of sintering conditions for improved microstructural and mechanical properties of dense $\text{Ce}_{0.8}\text{Gd}_{0.2}\text{O}_{2-\delta}\text{-FeCo}_2\text{O}_4$ oxygen transport membranes

Abstract

$\text{Ce}_{0.8}\text{Gd}_{0.2}\text{O}_{2-\delta}\text{-FeCo}_2\text{O}_4$ composite is an excellent oxygen transport membrane material with good chemical stability for applications in oxygen separation and membrane reactors. To improve microstructural and mechanical properties, sintering profiles for $\text{Ce}_{0.8}\text{Gd}_{0.2}\text{O}_{2-\delta}\text{-FeCo}_2\text{O}_4$ composites were optimized. Different sintering temperatures are selected based on our study of phase interactions among the initial powder mixtures using high-temperature X-ray diffraction. The results reveal that the phase interaction at ~ 1050 °C accelerates densification process, and a further increase of sintering temperature to 1200 °C contributes to the homogenization of the pore distribution. A higher density and an improved homogeneity of pore distribution result in enhanced mechanical strength. However, the density decreases once the sintering temperature reaches 1350 °C. Hence, the optimal sintering temperature considering both microstructural and mechanical properties appears to be 1200 °C. Sintering at this temperature results in a microstructure with a density exceeding 99 % with only small surface defects and a high average flexural strength of approximately 266 MPa.

This chapter has been published as: F. Zeng, J. Malzbender, S. Baumann, A. Nijmeijer, L. Winnubst, M. Ziegner, O. Guillon, R. Schwaiger, W.A. Meulenber, Optimization of sintering conditions for improved microstructural and mechanical properties of dense $\text{Ce}_{0.8}\text{Gd}_{0.2}\text{O}_{2-\delta}\text{-FeCo}_2\text{O}_4$ oxygen transport membranes, *Journal of the European Ceramic Society* 41(1) (2021) 509-516.

DOI: 10.1016/j.jeurceramsoc.2020.09.009.

4.1 Introduction

Oxygen transport ceramic membrane materials have attracted great attention due to their potential economic and environmental benefits for application in oxygen separation [1-3], partial oxidation of hydrocarbons [4-6], and oxyfuel coal combustion [7-9]. Dense dual phase ceramic composites, consisting of ionic conducting and electronic conducting phases, are deemed to be promising material candidates as oxygen transport membranes [10, 11]. They show appreciable oxygen permeability and excellent chemical stability during operation in corrosive atmospheres (e.g. SO₂, CO₂) at elevated temperature (~ 850 °C) [12-21]. The 85 wt% Ce_{0.8}Gd_{0.2}O_{2-δ}-15 wt% FeCo₂O₄ (CF) composite, as one typical example, maintained a stable phase structure and a constant oxygen permeation flux with the presence of flue gases at 850 °C for as long as 200 h [13]. The phase interactions between Ce_{0.8}Gd_{0.2}O_{2-δ} and FeCo₂O₄ appeared to be of non-hindrance to oxygen permeability since the phase interaction product, i.e. Gd_{0.9}Ce_{0.1}Fe_{0.8}Co_{0.2}O₃ (GCFCO) [22-24], exhibited a relatively high electrical conductivity [22, 23]. Similar phase interactions and phase interaction products were even reported to enhance grain boundary ionic conductivity and oxygen permeation flux of the 60 vol% Ce_{0.8}Gd_{0.2}O_{2-δ}-40 vol% Fe₂CoO₄ composite [25].

Although the research activities on dense dual phase oxygen transport membranes showed a preference towards chemical properties, e.g. conductivity, oxygen permeability, and chemical stability [11-21, 26-28], investigation and optimization of the mechanical properties are also indispensable for the realization of a long-term reliable operation [29-32].

Mechanical properties of most ceramic materials are governed by microstructural characteristics, e.g. defect, porosity, and grain size [33, 34]. There is a general agreement that a reduction of porosity tends to improve the mechanical properties [35-39], while the grain size effect differs for the different types of mechanical properties. For instance, hardness increases with decreasing grain size [40, 41], following a Hall-Petch relationship, while the elastic modulus usually does not

depend on the grain size [39, 40, 42, 43]. A higher mechanical strength has been reported for ceramics with smaller grain size [34, 44, 45]. According to the limited reported studies [24, 30, 31, 46], the mechanical properties of dense dual phase oxygen transport membranes show comparable dependence on microstructural characteristics such as porosity and grain size.

To improve the microstructural characteristics and the mechanical properties, optimizing the sintering profile represents an effective and straightforward way [34, 40, 47, 48]. Generally, both grain size and density of ceramic materials increase with the sintering temperature [49], which is followed by agglomeration and size-proportional growth of pores [33]. Particularly known is a de-densification phenomenon [50], i.e. the density starts to decrease with increasing sintering temperature after having reached a maximum value, as also reported for some ionic conducting ceramics [47, 51]. For example, large pores formed in zirconia sintered at temperatures above 1600 °C [47]. Similar pore formation and swelling effects were also reported for nano-size CeO₂ powder compact sintered at 1350 °C, apparently induced by oxygen gas produced by the redox reaction of Ceria [51]. Furthermore, the de-densification behaviour of CeO₂ was affected by doping with Gd [48], as well as the introduction of sintering agents such as CoO [52], Bi₂O₃ [53], and Fe₂O₃ [54]. The reduced density resulting from the de-densification process was attributed to being the dominating reason for reductions of elastic modulus and mechanical strength [47, 48].

Among the studies on dual phase oxygen transport membranes, only a few discussed the correlation between sintering profile and mechanical reliability [31, 46]. It was concluded for 50 vol% Ce_{0.9}Gd_{0.1}O_{2-δ}-50 vol% La_{0.6}Sr_{0.4}Co_{0.2}Fe_{0.8}O_{3-δ} composite that an intermediate sintering temperature of 1250 °C resulted in a relatively dense microstructure with fine grains, and thereby permitted a sufficient mechanical strength for safe application as oxygen transport membrane [46].

The current work aims for improving the microstructural and mechanical characteristics of CF composites by optimizing the sintering profiles. The

abovementioned phase interactions are characterized using high-temperature X-ray diffraction. The determined phase interaction temperatures were selected as sintering temperatures to assess the effect of the phase interactions on microstructural characteristics. The relations between the mechanical properties and the microstructural changes are discussed, and finally, an optimal sintering temperature is suggested.

4.2 Experimental

The composites were fabricated by solid state reaction. Powder mixtures containing 85 wt% $\text{Ce}_{0.8}\text{Gd}_{0.2}\text{O}_{1.9}$ (Treibacher Industrie AG, 99 %), 10 wt% Co_3O_4 (Alfa Aesar, 99.7 %) and 5 wt% Fe_2O_3 (Sigma-Aldrich, 99 %) were mixed in a plastic bottle with ethanol and zirconia balls, and ball milled on a roller bench in two steps. In the first step, the 5 mm diameter zirconia balls were used and the milling time was 3 days. In the second step, the 5 mm diameter zirconia balls were replaced with balls having 1 mm diameter, the milling time was 7 days. The ratio of powder-ball-ethanol for all the milling steps was set at 1:2:3. After drying, the powder mixtures were investigated by X-ray diffraction (see Figure A4.1), and Energy-dispersive X-ray spectroscopy mapping (see Figure A4.2). No additional phase or contamination was found. The powder mixtures were uniaxially pressed into pellets using a pressure of 19 MPa. Each pellet had a diameter of 20 mm and a thickness of ~ 0.8 mm. These pellets were then sintered in air at four different temperatures, i.e. 900 °C, 1050 °C, 1200 °C, and 1350 °C, respectively. The dwell time at each sintering temperature was 10 hours. The heating rate was set to 3 K/min. The cooling rate was the same, except for the temperature range between 900 °C and 800 °C, where the cooling rate was reduced to 0.5 K/min to permit a complete phase transformation from CoO rock salt to $\text{Fe}_x\text{Co}_{3-x}\text{O}_4$ ($0 < x < 3$) spinel [10]. In the following, the sintered samples are abbreviated as CF-900, CF-1050, CF-1200, and CF-1350 according to their respective sintering temperatures. For the microstructural characterization, the samples' cross-sections were ground using SiO_2 -sandpaper with grit sizes ascending from 400 to 2000, and then polished using a 50 nm colloidal silica suspension

including diamond paste with particle sizes stepwise reducing from 6 μm to 3 μm , then to 1 μm . The last polishing stage was conducted with the 50 nm colloidal silica suspension without diamond paste. Each step was continued until the defects and scratches from the previous step were removed. Finally, the sample s' cross-sections were polished to a mirror finish.

X-ray diffraction (XRD) (Empyrean, Malvern Panalytical Ltd), equipped with a Cu long fine focus tube (40 kV / 40 mA), Bragg-Brentano^{HD} mirror (divergence = 0.4°), PIXcel3D detector (1D-mode, active length = 3.35°, 255 channels), and an Anton Paar HTK 1200N oven chamber, was used to characterize the crystal structures of the pressed powder mixtures at every 50 K during heating/cooling between room temperature and 1200 °C in air. The heating/cooling rate was 5 K/min.

Microstructures were assessed by scanning electron microscopy (SEM) (Merlin, Carl Zeiss Microscopy Ltd). Different phases were identified by electron backscatter diffraction (EBSD) (NordlysNano, Oxford Instruments Ltd). The grain size was then determined from image analysis using the HKL Channel 5 software packages.

The porosity was calculated as an area fraction of pores using the ImageJ software [55]. Binary pictures were generated from at least three SEM images of polished sample cross-sections based on the isodata threshold method [56, 57]. The pores and the bulk materials in these binary pictures appeared as black and white areas, respectively.

Fracture stresses of the as-sintered pellets were assessed by ring-on-ring tests using an electromechanical testing machine (Instron 1362, Lebow Ltd) following the general procedure outlined in ASTM C1499-05 [58], but only five specimens for each composite were available for testing. The diameter and thickness of each specimen were measured with a digital micrometer with a resolution of 1 μm . The standard deviation measured for the thickness is not larger than $\sim 5 \mu\text{m}$. The specimens met the requirements for tests using loading and supporting rings with diameters of 3.43 mm and 9.99 mm, respectively. The stress rate was maintained to

be 20 MPa/s. The average flexural stress (σ_f) and elastic modulus (E) were calculated by equation (4.1) and equation (4.2), respectively. The effective tensile surface areas of all samples are estimated to have similar values of $\sim 32 \text{ mm}^2$ according to ASTM C1499-05 [58]; the Weibull modulus of $\text{Ce}_{0.8}\text{Gd}_{0.2}\text{O}_{1.9}$ (~ 6.2 [59]) is used for the estimate.

$$\sigma_f = \frac{3F}{2\pi \cdot t^2} \cdot \left[(1 - \nu) \cdot \frac{d_s^2 - d_l^2}{2d^2} + (1 + \nu) \cdot \ln \frac{d_s}{d_l} \right] \quad (4.1)$$

$$E = \frac{3(1 - \nu^2) \cdot \left(\frac{d_l}{2}\right)^2 \cdot \Delta F}{2\pi \cdot \Delta f \cdot t^3} \cdot \left[\frac{d_s^2}{d_l^2} - 1 - \ln \frac{d_s}{d_l} + \frac{1}{2} \cdot \left(\frac{1 - \nu}{1 + \nu}\right) \cdot \left(\frac{d_s^2 - d_l^2}{d^2}\right) \cdot \frac{d_s^2}{d_l^2} \right] \quad (4.2)$$

where F is the fracture force, ΔF and Δf are the load and displacement interval of the linear part of the load-displacement curve, respectively. And d is the sample diameter, t the sample thickness, ν the Poisson's ratio, d_s and d_l are the diameters of support and loading ring, respectively. Poisson's ratio was assumed to have a typical value of 0.3 [59].

The fracture surfaces were investigated through SEM for fracture modes and fracture origins. The fracture origin size, i.e. the radius of circular/semicircular origin or minor axis length of elliptical/semielliptical origin, was measured and compared with the values estimated by equation (4.3) [60]:

$$\sqrt{C} = \frac{K_{IC}}{Y \cdot \sigma_f} \quad (4.3)$$

where C , K_{IC} , and Y are fracture origin size, fracture toughness, and stress intensity factor, respectively. Several Y values for origins with different shapes and sizes are given in ASTM C1322-15 [60].

The fracture toughness and hardness were determined using the Vickers indentation method [61], which has been effectively applied before to determine K_{IC} of the $\text{Ce}_{0.9}\text{Gd}_{0.1}\text{O}_{2-\delta}$ - $\text{La}_{0.6}\text{Sr}_{0.4}\text{CO}_{0.2}\text{Fe}_{0.8}\text{O}_{3-\delta}$ dual phase oxygen membranes [31, 44]. Vickers indentations at two different loads of 1 N and 5 N were made on the polished sample cross-sections using a macro indentation machine (Micromet® 1, Buehler

Ltd). Twenty indentation tests at each load were conducted with a distance of 500 μm between the indents. The hardness (H) was determined by equation (4.4) [31]. The fracture toughness (K_{IC}) values were calculated by equation (4.5) with a c/a (a and c denote the measured half-diagonal of the impression and the crack length, respectively) value higher than 2.5 [61, 62].

$$H = 1.854 \cdot \frac{P}{(2a)^2} \quad (4.4)$$

$$K_{IC} = 0.016 \cdot \left(\frac{E}{H}\right)^{0.5} \cdot \left(\frac{P}{c}\right)^{1.5} \quad (4.5)$$

where P represents the indentation load. It should be noted that equation (4.5) can only provide a rough estimate of the fracture toughness, which can be used for a qualitative assessment of the different samples but cannot be used for a quantitative study.

4.3 Results and discussion

4.3.1 Characterization of phase transformations

The results of the XRD in-situ observations of phase transformations within the powder compacts as a function of temperature are presented in Figure 4.1. Seven characteristic temperatures could be labeled with corresponding transitions listed in Table 4.1.

During the heating process, the Fe_2O_3 starts to form an iron cobalt spinel phase at 750 $^\circ\text{C}$ together with Co_3O_4 . But initial diffraction patterns of the formed spinel do not fit well with that of FeCo_2O_4 spinel due to the bimodal peaks at several angles, which indicates that more than one kind of spinel, with a variation of the Fe to Co ratio, is formed. Thus, the formed spinels are denoted as $\text{Fe}_x\text{Co}_{3-x}\text{O}_4$ ($0 < x < 3$) (FCO). When the temperature increases to 900 $^\circ\text{C}$, these bimodal peaks converge into unimodal peaks at the respective angles, and the spinel formed at 900 $^\circ\text{C}$ can be fitted well as FeCo_2O_4 . At 950 $^\circ\text{C}$, the FeCo_2O_4 begins to decompose into CoO and FCO.

Upon further heating, the GCFCO perovskite phase appears at 1050 °C, and FCO is no longer detectable at 1150 °C. The formation of GCFCO consumes Gd from $\text{Ce}_{0.8}\text{Gd}_{0.2}\text{O}_{1.9}$ and initiates a stoichiometry change from $\text{Ce}_{0.8}\text{Gd}_{0.2}\text{O}_{1.9}$ to $\text{Ce}_{1-y}\text{Gd}_y\text{O}_{2-\delta}$ ($0 < y < 0.2$) (CGO). The GCFCO is stable once formed within the investigated temperature range, while the CoO is unstable upon cooling. The transition of CoO into FCO starts when the temperature is reduced to 900 °C, and CoO can hardly be detected anymore at 750 °C. Near the end of the experiment (100 °C - 25 °C), a small amount of Al_2O_3 materials of the oven chamber fell on the sample and produced corresponding reflections at 2θ angles of 25.5° , 35.1° and 43.1° .

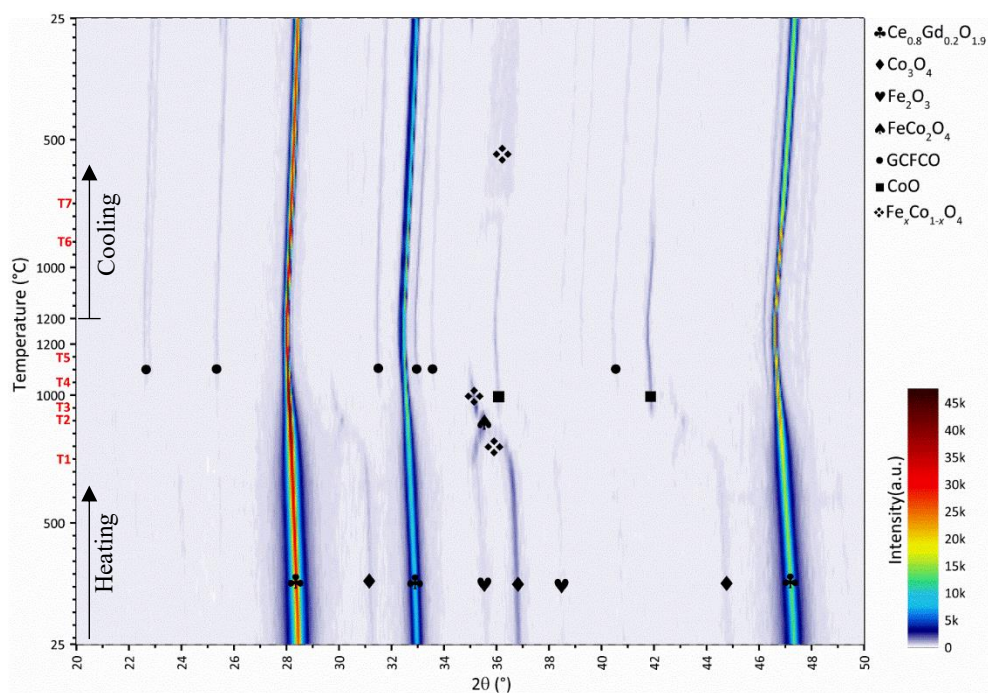


Figure 4.1 In-situ investigations of phase transformations of powder mixtures during heating and cooling by XRD.

Table 4.1 Phase transformations of powder mixtures referring to the temperatures labeled in Figure 4.1.

Label	Temperature (°C)	Emerged phase	Vanished phase
T1	750	$\text{Fe}_x\text{Co}_{3-x}\text{O}_4$	Fe_2O_3
T2	900	FeCo_2O_4	$\text{Fe}_x\text{Co}_{3-x}\text{O}_4$
T3	950	CoO , $\text{Fe}_x\text{Co}_{3-x}\text{O}_4$	-
T4	1050	GCFCO , $\text{Ce}_{1-y}\text{Gd}_y\text{O}_{2-\delta}$	-
T5	1150	-	$\text{Fe}_x\text{Co}_{3-x}\text{O}_4$
T6	900	$\text{Fe}_x\text{Co}_{3-x}\text{O}_4$	-
T7	750	-	CoO

Hence, 900 °C and 1050 °C are very interesting temperatures for sintering the CF material, as phase interactions triggered at these temperatures might further influence the densification process. It should, however, be noted that these temperatures will result in CF materials with different phase constituents.

4.3.2 Microstructural investigations

The microstructures of samples sintered at the various temperatures are illustrated in Figure 4.2. Three phases can be distinguished by either intensity or topography, as indicated in Figure 4.2(g), for CF-1050, CF-1200, and CF-1350, whereas, only two phases are observed in CF-900, i.e. CGO and FCO, as shown in Figure 4.2(a)&(b). The CGO and FCO grains appear as light grey and dark grey, respectively.

The porosities of all samples were given in Table 4.2. Although the image-based method for porosity determination can induce large uncertainty for materials with high porosity [63], the porosity data presented here are still effective for a qualitative and in particular a relative assessment of the different samples.

CF-900 possesses the highest porosity and contains the smallest grains among all the samples, as can be seen in Table 4.2 and Figure 4.2(a)&(b), respectively. Thus, the

phase interaction between the minor phases - Co_3O_4 and Fe_2O_3 at $900\text{ }^\circ\text{C}$, which results in FCO, has a limited contribution to the densification process.

By contrast, when the sintering temperature rises to $1050\text{ }^\circ\text{C}$ for CF-1050, the porosity is strongly reduced to $\sim 1.4\%$ (see Figure 4.2(c-e) and Table 4.2), but small pores are concentrated in a few areas as shown in Figure 4.2(d). This is an indication that the microstructure of CF-1050 is not homogeneously densified even though the total porosity is low. A further increase of the sintering temperature for CF-1200 helps to improve the density to $\sim 99.3\%$, and it is difficult to find areas with a significant concentration of pores (Figure 4.2(f,g)). Such improvement of the density for CF-1050 and CF-1200 can be attributed to the formation of the GCFCO phase. Additionally, the average grain sizes of CF-1050 and CF-1200 were characterized and analyzed on the basis of EBSD phase mapping results, see Figure A4.3. The grain sizes of CGO, FCO, and GCFCO in CF-1200 are $\sim 0.5\text{ }\mu\text{m}$, $\sim 0.3\text{ }\mu\text{m}$, and $\sim 0.4\text{ }\mu\text{m}$, respectively, and around two times larger than the respective phases in CF-1050. Such a difference in grain size might affect the mechanical properties [39, 42].

Unexpectedly, when the sintering temperature is increased further to $1350\text{ }^\circ\text{C}$ for CF-1350, rather large and isolated pores are formed and the total porosity increases as shown in Figure 4.2(h)&(i). The few pores observed in CF-1350 with sizes close to the grain size could be a result of the coarsening of the residual pores formed at lower sintering temperatures, e.g. $1200\text{ }^\circ\text{C}$. But the vast number of pores with unusually large sizes are visible in CF-1350, as shown in Figure 4.2(h), whereas, such large pores did not appear in CF-1200 (see Figure 4.2(f)). Hence, pore coarsening driven by grain growth does not appear to be the dominant mechanism for the formation of the large pores in CF-1350. Hence, the creation of oxygen gas by the reduction of Ce^{4+} to Ce^{3+} could be a possible origin [51]. Further investigations are necessary to clarify the mechanisms, which are out of the scope of the current work. Nevertheless, such large closed pores will induce additional oxygen exchange steps at the pore surfaces regarding oxygen permeation [64], which potentially leads to a further decrease of the permeation flux. Moreover, they might also decrease the

mechanical properties [35, 65]. Hence, the sintering temperature should be limited to remain below 1350 °C.

With the goal to sinter a dense microstructure, sintering temperatures for CF material should, therefore, be between 1050 °C and 1200 °C.

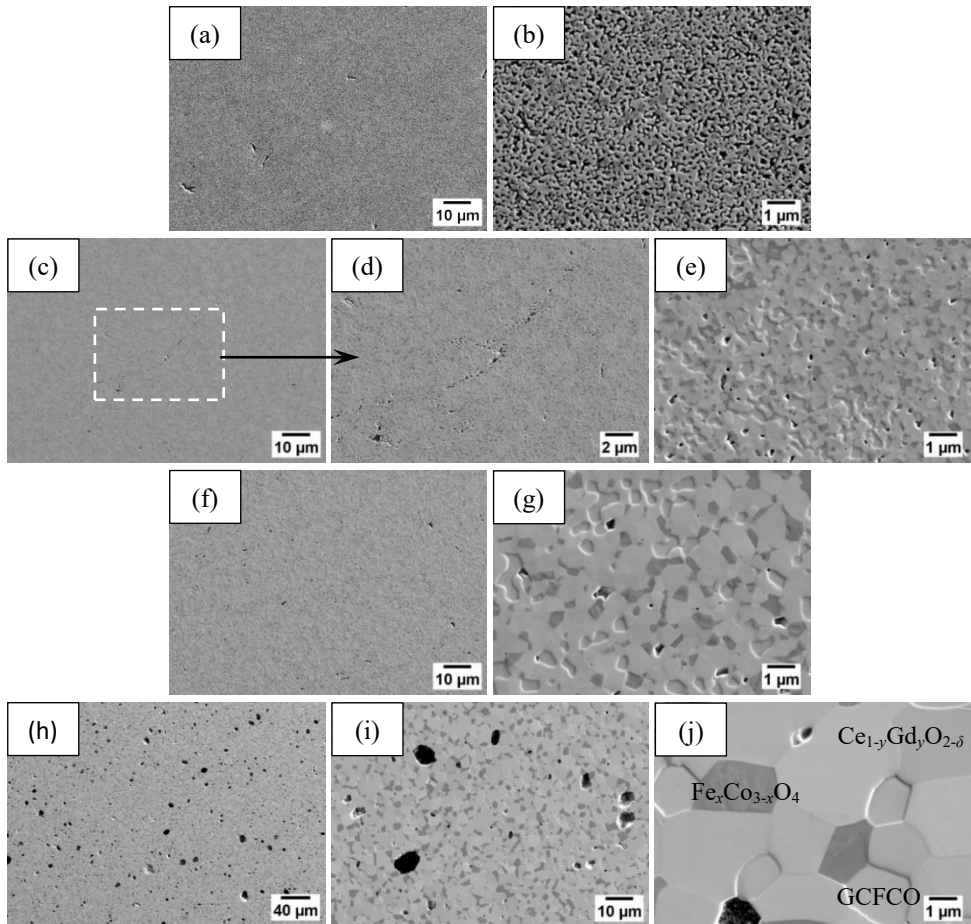


Figure 4.2 Microstructures of (a)-(b) CF-900, (c)-(e) CF-1050, (f)-(g) CF-1200 and (h)-(j) CF-1350.

Table 4.2 Porosities of the CF materials sintered at different temperatures. (\pm describes one standard deviation).

Sample name	Porosity (%)
CF-900	29.7 ± 2.2
CF-1050	1.4 ± 0.4
CF-1200	0.7 ± 0.1
CF-1350	2.6 ± 0.2

4.3.3 Mechanical properties

Since, as verified above, the first target of sintering a dense microstructure has been reached, a subsequent step is the investigation of the mechanical properties and comparison of the prepared dense samples, i.e. CF-1050 and CF-1200. It is verified by the phase and microstructure characterization results that the compositions are almost the same for CF-1050 and CF-1200. Hence, any potential difference in the mechanical properties of CF-1050 and CF-1200 should be a result of the different microstructural characteristics, i.e. porosity and grain size.

The measured mechanical properties are summarized in Table 4.3. The E value of CF-1200 is higher than that of CF-1050, which is mainly attributed to the higher density of CF-1200. The E value of CF-1050 exhibits a relatively high standard deviation, which is probably induced by a wide variation of porosities of the different CF-1050 samples. Such big porosity variation is not reflected in the porosity as determined from ImageJ (Table 4.2), though, which could be due to the fact that the image analysis represents a local measure of the porosity and that there may be more area with a greater number of pores. By contrast, the H value of CF-1200 is marginally lower than the one of CF-1050, and no load dependence is observed within the limits of the experimental uncertainty. Apparently, the porosity does not affect the hardness, while some grain boundary strengthening is observed, as

explained in the following. CF-1050 possesses a finer microstructure with a larger number of grain boundaries than CF-1200, as indicated in Figure 4.2(e)&(g). This could be the dominant reason for the slightly higher H value of CF-1050, and any reduction of the H value of CF-1050 induced by the higher porosity is overbalanced.

Table 4.3 Mechanical properties of CF-1050 and CF-1200. (\pm describes one standard deviation).

Sample name	E (GPa)	H (GPa)		K_{IC} (MPa·m ^{0.5})		σ_f (MPa)
		1 N	5 N	1 N	5 N	
CF-1050	163 \pm 24	10.3 \pm 0.4	10.0 \pm 0.3	0.84 \pm 0.04	0.86 \pm 0.08	135 \pm 57
CF-1200	205 \pm 5	9.5 \pm 0.2	9.1 \pm 0.2	0.86 \pm 0.06	0.93 \pm 0.07	266 \pm 34

The K_{IC} values provided in Table 4.3 are compared to reveal potential influence from microstructural variations, but cannot be used for design purposes since the indentation method is not an ideal method for deriving accurate fracture toughness values [66]. The K_{IC} values of CF-1050 and CF-1200 are almost the same, and approximately independent of indentation loads considering the experimental uncertainties. Furthermore, the K_{IC} values are barely affected by the porosities being below $\sim 2\%$. Typical Vickers indentations after applying loads of 5 N are shown in Figure 4.3. Rather well-defined indentations and crack profiles can be seen. The fracture toughness of some dual phase ceramics was reported to be influenced strongly by crack deflections [30, 67]. In addition, it was reported that cracks were attracted to the phase with the lower elastic modulus and lower thermal expansion coefficient in dual phase ceramics [30, 31]. Since the elastic modulus and thermal expansion coefficient of the major phase constituents within the CF materials are comparable [24, 68-72], extensive crack deflections are not expected. This is confirmed by the indentation cracks that mainly pass transgranularly through the grains (see Figure A4.4).

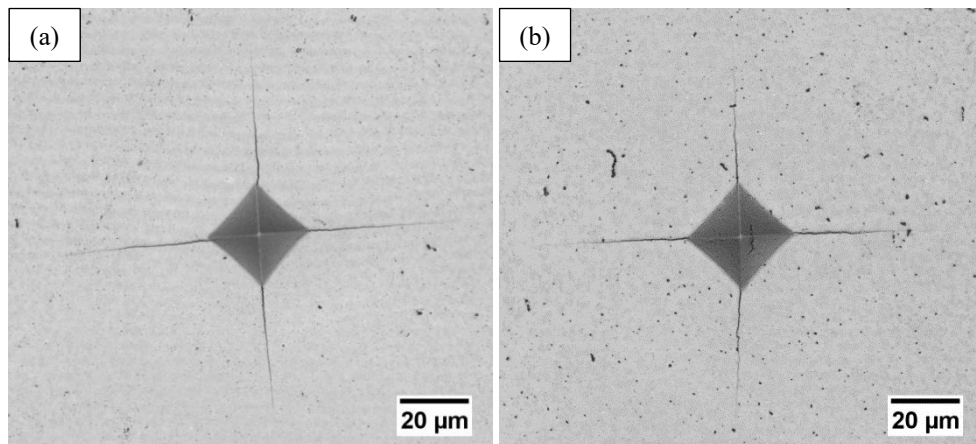


Figure 4.3 Vickers indentations on (a) CF-1050 and (b) CF-1200 induced at a load of 5 N.

The σ_f , however, shows a large difference for CF-1050 and CF-1200 as shown in Table 4.3. The average σ_f of CF-1200 is almost two times higher than that of CF-1050. And it is also higher than the ones of other typical single phase oxygen transport membranes, such as $\text{Ba}_{0.5}\text{Sr}_{0.5}\text{Co}_{0.8}\text{Fe}_{0.2}\text{O}_{3-\delta}$ (~ 100 MPa) [73], $\text{La}_{0.58}\text{Sr}_{0.4}\text{Co}_{0.2}\text{Fe}_{0.8}\text{O}_{3-\delta}$ (~ 94 MPa) [74] and $\text{SrTi}_{0.65}\text{Fe}_{0.35}\text{O}_{3-\delta}$ (~ 117 MPa) [75], which were tested using a similar specimen geometry.

The investigations of the fracture origins were performed on the fracture surfaces of the samples with the highest and the lowest fracture stress. The results indicate that the most likely fracture origins for CF-1050 and CF-1200 can be located near and at the tensile surface, respectively. Moreover, the measured origin size for CF-1050 is larger than that for CF-1200 (see Figure 4.4). Large pore agglomerations, which are similar to the pore-enriched areas as indicated in Figure 4.2(d), are characterized as fracture origins in CF-1050 (see Figure 4.4(b)). Furthermore, the measured origin sizes are also comparable with the estimated ones considering the uncertainties induced by measurement and Y value, see Table 4.4.

It appears that the finer grains do not contribute to an improvement of the strength, and that the strength is governed by larger defects. However, a possible residual

stress will also affect the mechanical strength, which will be the focus of our upcoming works.

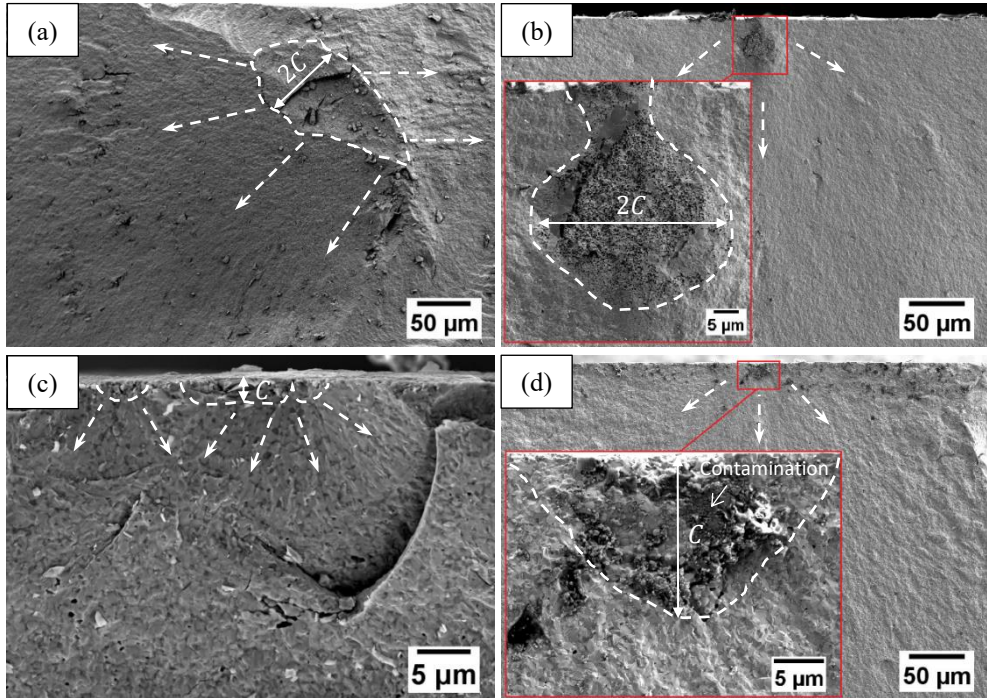


Figure 4.4 Fracture surfaces of (a,b) CF-1050 and (c,d) CF-1200 with individual fracture stress of (a) 80 MPa, (b) 221 MPa, (c) 212 MPa and (d) 303 MPa. The defects inside the marked regions are the possible fracture origins and the arrows are possible crack propagation paths. (Note that the dark contamination of the fracture origin in (b) did not affect the fracture stress but occurred after testing).

Table 4.4 Measured and estimated flaw sizes for the samples with the lowest and highest fracture stresses.

Sample name	σ_f (MPa)	Y [60]	C (μm) – measured	C (μm) – estimated by equation 4.3
CF-1050	80	1.77	36	36
	221	1.13	19	12
CF-1200	212	1.99	2	4
	303	1.29	10	5

Further observations of the fracture surfaces reveal that the fracture paths of CF-1050 and CF-1200 are mainly transgranular (Figure 4.5), but there are also few localized intergranular structures as can be seen in the highlighted regions in Figure 4.5. Our observations might indicate that the mechanical properties and the stress states of the individual phases are similar, and, therefore, the cracks do not show a clear tendency towards propagating through individual grains or along grain interfaces [29, 30]. The fracture surface of CF-1200 is more even than that of CF-1050, while large connected voids appeared in the fracture surface of CF-1050 (see the line with long dashes in Figure 4.5(a)). These might result from cracks propagating through regions with concentrated pores as identified in Figure 4.2(d).

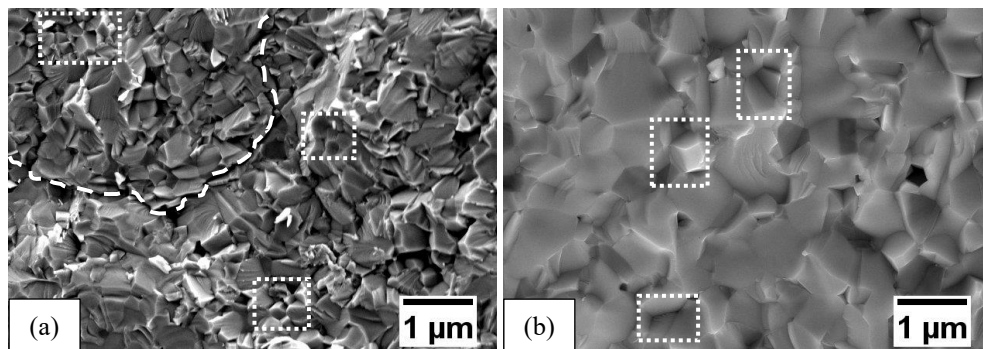


Figure 4.5 Fracture surfaces of (a) CF-1050 and (b) CF-1200. (The dashed line and the areas inside the marked rectangular regions denote the connected voids and some typical intergranular fracture areas, respectively).

Regarding the mechanical properties, the optimal sintering temperature for the CF material is identified as 1200 °C, since sintering at this temperature leads to a relatively high elastic modulus and high flexural strength.

4.4 Conclusions

CF membranes were prepared by one-step thermal processing of powder mixture of $\text{Ce}_{0.8}\text{Gd}_{0.2}\text{O}_{1.9}$, Fe_2O_3 , and Co_3O_4 . Different sintering temperatures were selected and applied according to the phase interactions among the powder mixture characterized by high-temperature XRD. It was revealed that the formation of iron cobalt spinel and GCFCO starts at 750 °C and 1050 °C, respectively, while the formation of iron cobalt spinel has a limited contribution regarding the reduction of the porosity. The densification process is dominated by the formation of GCFCO. The membrane sintered at 1050 °C reaches an almost fully densified microstructure with rather small grains ($\sim 0.2 \mu\text{m}$), but a large number of small pores are concentrated in some areas. A higher sintering temperature of 1200 °C increases the density as well as the grain size, while the distribution of pores is homogenized. However, a further increase of the sintering temperature up to 1350 °C reduces the density due to the formation of large and isolated pores.

The mechanical properties of the membranes with rather dense microstructures, i.e. CF-1050 and CF-1200, are characterized and compared. The elastic modulus of CF-1050 appears to be lower than the ones of CF-1200, while the hardness of CF-1050 is slightly higher than the one of CF-1200 due to some grain boundary strengthening effects. The fracture toughnesses of CF-1050 and CF-1200 are almost identical. Besides, the flexural strength of CF-1200 is much higher than that of CF-1050. The lower strength of CF-1050 can be attributed to the larger defects that appeared in the inhomogeneously densified microstructure.

In conclusion, the optimal sintering temperature for the CF membrane, which is beneficial for both the microstructural and the mechanical properties is suggested to be 1200 °C.

References

- [1] J. Sunarso, S. Baumann, J.M. Serra, W.A. Meulenber, S. Liu, Y.S. Lin, J.C. Diniz da Costa, Mixed ionic-electronic conducting (MIEC) ceramic-based membranes for oxygen separation, *Journal of Membrane Science* 320(1) (2008) 13-41.
- [2] L.L. Anderson, P.A. Armstrong, R.R. Broekhuis, M.F. Carolan, J. Chen, M.D. Hutcheon, C.A. Lewinsohn, C.F. Miller, J.M. Repasky, D.M. Taylor, Advances in ion transport membrane technology for oxygen and syngas production, *Solid State Ionics* 288 (2016) 331-337.
- [3] P.V. Hendriksen, P.H. Larsen, M. Mogensen, F.W. Poulsen, K. Wiik, Prospects and problems of dense oxygen permeable membranes, *Catalysis Today* 56(1-3) (2000) 283-295.
- [4] H.J. Bouwmeester, Dense ceramic membranes for methane conversion, *Catalysis Today* 82(1-4) (2003) 141-150.
- [5] M.T. Ravanchi, T. Kaghazchi, A. Kargari, Application of membrane separation processes in petrochemical industry: a review, *Desalination* 235(1-3) (2009) 199-244.
- [6] W. Deibert, M.E. Ivanova, S. Baumann, O. Guillon, W.A. Meulenber, Ion-conducting ceramic membrane reactors for high-temperature applications, *Journal of membrane science* 543 (2017) 79-97.

- [7] H. Stadler, F. Beggel, M. Habermehl, B. Persigehl, R. Kneer, M. Modigell, P. Jeschke, Oxyfuel coal combustion by efficient integration of oxygen transport membranes, *International Journal of Greenhouse Gas Control* 5(1) (2011) 7-15.
- [8] M. Czaperek, P. Zapp, H.J.M. Bouwmeester, M. Modigell, K. Ebert, I. Voigt, W.A. Meulenber, L. Singheiser, D. Stöver, Gas separation membranes for zero-emission fossil power plants: MEM-BRAIN, *Journal of membrane science* 359(1-2) (2010) 149-159.
- [9] M. Czaperek, P. Zapp, H.J.M. Bouwmeester, M. Modigell, K.V. Peinemann, I. Voigt, W.A. Meulenber, L. Singheiser, D. Stöver, MEM-BRAIN gas separation membranes for zero-emission fossil power plants, *Energy Procedia* 1(1) (2009) 303-310.
- [10] M. Ramasamy, Dual phase oxygen transport membrane for efficient oxyfuel combustion, PhD thesis, Bochum University, Bochum, Germany, 2016.
- [11] W. Fang, F. Liang, Z. Cao, F. Steinbach, A. Feldhoff, A mixed ionic and electronic conducting dual phase membrane with high oxygen permeability, *Angewandte Chemie International Edition* 54(16) (2015) 4847-4850.
- [12] H. Luo, H. Jiang, K. Efimov, F. Liang, H. Wang, J.r. Caro, CO₂-tolerant oxygen-permeable Fe₂O₃-Ce_{0.9}Gd_{0.1}O_{2-δ} dual phase membranes, *Industrial & Engineering Chemistry Research* 50(23) (2011) 13508-13517.
- [13] M. Ramasamy, E. Persoon, S. Baumann, M. Schroeder, F. Schulze-Küppers, D. Görtz, R. Bhave, M. Bram, W. Meulenber, Structural and chemical stability of high performance Ce_{0.8}Gd_{0.2}O_{2-δ}-FeCo₂O₄ dual phase oxygen transport membranes, *Journal of Membrane Science* 544 (2017) 278-286.
- [14] Z. Wang, W. Sun, Z. Zhu, T. Liu, W. Liu, A novel cobalt-free, CO₂-stable, and reduction-tolerant dual phase oxygen-permeable membrane, *ACS applied materials & interfaces* 5(21) (2013) 11038-11043.
- [15] X. Zhu, Y. Liu, Y. Cong, W. Yang, Ce_{0.85}Sm_{0.15}O_{1.925}-Sm_{0.6}Sr_{0.4}Al_{0.3}Fe_{0.7}O₃ dual phase membranes: one-pot synthesis and stability in a CO₂ atmosphere, *Solid State Ionics* 253 (2013) 57-63.
- [16] K.S. Yun, C.-Y. Yoo, S.-G. Yoon, J.H. Yu, J.H. Joo, Chemically and thermo-mechanically stable LSM-YSZ segmented oxygen permeable ceramic membrane, *Journal of membrane science* 486 (2015) 222-228.
- [17] H. Luo, K. Efimov, H. Jiang, A. Feldhoff, H. Wang, J. Caro, CO₂-stable and cobalt-free dual phase membrane for oxygen separation, *Angewandte Chemie International Edition* 50(3) (2011) 759-763.

- [18] S. Guo, Z. Liu, J. Zhu, X. Jiang, Z. Song, W. Jin, Highly oxygen-permeable and CO₂-stable Ce_{0.8}Sm_{0.2}O_{2-δ}-SrCo_{0.9}Nb_{0.1}O_{3-δ} dual phase membrane for oxygen separation, *Fuel Processing Technology* 154 (2016) 19-26.
- [19] M. Balaguer, J. García-Fayos, C. Solís, J.M. Serra, Fast oxygen separation through SO₂- and CO₂-stable dual phase membrane based on NiFe₂O₄-Ce_{0.8}Tb_{0.2}O_{2-δ}, *Chemistry of Materials* 25(24) (2013) 4986-4993.
- [20] B. Wang, J. Yi, L. Winnubst, C. Chen, Stability and oxygen permeation behavior of Ce_{0.8}Sm_{0.2}O_{2-δ}-La_{0.8}Sr_{0.2}CrO_{3-δ} composite membrane under large oxygen partial pressure gradients, *Journal of membrane science* 286(1-2) (2006) 22-25.
- [21] S. Pirou, J.M. Bermudez, B.T. Na, S. Ovtar, J.H. Yu, P.V. Hendriksen, A. Kaiser, T.R. Reina, M. Millan, R. Kiebach, Performance and stability of (ZrO₂)_{0.89}(Y₂O₃)_{0.01}(Sc₂O₃)_{0.10}-LaCr_{0.85}Cu_{0.10}Ni_{0.05}O_{3-δ} oxygen transport membranes under conditions relevant for oxy-fuel combustion, *Journal of Membrane Science* 552 (2018) 115-123.
- [22] M. Ramasamy, S. Baumann, A. Opitz, R. Iskandar, J. Mayer, D. Udomsilp, U. Breuer, M. Bram, Phase Interaction and Distribution in Mixed Ionic Electronic Conducting Ceria-Spinel Composites, *Advances in Solid Oxide Fuel Cells Electronic Ceramics II: Ceramic Engineering Science Proceedings* 37(3) (2017) 99-112.
- [23] F. Zeng, J. Malzbender, S. Baumann, M. Krüger, L. Winnubst, O. Guillon, W.A. Meulenber, Phase and microstructural characterizations for Ce_{0.8}Gd_{0.2}O_{2-δ}-FeCo₂O₄ dual phase oxygen transport membranes, *Journal of the European Ceramic Society*, 40 (2020) 5646-5652.
- [24] F. Zeng, J. Malzbender, S. Baumann, F. Schulze-Küppers, M. Krüger, A. Nijmeijer, O. Guillon, W.A. Meulenber, Micro-mechanical characterization of Ce_{0.8}Gd_{0.2}O_{2-δ}-FeCo₂O₄ dual phase oxygen transport membranes, *Advanced Engineering Materials* (2020) 1901558.
- [25] Y. Lin, S. Fang, D. Su, K.S. Brinkman, F. Chen, Enhancing grain boundary ionic conductivity in mixed ionic-electronic conductors, *Nature communications* 6 (2015) 6824.
- [26] Y. He, L. Shi, F. Wu, W. Xie, S. Wang, D. Yan, P. Liu, M.-R. Li, J. Caro, H. Luo, A novel dual phase membrane 40 wt% Nd_{0.6}Sr_{0.4}CoO_{3-δ}-60 wt% Ce_{0.9}Nd_{0.1}O_{2-δ}: design, synthesis and properties, *Journal of Materials Chemistry A* 6(1) (2018) 84-92.
- [27] Y. Ji, J.A. Kilner, M.F. Carolan, Electrical conductivity and oxygen transfer in gadolinia-doped ceria (CGO)-Co₃O_{4-δ} composites, *Journal of the European Ceramic Society* 24(14) (2004) 3613-3616.

- [28] V.V. Kharton, A.V. Kovalevsky, A.P. Viskup, F.M. Figueiredo, A.A. Yaremchenko, E.N. Naumovich, F.M.B. Marques, Oxygen Permeability of $\text{Ce}_{0.8}\text{Gd}_{0.2}\text{O}_{2-\delta}\text{-La}_{0.7}\text{Sr}_{0.3}\text{MnO}_{3-\delta}$ Composite Membranes, *Journal of the Electrochemical Society* 147(7) (2000) 2814-2821.
- [29] P.-M. Geffroy, J. Fouletier, N. Richet, T. Chartier, Rational selection of MIEC materials in energy production processes, *Chemical engineering science* 87 (2013) 408-433.
- [30] T. Nithyanantham, S. Biswas, N. Nagendra, S. Bandopadhyay, Studies on mechanical behavior of LSFT-CGO dual phase membranes at elevated temperatures in ambient air and slightly reducing environments, *Ceramics International* 40(6) (2014) 7783-7790.
- [31] S. Kim, S.H. Kim, K.S. Lee, J.H. Yu, Y.-H. Seong, I.S. Han, Mechanical properties of LSCF ($\text{La}_{0.6}\text{Sr}_{0.4}\text{Co}_{0.2}\text{Fe}_{0.8}\text{O}_{3-\delta}$)-GDC ($\text{Ce}_{0.9}\text{Gd}_{0.1}\text{O}_{2-\delta}$) for oxygen transport membranes, *Ceramics International* 43(2) (2017) 1916-1921.
- [32] S. Lia, W. Jin, N. Xu, J. Shi, Mechanical strength, and oxygen and electronic transport properties of $\text{SrCo}_{0.4}\text{Fe}_{0.6}\text{O}_{3-\delta}$ -YSZ membranes, *Journal of Membrane Science* 186(2) (2001) 195-204.
- [33] J.L. Shi, Relation between coarsening and densification in solid-state sintering of ceramics: Experimental test on superfine zirconia powder compacts, *Journal of materials research* 14(4) (1999) 1389-1397.
- [34] J.B. Wachtman, W.R. Cannon, M.J. Matthewson, *Mechanical properties of ceramics*, Wiley, Hoboken, USA, 2009.
- [35] R. Pal, Porosity-dependence of effective mechanical properties of pore-solid composite materials, *Journal of Composite Materials* 39(13) (2005) 1147-1158.
- [36] M. Lipińska-Chwałek, F. Schulze-Küppers, J. Malzbender, Mechanical properties of pure and doped cerium oxide, *Journal of the European Ceramic Society* 35(5) (2015) 1539-1547.
- [37] R.M. Spriggs, Effect of Open and Closed Pores on Elastic Moduli of Polycrystalline Alumina, *Journal of the American Ceramic Society* 45(9) (1962) 454-454.
- [38] R.W. Rice, Microstructure dependence of mechanical behavior of ceramics, *Treatise on Materials Science & Technology* 11 (1977) 199-381.
- [39] R. Chaim, M. Hefetz, Effect of grain size on elastic modulus and hardness of nanocrystalline ZrO_{2-3} wt% Y_2O_3 ceramic, *Journal of materials science* 39(9) (2004) 3057-3061.
- [40] M. Yan, T. Mori, J. Zou, H. Huang, J. Drennan, Microstructures and mechanical properties of $\text{Ce}_{1-x}\text{Ca}_x\text{O}_{2-y}$ ($x = 0.05, 0.1, 0.2$) with different sintering temperatures, *Journal of the European Ceramic Society* 30(3) (2010) 669-675.

- [41] M. Trunec, Effect of grain size on mechanical properties of 3Y-TZP ceramics, *Ceramics–Silikáty* 52 (2008) 165-71.
- [42] O. Tokariev, L. Schnetter, T. Beck, J. Malzbender, Grain size effect on the mechanical properties of transparent spinel ceramics, *Journal of the European Ceramic Society* 33(4) (2013) 749-757.
- [43] J. Zhou, Y. Li, R. Zhu, Z. Zhang, The grain size and porosity dependent elastic moduli and yield strength of nanocrystalline ceramics, *Materials Science and Engineering: A* 445 (2007) 717-724.
- [44] E. Orowan, Fracture and strength of solids, *Reports on progress in physics* 12(1) (1949) 185.
- [45] A. Zimmermann, J. Rödel, Generalized Orowan-Petch plot for brittle fracture, *Journal of the American Ceramic Society* 81(10) (1998) 2527-2532.
- [46] K. Raju, S. Kim, C.J. Hyung, J.H. Yu, Y.-H. Seong, S.-H. Kim, I.-S. Han, Optimal sintering temperature for $\text{Ce}_{0.9}\text{Gd}_{0.1}\text{O}_{2-\delta}\text{-La}_{0.6}\text{Sr}_{0.4}\text{Co}_{0.2}\text{Fe}_{0.8}\text{O}_{3-\delta}$ composites evaluated through their microstructural, mechanical and elastic properties, *Ceramics International* 45(1) (2019) 1460-1463.
- [47] B. Stawarczyk, M. Özcan, L. Hallmann, A. Ender, A. Mehl, C.H.F. Hämmerlet, The effect of zirconia sintering temperature on flexural strength, grain size, and contrast ratio, *Clinical oral investigations* 17(1) (2013) 269-274.
- [48] K. Yasuda, K. Uemura, T. Shiota, Sintering and mechanical properties of gadolinium-doped ceria ceramics, *Journal of Physics: Conference Series* 339 (2012) 012006.
- [49] M.N. Rahaman, *Sintering of ceramics*, CRC press, University of Missouri-Rolla, USA, 2007.
- [50] C. Chambon, S. Vaudez, J.M. Heintz, De-densification mechanisms of yttria-doped cerium oxide during sintering in a reducing atmosphere, *Journal of the American Ceramic Society* 101(11) (2018) 4956-4967.
- [51] Y. Zhou, M.N. Rahaman, Effect of redox reaction on the sintering behavior of cerium oxide, *Acta materialia* 45(9) (1997) 3635-3639.
- [52] T. Zhang, P. Hing, H. Huang, J. Kilner, Sintering and grain growth of CoO-doped CeO_2 ceramics, *Journal of the European Ceramic Society* 22(1) (2002) 27-34.
- [53] V. Gil, J. Tartaj, C. Moure, P. Durán, Sintering, microstructural development, and electrical properties of gadolinia-doped ceria electrolyte with bismuth oxide as a sintering aid, *Journal of the European Ceramic Society* 26(15) (2006) 3161-3171.

- [54] T. Zhang, P. Hing, H. Huang, J. Kilner, Densification, microstructure and grain growth in the CeO₂-Fe₂O₃ system ($0 \leq \text{Fe/Ce} \leq 20\%$), *Journal of the European Ceramic Society* 21(12) (2001) 2221-2228.
- [55] C.A. Schneider, W.S. Rasband, K.W. Eliceiri, NIH Image to ImageJ: 25 years of image analysis, *Nature methods* 9(7) (2012) 671-675.
- [56] S.M. Hartig, Basic Image Analysis and Manipulation in ImageJ, *Current Protocols in Molecular Biology* 102(1) (2013) 14-15.
- [57] T.W. Ridler, S. Calvard, Picture Thresholding Using an Iterative Selection Method, *Ieee T Syst Man Cyb* 8(8) (1978) 630-632.
- [58] ASTM, C1499-05: Standard test method for monotonic equibiaxial flexural strength of advanced ceramics at ambient temperature, ASTM International, West Conshohocken, PA, 2003.
- [59] A. Atkinson, A. Selcuk, Mechanical behaviour of ceramic oxygen ion-conducting membranes, *Solid State Ionics* 134(1-2) (2000) 59-66.
- [60] ASTM, C1322-15: Standard practice for fractography and characterization of fracture origins in advanced ceramics, ASTM International, West Conshohocken, PA, 2010.
- [61] G.R. Anstis, P. Chantikul, B.R. Lawn, D.B. Marshall, A critical evaluation of indentation techniques for measuring fracture toughness: I, direct crack measurements, *Journal of the American Ceramic Society* 64(9) (1981) 533-538.
- [62] K. Niihara, R. Morena, D.P.H. Hasselman, Evaluation of K_{IC} of brittle solids by the indentation method with low crack-to-indent ratios, *Journal of materials science letters* 1(1) (1982) 13-16.
- [63] M.R. Hossen, M.W. Talbot, R. Kennard, D.W. Bousfield, M.D. Mason, A comparative study of methods for porosity determination of cellulose based porous materials, *Cellulose* 27(12) (2020) 6849-6860.
- [64] Z. Wang, H. Liu, X. Tan, Y. Jin, S. Liu, Improvement of the oxygen permeation through perovskite hollow fibre membranes by surface acid-modification, *Journal of Membrane Science* 345(1-2) (2009) 65-73.
- [65] G. Pećanac, S. Foghmoes, M. Lipińska-Chwałek, S. Baumann, T. Beck, J. Malzbender, Strength degradation and failure limits of dense and porous ceramic membrane materials, *Journal of the European Ceramic Society* 33(13-14) (2013) 2689-2698.
- [66] G.D. Quinn, R.C. Bradt, On the Vickers Indentation Fracture Toughness Test, *Journal of the American Ceramic Society* 90(3) (2007) 673-680.

- [67] P. Bhargava, B.R. Patterson, Quantitative Characterization of Indentation Crack Path in a Cubic Zirconia-10 vol% Alumina Composite, *Journal of the American Ceramic Society* 80(7) (1997) 1863-1867.
- [68] K. Orlinski, R. Diduszko, M. Kopcewicz, D.A. Pawlak, The influence of chromium substitution on crystal structure and shift of Néel transition in $\text{GdFe}_{1-x}\text{Cr}_x\text{O}_3$ mixed oxides, *Journal of Thermal Analysis Calorimetry* 127(1) (2017) 181-187.
- [69] R. Korobko, C.T. Chen, S. Kim, S.R. Cohen, E. Wachtel, N. Yavo, I. Lubomirsky, Influence of Gd content on the room temperature mechanical properties of Gd-doped ceria, *Scripta Mater* 66(3-4) (2012) 155-158.
- [70] Z. Zhang, J. Koppensteiner, W. Schranz, M.A. Carpenter, Variations in elastic and anelastic properties of Co_3O_4 due to magnetic and spin-state transitions, *American Mineralogist* 97(2-3) (2012) 399-406.
- [71] A.S. Verma, A. Kumar, Bulk modulus of cubic perovskites, *Journal of Alloys and Compounds* 541 (2012) 210-214.
- [72] M. Ramasamy, S. Baumann, J. Palisaitis, F. Schulze-Küppers, M. Balaguer, D. Kim, W.A. Meulenber, J. Mayer, R. Bhave, O. Guillon, Influence of Microstructure and Surface Activation of Dual phase Membrane $\text{Ce}_{0.8}\text{Gd}_{0.2}\text{O}_{2-\delta}\text{-FeCo}_2\text{O}_4$ on Oxygen Permeation, *Journal of the American Ceramic Society* 99(1) (2016) 349-355.
- [73] B.X. Huang, J. Malzbender, R.W. Steinbrech, L. Singheiser, Discussion of the complex thermo-mechanical behavior of $\text{Ba}_{0.5}\text{Sr}_{0.5}\text{Co}_{0.8}\text{Fe}_{0.2}\text{O}_{3-\delta}$, *Journal of Membrane Science* 359(1) (2010) 80-85.
- [74] B. Huang, J. Malzbender, R. Steinbrech, E. Wessel, H. Penkalla, L. Singheiser, Mechanical aspects of ferro-elastic behavior and phase composition of $\text{La}_{0.58}\text{Sr}_{0.4}\text{Co}_{0.2}\text{Fe}_{0.8}\text{O}_{3-\delta}$, *Journal of Membrane Science* 349(1-2) (2010) 183-188.
- [75] R.O. Silva, J. Malzbender, F. Schulze-Küppers, S. Baumann, O. Guillon, Mechanical properties and lifetime predictions of dense $\text{SrTi}_{1-x}\text{Fe}_x\text{O}_{3-\delta}$ ($x = 0.25, 0.35, 0.5$), *Journal of the European Ceramic Society* 37(7) (2017) 2629-2636.

Appendix A4

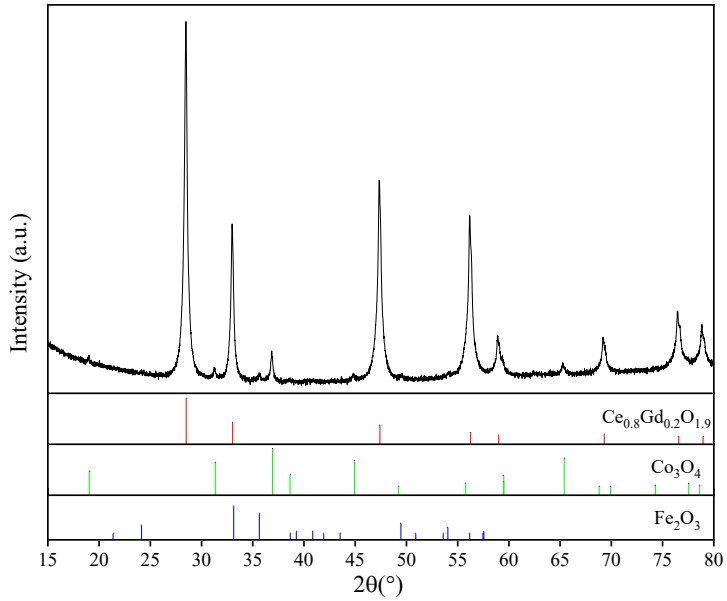


Figure A4.1 X-ray diffraction patterns of initial powder mixtures.

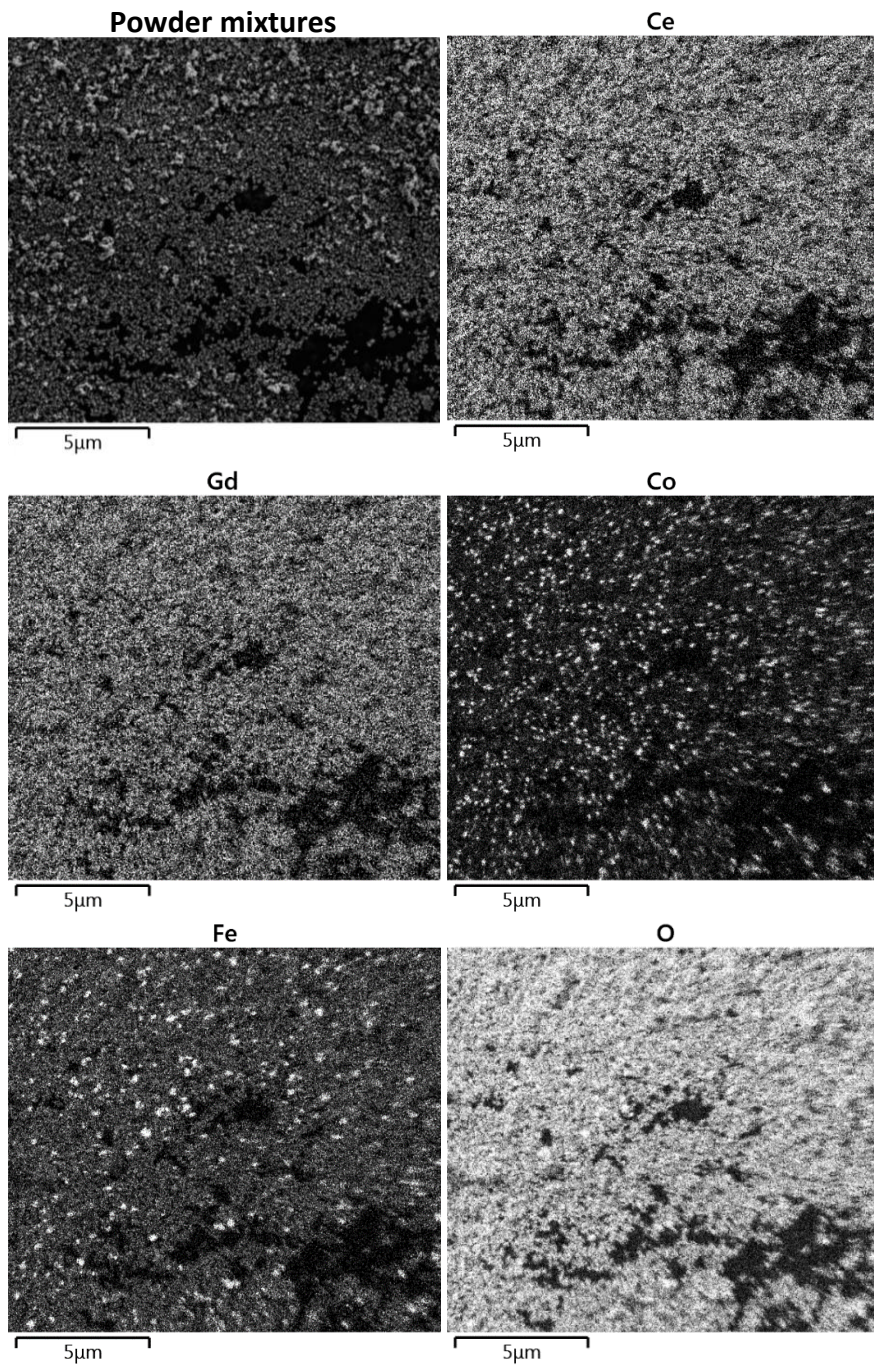


Figure A4.2 Elemental mapping results of powder mixtures by Energy-dispersive X-ray spectroscopy.

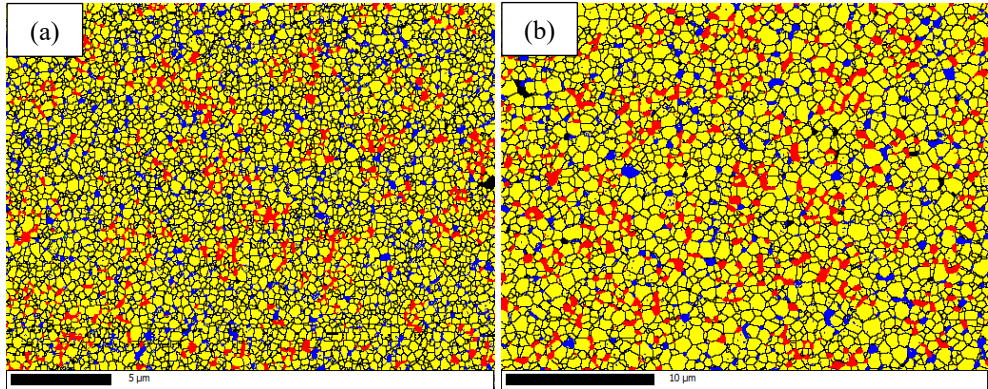


Figure A4.3 Electron backscatter diffraction (EBSD) phase mapping results of (a) CF-1050 and (b) CF-1200: the yellow, blue, red and green grains are $\text{Ce}_{1-x}\text{Gd}_x\text{O}_{2-\delta}$, $\text{Fe}_x\text{Co}_{3-x}\text{O}_4$, GCFCO, and CoO, respectively. (The CoO is only found in CF-1050 with a rather low volume fraction of $\sim 0.2\%$).

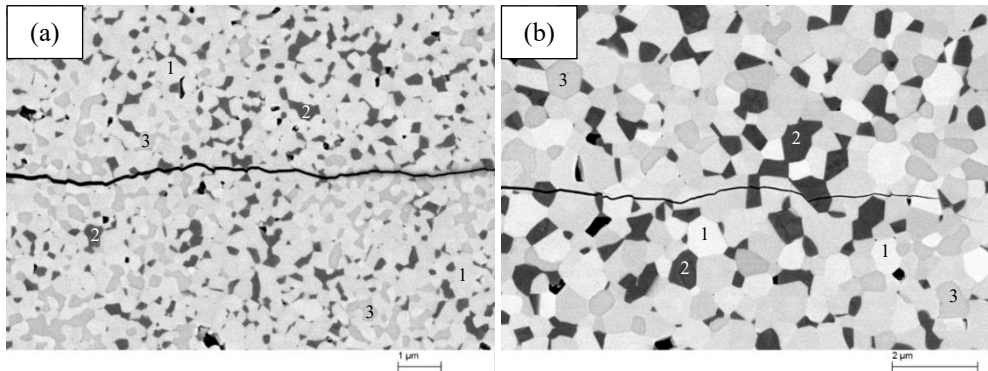


Figure A4.4 Indentation cracks initiated on (a) CF-1050 and (b) CF-1200 with a load of 5 N. (The CGO, FCO and GCFCO phase are denoted as 1, 2 and 3, respectively).

CHAPTER 5

Micro-mechanical characterization of $\text{Ce}_{0.8}\text{Gd}_{0.2}\text{O}_{2-\delta}$ - FeCo_2O_4 dual phase oxygen transport membranes

Abstract

Aiming towards an optimization of dual phase oxygen transport membrane materials for oxygen separation applications, ceramic composites consisting of a $\text{Ce}_{1-x}\text{Gd}_x\text{O}_{2-\delta}$ ($0 < x < 0.2$) fluorite phase, $\text{Gd}_{0.9}\text{Ce}_{0.1}\text{Fe}_{0.8}\text{Co}_{0.2}\text{O}_3$ perovskite phase, $\text{Fe}_x\text{Co}_{3-x}\text{O}_4$ ($0 < x < 1$) spinel phase, and CoO rock salt phase are developed and micro-mechanical properties (elastic modulus and hardness) of $z\text{Ce}_{0.8}\text{Gd}_{0.2}\text{O}_{2-\delta} - (1-z)\text{FeCo}_2\text{O}_4$ ($50 \text{ wt}\% \leq z \leq 90 \text{ wt}\%$) composites are characterized via indentation testing at room temperature. Based on results obtained at low indentation loads, it can be indicated that the magnitude of the elastic moduli of the different phases is in the order $\text{Gd}_{0.9}\text{Ce}_{0.1}\text{Fe}_{0.8}\text{Co}_{0.2}\text{O}_3 > \text{Ce}_{1-x}\text{Gd}_x\text{O}_{2-\delta} \approx \text{Fe}_x\text{Co}_{3-x}\text{O}_4 > \text{CoO}$, and furthermore, hardness values are also in the same order. The hardness values of the obtained composites at higher impression loads reveal a stronger dependency on porosity rather than on composition due to similar hardness values of the main phases. Any compositional effect appears to diminish above a porosity $\sim 1 \%$.

This Chapter has been published as: F. Zeng, J. Malzbender, S. Baumann, F. Schulze-Küppers, M. Krüger, A. Nijmeijer, O. Guillon, W.A. Meulenber, Micromechanical Characterization of $\text{Ce}_{0.8}\text{Gd}_{0.2}\text{O}_{2-\delta}$ - FeCo_2O_4 Dual Phase Oxygen Transport Membranes, *Advanced Engineering Materials* 22(6) (2020) 1901558.

DOI: 10.1002/adem.201901558.

5.1 Introduction

Oxygen transport membranes, that exhibit an almost 100 % permeation selectivity regarding oxygen [1], are a promising option to realize environmental friendly, economically sound and efficient processes for pure oxygen production [1-4], oxy-combustion [5-7], and conversion of carbonaceous products [8-12]. These applications typically involve harsh environments, in particular high temperatures, and oxygen partial pressure gradients as well as the exposure to flue gas, which can be detrimental to the chemical and mechanical stability of the respective membrane components [13,14].

Ceramic dual phase oxygen transport membranes are promising candidates for long-term stable operation under application relevant conditions [15-19]. These dual phase membranes consist of two separated phases responsible for ionic and electronic conductivity, respectively [1]. Flexible tailoring regarding chemical properties and stability is permitted by a choice of plenty of possible materials for the individual phases with sufficient ionic or electronic conductivity [20-23].

In fact, it has been indicated that the use of $\text{Ce}_{0.8}\text{Gd}_{0.2}\text{O}_{1.9}$ as ionic conducting phase enables the formation of mechanically and chemically stable composites [15,18,24-26]. Furthermore, it appears that the performance of $\text{Ce}_{0.8}\text{Gd}_{0.2}\text{O}_{1.9}$ -based dual phase membranes can benefit from phase interactions between the two phases in the composites [27,28].

To limit thermal stresses that might induce micro-cracking and failure, the selection of an electronic conducting phase for $\text{Ce}_{0.8}\text{Gd}_{0.2}\text{O}_{1.9}$ -based dual phase membranes should not only be based on performance regarding conductivity, but also on a matching coefficient of thermal expansion (TEC) with that of $\text{Ce}_{0.8}\text{Gd}_{0.2}\text{O}_{1.9}$. Hence, FeCo_2O_4 is an excellent candidate because of its high electronic conductivity of 18 S/cm at 800 °C. It furthermore possesses a TEC that is close to that of $\text{Ce}_{0.8}\text{Gd}_{0.2}\text{O}_{1.9}$ ($\sim 12 \times 10^{-6} \text{ K}^{-1}$) [13].

In fact, composites of $z\text{Ce}_{0.8}\text{Gd}_{0.2}\text{O}_{2-\delta}-(1-z)\text{FeCo}_2\text{O}_4$ ($60 \text{ wt}\% \leq z \leq 90 \text{ wt}\%$) (CF) were reported to possess a remarkable chemical stability under flue gas conditions [19]. These composites are multi-phase systems consisting of $\text{Ce}_{1-x}\text{Gd}_x\text{O}_{2-\delta}$ ($0 < x < 0.2$) (CGO) fluorite phase, $\text{Fe}_x\text{Co}_{3-x}\text{O}_4$ ($0 < x < 1$) (FCO) spinel phase, (Fe,Co)O rock salt phase, and $\text{Gd}_{0.85}\text{Ce}_{0.15}\text{Fe}_{0.75}\text{Co}_{0.25}\text{O}_3$ (GCFCO) perovskite phase formed via phase reaction between $\text{Ce}_{0.8}\text{Gd}_{0.2}\text{O}_{2-\delta}$ (CGO20) and FeCo_2O_4 (FC2O) [19,28]. In this case the newly formed electronic conductive phases, i.e. (Fe,Co)O and GCFCO, contributed to an improved ambipolar conductivity [19,28].

There are a number of reports on the mechanical properties of single phase oxygen transport membranes [29,30-33], however, studies on the mechanical properties of dual phase membranes are limited [18,34,35]. Currently, no study has been reported on the mechanical properties of CF composites. Hence, in this work, we report on the investigation of the mechanical properties of initial CF composites and subsequently formed phase components by indentation testing. The grain sizes of individual phases in composites were optimized for the mechanical properties assessment via indentation testing. The relationships between mechanical properties of the composites and compositional variations as well as porosities are discussed.

5.2 Experimental

All powders were manufactured by mixing of stoichiometric amounts of $\text{Ce}_{0.8}\text{Gd}_{0.2}\text{O}_{1.9}$ (CGO20) (Treibacher Industrie AG, 99 %), Co_3O_4 (Merck, 99 %) and Fe_2O_3 (Merck, 99 %) (the mole ratio of $\text{Co}_3\text{O}_4/\text{Fe}_2\text{O}_3$ was fixed at 4:3 to form FeCo_2O_4 spinel (FC2O)) via ball milling in ethanol. The powder mixtures were dried at 75°C for 3 days, then they were uniaxial pressed into discs and sintered at 1200°C for 10 h in air to obtain CF composites [6]. Finally, five CGO20/FC2O ratios were synthesized, and they were abbreviated as 50CF, 60CF, 70CF, 85CF and 90CF with weight fractions of CGO20 in raw powder mixtures equal to 50 wt%, 60 wt%, 70 wt%, 85 wt%, and 90 wt%, respectively.

Two other kinds of powder mixtures were also prepared to obtain composites with grains as large as 6 μm . One was used to sinter composites with large FCO grains. It was mixed by 85 wt% CGO20 and 15 wt% manually crushed and milled FC2O particles from bulk FC2O samples. The sintered composite was named CF_L. The other powder mixture was used to prepare a composite with large GCFCO grains sintered at 1500 °C for 10 h. The cobalt and iron oxides in the powder mixtures were restrained to an amount needed to form the GCFCO phase to reduce the amount of a liquid phase formed at high temperatures [27,36]. This amount was calculated by assuming no oxygen loss or gain in the powder mixtures after sintering according to the reported compositions for 85CF [13]. The sintered composite with only CGO and GCFCO was named as CG.

The sintered samples were embedded in resin and ground with SiC paper to remove the as-sintered surface. Then the ground samples were polished in a colloidal silica solution for at least 4 hours until all scratches were removed.

Crystalline structure characterization, phase composition determination and quantification were performed via X-ray diffraction (XRD) (Empyrean, Malvern Panalytical Ltd). The instrument was equipped with a Cu LFF tube, BBHD mirror, and a PIXcel3D detector. Microstructures including grain size and volume fraction were assessed with scanning electron microscopy (SEM) (Merlin, Carl Zeiss Microscopy Ltd) and electron backscatter diffraction (EBSD) (NordlysNano, Oxford Instruments Ltd). The porosities of the samples were calculated as area fraction of pores measured via the ImageJ software based on binary pictures of polished sample cross-sections from at least three SEM images via the so-called isodata threshold method [37,38].

Instrumented indentation tests (NanoTest Xtreme, Micro Materials Ltd) were performed on polished samples according to ASTM E2546-15 [39] using a constant loading/unloading time of 10 s and a holding time of 8 s. The number of measurements is specified in the results and discussion section. The positioning of the imprint was assisted by an optical microscope equipped with an objective lens of

50 \times , where large pores and cracks were avoided. The mechanical properties were then deduced according to the methodology proposed by Oliver and Pharr [40].

5.3 Results and discussion

5.3.1 Phase and microstructure characterizations

As the first step, the phase components of composites were investigated via XRD. The XRD patterns of CF and CF_L reveal the coexistence of CGO fluorite, GdFeO₃-type perovskite, CoO rock salt, and FCO spinel with variations in cobalt/iron ratio (see supporting information Figure A5.1). The lattice parameters of the individual phases except the FCO spinel phase in CF and CF_L appear to be rather independent of composition (see supporting information Table A5.1). Whereas, the XRD pattern of CG confirms the presence of only CGO fluorite and GdFeO₃-type perovskite phases, which indicates a successfully synthesized dual phase composite membrane. Furthermore, the lattice parameter of the GdFeO₃-type perovskite is close to that of the CF composites.

Microstructures of the polished cross-sections of the composite are shown in Figure 5.1(a-h). Three phases are distinguishable either by intensity or topography. Some grains are concave possibly due to differences in elastic, plastic and fracture properties. The grey grains, denoted as 1, appear to be CGO grains in all composites, as determined via EDS point quantification. These grains only contain Ce and Gd (see supporting information Table A5.2). The Ce/Gd ratios in CGO are nearly the same in CF and CF_L, while the Ce/Gd ratios in CGO in CG are slightly larger. The investigated black grains, denoted as 2, in CF and CF_L consist of Co and Fe only. They are characterized as being FCO with varying Fe/Co content. The concave grains, denoted as 3, are composed of mainly Gd and Fe, which indicates that they are GdFeO₃-type perovskite grains.

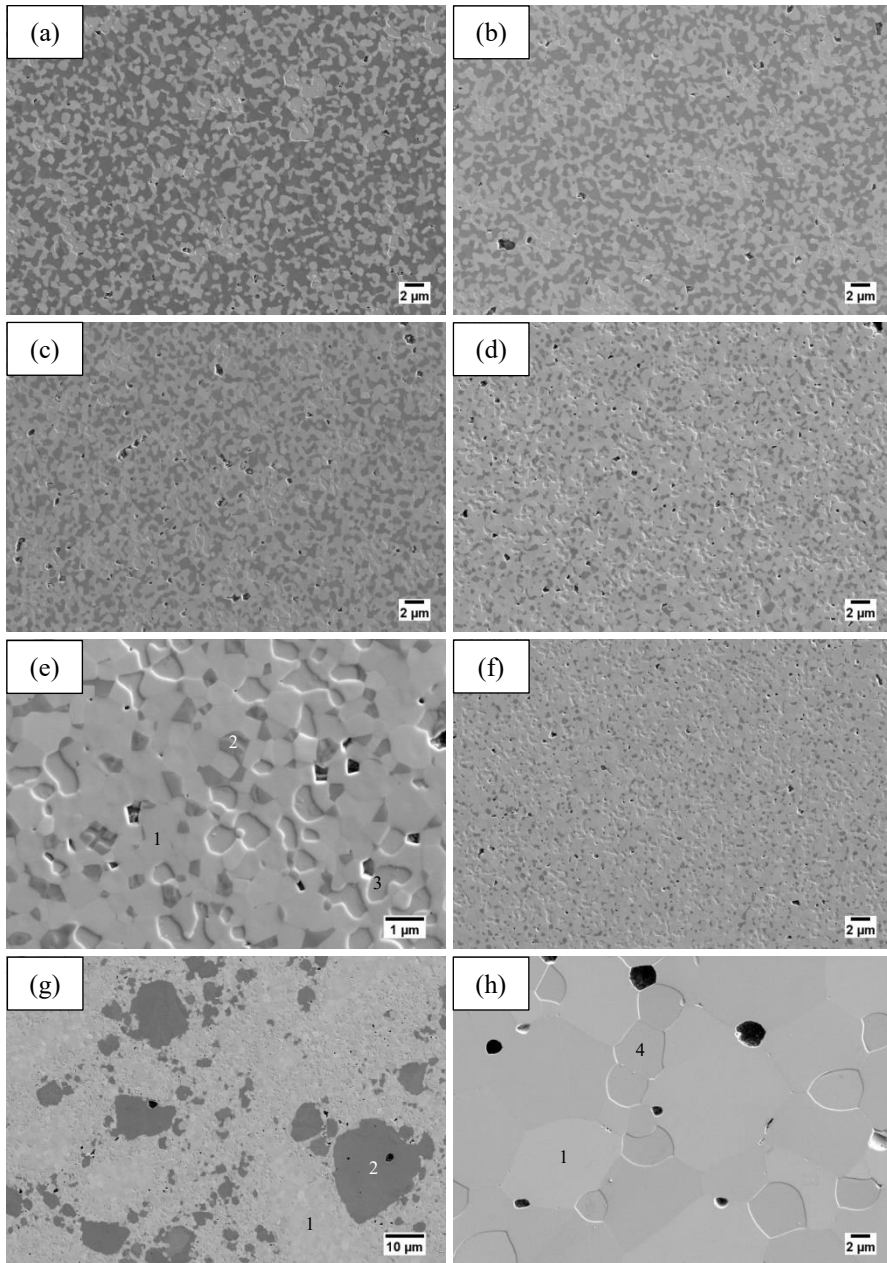


Figure 5.1 Microstructures of (a) 50CF, (b) 60CF, (c) 70CF, (d) 85CF, (e) 85CF with larger magnification and labeled grains, (f) 90CF, (g) CFL, and (h) CG. (CGO, FCO, GCFCO and GCFO are denoted as 1, 2, 3 and 4, respectively).

The element ratios indicate that the GdFeO_3 -type perovskite in CF and CF_L is doped by Ce and Co at the A and B sites [28], and the molar ratio of $(\text{Gd}+\text{Ce})/(\text{Fe}+\text{Co})$ is approximately equal to 1 (see supporting information Table A5.2). Consequently, the composition of the GdFeO_3 -type perovskite in CF and CF_L is estimated to be $\text{Gd}_{0.9}\text{Ce}_{0.1}\text{Fe}_{0.8}\text{Co}_{0.2}\text{O}_3$ (GCFCO) within the assessed grains. However, the composition of the investigated GdFeO_3 -type perovskite grains in CG is estimated to be $\text{Gd}_{0.9}\text{Ce}_{0.1}\text{FeO}_3$ (GCFO) and contains no Co. The similar lattice parameters of GCFCO and GCFO can be seen as an indication of similar chemical bonding strengths between atoms, hence this might already imply that GCFCO and GCFO possess similar elastic moduli and hardness values.

Nevertheless, the rock salt phase CoO could not be detected via SEM. Thus, additional EBSD measurements were performed on CF to quantify all phases. An example of the EBSD phase mapping result for 50CF is shown in Figure 5.2. Four phases are detected via EBSD including CGO fluorite, GCFCO perovskite, CoO rock salt, and FCO spinel, which is in good agreement with the XRD results. The minor phase, i.e. GCFCO and CoO in 50CF appear to be rather inhomogeneously distributed in a 2D image (see Figure 5.2). It should be noted that some small grains or small grain surfaces might be not identified correctly under the current resolution. Moreover, 3D reconstructions were not yet successful due to complexity, i.e. four phases of similar compositions with small grain size. Further analysis is necessary to clarify the exact phase evolution and distribution.

The volume fractions of all individual phases in CF are presented in Figure 5.3. The average grain sizes of the respective phases are summarized in Table 5.1. CGO is the most prominent phase with the highest volume fraction possessing a grain size of $0.5\ \mu\text{m}$ in the investigated composites. FCO is the second most abundant phase with grain sizes being close to that of CGO. The GCFCO volume fraction increases marginally with CGO20/FC2O ratio with a maximum at a CGO20 content of 85 wt%. The grain size of GCFCO decreases slightly with increasing CGO20 content. A small

amount of CoO phase is only detectable in 50CF and 60CF with grain sizes similar to that of CGO.

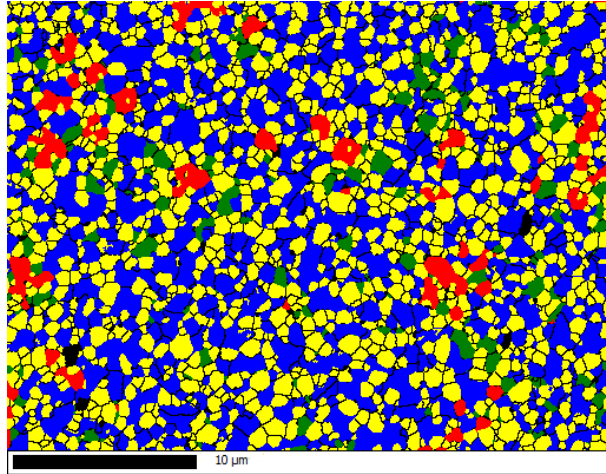


Figure 5.2 EBSD phase mapping on 50CF: the yellow, red, blue and green phase are CGO, GFCCO, FCO and CoO, respectively.

It should also be noticed that the volume fraction of the GCFCO phase in these small grains might be underestimated because of a topography effect of grain boundaries from the concave grains (Figure 5.1).

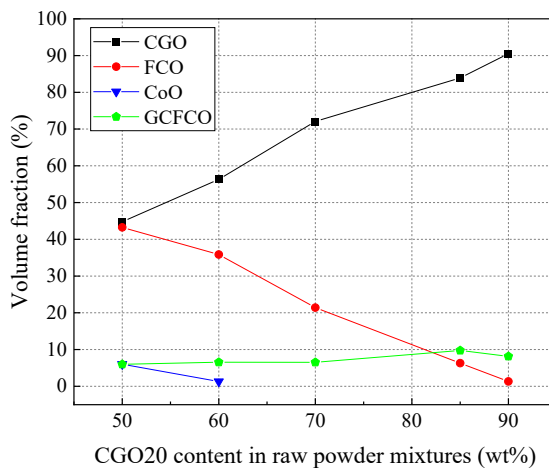


Figure 5.3 Volume fractions of the individual phases in CF.

Table 5.1 Average grain sizes of phases in CF.

Composite \ Grain size	CGO (μm)	FCO (μm)	GCFCO (μm)	CoO (μm)
50CF	0.5 ± 0.2	0.7 ± 0.4	1.0 ± 0.5	0.5 ± 0.2
60CF	0.5 ± 0.2	0.6 ± 0.3	0.8 ± 0.4	0.4 ± 0.2
70CF	0.5 ± 0.2	0.5 ± 0.2	0.5 ± 0.2	-
85CF	0.5 ± 0.2	0.3 ± 0.1	0.4 ± 0.2	-
90CF	0.5 ± 0.2	0.3 ± 0.1	0.4 ± 0.1	-

5.3.2 Mechanical properties

The indentation technique provides a convenient characterization method of the mechanical properties from macroscale to nanoscale [42], creating the capability to obtain macroscopically and non-destructively the local mechanical properties of individual phases in composites via imprints with dimensions restrained to $\sim 1/10$ or less of the size of targeted single grain or isolated phase area, i.e. less than 50 nm for CF. It is not possible to locate imprints on grains smaller than $\sim 2 \mu\text{m}$ via the available optical microscope with a $50\times$ objective lens.

Therefore, CG and CF_L materials with larger grain sizes were used for targeted indentations tests with a load of 5 mN to characterize the mechanical properties of the individual phases. The tests were carried out for individual grains (like the grain denoted as 2 in Figure 5.1(g) and 4 in Figure 5.1(h), respectively) or phase areas (as the area denoted as 1 in Figure 5.1(g)) with a diameter larger than $6 \mu\text{m}$ since they can be expected to be more than ten times larger than the indentation sizes (plastic and elastic zone) and can hence be easily identified by color and topography with the optical microscope.

For CG, indents were located close to the centers of 20 concave GCFCO grains. And for CF_L, indentations were initially located close to the centers of 20 isolated white CGO phase areas. Subsequently, in order to identify the mechanical properties of FCO and CoO grains, special indentation test schedules were developed combined with EBSD investigations on indented areas as outlined in the following.

A 15 × 15 grid of indentations with a load of 5 mN were imprinted on CF_L, where in particular large black grains were selected. The distance between each indent was set to ~ 3 μm, which is approximately 3 times larger than the indentation sizes (< 1 μm) to minimize influence from neighboring imprints [43,44]. The indented areas were afterward characterized via EBSD to verify phases.

The phase mapping of the indented area is illustrated in Figure 5.4(b) for comparison along with an optical micrograph (Figure 5.4(a)). It shows that the brownish grains are FCO grains (Figure 5.4(a)), and most CoO grains visible as greyish are embedded within the FCO grains. Hence, the large grey grains inside brownish FCO grains could be targeted as CoO grains for the indentation tests under the optical microscope.

The derived elastic modulus (E) and hardness (H) mappings of the grid of imprints are presented in Figure 5.4(c) and Figure 5.4(d), respectively. Some indents were located on cracks, grain boundaries and pores leading to low E and H values. These artifacts will not be considered during the subsequent analysis and discussion.

The CoO grains have an E value close to that of the FCO grains, which is lower than the E value of their surrounding grains (CGO and GCFCO), while the H value of the CoO grains is much lower than the H value of FCO.

In order to get statistical relevant values of the mechanical properties of the FCO and CoO phases, indents were subsequently imprinted in an additional test series in the middle of a number of individual grains including 50 FCO grains and 20 CoO grains. Because of the variations in cobalt content, a higher number of FCO grains were investigated to derive reliable statistical values.

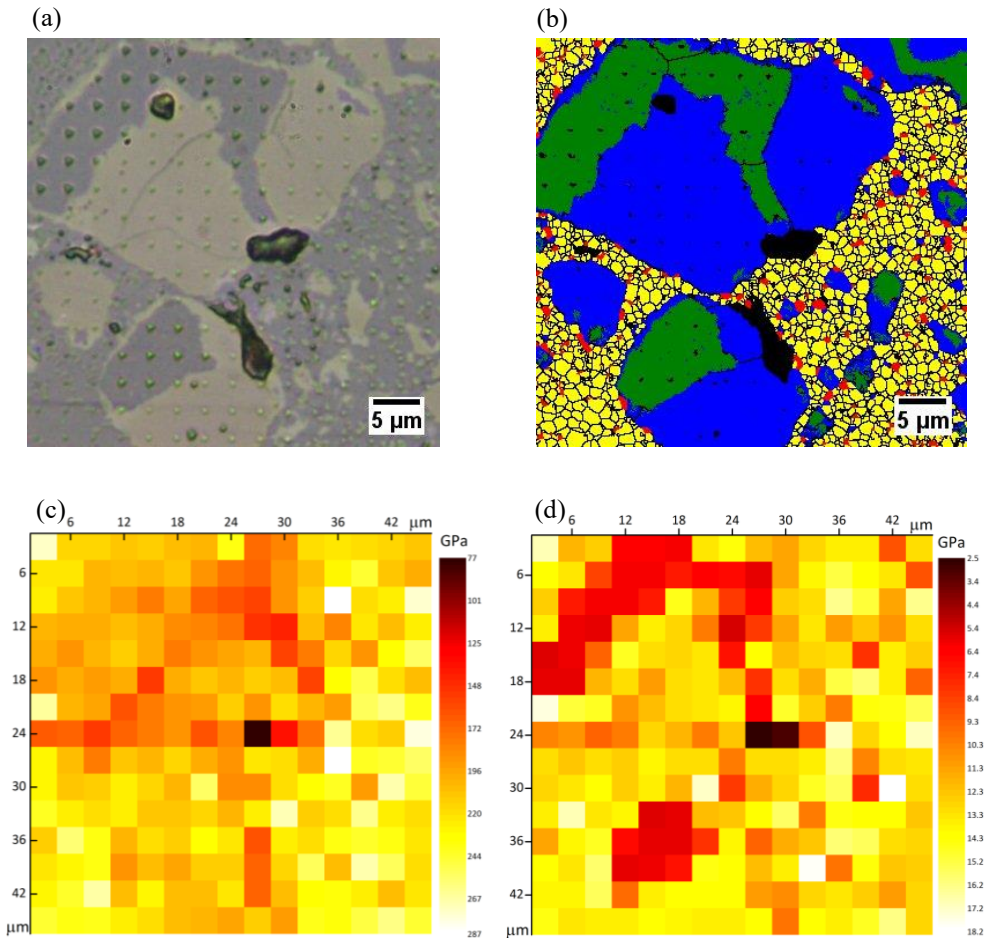


Figure 5.4 Investigation of grid indentation array via (a) optical micrograph, (b) EBSD phase mapping (the blue, green, yellow and red grains correspond to FCO, CoO, CGO and GCFCO, respectively), and the corresponding (c) elastic modulus mapping, and (d) hardness mapping.

The derived mechanical properties of the individual phases are summarized in Table 5.2. The E and H values of GCFO are significantly larger than those of the other phases, and they are the same as for GCFCO. CGO and FCO show similar E and H values within the limits of statistical uncertainty. CoO possesses a similar elastic modulus, but a much lower hardness when compared with CGO and FCO. Furthermore, the mechanical properties of FCO are barely influenced by variations in cobalt content as the standard deviation of the E and H values of FCO are close to

that of CGO. These deviations might be induced by the noise in the device [45]. In summary, the E values decrease according to $\text{GCFCO} \approx \text{GCFO} > \text{CGO} \approx \text{FCO} > \text{CoO}$, and the H values descend in the same order.

Table 5.2 Mechanical properties of CGO, FCO, CoO and GCFO phases.

Phase \ Property	Elastic modulus (GPa)	Hardness (GPa)
GCFO	284 ± 21	31.7 ± 1.9
CGO	229 ± 10	13.6 ± 0.7
FCO	209 ± 12	13.3 ± 0.8
CoO	193 ± 17	6.1 ± 0.6

Therefore, on the basis of mechanical properties and volume fractions of the phase constituents in CF, it can be predicted that the elastic modulus and hardness of CF improve as a function of CGO content due to the associated increase in CGO and GCFCO content in the composites (Figure 5.3), whereas the small amount of CoO rock salt phase is expected to have only a minor effect.

In order to assess the average elastic modulus and hardness of CGO20-F2CO considering it as a kind of homogeneous material, imprints should be significantly larger than the representative volume element of the composites [46]. The small grain size and good homogeneity of the individual phases in CGO20-F2CO suggests that imprints with a size around ten times larger ($> 5 \mu\text{m}$) than the grain size will be appropriate for yielding reliable effective elastic modulus and hardness for the composites. Thus, 20 indentation tests with a higher load of 150 mN were conducted on the polished sample cross-sections in subsequent tests. The resulting imprints were larger than $5 \mu\text{m}$ and covered a representative area of the microstructure of the composites.

The derived mechanical properties for the CF composite are presented in Figure 5.5. The E value starts to rise marginally when the CGO phase is above 72 vol%, whereas the H value shows no clear dependence on CGO content, but shows a minimum value when CGO is 72 vol%, coinciding with the highest porosity obtained for the range of compositions in this work.

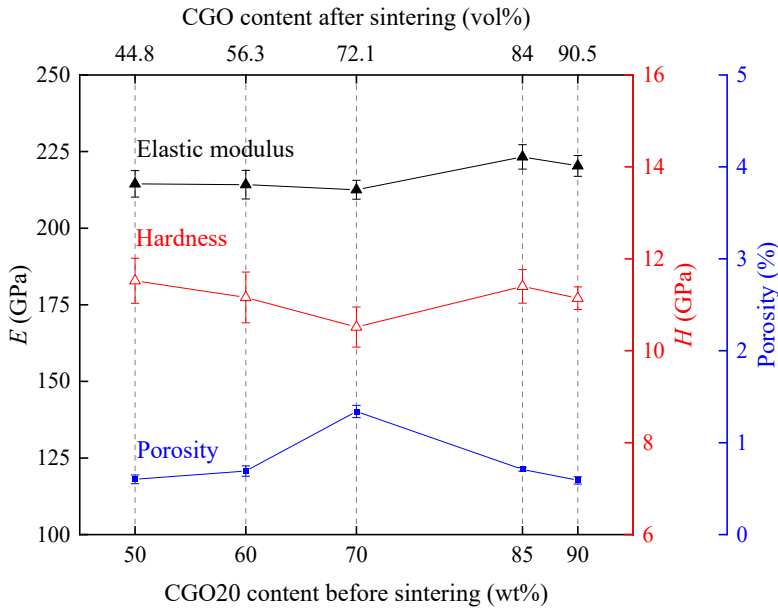


Figure 5.5 Elastic modulus, hardness and porosities of CF.

Usually, both E value and H value of ceramic materials decrease with increasing porosities [31,47]. The porosities of CF except 70CF vary between ~ 0.6 % and ~ 0.7 % (Figure 5.5), and they barely change with composition, while 70CF has a relatively higher porosity of ~ 1.3 %, which leads to a slight decrease of the H value but no significant influence on the E value. Thus, the porosity dependence of the H value is stronger than that of the E value, and the E value is more dependent on composition (note, the elastic zone is around ten times larger than the plastic zone, hence, the hardness is stronger affected by local effects).

In the interest of validating the influence of porosities on indentation test results, an 85CF composite with a higher porosity of $\sim 3.8\%$, but with the same composition, abbreviated as 85CF_p, was prepared by a Pechini process. Details on the synthesis route and microstructure were reported elsewhere [6]. Both E value and H value of 85CF_p, as derived from the indentation tests with a load of 150 mN, are smaller than the values obtained for the 85CF composition (Table 5.3). They are even lower than that of 50CF with a porosity of 0.6 % despite the high CGO and GCFCO content. Therefore, it can be concluded that the porosity has a stronger effect than the composition on elastic modulus and hardness of CF when the porosity exceeds $\sim 1\%$.

Table 5.3 Mechanical properties of 85CF with different porosities.

Composite \ Property	Porosity (%)	Elastic modulus (GPa)	Hardness (GPa)
85CF	0.7 ± 0.02	223 ± 4	11.4 ± 0.4
85CF _p	3.8 ± 1.7	196 ± 5	9.7 ± 0.5

5.4 Conclusions

Four phases including CGO, GCFCO, FCO, and CoO were identified in CF composites, which were synthesized by solid state reaction. Their individual elastic modulus and hardness values are derived from targeted indentation measurements on composites with optimized microstructures. The results indicate that the E values decrease according to GCFCO > CGO \approx FCO > CoO, and the H values descend in the same order. The E value mainly depends on the composition, and slightly increases with CGO content, while the H value is also biased to a stronger extent by porosity rather than composition. Furthermore, it can also be concluded from indentation test results that a porosity above $\sim 1\%$ has a stronger effect on the elastic modulus and hardness than the composition for CF composites. Overall, this work provides elastic modulus and hardness of all individual phases in CF materials,

including apparently high temperature stable phases and phase interaction products. The results can be applied for further mechanical modeling.

References

- [1] X. Zhu, W. Yang, Mixed conducting ceramic membranes, Springer-Verlag, Berlin, Germany, 2017.
- [2] P. Niehoff, F. Schulze-Kueppers, S. Baumann, W.A. Meulenber, O. Guillon, R. Vassen, Fabrication of laboratory-scale planar oxygen separation membrane modules, *American Ceramic Society Bulletin* 94(1) (2015) 28-31.
- [3] K. Zhang, J. Sunarso, Z. Shao, W. Zhou, C. Sun, S. Wang, S. Liu, Research progress and materials selection guidelines on mixed conducting perovskite-type ceramic membranes for oxygen production, *RSC Advances* 1(9) (2011) 1661-1676.
- [4] H. Wang, S. Werth, T. Schiestel, J. Caro, Perovskite hollow-fiber membranes for the production of oxygen-enriched air, *Angewandte Chemie International Edition* 44(42) (2005) 6906-6909.
- [5] H. Stadler, F. Beggel, M. Habermehl, B. Persigehl, R. Kneer, M. Modigell, P. Jeschke, Oxyfuel coal combustion by efficient integration of oxygen transport membranes, *International Journal of Greenhouse Gas Control* 5(1) (2011) 7-15.
- [6] M. Ramasamy, Dual phase oxygen transport membrane for efficient oxyfuel combustion, PhD thesis, Bochum University, Bochum, Germany, 2016.
- [7] X. Zhu, H. Liu, Y. Cong, W. Yang, Novel dual-phase membranes for CO₂ capture via an oxyfuel route, *Chemical Communications* 48(2) (2012) 251-253.
- [8] P.-M. Geffroy, J. Fouletier, N. Richet, T. Chartier, Rational selection of MIEC materials in energy production processes, *Chemical Engineering Science* 87 (2013) 408-433.
- [9] C. Karakaya, R.J. Kee, Progress in the direct catalytic conversion of methane to fuels and chemicals, *Progress in Energy and Combustion Science* 55 (2016) 60-97.
- [10] H. Jiang, H. Wang, S. Werth, T. Schiestel, J. Caro, Simultaneous Production of Hydrogen and Synthesis Gas by Combining Water Splitting with Partial Oxidation of Methane in a Hollow-Fiber Membrane Reactor, *Angewandte Chemie International Edition* 47(48) (2008) 9341-9344.
- [11] H.J. Bouwmeester, Dense ceramic membranes for methane conversion, *Catalysis Today* 82(1-4) (2003) 141-150.

- [12] X. Dong, W. Jin, N. Xu, K. Li, Dense ceramic catalytic membranes and membrane reactors for energy and environmental applications, *Chemical Communications* 47(39) (2011) 10886-10902.
- [13] M. Ramasamy, S. Baumann, J. Palisaitis, F. Schulze-Küppers, M. Balaguer, D. Kim, W.A. Meulenber, J. Mayer, R. Bhawe, O. Guillon, Influence of Microstructure and Surface Activation of Dual-Phase Membrane $Ce_{0.8}Gd_{0.2}O_{2-\delta}$ - $FeCo_2O_4$ on Oxygen Permeation, *Journal of the American Ceramic Society* 99(1) (2016) 349-355.
- [14] L.L. Anderson, P.A. Armstrong, R.R. Broekhuis, M.F. Carolan, J. Chen, M.D. Hutcheon, C.A. Lewinsohn, C.F. Miller, J.M. Repasky, D.M. Taylor, Advances in ion transport membrane technology for oxygen and syngas production, *Solid State Ionics* 288 (2016) 331-337.
- [15] H. Luo, H. Jiang, K. Efimov, F. Liang, H. Wang, J.r. Caro, CO_2 -tolerant oxygen-permeable Fe_2O_3 - $Ce_{0.9}Gd_{0.1}O_{2-\delta}$ dual phase membranes, *Industrial & Engineering Chemistry Research* 50(23) (2011) 13508-13517.
- [16] S. Guo, Z. Liu, J. Zhu, X. Jiang, Z. Song, W. Jin, Highly oxygen-permeable and CO_2 -stable $Ce_{0.8}Sm_{0.2}O_{2-\delta}$ - $SrCo_{0.9}Nb_{0.1}O_{3-\delta}$ dual-phase membrane for oxygen separation, *Fuel Processing Technology* 154 (2016) 19-26.
- [17] H. Luo, K. Efimov, H. Jiang, A. Feldhoff, H. Wang, J. Caro, CO_2 -stable and cobalt-free dual-phase membrane for oxygen separation, *Angewandte Chemie International Edition* 50(3) (2011) 759-763.
- [18] S. Kim, S.H. Kim, K.S. Lee, J.H. Yu, Y.-H. Seong, I.S. Han, Mechanical properties of LSCF ($La_{0.6}Sr_{0.4}Co_{0.2}Fe_{0.8}O_{3-\delta}$)-GDC ($Ce_{0.9}Gd_{0.1}O_{2-\delta}$) for oxygen transport membranes, *Ceramics International* 43(2) (2017) 1916-1921.
- [19] M. Ramasamy, E. Persoon, S. Baumann, M. Schroeder, F. Schulze-Küppers, D. Görtz, R. Bhawe, M. Bram, W.A. Meulenber, Structural and chemical stability of high performance $Ce_{0.8}Gd_{0.2}O_{2-\delta}$ - $FeCo_2O_4$ dual phase oxygen transport membranes, *Journal of Membrane Science* 544 (2017) 278-286.
- [20] B.C. Steele, Ceramic ion conducting membranes, *Current Opinion in Solid State Materials Science* 1(5) (1996) 684-691.
- [21] V. Kharton, A. Kovalevsky, A. Viskup, A. Shaula, F. Figueiredo, E. Naumovich, F. Marques, Oxygen transport in $Ce_{0.8}Gd_{0.2}O_{2-\delta}$ -based composite membranes, *Solid State Ionics* 160(3-4) (2003) 247-258.
- [22] A. Petric, H. Ling, Electrical Conductivity and Thermal Expansion of Spinel at Elevated Temperatures, *Journal of the American Ceramic Society* 90(5) (2007) 1515-1520.

- [23] E. Verwey, P. Haayman, F. Romeijn, Physical properties and cation arrangement of oxides with spinel structures II. Electronic conductivity, *The Journal of Chemical Physics* 15(4) (1947) 181-187.
- [24] A.J. Samson, M. Søgaaard, P.V. Hendriksen, (Ce,Gd)O_{2-δ}-based dual phase membranes for oxygen separation, *Journal of Membrane Science* 470 (2014) 178-188.
- [25] W. Fang, F. Liang, Z. Cao, F. Steinbach, A. Feldhoff, A mixed ionic and electronic conducting dual-phase membrane with high oxygen permeability, *Angewandte Chemie International Edition* 54(16) (2015) 4847-4850.
- [26] M. Lipińska-Chwałek, F. Schulze-Küppers, J. Malzbender, Mechanical properties of pure and doped cerium oxide, *Journal of the European Ceramic Society* 35(5) (2015) 1539-1547.
- [27] Y. Lin, S. Fang, D. Su, K.S. Brinkman, F. Chen, Enhancing grain boundary ionic conductivity in mixed ionic-electronic conductors, *Nature communications* 6 (2015) 6824.
- [28] M. Ramasamy, S. Baumann, A. Opitz, R. Iskandar, J. Mayer, D. Udomsilp, U. Breuer, M. Bram, Phase Interaction and Distribution in Mixed Ionic Electronic Conducting Ceria-Spinel Composites, *Advances in Solid Oxide Fuel Cells Electronic Ceramics II: Ceramic Engineering Science Proceedings* 37(3) (2017) 99-112.
- [29] G. Pećanac, S. Baumann, J. Malzbender, Mechanical properties and lifetime predictions for Ba_{0.5}Sr_{0.5}Co_{0.8}Fe_{0.2}O_{3-δ} membrane material, *Journal of Membrane Science* 385 (2011) 263-268.
- [30] B. Huang, J. Malzbender, R. Steinbrech, E. Wessel, H. Penkalla, L. Singheiser, Mechanical aspects of ferro-elastic behavior and phase composition of La_{0.58}Sr_{0.4}Co_{0.2}Fe_{0.8}O_{3-δ}, *Journal of Membrane Science* 349(1-2) (2010) 183-188.
- [31] G. Pećanac, S. Foghmoes, M. Lipińska-Chwałek, S. Baumann, T. Beck, J. Malzbender, Strength degradation and failure limits of dense and porous ceramic membrane materials, *Journal of the European Ceramic Society* 33(13-14) (2013) 2689-2698.
- [32] J. Malzbender, Mechanical aspects of ceramic membrane materials, *Ceramics International* 42(7) (2016) 7899-7911.
- [33] R.O. Silva, J. Malzbender, F. Schulze-Küppers, S. Baumann, O. Guillon, Mechanical properties and lifetime predictions of dense SrTi_{1-x}Fe_xO_{3-δ} ($x = 0.25, 0.35, 0.5$), *Journal of the European Ceramic Society* 37(7) (2017) 2629-2636.
- [34] T. Nithyanantham, S. Bandopadhyay, Effect of Temperature and Environment on the Mechanical Properties of LSFT-CGO Membranes, *Advances in Solid Oxide Fuel Cells III: a collection of papers presented at the 31st International Conference on Advanced Ceramics*

and Composites, January 21-26, 2007, Daytona Beach, Florida, Wiley-American Ceramic Society, 2007, p. 377.

[35] T. Nithyanantham, S. Biswas, N. Nagendra, S. Bandopadhyay, Studies on mechanical behavior of LSFT-CGO dual-phase membranes at elevated temperatures in ambient air and slightly reducing environments, *Ceramics International* 40(6) (2014) 7783-7790.

[36] C. Kleinogel, L.J. Gauckler, Sintering and properties of nanosized ceria solid solutions, *Solid State Ionics* 135(1-4) (2000) 567-573.

[37] S.M. Hartig, Basic Image Analysis and Manipulation in ImageJ, *Current Protocols in Molecular Biology* 102(1) (2013) 14-15.

[38] T.W. Ridler, S. Calvard, Picture Thresholding Using an Iterative Selection Method, *Ieee Transactions on Systems Man and Cybernetics* 8(8) (1978) 630-632.

[39] ASTM, E2546-15: Standard Practice for Instrumented Indentation Testing, ASTM International, West Conshohocken, PA, 2015.

[40] W.C. Oliver, G.M. Pharr, An improved technique for determining hardness and elastic modulus using load and displacement sensing indentation experiments, *Journal of Materials Research* 7(6) (1992) 1564-1583.

[41] A.S. Verma, A. Kumar, Bulk modulus of cubic perovskites, *Journal of Alloys and Compounds* 541 (2012) 210-214.

[42] E. Broitman, Indentation hardness measurements at macro-, micro-, and nanoscale: a critical overview, *Tribology Letters* 65(1) (2017) 23.

[43] P. Haušild, A. Materna, L. Kocmanová, J. Matějček, Determination of the individual phase properties from the measured grid indentation data, *Journal of Materials Research* 31(22) (2016) 3538-3548.

[44] N.X. Randall, M. Vandamme, F.-J. Ulm, Nanoindentation analysis as a two-dimensional tool for mapping the mechanical properties of complex surfaces, *Journal of Materials Research* 24(3) (2009) 679-690.

[45] J. Menčík, Uncertainties and errors in nanoindentation, *Nanoindentation in Materials Science* 54 (2012) 53-86.

[46] G. Constantinides, K.R. Chandran, F.-J. Ulm, K. Van Vliet, Grid indentation analysis of composite microstructure and mechanics: Principles and validation, *Materials Science Engineering: A* 430(1-2) (2006) 189-202.

[47] R. Pal, Porosity-dependence of effective mechanical properties of pore-solid composite materials, *Journal of Composite Materials* 39(13) (2005) 1147-1158.

Appendix A5

Table A5.1 Lattice parameters of composites.

Lattice parameter Composite	CGO fluorite	GdFeO ₃ -type perovskite			CoO rock salt
	a (Å)	a (Å)	b (Å)	c (Å)	a (Å)
50CF	5.41	5.34	5.61	7.66	4.26
60CF	5.42	5.34	5.62	7.66	-
70CF	5.42	5.34	5.61	7.66	4.26
85CF	5.42	5.34	5.61	7.66	4.26
90CF	5.42	5.34	5.61	7.65	4.26
CF _L	5.42	5.34	5.61	7.66	4.26
CG	5.42	5.37	5.60	7.70	-

Table A5.2 Average EDS point quantification results of all individual phases in composites.

Spectrum	Element	Ce (mol%)	Gd (mol%)	Fe (mol%)	Co / (mol%)	Ce/(Gd+ Ce)	Co/(Fe+ Co)	(Gd+Ce)/(Fe +Co)
Grey grain	CF	77.9 ± 2.2	22.1 ± 2.2	-	-	0.78 ± 0.02	-	-
	CF _L	78.4 ± 4.7	21.6 ± 4.7	-	-	0.78 ± 0.05	-	-
	CG	85.1 ± 0.3	14.9 ± 0.3	-	-	0.85 ± 0.003	-	-
Black grain	CF	-	-	26.7 ± 18.7	73.3 ± 18.7	-	0.73 ± 0.19	-
	CF _L	-	-	13.7 ± 17.1	86.3 ± 17.1	-	0.86 ± 0.17	-
Conca ve grain	CF	5.1 ± 1.4	47.6 ± 1.8	37.6 ± 1.4	9.7 ± 3.5	0.10 ± 0.02	0.20 ± 0.06	1.12 ± 0.09
	CF _L	4.0 ± 1.3	49.3 ± 1.2	37.6 ± 1.0	9.1 ± 1.2	0.07 ± 0.03	0.20 ± 0.02	1.14 ± 0.01
	CG	7.9 ± 0.4	43.7 ± 0.6	48.4 ± 0.4	-	0.15 ± 0.01	-	1.07 ± 0.02

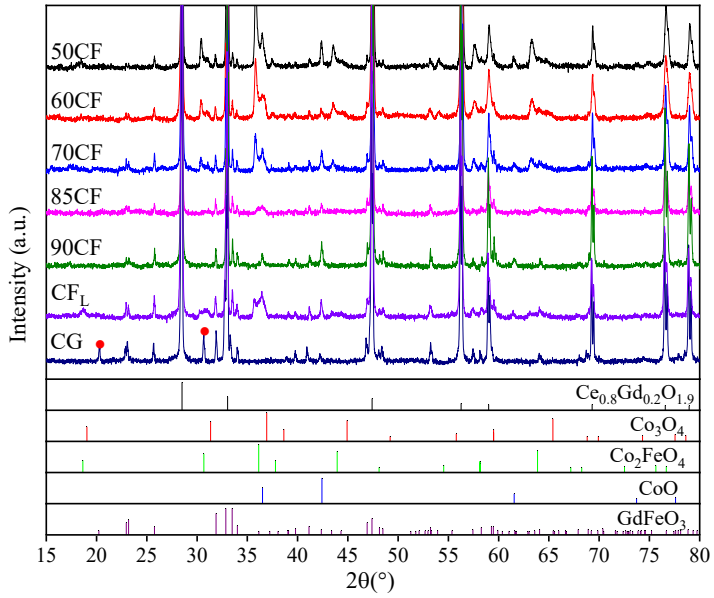


Figure A5.1 XRD patterns of composites (two unidentified peaks are marked as red dots).

CHAPTER 6

Residual stress and mechanical strength of $\text{Ce}_{0.8}\text{Gd}_{0.2}\text{O}_{2-\delta}$ - FeCo_2O_4 dual phase oxygen transport membranes

Abstract

$\text{Ce}_{0.8}\text{Gd}_{0.2}\text{O}_{2-\delta}$ - FeCo_2O_4 membranes, benefiting from their excellent chemical stability, exhibit a broad application potential in oxygen-consuming industrial processes running in harsh environments. For long-term reliable operation, the membrane needs to possess sufficient mechanical strength. This paper characterizes the typical aspects that challenge the mechanical stability of the sintered membrane, including composition and microstructural defects as well as residual stress and residual stress gradients. It is revealed that mechanical strengths of the sintered membranes increase with decreasing iron cobalt spinel content, that the high iron cobalt spinel content induces microcracks, and that high residual tensile stress gradually decreases from the as-sintered surface to the bulk. Although the residual tensile stress can be reduced by applying an extensive elevated temperature dwell time during cooling, it is suggested to limit the iron cobalt spinel content to a nominal value of 15 wt% to eliminate the residual tensile stress while maintaining a high mechanical strength.

This chapter has been submitted for publication as: F. Zeng, J. Malzbender, S. Baumann, A. Nijmeijer, L. Winnubst, O. Guillon, R. Schwaiger, W. A. Meulenber, Residual stress and mechanical strength of $\text{Ce}_{0.8}\text{Gd}_{0.2}\text{O}_{2-\delta}$ - FeCo_2O_4 dual phase oxygen transport membranes, Journal of the European Ceramic Society.

6.1 Introduction

Ceramic oxygen transport membranes possess substantial economic and environmental benefits for industrial processes related to high purity oxygen separation and production [1-3], partial oxidation of hydrocarbons [4-6], and oxy-combustion [7-9]. Single phase perovskite membranes, such as $\text{Ba}_{0.5}\text{Sr}_{0.5}\text{Co}_{0.8}\text{Fe}_{0.2}\text{O}_{3-\delta}$ [10], and $\text{La}_{0.6}\text{Sr}_{0.4}\text{Co}_{0.2}\text{Fe}_{0.8}\text{O}_{3-\delta}$ [11], exhibit high oxygen permeation fluxes but suffer from chemical and thermo-mechanical instabilities under practical application-relevant conditions [12-19]. By contrast, it has been verified that dual phase membranes consisting of ion conducting phase(s) and electron conducting phase(s) possess excellent chemical stability under harsh application environments [20-28]. The CGO fluorite is often chosen as the ionic conducting phase for dual phase membranes because of its high ionic conductivity [29], as well as high chemical stability [20-22, 24, 28, 30-34]. Spinel oxides, e.g. $\text{Fe}_x\text{Co}_{3-x}\text{O}_4$ ($x = 1$ or 2), NiFe_2O_4 , and $\text{Mn}_{1.5}\text{Co}_{1.5}\text{O}_4$, have been widely used as electron conducting phase for CGO-based dual phase membranes to realize high mixed ionic-electron conductivity [20, 35-38]. As an example, 85 wt% $\text{Ce}_{0.8}\text{Gd}_{0.2}\text{O}_{2-\delta}$ -15 wt% FeCo_2O_4 membrane, which contains an ion conducting phase- $\text{Ce}_{1-x}\text{Gd}_x\text{O}_{2-\delta}$ ($0 < x < 0.2$) (CGO) and two electron conducting phases- $\text{Fe}_y\text{Co}_{3-y}\text{O}_4$ ($0 < y < 2$) (FCO) and $\text{Gd}_{0.85}\text{Ce}_{0.15}\text{Fe}_{0.75}\text{Co}_{0.25}\text{O}_3$ (GCFCO) [20, 39, 40] after sintering, has been shown to be chemically and functionally stable in CO_2 - and SO_2 -containing gas mixtures at 850 °C over at least 200 h under an oxygen partial pressure gradient [20].

For the long-term safe operation of oxygen transport membranes under application-relevant conditions, in addition to oxygen permeation flux and chemical stability also the mechanical strength needs to be considered as one critical aspect [15, 41]. However, only a few studies have yet focused on the mechanical strength of dual phase membranes [40, 42-45].

Microstructural defects, e.g. cracks, impurities, inhomogeneities and voids, are known to be typical fracture origins of ceramic materials [46]. In addition, residual stresses and residual stress gradients also affect the fracture behavior of ceramic

materials [47]. A residual tensile stress can lead to a decrease of the apparent mechanical strength by inducing cracks and increasing the stress intensity at potential fracture origins. Compositional and/or stoichiometric gradients over the thickness of the ceramic sample, which can be induced by inhomogeneous phase transformations and/or stoichiometric differences, may result in residual stress gradients [47]. Dual phase membranes, for example, comprising fluorite and Co-containing spinel phases, have typical sintering temperatures between 1200 °C and 1400 °C [20, 35-37], which is a temperature range where a CoO rock salt phase exists [40]. The spinel phase results from a phase transformation of the rock salt phase during cooling after sintering [40]. This phase transformation process appears to be slower in the bulk than at the surface of the ceramic due to the presence of the CGO and GCFCO phases, hence, a small amount of rock salt was reported to remain in the bulk of 50 wt% $\text{Ce}_{0.8}\text{Gd}_{0.2}\text{O}_{2-\delta}$ -50wt% FeCo_2O_4 membranes even after applying a slow cooling rate of 0.5 K/min in the critical temperature range of 900 °C-800 °C [39, 48]. In addition to the different amounts of the rock salt phase over the membrane thickness, the crystal structure of the fluorite phase (CGO) in 50 wt% $\text{Ce}_{0.8}\text{Gd}_{0.2}\text{O}_{2-\delta}$ -50wt% FeCo_2O_4 and 85 wt% $\text{Ce}_{0.8}\text{Gd}_{0.2}\text{O}_{2-\delta}$ -15wt% FeCo_2O_4 membranes also varies between the surface and the bulk materials: the lattice constant of CGO in the bulk is larger than that at the surface, which indicates that the oxygen non-stoichiometry in CGO in the bulk is higher than that at the surface [49]. Such oxygen stoichiometry variations between surface and bulk are likely origins of residual tensile stresses that gradually decreases from surface to bulk [49].

The current work focuses on the characterization of the residual stress and its effect on the fracture strength as well as on the development of thermal processing steps to alleviate any detrimental residual stresses, i.e. tensile stresses, for $\text{Ce}_{0.8}\text{Gd}_{0.2}\text{O}_{2-\delta}$ - FeCo_2O_4 dual phase membranes. The microstructural, compositional and crystal-structure variations across the disc-shaped membrane were investigated in detail as potential causes of residual stress. The residual stress and residual stress gradient within the membrane were analyzed by X-ray diffraction (based on the $\sin^2 \psi$ method) and indentation. The relation between fracture strength and residual stress

is discussed, aided by fractographic analysis of fractured membranes that experience different residual stress states.

6.2 Experimental

$\text{Ce}_{0.8}\text{Gd}_{0.2}\text{O}_{2-\delta}$ - FeCo_2O_4 composites were synthesized by solid-state reaction with one-step thermal processing. Stoichiometric amounts of $\text{Ce}_{0.8}\text{Gd}_{0.2}\text{O}_{2-\delta}$ (Treibacher Industrie AG, 99 %), Co_3O_4 (Alfa Aesar, 99.7 %) and Fe_2O_3 (Sigma-Aldrich, 99 %) were mixed as precursor powder mixtures to prepare three different nominal weight ratios of $\text{Ce}_{0.8}\text{Gd}_{0.2}\text{O}_{2-\delta}$ to FeCo_2O_4 , being 50:50, 70:30 and 85:15; the Co/Fe mole ratio was fixed at a value of two in order to form FeCo_2O_4 nominally [40]. The powder mixtures, ethanol and zirconia balls were filled up to relative ~30 vol% in a polyethylene bottle and milled on a roller bench. Other details regarding milling parameters and procedures can be found in our previous work [40]. The ball-milled powder mixtures were then dried at 75 °C for 3 days and subsequently uniaxially pressed into discs with diameters of 20 mm using a pressure of 19 MPa [40, 48]. The obtained discs were sintered in air at 1200 °C for 10 hours at a heating rate of 3 K/min. Two different cooling procedures were applied to complete the oxidation of the CoO rock salt phase [50-52]. The first one included a slow cooling step of 0.5 K/min between 900 °C and 800 °C, while the cooling rate for the other temperature ranges was 3 K/min. Three composites, which are referred to as 50CF, 70CF and 85CF in the following, were obtained with this cooling procedure. The numbers of the abbreviations correspond to the nominal fractions of $\text{Ce}_{0.8}\text{Gd}_{0.2}\text{O}_{2-\delta}$ content in the starting powder mixtures. The second cooling procedure included an extended dwelling step at 850 °C for 100 hours, while the cooling rate for the entire temperature range was 3 K/min. This cooling procedure was only applied for the sintering of 50CF, which will be referred to as dwelled-50CF.

The materials below the as-sintered surfaces of the 1 mm thick sintered discs were gradually exposed by controlled grinding and polishing steps, as outlined in detail in our previous work [49]. Residual stresses potentially induced by the grinding were

removed by multiple fine-polishing steps to achieve a mirror finish [53]. In this way, two materials' subsurfaces at respective depths of ~ 30 and ~ 300 μm below the original as-sintered surface, termed in the following sub-surface and bulk surface, respectively, were exposed. For the sample 50CF, both sub-surface and bulk surface were investigated, while for 70CF and 85CF, only the bulk surfaces were characterized.

The crystallographic structure of the as-sintered surface was characterized by X-ray diffraction (XRD) (Empyrean, Malvern Panalytical Ltd) for all composites. The instrument was equipped with a Cu long fine focus tube (40 kV / 40 mA), Bragg-BrentanoHD mirror (divergence = 0.4°), and PIXcel3D detector (1D-mode, active length = 3.35° , 255 channels). For sample 50CF, additionally sub-surface and bulk surface were characterized.

Microstructures were assessed by scanning electron microscopy (SEM) (Merlin, Carl Zeiss Microscopy, Oberkochen, Germany). The porosity was estimated as the area fraction of pores using the software ImageJ [54].

The residual stresses (σ_r) within individual phases at different surfaces, including the as-sintered and bulk surfaces of all composites (i.e. 50CF, dwelled-50CF, 70CF, and 85CF) and the sub-surface of 50CF, were determined by XRD based on the $\sin^2 \psi$ method [55]. The diffraction peaks at high 2θ angles ($>85^\circ$) were recorded providing sufficient intensity for analysis using a Philips MRD Pro diffractometer with Cr-K α (35 kV / 50 mA) radiation. Lattice spacings (d) of crystal planes CGO(311), FCO(440), GCFCO(133) and CoO(220) were derived based on the diffraction peaks obtained at different angles (ψ). For a crystal plane experiencing a uniform stress state, the lattice d-spacing (d) is in general approximately linearly proportional to $\sin^2 \psi$ [55]. The σ_r value was calculated for the different crystal planes representing the residual stress in the individual phases [55]:

$$\sigma_r = \frac{E}{\nu + 1} \cdot \frac{1}{d_{ref}} \cdot \frac{\partial d_\psi}{\partial \sin^2 \psi} \quad (6.1)$$

where E and ν are elastic moduli and Poisson's ratios; d_ψ is lattice spacing measured with an inclined angle of ψ , d_{ref} the lattice spacing in a stress-free sample as a reference. Assuming that the lattice of a phase exhibits isotropic elasticity, the E value of the investigated crystal plane was estimated to be equal to the average E values determined from nano-indentation of individual grains, as described in our previous work [48]. The ν was assumed to be 0.3, which is a typical value of ceramics [56].

The indentation method was applied to estimate the average residual stresses at the as-sintered surfaces for 50CF and dwelled-50CF [57]. Assuming that the indentation crack is shorter than the thickness of the layer exhibiting a residual stress gradient, Vickers indentations at loads of 0.245 N and 1 N were imprinted using a macro indentation machine (Micromet® 1, Buehler Ltd). At each load, five indentations with a distance of 500 μm in-between were conducted while avoiding obvious microstructural defects, e.g. pores and microcracks. The stress intensity (K_C) of indentations for a c/a value greater than 2.5 (a and c are half-diagonal and crack length of the indent, respectively) was calculated by [40]:

$$K_C = 0.016 \cdot \left(\frac{E}{H}\right)^{0.5} \cdot \left(\frac{P}{c}\right)^{1.5} \quad (6.2)$$

where E and H are elastic modulus and hardness, respectively, as taken from our previous work [48], and P is the indentation load.

The K_C obtained at a stress-free surface can be considered to be equal to the fracture toughness (K_{IC}), while K_C derived at a surface experiencing residual stress is composed of two terms [57]:

$$K_C = K_{IC} - K_{res} \quad (6.3)$$

where K_{res} represents the stress intensity for a crack in the residual stress field, given by [57]:

$$K_{res} = Y \cdot \sigma_r \cdot \sqrt{c} \quad (6.4)$$

where Y is the stress intensity factor with a value approximately equal to $1.12\sqrt{\pi}$ for a half-penny shaped crack [58, 59].

The fracture strength, i.e. being in the current work defined as the average fracture stress, was determined by ring-on-ring bending tests using an electromechanical testing machine (Instron 1362, Lebow Ltd) following the general procedure outlined in ASTM C1499-05 [60]. Either the as-sintered surface or the bulk surface was in tension during the test. Loading and supporting rings with diameters of 3.43 and 9.99 mm, respectively, were used. The stress rate was 20 MPa/s [49]. Five as-sintered specimens were tested for each composite. To test with the bulk surface in tension, five as-sintered 50CF discs were ground and polished at one side to obtain bulk surfaces. The specimen thickness after the surface layer removal was less uniform than before (the average standard deviation of all specimens was $\sim 29 \mu\text{m}$). Hence, the fracture stress of each ground and polished 50CF was calculated using the smallest and largest thickness measured within the effectively tested area. The fracture stress (σ_f) was derived from equation (6.5) [40, 49, 60], and averaged for each composite.

$$\sigma_f = \frac{3F}{2\pi \cdot t^2} \cdot \left[(1 - \nu) \cdot \frac{r_s^2 - r_l^2}{2r_p^2} + (1 + \nu) \cdot \ln \frac{r_s}{r_l} \right] \quad (6.5)$$

where F is the fracture force; r is the radii, t the thickness; subscripts s , l , and p denote the support ring, loading ring, and the tested disc, respectively.

The fracture surfaces were investigated using SEM to reveal the likely fracture origins. The measured fracture origin size (C), i.e. the equivalent radius of circular/semicircular origin or minor axis length of elliptical/semielliptical origin, was compared with the values estimated by [40, 49]:

$$\sqrt{C} = \frac{K_{IC}}{Y \cdot \sigma} \quad (6.6)$$

where σ is the stress at the fracture origin. Several Y values for origins with different shapes, in addition to the Y value for a half-penny shaped crack (see also above), are given in ASTM C1322-15 [46].

6.3 Results and discussion

6.3.1 Microstructure

The microstructures of the as-sintered surface, the sub-surface and the bulk surface of 50CF as investigated by SEM are presented in Figure 6.1. The different phases can be distinguishable by the different greyscale level. According to our previous electron backscatter diffraction phase mapping studies on the same composite with an identical microstructure, a CoO rock salt phase existed in the bulk of the sintered 50CF [48]. This CoO cannot be distinguished with the FCO phase due to a similar contrast in the BSEM micrographs [48]. Apparently, a longer time is needed for the large amount of CoO rock salt phase in the bulk of 50CF to oxidize into the spinel during cooling, while the oxidization of the CoO rock salt phase can be completed at the surface upon exposure to the excess oxygen in air [49]. As confirmed by XRD diffractions (see Figure A6.1), the CoO only exists in the sub-surface and bulk surface regions of 50CF, while CGO, FCO and GCFCO can be found in all surfaces. Thus, the black grains at the as-sintered surface, as shown in Figure 6.1(a), are FCO spinel grains, while the ones at the sub-surface and bulk surface, as shown in Figure 6.1(b,c), can be either CoO or FCO grains. The incomplete oxidization of CoO indicates oxygen deficiency within the bulk of 50CF. The grey and light grey grains in the bulk of the composites are CGO and GCFCO grains, respectively (see Figure 6.1(b,c)) [39,40]. However, CGO and GCFCO grains cannot be distinguished at the as-sintered surfaces. No significant phase composition variations across the discs are observed. Furthermore, a considerable number of long microcracks were observed at the as-sintered surface of 50CF (see Figure 6.1(a)), which possibly also propagate towards the sub-surface (see Figure 6.1(b)) and are not visible anymore at the bulk surface (see Figure 6.1(c)).

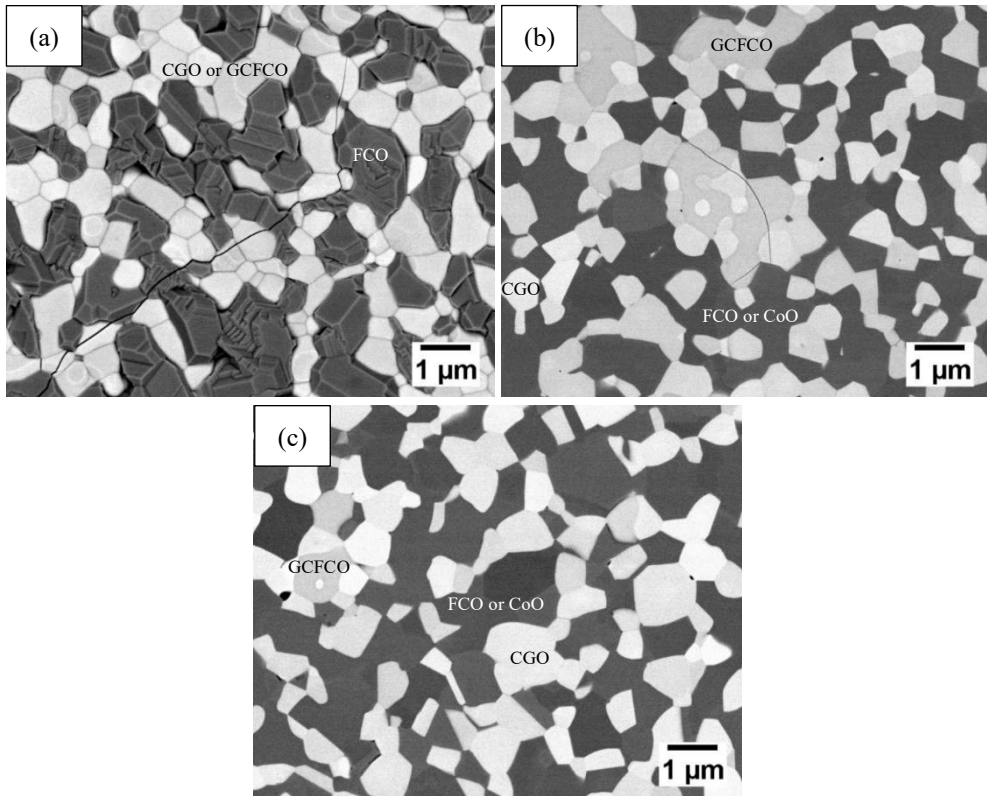


Figure 6.1 BSEM micrographs of (a) the as-sintered surface, (b) the sub-surface, and (c) the bulk surface of 50CF.

For 70CF and 85CF, it was reported that the CoO phase did not residual in the bulk after sintering [48]. Hence, the black grains at the as-sintered and bulk surfaces, as shown in Figure 6.2 for 85CF as examples, are FCO spinel grains. Besides, 70CF and 85CF appear to be free of microcracks for both the as-sintered and bulk surfaces, as, e.g. shown in Figure 6.2 for 85CF. The individual phases in 70CF and 85CF show no significant volume variations regarding phase content across the sintered discs.

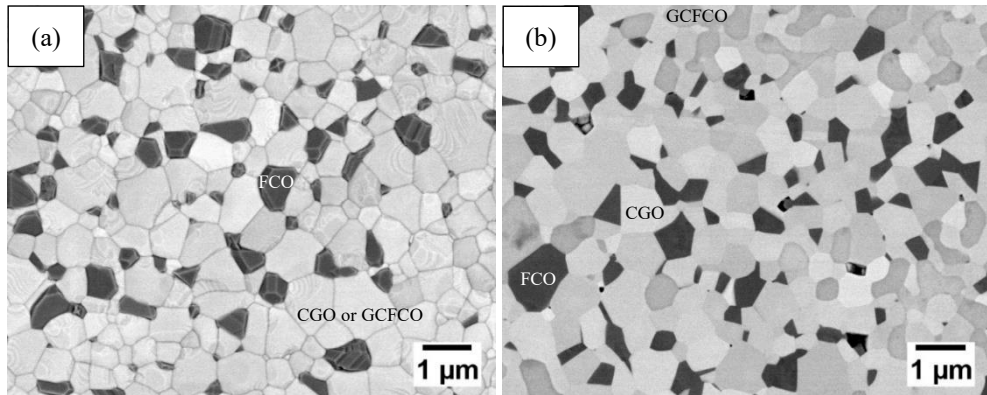


Figure 6.2 BSEM micrographs of (a) the as-sintered surface, and (b) the bulk surface of 85CF.

For dwelled-50CF, no microcracks are visible at the as-sintered and bulk surface, as illustrated in Figure 6.3. Furthermore, the CoO phase in the bulk is fully oxidized into the spinel phase, as confirmed by the XRD patterns (see Figure A6.1).

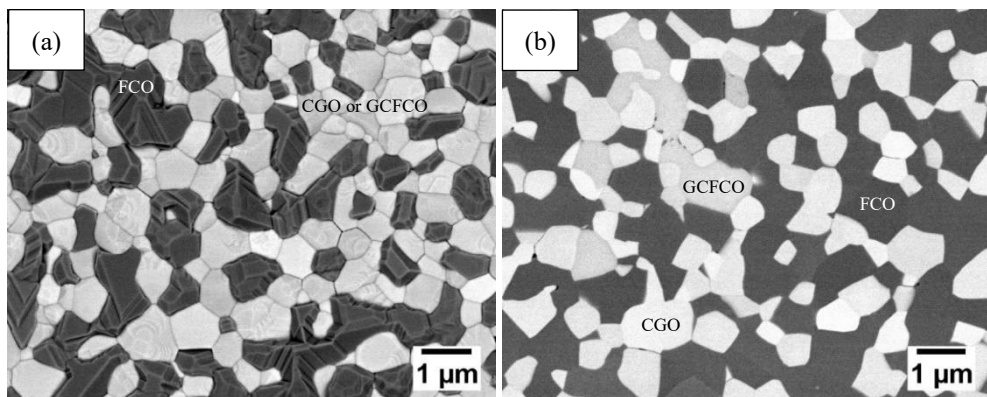


Figure 6.3 BSEM micrographs of (a) the as-sintered surface, and (b) the bulk surface of dwelled-50CF.

6.3.2 Lattice constants

The lattice constants of CGO, GCFCO and CoO as obtained at the as-sintered and bulk surfaces are compared in the following for all composites, while it was not

possible to determine one lattice constant for FCO due to the variation of the cobalt-to-iron ratios of FCO [48].

For 50CF, the lattice constants of CGO and GCFCO in the bulk are slightly larger than the one at the as-sintered surface (see Figure 6.4 and Table A6.1). The different lattice constants might indicate differences in the oxygen stoichiometry. The lower oxygen stoichiometry in CGO and GCFCO are possibly caused by an oxygen deficiency within the bulk of 50CF, as supported by the existence of the CoO phase that did not oxidize into the spinel during cooling.

For 70CF and 85CF, the lattice constants of CGO and GCFCO share similar values at the as-sintered and bulk surfaces (see Figure 6.4 and Table A6.1). However, according to our previous work on 85CF containing larger FCO grains [49], the lattice constant of CGO is marginally larger in the bulk than at the as-sintered surface. This indicates that differences in the lattice constant of CGO over the cross section of 85CF cannot be observed due to the reduced grain size of FCO.

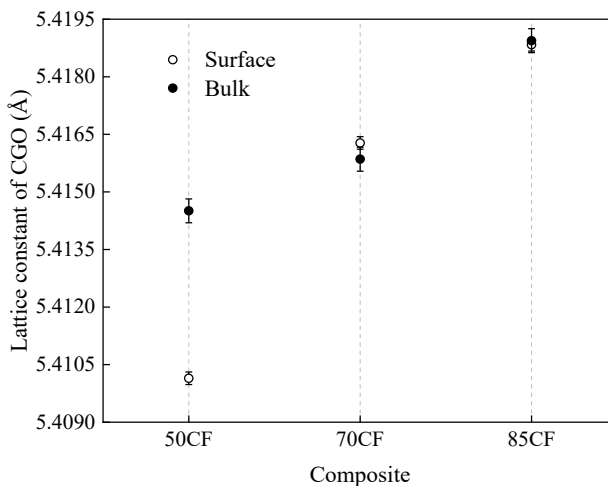


Figure 6.4 Lattice constants of CGO at the as-sintered and in bulk surfaces of the different composites.

For dwelled-50CF, the lattice constants of CGO are almost identical ($\sim 5.412 \text{ \AA}$) at the as-sintered and the bulk surfaces, as shown in Figure A6.1. And the CoO appears to be absent within the bulk. Therefore, the potential oxygen stoichiometry deviations across the sample can be smoothed out after the dwelling step.

6.3.3 Residual stress

6.3.3.1 XRD

For 50CF, at the as-sintered surface, the lattice spacings of CGO(311) and FCO(440) exhibit a linear dependency on $\sin^2 \psi$, as shown in Figure 6.5. Residual tensile stresses were determined from the corresponding positive slopes according to equation (6.1). Due to the low intensity of the associated diffraction peaks, it was not possible to directly assess the residual stress associated with the GCFCO phase. Note, the GCFCO phase, with a volume fraction of only $\sim 6 \text{ vol\%}$, distributes as isolated islands surrounded by the other phases [61], and it possesses a thermal expansion coefficient comparable to that of CGO and/or FCO ($\sim 12 \times 10^{-6} \text{ K}^{-1}$) [49]. Hence, the GCFCO phase is expected also to exhibit residual tensile stress. Therefore, it can be concluded that the entire as-sintered surface exhibits a residual tensile stress. By contrast, at the sub-surface, measured d values of CGO(311) and FCO(440) are almost independent of $\sin^2 \psi$ values (see Figure A6.2), suggesting an almost stress-free state of the sub-surface. At the bulk surface, the d of CGO(311) decreases with $\sin^2 \psi$ values; the linear fitting yields a negative slope with relatively large uncertainty, which corresponds to a small compressive stress value (see Figure 6.6). The d values of FCO(440) and CoO(220) are almost independent of $\sin^2 \psi$ values (see Figure A6.3), suggesting a stress-free state for the sub-surface in FCO and CoO. Since the content of CGO in 50CF is lower than 50 vol% [48], the average stress in the bulk surface of 50CF appears to be negligible. Therefore, it can be concluded that a residual stress gradient across the 50CF disc exists, which can be attributed to differences in lattice shrinkage at the surface and in the bulk. The lattice shrinkage during cooling can be expected to be more pronounced at the surface than in the bulk,

since more oxygen vacancies are present in the bulk than at the surface after sintering. This is indeed supported by our investigations showing that the lattice constant of CGO and GCFCO is greater in the bulk than at the as-sintered surface (see Figure 6.4 and Table A6.1).

For 70CF, d of CGO(311) and FCO(440) at the as-sintered surface slightly increase with $\sin^2 \psi$ values in a nonlinear manner (see Figure 6.5), suggesting an almost stress-free as-sintered surface [55].

For 85CF, it has been difficult to analyze the residual stress of the FCO phase due to the low intensity of the diffraction peaks, the peak broadening, and the overlapping induced by the variation of Co-to-Fe ratio [49]. However, the diffraction peaks of CGO and GCFCO exhibited sufficient intensities for residual stress analysis. At the as-sintered surface, as can be seen from Figure 6.5(a), a linear dependency of d on $\sin^2 \psi$ values is observed for CGO(311) in 85CF being an indication of a relatively small residual compressive stress. This small compressive stress was confirmed by another set of XRD measurements for CGO(331) yielding a compressive stress value of $\sim 74 \pm 4$ MPa, as shown in Figure A6.4(a). Note, in Figure A6.4(b), the lattice spacings of GCFCO(133) decrease with increasing $\sin^2 \psi$ values in a nonlinear manner, indicating a rather inhomogeneous strain distribution among the GCFCO grains. At the bulk surface, as revealed in Figure 6.6, the linear dependency of d on $\sin^2 \psi$ for CGO(311) yields a residual compressive stress value that is comparable to the one measured at the as-sintered surface (see Figure 6.5(a)). This observation was confirmed by a second measurement for CGO(331) also indicating a compressive stress value of $\sim 53 \pm 1$ MPa (see Figure A6.5). Thus, the CGO across the sintered 85CF disc experiences a rather uniform compressive stress state, indicating that no residual stress gradient exists. After a thermal annealing using the sintering program described above, CGO (311) at the bulk surface of 85CF experiences a residual compressive stress of $\sim 63 \pm 3$ MPa (see Figure A6.6). Hence, the thermal annealing has not alleviated the residual compressive stress.

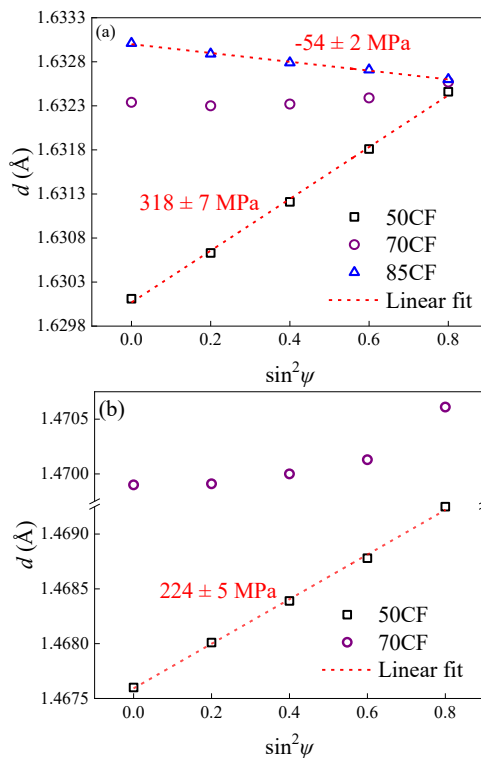


Figure 6.5 Dependencies of d on $\sin^2 \psi$ values and residual stresses derived for (a) CGO(311) and (b) FCO(440) at the as-sintered surfaces. The residual stresses were determined from equation (6.1).

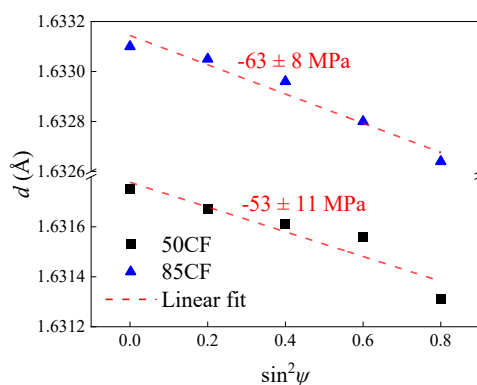


Figure 6.6 Dependencies of d on $\sin^2 \psi$ values and residual stresses derived for CGO(311) at the bulk surfaces. The residual stresses were determined from equation (6.1).

For dwelled-50CF, the residual tensile stresses in CGO(311) and FCO(440) at the as-sintered surface are much lower than the ones at the as-sintered surface of the initial 50CF (see Figure 6.7). This suggests that the residual tensile stress of 50CF is reduced but not eliminated by the dwelling step.

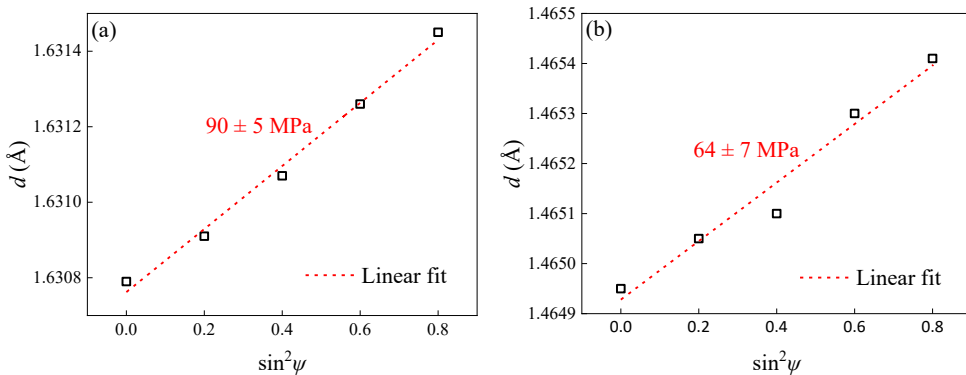


Figure 6.7 Dependencies of d on $\sin^2\psi$ values derived for (a) CGO(311), and (b) FCO(440) at the as-sintered surface of dwelled-50CF. The residual stresses were determined from equation (6.1).

6.3.3.2 Indentation method

Since the average penetration depth of X-rays exceeds a few microns [62], the XRD method yielded residual stress values averaged over a thin surficial layer. Both 50CF and dwelled-50CF exhibited an apparent residual stress gradient, which was further complementary investigated by imprinting indentations to different depths. The presence of residual stress will affect the indentation crack extensions within a material layer. Residual stress values can be estimated from the differences between stress intensities with and without the influence of the residual stress (as can be seen from equation (6.3, 6.4)).

The indentation induced crack lengths were firstly measured for the bulk surfaces, and the obtained indentation stress intensity (see Table 6.1) can be regarded as a representation of the fracture toughness due to the negligible residual stress.

At the bulk surface of 50CF, well-defined indentations with ideal crack profiles are obtained after the application of a load of 1 N (see Figure 6.8(a)), and the c/a value was larger than 2.5 indicating a half-penny shaped crack (length equals to depth) [63, 64]. Accordingly, the fracture toughness was derived to be $\sim 0.82 \pm 0.03 \text{ MPa}\cdot\text{m}^{0.5}$ (see Table 6.1). For indentation loads of 0.245 N, cracks could hardly be generated (see Figure A6.7(a)). According to our previous study on the stress-free 50CF with large grains, the indentation fracture toughness with a value of $\sim 0.88 \pm 0.11 \text{ MPa}\cdot\text{m}^{0.5}$ at 1 N is almost independent of the indentation load for this type of material [49]. Thus, the expected fracture toughness obtained at 0.245 and 1 N should be equal. Furthermore, indentation cracks, as shown in Figure 6.8 and Figure A6.7, exhibit a mainly transgranular mode with limited deflections along the grains, indicating that similar stress intensities can be expected for different grains.

At the bulk surfaces of 70CF and 85CF, the obtained fracture toughness values were comparable with those obtained at the bulk surface of 50CF (see Table 6.1). The fracture toughness appears to be independent of the composition, indicating that the apparent compressive stress in CGO in 50CF and 85CF (see Figure 6.6) has a limited influence on the fracture toughness.

Table 6.1 Indentation stress intensities (apparent fracture toughness) derived for the bulk surfaces.

Composite	$K_C (\approx K_{IC})$ ($\text{MPa}\cdot\text{m}^{0.5}$)	Reference
50CF	0.82 ± 0.03	This work
70CF	0.81 ± 0.03	
85CF	0.86 ± 0.06	[40]

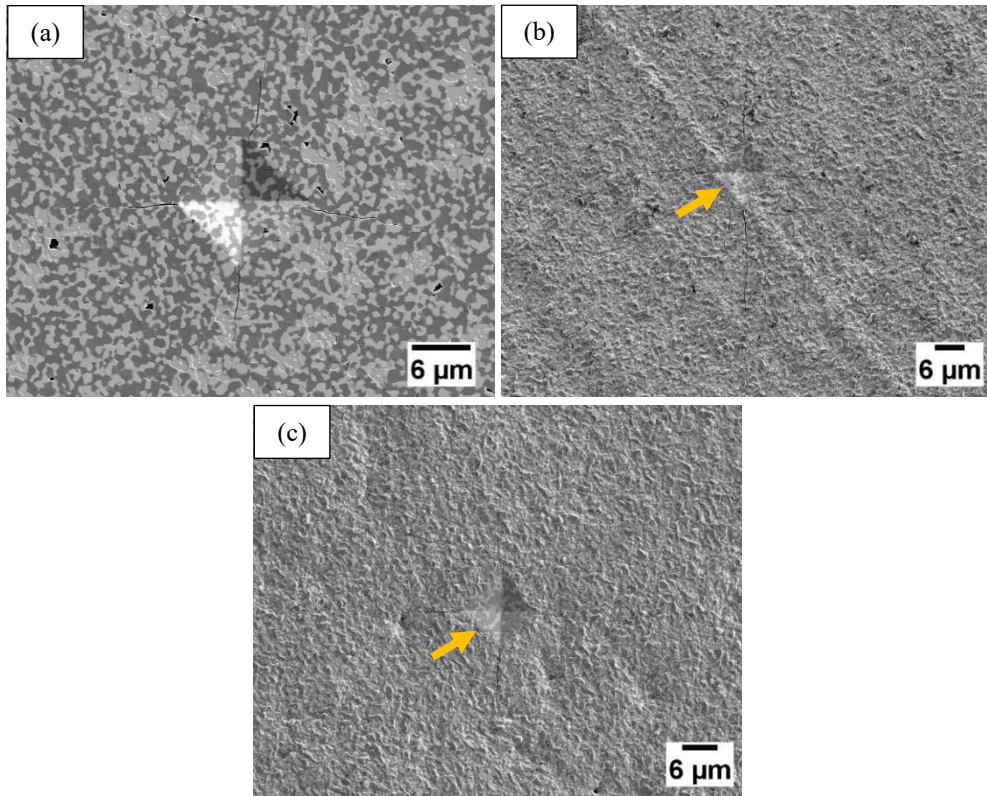


Figure 6.8 Vickers indentations at a load of 1N imaged by SEM on the (a) bulk surface of 50CF, (b) as-sintered surface of 50CF, and (c) as-sintered surface of dwell-50CF. Imprints in (b) and (c) are marked by arrows. It should be noted that the scale bars are different.

Into the as-sintered surface of 50CF and dwell-50CF, imprints with well-defined crack profiles were induced by both loads (see Figure 6.8(b) and Figure A6.7), from which low indentation stress intensity values were calculated (see Table 6.2).

For the as-sintered surface of 50CF, the indentation stress intensity appears to be independent of the indentation load and is significantly lower than the fracture toughness value measured at the bulk surface of 50CF (see Table 6.1), indicating the significant contribution of the residual tensile stress. The residual tensile stress calculated from indentations at 0.245 N is marginally higher than the one for indentation at 1 N considering the experimental uncertainties (see Table 6.2).

Compared to the residual tensile stress values obtained from the XRD method (see Figure 6.5), the stress values from the indentation method are much lower. This can probably be associated with the presence of the stress gradient, which implies that the indentation method reflects the effect of a stressed layer that is thicker than the one directly measured by the XRD method. As the indentation cracks induced by 1 N (resulting in a crack depth of $\sim 45 \pm 4 \mu\text{m}$) are longer than the extend of the almost stress-free sub-surface region ($\sim 30 \mu\text{m}$), the residual tensile stress value derived by indentation at 1 N can be regarded as an average stress value over the whole stressed layer. The apparent indentation crack depth induced by 0.245 N ($\sim 18 \pm 4 \mu\text{m}$), however, is shorter than $\sim 30 \mu\text{m}$, but still exceeds the penetration depth of X-rays. The residual stress value from indentations at 0.245 N reflects the average residual tensile stress of a section of the stressed layer.

Table 6.2 Indentation stress intensities and residual stresses determined for the as-sintered surfaces of 50CF and dwelled 50CF.

Sample	K_C (MPa·m ^{0.5})		Residual stress (MPa)	
	0.245 N	1 N	0.245 N	1 N
50CF	0.24 ± 0.07	0.23 ± 0.03	69 ± 17	44 ± 6
Dwelled 50CF	0.69 ± 0.06	0.66 ± 0.05	21 ± 12	18 ± 7

For the as-sintered surface of dwelled-50CF, the indentation stress intensity is again independent of the indentation load (see Table 6.2). The values are significantly larger than the ones obtained for the as-sintered surface of 50CF, but slightly lower than the fracture toughness value determined for the bulk surface of 50CF (see Table 6.1). The apparent indentation crack depths induced by 0.245 N and 1 N are $\sim 8 \pm 1 \mu\text{m}$ and $\sim 22 \pm 1 \mu\text{m}$, respectively. The calculated apparent residual tensile stresses are rather small and independent of the indentation load when the uncertainties are considered (see Table 6.2), and again lower than the residual tensile stresses obtained from XRD (see Figure 6.7). This suggests that the apparent indentation crack depth

induced by the minimum load of 0.245 N used in the current study is already sufficient to reflect the effect of the average residual tensile stress within the entire stressed layer.

6.3.4 Strength and fractography

For composites that were broken via the ring-on-ring test with the as-sintered surfaces in tension, the average fracture stress (strength) increases with increasing CGO content (see Figure 6.9). The 50CF possesses the lowest average fracture stress, which might be a result of the rather long microcracks existing in this material (see Figure 6.1(b)), as well as the rather high residual tensile stress (see Figure 6.4).

When compared with the fracture stress values of other typical single-phase oxygen transport membranes, e.g. $\text{Ba}_{0.5}\text{Sr}_{0.5}\text{Co}_{0.8}\text{Fe}_{0.2}\text{O}_{3-\delta}$ (~ 100 MPa) [65], $\text{La}_{0.58}\text{Sr}_{0.4}\text{Co}_{0.2}\text{Fe}_{0.8}\text{O}_{3-\delta}$ (~ 94 MPa) [66] and $\text{SrTi}_{0.65}\text{Fe}_{0.35}\text{O}_{3-\delta}$ (~ 117 MPa) [58], which were determined using similar specimens, the average fracture stress of 50CF is lower, while the average fracture stress of 85CF is significantly higher.

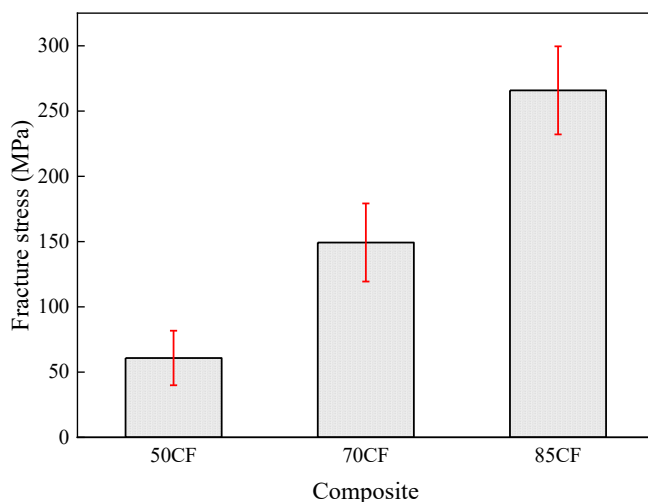


Figure 6.9 Average fracture stresses of composites determined for the as-sintered surfaces. The average fracture stress of 85CF has been taken from our previous work [40].

The likely fracture origins were assessed by SEM investigation on the fractured surfaces of tested samples with the lowest fracture stresses. As reported for 85CF fractured with the as-sintered surface in tension, the fracture appears to initiate from small surface-located flaws, whose sizes are comparable with the ones estimated by equation (6.6) [40]. For 50CF and 70CF with the as-sintered surfaces in tension, surface-located flaws were also characterized as the likely fracture origins, as shown in Figure 6.10 (a, b). The likely fracture origin presented in Figure 6.10(a) noticeably possesses a depth that is close to the length of the microcracks shown in Figure 6.1(a), which supports that fracture can initiate from such microcracks.

The measured sizes of the likely fracture origins are summarized in Table 6.3. For comparison, the size of the fractured origins was also estimated using equation (6.6). It is assumed that the maximum stress acting at the critical defect is equal to the maximum stress applied externally during the ring-on-ring bending test, i.e. the calculated fracture stress, and that the residual stress is not contributive. For 70CF, the measured size is almost identical to the estimated one, suggesting that the sample is almost free of any effect related to internal residual stress superimposed on the calculated fracture stress.

For 50CF fractured with the as-sintered surfaces in tension, however, the measured size of the likely fracture origin is significantly smaller than the estimated ones. The stresses used for estimating the fracture origin size might therefore be underestimated because the contribution of residual stress is not considered. Since the measured size of the likely fracture origin is close to the depth of the indentation induced crack at 0.245 N ($\sim 18 \pm 4 \mu\text{m}$), the average residual stress obtained from indentations at 0.245 N (see Table 6.2) is included in the calculation of fracture origin size so that the stress at the fracture origin is corrected to be equal to the sum of the internal stress (average residual stress of $\sim 69 \text{ MPa}$) and the maximum applied external stress (fracture stress of $\sim 40 \text{ MPa}$). The fracture origin obtained by this adjusted stress value, of $\sim 109 \text{ MPa}$, is $\sim 14 \mu\text{m}$, which is almost equal to the measured fracture origin size (see Table 6.3). This confirms the significant influence

of the residual stress on strength, which is probably a result of the fracture origin size being comparable to the thickness of the stressed layer.

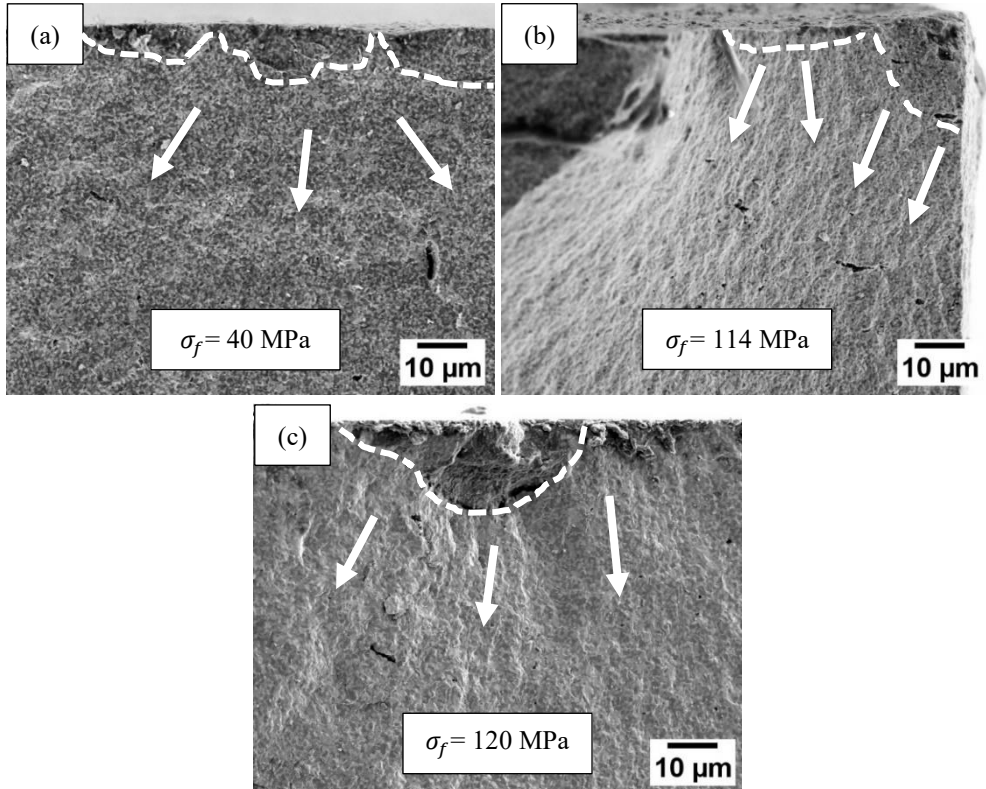


Figure 6.10 Fracture surfaces (SEM) of (a) 50CF, (b) 75CF fractured at the as-sintered surfaces, and (c) 50CF fractured at the bulk surface. Samples exhibiting the lowest fracture stresses are shown. The dashed lines represent the likely boundaries of the fracture origins. The fracture lines are indicated by the arrows.

Table 6.3 Estimated and measured fracture origin sizes.

Composite	Fractured surface	$\sigma = \sigma_f$ (MPa)	Y [46]	C (μm)		Reference
				Estimated	Measured	
50CF	As-sintered	40	1.99	107	14	This work
	Bulk	120	1.39	24	20	
70CF	As-sintered	114	1.39	26	27	
85CF	As-sintered	212	1.99	4	2	[40]

To further confirm the reduction of the apparent fracture stress through the presence of residual tensile stresses, the fracture stress of 50CF for the almost stress-free bulk surfaces was measured and determined to be $\sim 151 \pm 31$ MPa, which is significantly higher than the fracture strength of 50CF measured for the as-sintered surface ($\sim 61 \pm 21$ MPa). The likely fracture origins were surface located (see Figure 6.10(c)). The fracture origin size, measured for the sample with the lowest fracture stress is ~ 20 μm (see Table 6.2), which is close to the one estimated without consideration of the residual stress. Hence, no significant contribution from the residual stresses on the fracture stress has been observed. The bulk surface can be considered free of residual stress, which agrees well with the XRD results (see Figure 6.6 and Figure A6.3). Thus, the fracture stress is only determined by the maximum tolerable stress intensity induced by the externally applied stress at the flaws located at the surface.

For the disc-shaped 50CF membrane, it appears to be an effective way to enhance the strength by removing the layer with residual tensile stress and microcracks, however, this is not practical for a large membrane component or a nonplanar, e.g. tubular, membrane component.

6.4 Conclusions

The apparent mechanical strengths (i.e. average fracture stresses) of $\text{Ce}_{0.8}\text{Gd}_{0.2}\text{O}_{2-\delta}$ - FeCo_2O_4 membrane materials, as determined from ring-on-ring tests, increase as a function of the nominal fractions of $\text{Ce}_{0.8}\text{Gd}_{0.2}\text{O}_{2-\delta}$ content in the starting powder. The low strength of 50CF specimens appears to be a result of the presence of microcracks within the as-sintered surface that act as fracture origins, as well as high residual tensile stress that gradually decreases from the as-sintered surface to the bulk. This residual tensile stress gradient, as determined by X-ray diffraction and indentation, is likely caused by an oxygen stoichiometry variation between the surface and bulk material. The fracture stress of 50CF is reduced significantly by the residual tensile stress since the likely fracture origins are located within the residual stress gradient zone. After removal of the material layer with residual tensile stress and microcracks, the fracture stress of 50CF is significantly improved. Besides, the residual tensile stress within the as-sintered surface of 50CF is successfully reduced by applying an extended dwelling step during cooling. However, it is recommended to limit the iron-cobalt spinel content to a nominal value of 15 wt% to eliminate the residual tensile stress and obtain a membrane with small surface defects, thus, yielding a material with high mechanical strength.

References

- [1] P. Niehoff, F. Schulze-Kueppers, S. Baumann, W.A. Meulenberg, O. Guillon, R. Vassen, Fabrication of laboratory-scale planar oxygen separation membrane modules, *American Ceramic Society Bulletin* 94(1) (2015) 28-31.
- [2] K. Zhang, J. Sunarso, Z. Shao, W. Zhou, C. Sun, S. Wang, S. Liu, Research progress and materials selection guidelines on mixed conducting perovskite-type ceramic membranes for oxygen production, *RSC Advances* 1(9) (2011) 1661-1676.
- [3] H. Wang, S. Werth, T. Schiestel, J. Caro, Perovskite hollow-fiber membranes for the production of oxygen-enriched air, *Angewandte Chemie International Edition* 44(42) (2005) 6906-6909.

- [4] H.J. Bouwmeester, Dense ceramic membranes for methane conversion, *Catalysis Today* 82(1-4) (2003) 141-150.
- [5] M.T. Ravanchi, T. Kaghazchi, A. Kargari, Application of membrane separation processes in petrochemical industry: a review, *Desalination* 235(1-3) (2009) 199-244.
- [6] W. Deibert, M.E. Ivanova, S. Baumann, O. Guillon, W.A. Meulenberg, Ion-conducting ceramic membrane reactors for high-temperature applications, *Journal of Membrane Science* 543 (2017) 79-97.
- [7] H. Stadler, F. Beggel, M. Habermehl, B. Persigehl, R. Kneer, M. Modigell, P. Jeschke, Oxyfuel coal combustion by efficient integration of oxygen transport membranes, *International Journal of Greenhouse Gas Control* 5(1) (2011) 7-15.
- [8] M. Ramasamy, Dual phase oxygen transport membrane for efficient oxyfuel combustion, PhD thesis, Bochum University, Bochum, Germany, 2016.
- [9] X. Zhu, H. Liu, Y. Cong, W. Yang, Novel dual-phase membranes for CO₂ capture via an oxyfuel route, *Chemical Communications* 48(2) (2012) 251-253.
- [10] S. Baumann, J. Serra, M. Lobera, S. Escolástico, F. Schulze-Küppers, W.A. Meulenberg, Ultrahigh oxygen permeation flux through supported Ba_{0.5}Sr_{0.5}Co_{0.8}Fe_{0.2}O_{3-δ} membranes, *Journal of Membrane Science* 377(1-2) (2011) 198-205.
- [11] J.M. Serra, J. Garcia-Fayos, S. Baumann, F. Schulze-Küppers, W.A. Meulenberg, Oxygen permeation through tape-cast asymmetric all-La_{0.6}Sr_{0.4}Co_{0.2}Fe_{0.8}O_{3-δ} membranes, *Journal of Membrane Science* 447 (2013) 297-305.
- [12] M. Arnold, H. Wang, A. Feldhoff, Influence of CO₂ on the oxygen permeation performance and the microstructure of perovskite-type (Ba_{0.5}Sr_{0.5})(Co_{0.8}Fe_{0.2})O_{3-δ} membranes, *Journal of Membrane Science* 293(1-2) (2007) 44-52.
- [13] A. Waindich, A. Möbius, M. Müller, Corrosion of Ba_{1-x}Sr_xCo_{1-y}Fe_yO_{3-δ} and La_{0.3}Ba_{0.7}Co_{0.2}Fe_{0.8}O_{3-δ} materials for oxygen separating membranes under Oxycoal conditions, *Journal of Membrane Science* 337(1-2) (2009) 182-187.
- [14] J. Gao, L. Li, Z. Yin, J. Zhang, S. Lu, X. Tan, Poisoning effect of SO₂ on the oxygen permeation behavior of La_{0.6}Sr_{0.4}Co_{0.2}Fe_{0.8}O_{3-δ} perovskite hollow fiber membranes, *Journal of Membrane Science* 455 (2014) 341-348.
- [15] T. Ramirez-Reina, J.L. Santos, N. García-Moncada, S. Ivanova, J.A. Odriozola, Development of Robust Mixed-Conducting Membranes with High Permeability and Stability, Perovskites and Related Mixed Oxides (2016) 719-738.

- [16] S. Engels, T. Markus, M. Modigell, L. Singheiser, Oxygen permeation and stability investigations on MIEC membrane materials under operating conditions for power plant processes, *Journal of Membrane Science* 370(1-2) (2011) 58-69.
- [17] M. Schulz, R. Kriegel, A. Kämpfer, Assessment of CO₂ stability and oxygen flux of oxygen permeable membranes, *Journal of Membrane Science* 378(1-2) (2011) 10-17.
- [18] X. Tan, N. Liu, B. Meng, J. Sunarso, K. Zhang, S. Liu, Oxygen permeation behavior of La_{0.6}Sr_{0.4}Co_{0.8}Fe_{0.2}O₃ hollow fibre membranes with highly concentrated CO₂ exposure, *Journal of Membrane Science* 389 (2012) 216-222.
- [19] S.J. Benson, D. Waller, J.A. Kilner, Degradation of La_{0.6}Sr_{0.4}Fe_{0.8}Co_{0.2}O_{3-δ} in Carbon Dioxide and Water Atmospheres, *Journal of the Electrochemical Society* 146(4) (1999) 1305.
- [20] M. Ramasamy, E. Persoon, S. Baumann, M. Schroeder, F. Schulze-Küppers, D. Görtz, R. Bhave, M. Bram, W.A. Meulenberg, Structural and chemical stability of high performance Ce_{0.8}Gd_{0.2}O_{2-δ}-FeCo₂O₄ dual phase oxygen transport membranes, *Journal of Membrane Science* 544 (2017) 278-286.
- [21] H. Luo, K. Efimov, H. Jiang, A. Feldhoff, H. Wang, J. Caro, CO₂-stable and cobalt-free dual-phase membrane for oxygen separation, *Angewandte Chemie International Edition* 50(3) (2011) 759-763.
- [22] H. Luo, H. Jiang, K. Efimov, F. Liang, H. Wang, J.r. Caro, CO₂-tolerant oxygen-permeable Fe₂O₃-Ce_{0.9}Gd_{0.1}O_{2-δ} dual phase membranes, *Industrial & Engineering Chemistry Research* 50(23) (2011) 13508-13517.
- [23] Z. Wang, W. Sun, Z. Zhu, T. Liu, W. Liu, A novel cobalt-free, CO₂-stable, and reduction-tolerant dual-phase oxygen-permeable membrane, *ACS applied materials & interfaces* 5(21) (2013) 11038-11043.
- [24] H. Cheng, N. Zhang, X. Xiong, X. Lu, H. Zhao, S. Li, Z. Zhou, Synthesis, Oxygen Permeation, and CO₂-Tolerance Properties of Ce_{0.8}Gd_{0.2}O_{2-δ}-Ba_{0.95}La_{0.05}Fe_{1-x}Nb_xO_{3-δ} Dual-Phase Membranes, *ACS Sustainable Chemistry & Engineering* 3(9) (2015) 1982-1992.
- [25] X. Zhu, Y. Liu, Y. Cong, W. Yang, Ce_{0.85}Sm_{0.15}O_{1.925}-Sm_{0.6}Sr_{0.4}Al_{0.3}Fe_{0.7}O₃ dual-phase membranes: One-pot synthesis and stability in a CO₂ atmosphere, *Solid State Ionics* 253 (2013) 57-63.
- [26] B. Wang, J. Yi, L. Winnubst, C. Chen, Stability and oxygen permeation behavior of Ce_{0.8}Sm_{0.2}O_{2-δ}-La_{0.8}Sr_{0.2}CrO_{3-δ} composite membrane under large oxygen partial pressure gradients, *Journal of Membrane Science* 286(1-2) (2006) 22-25.

- [27] S. Guo, Z. Liu, J. Zhu, X. Jiang, Z. Song, W. Jin, Highly oxygen-permeable and CO₂-stable Ce_{0.8}Sm_{0.2}O_{2-δ}-SrCo_{0.9}Nb_{0.1}O_{3-δ} dual-phase membrane for oxygen separation, *Fuel Processing Technology* 154 (2016) 19-26.
- [28] S.K. Kim, M.J. Shin, J. Rufner, K. van Benthem, J.H. Yu, S. Kim, Sr_{0.95}Fe_{0.5}Co_{0.5}O_{3-δ}-Ce_{0.9}Gd_{0.1}O_{2-δ} dual-phase membrane: Oxygen permeability, phase stability, and chemical compatibility, *Journal of Membrane Science* 462 (2014) 153-159.
- [29] S. Wang, T. Kobayashi, M. Dokiya, T. Hashimoto, Electrical and ionic conductivity of Gd-doped ceria, *Journal of the Electrochemical Society* 147(10) (2000) 3606-3609.
- [30] Y. Ji, J.A. Kilner, M.F. Carolan, Electrical conductivity and oxygen transfer in gadolinia-doped ceria (CGO)-Co₃O_{4-δ} composites, *Journal of the European Ceramic Society* 24(14) (2004) 3613-3616.
- [31] V. Kharton, A. Kovalevsky, A. Viskup, A. Shaula, F. Figueiredo, E. Naumovich, F. Marques, Oxygen transport in Ce_{0.8}Gd_{0.2}O_{2-δ}-based composite membranes, *Solid State Ionics* 160(3-4) (2003) 247-258.
- [32] A.J. Samson, M. Søgaaard, P.V. Hendriksen, (Ce,Gd)O_{2-δ}-based dual phase membranes for oxygen separation, *Journal of Membrane Science* 470 (2014) 178-188.
- [33] V.V. Kharton, A.V. Kovalevsky, A.P. Viskup, F.M. Figueiredo, A.A. Yaremchenko, E.N. Naumovich, F.M.B. Marques, Oxygen Permeability of Ce_{0.8}Gd_{0.2}O_{2-δ}-La_{0.7}Sr_{0.3}MnO_{3-δ} Composite Membranes, *Journal of the Electrochemical Society* 147(7) (2000) 2814-2821.
- [34] U. Nigge, H.D. Wiemhöfer, E.W.J. Römer, H.J.M. Bouwmeester, T.R. Schulte, Composites of Ce_{0.8}Gd_{0.2}O_{1.9} and Gd_{0.7}Ca_{0.3}CoO_{3-δ} as oxygen permeable membranes for exhaust gas sensors, *Solid State Ionics* 146(1-2) (2002) 163-174.
- [35] Y. Lin, S. Fang, D. Su, K.S. Brinkman, F. Chen, Enhancing grain boundary ionic conductivity in mixed ionic-electronic conductors, *Nature communications* 6 (2015) 6824.
- [36] J. Garcia-Fayos, M. Balaguer, J.M. Serra, Dual-Phase Oxygen Transport Membranes for Stable Operation in Environments Containing Carbon Dioxide and Sulfur Dioxide, *ChemSusChem* 8(24) (2015) 4242-4249.
- [37] H. Luo, H. Jiang, T. Klande, F. Liang, Z. Cao, H. Wang, J. Caro, Rapid glycine-nitrate combustion synthesis of the CO₂-stable dual phase membrane 40Mn_{1.5}Co_{1.5}O_{4-δ}-60Ce_{0.9}Pr_{0.1}O_{2-δ} for CO₂ capture via an oxy-fuel process, *Journal of Membrane Science* 423-424 (2012) 450-458.
- [38] C. Zhang, J. Sunarso, S. Liu, Designing CO₂-resistant oxygen-selective mixed ionic-electronic conducting membranes: guidelines, recent advances, and forward directions, *Chemical Society Reviews* 46(10) (2017) 2941-3005.

- [39] F. Zeng, J. Malzbender, S. Baumann, M. Krüger, L. Winnubst, O. Guillon, W.A. Meulenberg, Phase and microstructural characterizations for $\text{Ce}_{0.8}\text{Gd}_{0.2}\text{O}_{2-\delta}\text{-FeCo}_2\text{O}_4$ dual phase oxygen transport membranes, *Journal of the European Ceramic Society* 40(15) (2020) 5646-5652.
- [40] F. Zeng, J. Malzbender, S. Baumann, A. Nijmeijer, L. Winnubst, M. Ziegner, O. Guillon, R. Schwaiger, W.A. Meulenberg, Optimization of sintering conditions for improved microstructural and mechanical properties of dense $\text{Ce}_{0.8}\text{Gd}_{0.2}\text{O}_{2-\delta}\text{-FeCo}_2\text{O}_4$ oxygen transport membranes, *Journal of the European Ceramic Society* 41(1) (2021) 509-516.
- [41] P.-M. Geffroy, J. Fouletier, N. Richet, T. Chartier, Rational selection of MIEC materials in energy production processes, *Chemical Engineering Science* 87 (2013) 408-433.
- [42] S. Kim, S.H. Kim, K.S. Lee, J.H. Yu, Y.-H. Seong, I.S. Han, Mechanical properties of LSCF ($\text{La}_{0.6}\text{Sr}_{0.4}\text{Co}_{0.2}\text{Fe}_{0.8}\text{O}_{3-\delta}$)-GDC ($\text{Ce}_{0.9}\text{Gd}_{0.1}\text{O}_{2-\delta}$) for oxygen transport membranes, *Ceramics International* 43(2) (2017) 1916-1921.
- [43] T. Nithyanantham, S. Biswas, N. Nagendra, S. Bandopadhyay, Studies on mechanical behavior of LSFT-CGO dual-phase membranes at elevated temperatures in ambient air and slightly reducing environments, *Ceramics International* 40(6) (2014) 7783-7790.
- [44] S. Lia, W. Jin, N. Xu, J. Shi, Mechanical strength, and oxygen and electronic transport properties of $\text{SrCo}_{0.4}\text{Fe}_{0.6}\text{O}_{3-\delta}\text{-YSZ}$ membranes, *Journal of Membrane Science* 186(2) (2001) 195-204.
- [45] K. Raju, S. Kim, C.J. Hyung, J.H. Yu, Y.-H. Seong, S.-H. Kim, I.-S. Han, Optimal sintering temperature for $\text{Ce}_{0.9}\text{Gd}_{0.1}\text{O}_{2-\delta}\text{-La}_{0.6}\text{Sr}_{0.4}\text{Co}_{0.2}\text{Fe}_{0.8}\text{O}_{3-\delta}$ composites evaluated through their microstructural, mechanical and elastic properties, *Ceramics International* 45(1) (2019) 1460-1463.
- [46] ASTM, C1322-15: Standard practice for fractography and characterization of fracture origins in advanced ceramics, ASTM International, West Conshohocken, PA, 2010.
- [47] A. Lanin, Effect of residual stresses on the strength of ceramic materials, *Russian Metallurgy (Metally)* 2012(4) (2012) 307-322.
- [48] F. Zeng, J. Malzbender, S. Baumann, F. Schulze-Küppers, M. Krüger, A. Nijmeijer, O. Guillon, W.A. Meulenberg, Micromechanical Characterization of $\text{Ce}_{0.8}\text{Gd}_{0.2}\text{O}_{2-\delta}\text{-FeCo}_2\text{O}_4$ Dual Phase Oxygen Transport Membranes, *Advanced Engineering Materials* 22(6) (2020) 1901558.
- [49] F. Zeng, J. Malzbender, S. Baumann, W. Zhou, M. Ziegner, A. Nijmeijer, O. Guillon, R. Schwaiger, W.A. Meulenberg, Mechanical reliability of $\text{Ce}_{0.8}\text{Gd}_{0.2}\text{O}_{2-\delta}\text{-FeCo}_2\text{O}_4$ dual

phase membranes synthesized by one-step solid-state reaction, *Journal of the American Ceramic Society* (2020).

[50] P.J. Murray, J.W. Linnett, Mössbauer studies in the spinel system $\text{Co}_x\text{Fe}_{3-x}\text{O}_4$, *Journal of Physics and Chemistry of Solids* 37(6) (1976) 619-624.

[51] H. Bordeneuve, S. Guillemet-Fritsch, A. Rousset, S. Schuurman, V. Poulain, Structure and electrical properties of single-phase cobalt manganese oxide spinels $\text{Mn}_{3-x}\text{Co}_x\text{O}_4$ sintered classically and by spark plasma sintering (SPS), *Journal of Solid State Chemistry* 182(2) (2009) 396-401.

[52] M. Ramasamy, S. Baumann, J. Palisaitis, F. Schulze-Küppers, M. Balaguer, D. Kim, W.A. Meulenber, J. Mayer, R. Bhave, O. Guillon, Influence of Microstructure and Surface Activation of Dual-Phase Membrane $\text{Ce}_{0.8}\text{Gd}_{0.2}\text{O}_{2-\delta}\text{-FeCo}_2\text{O}_4$ on Oxygen Permeation, *Journal of the American Ceramic Society* 99(1) (2016) 349-355.

[53] Y. Zheng, J.M. Vieira, F.J. Oliveira, J.P. Davim, P. Brogueira, Relationship between flexural strength and surface roughness for hot-pressed Si_3N_4 self-reinforced ceramics, *Journal of the European Ceramic Society* 20(9) (2000) 1345-1353.

[54] C.A. Schneider, W.S. Rasband, K.W. Eliceiri, NIH Image to ImageJ: 25 years of image analysis, *Nature Methods* 9(7) (2012) 671-675.

[55] M.E. Fitzpatrick, A.T. Fry, P. Holdway, F.A. Kandil, J. Shackleton, L. Suominen, Determination of residual stresses by X-ray diffraction, National Physical Laboratory, Teddington, UK, 2005.

[56] A. Atkinson, A. Selcuk, Mechanical behaviour of ceramic oxygen ion-conducting membranes, *Solid State Ionics* 134(1-2) (2000) 59-66.

[57] J.E. Choi, J.N. Waddell, M.V. Swain, Pressed ceramics onto zirconia. Part 2: indentation fracture and influence of cooling rate on residual stresses, *Dental Materials* 27(11) (2011) 1111-1118.

[58] R.O. Silva, J. Malzbender, F. Schulze-Küppers, S. Baumann, O. Guillon, Mechanical properties and lifetime predictions of dense $\text{SrTi}_{1-x}\text{Fe}_x\text{O}_{3-\delta}$ ($x = 0.25, 0.35, 0.5$), *Journal of the European Ceramic Society* 37(7) (2017) 2629-2636.

[59] R. Bermejo, P. Supancic, C. Krautgasser, R. Morrell, R. Danzer, Subcritical crack growth in low temperature co-fired ceramics under biaxial loading, *Engineering Fracture Mechanics* 100 (2013) 108-121.

[60] ASTM, C1499-05: Standard test method for monotonic equibiaxial flexural strength of advanced ceramics at ambient temperature, ASTM International, West Conshohocken, PA, 2003.

- [61] W.M. Harris, K.S. Brinkman, Y. Lin, D. Su, A.P. Cocco, A. Nakajo, M.B. DeGostin, Y.-c.K. Chen-Wiegart, J. Wang, F. Chen, Characterization of 3D interconnected microstructural network in mixed ionic and electronic conducting ceramic composites, *Nanoscale* 6(9) (2014) 4480-4485.
- [62] K. Raju, S. Kim, J.H. Yu, S.-H. Kim, Y.-H. Seong, I.-S. Han, Rietveld refinement and estimation of residual stress in GDC-LSCF oxygen transport membrane ceramic composites, *Ceramics International* 44(9) (2018) 10293-10298.
- [63] G.R. Anstis, P. Chantikul, B.R. Lawn, D.B. Marshall, A critical evaluation of indentation techniques for measuring fracture toughness: I, direct crack measurements, *Journal of the American Ceramic Society* 64(9) (1981) 533-538.
- [64] A. Moradkhani, H. Baharvandi, M. Tajdari, H. Latifi, J. Martikainen, Determination of fracture toughness using the area of micro-crack tracks left in brittle materials by Vickers indentation test, *Journal of Advanced Ceramics* 2(1) (2013) 87-102.
- [65] B.X. Huang, J. Malzbender, R.W. Steinbrech, L. Singheiser, Discussion of the complex thermo-mechanical behavior of $\text{Ba}_{0.5}\text{Sr}_{0.5}\text{Co}_{0.8}\text{Fe}_{0.2}\text{O}_{3-\delta}$, *Journal of Membrane Science* 359(1) (2010) 80-85.
- [66] B. Huang, J. Malzbender, R. Steinbrech, E. Wessel, H. Penkalla, L. Singheiser, Mechanical aspects of ferro-elastic behavior and phase composition of $\text{La}_{0.58}\text{Sr}_{0.4}\text{Co}_{0.2}\text{Fe}_{0.8}\text{O}_{3-\delta}$, *Journal of Membrane Science* 349(1-2) (2010) 183-188.

Appendix A6

Table A6.1 Lattice constants of GCFCO in the sintered composites.

Composite	a	b	c	
50CF	Surface	5.337	5.608	7.638
	Bulk	5.338	5.614	7.659
70CF	Surface	5.340	5.614	7.658
	Bulk	5.339	5.611	7.658
85CF	Surface	5.340	5.611	7.658
	Bulk	5.339	5.611	7.659

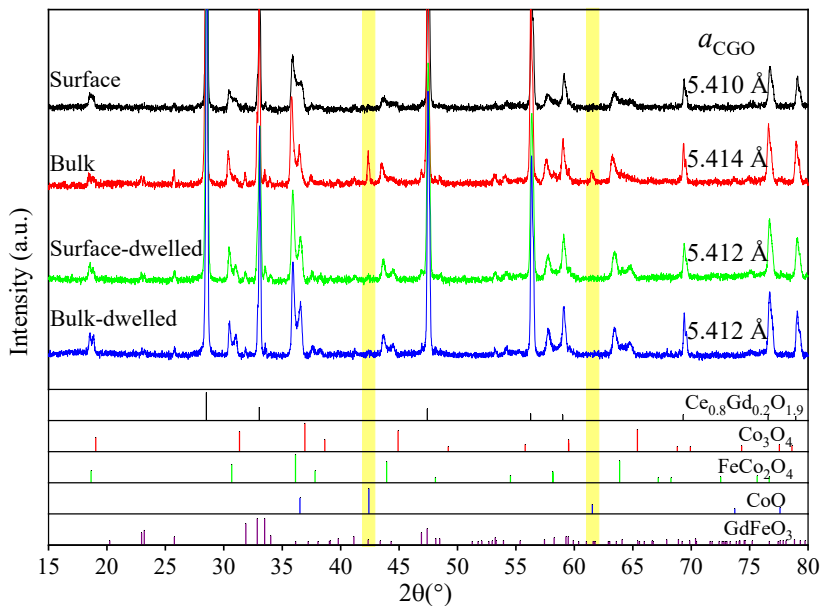


Figure A6.1 XRD patterns of 50CF. (The main diffraction peaks of CoO are highlighted as yellow).

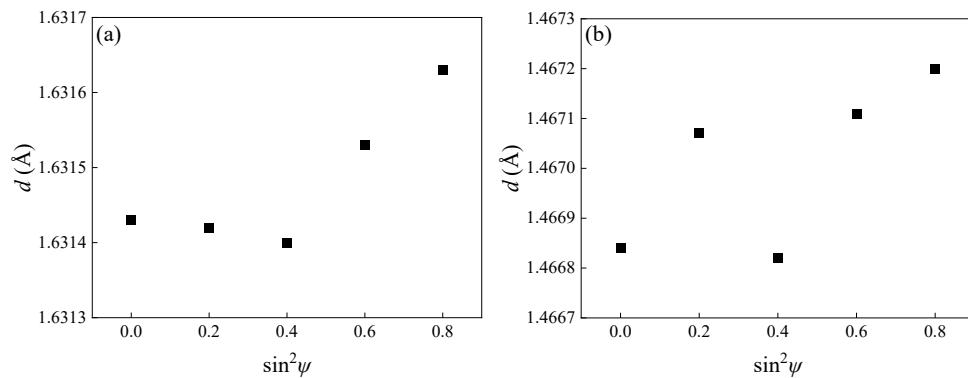


Figure A6.2 Dependencies of d on $\sin^2\psi$ values measured for (a) CGO(311) and (b) FCO(440) at the sub-surface of 50CF.

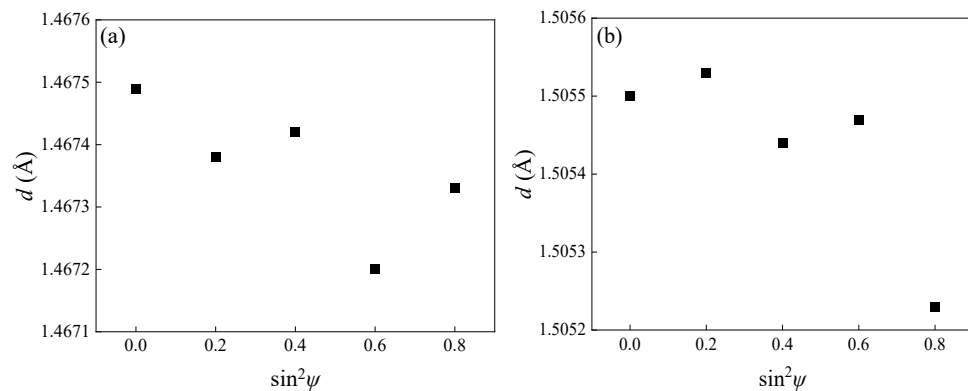


Figure A6.3 Dependencies of d on $\sin^2\psi$ values measured for (a) FCO(440) and (b) CoO(220) at the bulk surface of 50CF.

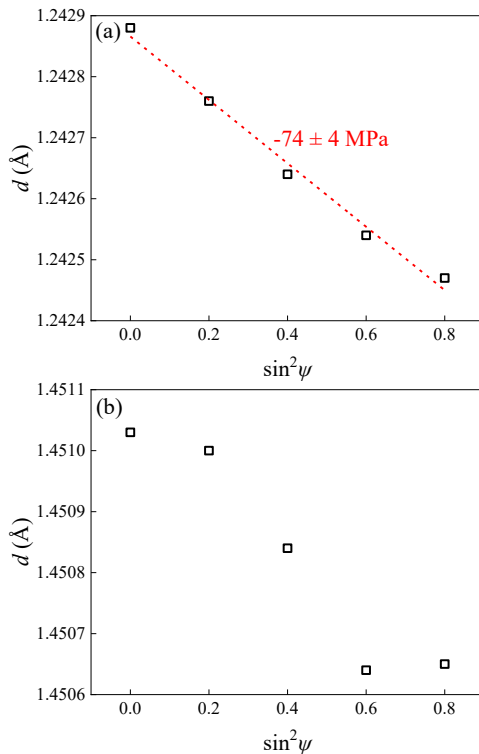


Figure A6.4 Dependencies of d on $\sin^2 \psi$ values measured for (a) CGO(331) and (b) GCFCO(133) at the as-sintered surface of 85CF. The residual stress was calculated according to equation (6.1).

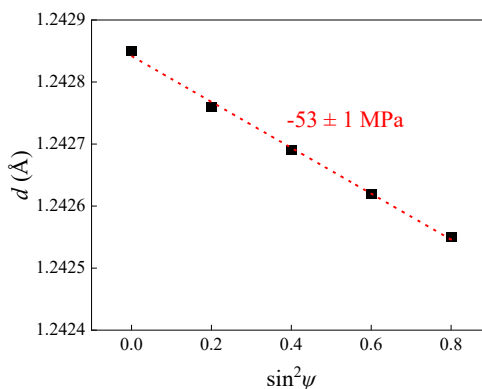


Figure A6.5 Dependencies of d on $\sin^2 \psi$ values and residual stresses measured for CGO(331) at the bulk surface of 85CF. The residual stress was calculated according to equation (6.1).

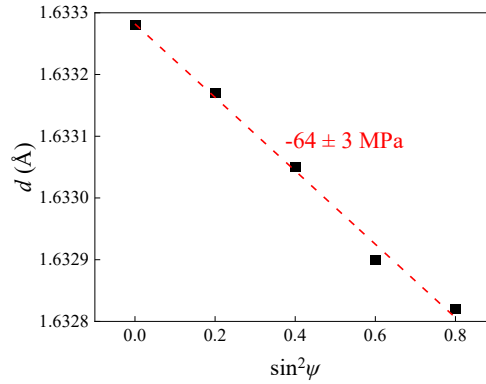


Figure A6.6 Dependencies of d on $\sin^2\psi$ values and residual stresses measured for CGO(311) at the bulk surface of 85CF, which was thermally annealed using the sintering program. The residual stress was calculated according to equation (6.1).

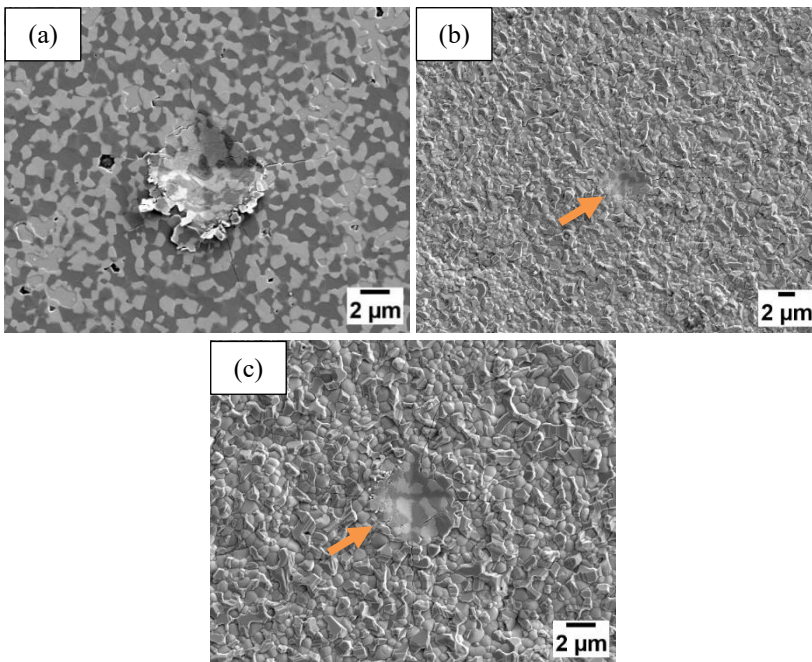


Figure A6.7 Vickers imprints on (a) the bulk surface of 50CF, (b) the as-sintered surface of 50CF and (c) the as-sintered surface of dwelled 50CF induced by a load of 0.245 N. Imprints in (b) and (c) are marked by arrows. It should be noted that the scale bars are different.

CHAPTER 7

Enhancing oxygen permeation of solid-state reactive sintered $\text{Ce}_{0.8}\text{Gd}_{0.2}\text{O}_{2-\delta}$ - FeCo_2O_4 composite by optimizing the powder preparation method

Abstract

Dual phase membranes with mixed ionic-electronic conductivity exhibit promising properties for applications in pure oxygen separation under harsh atmospheres. The conductivity of an individual phase within dual phase membranes is often attenuated by the blocking effects from the other phase(s). Here, facile but effective ways are reported to alleviate such effects by optimizing the powder preparation method for a solid-state reactive sintering process. Powder mixtures with a nominal composition 85 wt% $\text{Ce}_{0.8}\text{Gd}_{0.2}\text{O}_{2-\delta}$ -15 wt% FeCo_2O_4 were prepared by traditional wet ball milling methods, as well as a moderate dry mixing approach. Using a modified ball milling procedure, homogenous powder mixtures with fine particle size are obtained and the synthesized membrane shows a fine and homogenous microstructure that realizes high oxygen permeance. Besides, a novel “dual phase” membrane having one monophasic ionic conductive phase zone and one multiphase mixed ionic-electronic phase zone was sintered using dry-mixed powder mixtures. With individual mesoscale percolations, two phase zones provide relatively straight paths for ionic conduction and electronic conduction, respectively, which contributes to achieving the highest oxygen permeance among all the sintered membranes.

This chapter has been submitted for publication as: F. Zeng, S. Baumann, J. Malzbender, A. Nijmeijer, L. Winnubst, O. Guillon, R. Schwaiger, W. A. Meulenber, Enhancing oxygen permeation of solid-state reactive sintered $\text{Ce}_{0.8}\text{Gd}_{0.2}\text{O}_{2-\delta}$ - FeCo_2O_4 composite by optimizing the powder preparation method, *Journal of Membrane Science*.

7.1 Introduction

Ceramic oxygen permeation membranes, which are composed of mixed ionic-electronic conducting ceramic oxides, have been developed for in situ separation of oxygen for use in clean energy schemes such as pre-combustion carbon capture, and oxyfuel technology for power plants [1-5]; these applications entail a harsh atmosphere containing CO₂, H₂O and traces of SO₂ [6], which challenges the stability of the membrane materials. The typical high permeable perovskite-type membrane materials, e.g. Ba_{0.5}Sr_{0.5}Co_{0.8}Fe_{0.2}O_{3-δ} and La_{0.6}Sr_{0.4}Co_{0.2}Fe_{0.8}O_{3-δ} [7, 8], suffer from irreversible material deteriorations due to carbonating and sulfating reactions. Furthermore, these perovskite oxides also suffer from mechanical instability, e.g. cracking and delamination, caused by their high thermal and chemical expansion [9, 10].

By contrast, some dual phase membranes exhibit high stability under the CO₂- and SO₂-containing environments at high temperatures [11], and hence, they appear to be more attractive candidates than single phase perovskite-type oxides. Dual phase membranes comprise of two different kinds of phases providing ionic and electronic conductivity, respectively. Fluorite oxides, e.g. gadolinium- or samarium-doped ceria, and yttria-stabilized zirconia, are often chosen as the ionic conducting phase for dual phase membranes because of their high ionic conductivity as well as high chemical stability in an acidic atmosphere [12-14]; spinel oxides, e.g. Fe_xCo_{3-x}O₄ ($x = 1$ or 2), NiFe₂O₄, and Mn_{1.5}Co_{1.5}O₄, have attracted considerable attention as suitable electronic conducting phases combined with fluorite oxides to form robust high-performance dual phase membranes [6, 11, 15-17]. As an example, 85 wt% Ce_{0.8}Gd_{0.2}O_{2-δ}-15 wt% FeCo₂O₄ composite, which consists of a Ce_{1-x}Gd_xO_{2-δ} ($0 < x < 0.2$) (CGO) fluorite phase, a Fe_yCo_{3-y}O₄ ($0 < y < 2$) (FCO) spinel phase and a Gd_{0.85}Ce_{0.15}Fe_{0.75}Co_{0.25}O₃ (GCFCO) perovskite phase [15, 18-20], was verified to possess high tolerance over 200 h in CO₂- and SO₂-containing gas mixtures at 850 °C under an oxygen partial pressure gradient [15].

Oxygen permeation through ceramic oxygen permeation membranes can be classified into two kinds of processes [21]: gas-solid interfacial exchange at the surface (surface exchange) and ion/electron diffusion in the bulk. For a dual phase membrane comprising two kinds of phases possessing pure ionic conductivity and pure electronic conductivity, respectively, the surface exchange only takes place at triple phase boundaries (TPBs) [22], which are the connection lines of ion conducting grains, electron conducting grains and the gas phase. Thus, to improve the surface exchange for these membranes, an effective way is to extend the available length of the TPBs by microstructural optimizations, e.g. increasing the homogeneity of the two kinds of phases [23], and reducing the grain size [24], as well as coating a porous activation layer with mixed ionic-electronic conductivity on the surfaces [22].

The bulk diffusion within a dual phase membrane is realized by the ambipolar conductivity, i.e. the ambipolar conduction of ions and electrons through continuous paths formed by the two kinds of phases, respectively [21]. The ambipolar conductivity (σ_{amb}) can be expressed as [18]:

$$\sigma_{amb} = \frac{\sigma_{p,i} \cdot \sigma_{p,e}}{\sigma_{p,i} + \sigma_{p,e}} \quad (7.1)$$

where $\sigma_{p,i}$ and $\sigma_{p,e}$ represent the partial ionic and electronic conductivity, respectively. The partial ionic/electronic conductivity is proportional to the intrinsic ionic/electronic conductivity, as well as the contiguous phase volume transporting ions/electrons through the membrane according to [18].

$$\sigma_{p,i} = \sigma_i \cdot V_{eff,i} \quad (7.2)$$

$$\sigma_{p,e} = \sigma_e \cdot V_{eff,e} \quad (7.3)$$

where σ_i and σ_e are the intrinsic ionic and electronic conductivity, respectively. And $V_{eff,i}$ and $V_{eff,e}$ are the contiguous volumes providing, respectively, the effective paths for ionic and electronic transport through the membrane. The contiguous

volume is increasing as a function of the total volume for a randomly distributed phase constituent within a composite [18, 25].

The amount of ion and electron conductive phases often needs to be varied to realize a high ambipolar conductivity when intrinsic conductivities of the two kinds of phases do not match. It is essential to increase the volume fraction of the phase with the lowest conductivity but maintain percolation of the phase with the highest conductivity. In the case that the intrinsic conductivities of two kinds of phases are not of the same order of magnitude, e.g. the ionic conductivity of gadolinium-doped ceria is two orders of magnitude lower than the electronic conductivity of $\text{Fe}_x\text{Co}_{3-x}\text{O}_4$ ($x = 1$ or 2) [16, 22], the volume fraction of the phase with the highest conductivity should theoretically be much lower than 30 vol% to obtain a high ambipolar conductivity and high oxygen permeation flux [18]. For instance, the oxygen permeation fluxes of $z\text{Ce}_{0.8}\text{Gd}_{0.2}\text{O}_{2-\delta}-(1-z)\text{FeCo}_2\text{O}_4$ ($60 \text{ wt}\% \leq z \leq 90 \text{ wt}\%$) composites approach the maximum value when x reaches 15 wt% [15]. Such a small volume, however, is in practice a challenge for the formation of sufficiently continuous networks for electronic conduction. The total conductivity of 85wt% $\text{Ce}_{0.8}\text{Gd}_{0.2}\text{O}_{2-\delta}$ -15wt% FeCo_2O_4 composite is around one order of magnitude lower than that of 70wt% $\text{Ce}_{0.8}\text{Gd}_{0.2}\text{O}_{2-\delta}$ -30wt% FeCo_2O_4 composite [26]. Hence, for composites such as 80 vol% $\text{Ce}_{0.8}\text{Gd}_{0.2}\text{O}_{2-\delta}$ -20 vol% $\text{MnCo}_{1.9}\text{Fe}_{0.1}\text{O}_4$ [27], 85 wt% $\text{Ce}_{0.8}\text{Gd}_{0.2}\text{O}_{2-\delta}$ -15 wt% FeCo_2O_4 [15], and 85 vol% $\text{Ce}_{0.8}\text{Gd}_{0.2}\text{O}_{2-\delta}$ -15 vol% MnCo_2O_4 [28], electronic conduction, which is realized by a comparably small volume of electron conducting phases, is believed to be the bottleneck for bulk diffusion during oxygen permeation [26].

The existence of a nano-sized grain boundary phase was reported to contribute to the formation of electron conductive networks in $\text{Ce}_{0.8}\text{Gd}_{0.2}\text{O}_{2-\delta}$ - MnCo_2O_4 composite at a low volume of MnCo_2O_4 [28]. Besides, it was proven to be effective for a minor phase to form percolations through a dual phase membrane by reducing the grain size and increasing the inhomogeneity. Li et al. [29] investigated the electronic conductivity of 75wt% $\text{Ce}_{0.8}\text{Sm}_{0.2}\text{O}_{1.9}$ -25 wt% $\text{Sm}_{0.6}\text{Ca}_{0.4}\text{CoO}_{3-\delta}$ and 75wt%

$\text{Ce}_{0.8}\text{Sm}_{0.2}\text{O}_{1.9-25}$ wt% $\text{Sm}_{0.6}\text{Ca}_{0.4}\text{FeO}_{3-\delta}$ composites and found that only the latter possessed electronic conductivity that was sufficient for oxygen permeation due to the continuous electronic conducting networks formed by the $\text{Sm}_{0.6}\text{Ca}_{0.4}\text{FeO}_{3-\delta}$ grains that are one order of magnitude smaller than the $\text{Ce}_{0.8}\text{Sm}_{0.2}\text{O}_{1.9}$ grains. A study on 75 wt% $\text{Ce}_{0.85}\text{Sm}_{0.15}\text{O}_{3-\delta}$ -25 wt% $\text{Sm}_{0.6}\text{Sr}_{0.4}\text{FeO}_{3-\delta}$ revealed that the grain growth of the major phase, i.e. $\text{Ce}_{0.85}\text{Sm}_{0.15}\text{O}_{3-\delta}$, blocked the connectivity of the minor phase, i.e. $\text{Sm}_{0.6}\text{Sr}_{0.4}\text{FeO}_{3-\delta}$, and yielded a lower oxygen permeation flux [24]. In addition, Zhu et al. [30] used different methods to prepare 75 wt% $\text{Ce}_{0.85}\text{Sm}_{0.15}\text{O}_{1.925}$ -25 wt% $\text{Sm}_{0.6}\text{Sr}_{0.4}\text{Al}_{0.3}\text{Fe}_{0.7}\text{O}_3$ composite and concluded the membrane prepared by solid-state reaction shows the highest oxygen permeation flux and total conductivity due to the inhomogeneous distribution of small $\text{Sm}_{0.6}\text{Sr}_{0.4}\text{Al}_{0.3}\text{Fe}_{0.7}\text{O}_3$ grains.

Based on the realization of the importance of microstructural aspects regarding grain size and spatial distribution of each phase on the performance of the dual phase membranes, we are motivated to explore facile but effective ways to tailor the microstructural characteristics of dual phase membranes. In this work, the solid-state reactive sintering process was optimized to synthesize composites with a nominal composition 85 wt% $\text{Ce}_{0.8}\text{Gd}_{0.2}\text{O}_{2-\delta}$ -15 wt% FeCo_2O_4 showing enhanced oxygen permeation. The powder mixtures used for solid-state reactive sintering were prepared by applying different wet ball milling processes on powder mixtures of $\text{Ce}_{0.8}\text{Gd}_{0.2}\text{O}_{2-\delta}$, Co_3O_4 and Fe_2O_3 powders to homogenize the distribution of each compound as well as modify the particle size, which results in homogenous microstructures with different grain sizes for the sintered membranes. Besides, to synthesize a membrane having the minor conducting phases well connected through the membrane, inhomogeneous powder mixtures were prepared by dry mixing of 50 wt% monophasic phase powders ($\text{Ce}_{0.8}\text{Gd}_{0.2}\text{O}_{2-\delta}$) with fine and homogeneous composite ceramic powders having a nominal composition 70 wt% $\text{Ce}_{0.8}\text{Gd}_{0.2}\text{O}_{2-\delta}$ -30 wt% FeCo_2O_4 in a moderate way. This results in a novel type of composites comprised of a pure ionic conductor ($\text{Ce}_{0.8}\text{Gd}_{0.2}\text{O}_{2-\delta}$) with a mixed ionic electronic conductor, which is a composite itself (70 wt% $\text{Ce}_{0.8}\text{Gd}_{0.2}\text{O}_{2-\delta}$ -30 wt% FeCo_2O_4). The

nominal overall weight ratio $\text{Ce}_{0.8}\text{Gd}_{0.2}\text{O}_{2-\delta}$: FeCo_2O_4 in this composite is again 85:15, so that the properties can directly be compared to the classical composites. The microstructural characteristics and phase constituents of both the classical and the novel composite membranes were analyzed in detail, and their influence on oxygen permeation performance is discussed.

7.2 Experimental

Dual phase membranes were synthesized by a solid-state reactive sintering process using $\text{Ce}_{0.8}\text{Gd}_{0.2}\text{O}_{2-\delta}$ (Treibacher Industrie AG, 99 %), Co_3O_4 (Alfa Aesar, 99.7 %) and Fe_2O_3 (Sigma-Aldrich, 99 %) as precursor powders; the mole ratio of Co_3O_4 to Fe_2O_3 was fixed at 4:3 to form a nominal compound of FeCo_2O_4 during sintering; the weight ratio of ionic conductor ($\text{Ce}_{0.8}\text{Gd}_{0.2}\text{O}_{2-\delta}$) to electronic conductor (the nominal FeCo_2O_4) was maintained at 85:15. To obtain rather homogeneous powder mixtures with different particle sizes, two different wet ball milling procedures were applied. For both cases, the powder mixtures, ethanol and zirconia balls were filled up to ~ 30 vol% in a polyethylene bottle. The weight ratio of powder : ball : ethanol was 1:2:3 as also described in [19]. The milling procedures were conducted on a roller bench. The first powder mixture (referred to as CF-1) was obtained through a one-step ball milling for 3 days, using 5 mm (diameter) zirconia balls. The second powder mixture (referred to as CF-2) was obtained through a two-step ball milling including a first step for 3 days using 5 mm (diameter) zirconia balls and a second step for 7 days using 1 mm (diameter) zirconia balls [19]. After drying at 75 °C for 3 days and sieved by a 150 μm -mesh sieve, the one-step and two-step milled powder mixtures were uniaxially pressed into pellets at 19 MPa [19] and 50 MPa [18], respectively for powder CF-1 and CF-2.

In order to increase inhomogeneity and percolation of the minor compound (the nominal FeCo_2O_4) but maintain a constant weight ratio of $\text{Ce}_{0.8}\text{Gd}_{0.2}\text{O}_{2-\delta}$ to FeCo_2O_4 (i.e. 85:15) for powder mixtures, a dry mixing method was used instead of the wet ball milling method. However, dry mixing of 85 wt% $\text{Ce}_{0.8}\text{Gd}_{0.2}\text{O}_{2-\delta}$ powders with

15 wt% nominal FeCo_2O_4 powders does not lead to sufficient percolation of the minor compound in the membrane but results in many isolated islands. Therefore, inhomogeneous powder mixtures were prepared by dry mixing of 50 wt% $\text{Ce}_{0.8}\text{Gd}_{0.2}\text{O}_{2-\delta}$ powders with composite ceramic powders having a nominal composition 70 wt% $\text{Ce}_{0.8}\text{Gd}_{0.2}\text{O}_{2-\delta}$ -30 wt% FeCo_2O_4 . The composite powder was prepared using the procedures as described for powder CF-2. The mixing process was conducted in a moderate manual way within a limited time of ~ 10 min so that most of Co_3O_4 and Fe_2O_3 will not blend into the monophase powders ($\text{Ce}_{0.8}\text{Gd}_{0.2}\text{O}_{2-\delta}$) but keep concentrated in the composite ceramic powders. With a comparable amount, the monophase powders and the composite ceramic powders are expected to retain well individual percolation on the mesoscale after being moderately mixed. The obtained inhomogeneous powder mixtures (referred to as CF-D) were uniaxially pressed into pellets under 50 MPa.

All pellets were sintered in air at 1200 °C for 10 h; a slow cooling rate of 0.5 K/min was used between 900 °C and 800 °C [19], while the heating and cooling rate for the other temperature ranges was 3 K/min. The codes of the different membranes, obtained by solid-state reactive sintering, were the same as those of the powders, i.e. CF-1, CF-2 and CF-D, respectively.

The particle size distribution of precursor powders was determined by the laser diffraction method based on Mie theory using a Horiba LA 950 V2 analyzer (Retsch Technology GmbH, Haan, Germany). The specific surface area of precursor powders and powder mixtures was measured, respectively, by the Brunauer-Emmett-Teller (BET) single-point method by low-temperature N_2 adsorption using Areameter II (Ströhlein Instruments, Viersen, Germany).

The powder mixtures were investigated by scanning electron microscopy (SEM) (Merlin, Carl Zeiss Microscopy, Oberkochen, Germany) regarding particle morphology and by energy-dispersive X-ray spectroscopy (EDS) (Merlin, Carl Zeiss Microscopy, Oberkochen, Germany) with respect to elemental distributions. EDS

investigations were carried out at 4 kV accelerating voltage using an X-Max 80 detector and the AZtec data acquisition and analysis software package (Oxford Instruments Nanoanalysis, High Wycombe, United Kingdom). Before the EDS investigation, the powder mixtures were mixed with epoxy resin. After the resin hardened, the cross-section was ground using 800-grit SiC paper, and then polished by argon ion milling for 8 h at 6 kV / 150 μ A using a JEOL SM-09010 (JEOL Ltd., Tokyo, Japan) polisher.

Microstructures and phase constituents were investigated at the polished cross-sections of sintered membranes by scanning electron microscopy (SEM) (Merlin, Carl Zeiss Microscopy, Oberkochen, Germany) and electron backscatter diffraction (EBSD) (NordlysNano, Oxford Instruments, Wiesbaden, Germany), as well as EDS for element distribution. The area fraction of each phase was deduced by image analysis using the HKL Channel 5 software packages. The volume fraction was estimated to be equal to the area fraction for each phase in a random section through each composite [31]. The porosity was estimated as the area fraction of the pores using the ImageJ software [32].

The gas tightness of the sintered membrane was assessed using a He-leak detector (ASM 340, Pfeiffer Vacuum GmbH, Asslar, Germany). Helium was fed at one side of the membrane, while a vacuum was drawn on the other side. The helium flow gas passing through the sample was collected by the detector and calculated as helium leakage rate.

Oxygen permeation measurements were conducted using sintered pellets, which were polished at two sides to thicknesses of $\sim 0.95 \pm 0.02$ mm and ground to diameters of $\sim 14.65 \pm 0.05$ mm prior to gold sealing. Each pellet was sealed with a gold ring at each side in a glass tube setup at approx. 1020 °C for 5 hours under a spring load. Oxygen permeation flux in a steady-state was measured between approx. 1020 °C and 850 °C using air and argon as feed and sweep gas at a flow rate of 250 ml/min and 50 ml/min, respectively. The individual sample temperature was measured online with a thermocouple (type S) close to the pellet. The sample

temperature can vary maximally by approx. 20 K from sample to sample and in particular between two identical furnaces operated in parallel. One specimen of each of the bare CF-1, CF-2 and CF-D membrane types were assessed. In addition, oxygen permeation flux was also measured for the sintered pellets that are coated with surface activation layers. For that reason, the polished pellets were screen printed with a porous $\text{La}_{0.58}\text{Sr}_{0.4}\text{Co}_{0.2}\text{Fe}_{0.8}\text{O}_{3-\delta}$ (LSCF) coating at both sides, as described in [22], and then post-sintered at 1100 °C for 30 min. One coated CF-1, one coated CF-2 and two coated CF-D membranes were characterized.

7.3 Results and discussion

7.3.1 Powder characteristics

The microstructures of dual phase membranes, e.g. grain sizes and distributions of individual phases, are significantly affected by the sizes of particles, as well as agglomerates, within precursor powders. Hence, the dimensions of particles and agglomerates are investigated in detail using different characterization methods.

Figure 7.1 provides the morphologies of the as-received precursor powders. Most of the particles exhibit quasi-spherical shapes, while the as-received Fe_2O_3 has few particles with irregular shapes (see Figure 7.1(b)). The homogeneity of particle sizes of the as-received precursor powders decreases in the order of $\text{Co}_3\text{O}_4 > \text{Ce}_{0.8}\text{Gd}_{0.2}\text{O}_{2-\delta} > \text{Fe}_2\text{O}_3$. Notably, the as-received Co_3O_4 contains comparatively large round agglomerates (see Figure 7.1(d)), whereas it is relatively difficult to distinguish any agglomerates in the as-received $\text{Ce}_{0.8}\text{Gd}_{0.2}\text{O}_{2-\delta}$ and Fe_2O_3 .

The specific surface areas of the as-received $\text{Ce}_{0.8}\text{Gd}_{0.2}\text{O}_{2-\delta}$, Fe_2O_3 and Co_3O_4 powders are measured to be $\sim 7.9 \text{ m}^2/\text{g}$, $\sim 5.8 \text{ m}^2/\text{g}$ and $\sim 3.3 \text{ m}^2/\text{g}$, respectively. The rather low specific surface area for the as-received Co_3O_4 reflects that the nano-sized primary particles, as can be seen in Figure 7.1(d), are hard agglomerates with low inner porosities.

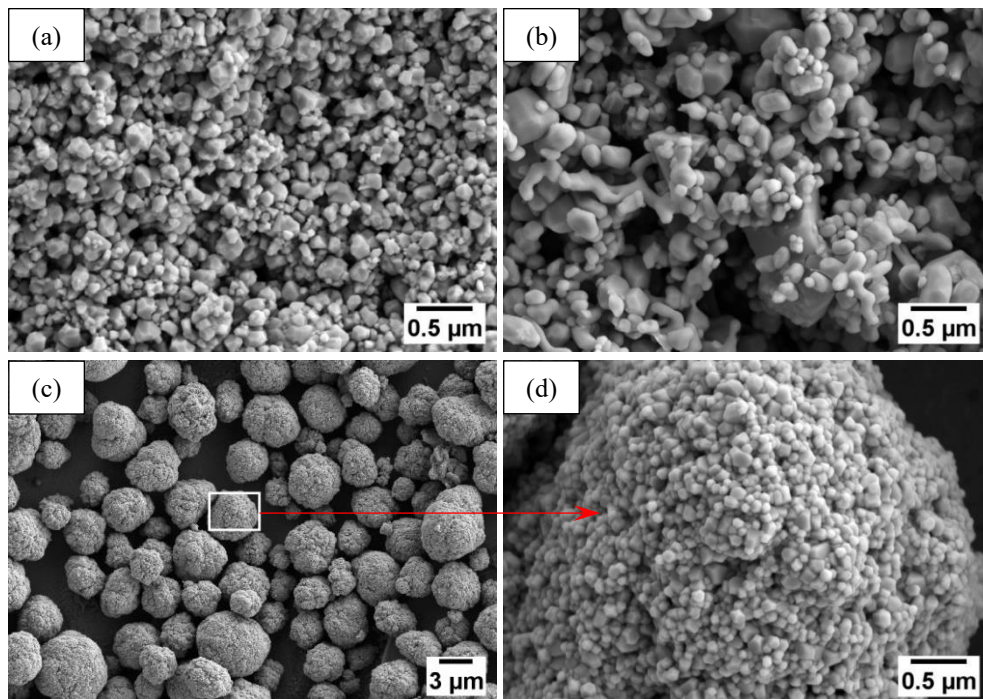


Figure 7.1 Particle morphologies of as-received precursor powders: (a) $\text{Ce}_{0.8}\text{Gd}_{0.2}\text{O}_{2-\delta}$, (b) Fe_2O_3 and (c) Co_3O_4 ; (d) is a magnified view of the agglomerate framed in (c).

The laser diffraction method can provide a quantitative analysis of apparent particle sizes that can reflect the sizes of hard agglomerates. For the as-received $\text{Ce}_{0.8}\text{Gd}_{0.2}\text{O}_{2-\delta}$ powders, although the median apparent particle size d_{50} ($\sim 0.1 \mu\text{m}$) is comparable to the average size of particles shown in Figure 7.1 (a), the measured apparent particle sizes reflect the sizes of both particles and agglomerates indicated by the bimodal particle size distribution profile (see Figure 7.2(a)). The apparent particle size distribution becomes gradually tighter with increasing milling steps, while d_{50} hardly changes; the specific surface area of the as-received $\text{Ce}_{0.8}\text{Gd}_{0.2}\text{O}_{2-\delta}$ is slightly increased to $\sim 10.6 \text{ m}^2/\text{g}$ by the two-step milling process, which suggests that the reduction of apparent particle size is mainly attributed to the breaking of agglomerates.

For the as-received Fe_2O_3 powders, the apparent particle size distribution shows a unimodal profile (see Figure 7.2(b)), and the d_{50} is measured to be $\sim 1.4 \mu\text{m}$, which is larger than the sizes of most particles shown in Figure 7.1 (b), which implies the existence of a large number of big agglomerates. The d_{50} is not modified by the one-step milling process, but dramatically reduced to $0.53 \mu\text{m}$ by the two-step milling process although there are still few ($< 20 \text{ vol}\%$) particles with apparent sizes above $1 \mu\text{m}$ (see Figure 7.2(b)). These large particle sizes can possibly be the sizes measured for the remaining agglomerates since the specific surface areas of Fe_2O_3 is changed insignificantly.

For the as-received Co_3O_4 powders, the apparent particle sizes are distributed in a unimodal profile (see Figure 7.2(c)), with d_{50} is $\sim 7.5 \mu\text{m}$, which is noticeably close to the sizes of agglomerates (see Figure 7.1(c)), indicating that the agglomerates are very compact and do not break during the measurement. The d_{50} is reduced by one-step milling and two-step milling to $\sim 3.0 \mu\text{m}$ and $0.35 \mu\text{m}$, respectively. The particle size distribution of the one-step milled Co_3O_4 powders shows a bimodal profile, while the two-step milled Co_3O_4 powders have a unimodal distribution profile (see Figure 7.2(c)). Although the specific surface area of the two-step milled Co_3O_4 is increased to $13.0 \text{ m}^2/\text{g}$, the d_{50} of the two-step milled Co_3O_4 is still larger than the particle size indicated in Figure 7.1(d). These observations indicate that large agglomerates in the as-received Co_3O_4 are milled into small agglomerates by two-step milling; the small agglomerates appear to be rather compact and cannot easily be shattered by ball milling.

Therefore, it can be concluded that the two-step milling method is an effective way to reduce the particle size and size distribution of the precursor powders. Such effects on different precursor powders decrease in the order of $\text{Co}_3\text{O}_4 > \text{Ce}_{0.8}\text{Gd}_{0.2}\text{O}_{2-\delta} > \text{Fe}_2\text{O}_3$. A further increase of the milling time for the two-step milling procedure is verified to make no significant change regarding the apparent particle sizes (not shown here).

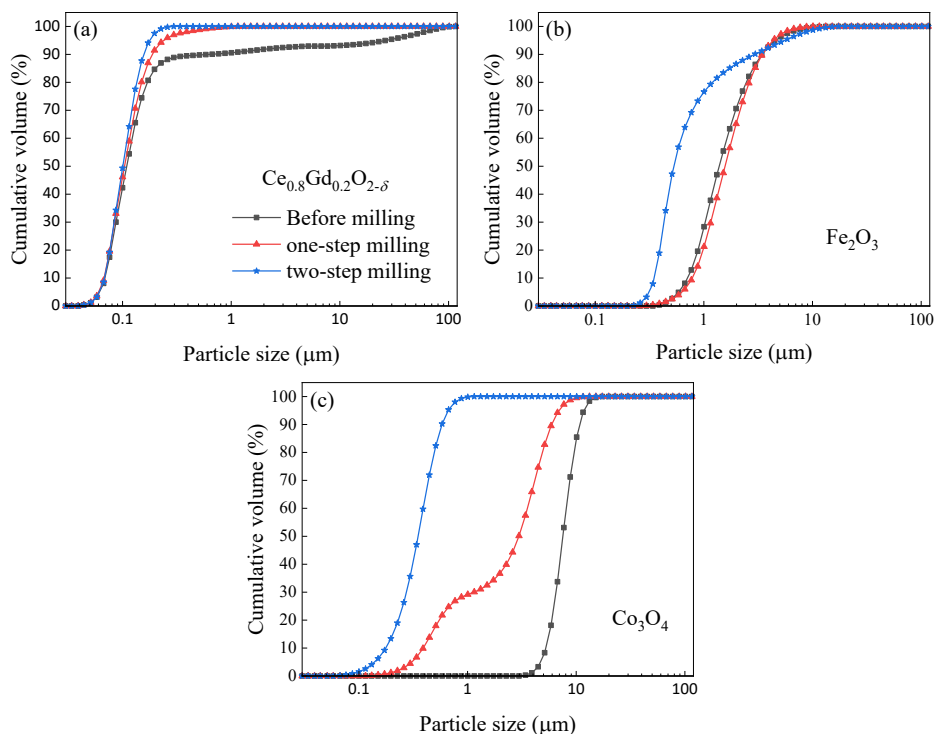


Figure 7.2 Particle size distribution of precursor powders before and after ball milling: (a) $\text{Ce}_{0.8}\text{Gd}_{0.2}\text{O}_{2-\delta}$, (b) Fe_2O_3 and (c) Co_3O_4 . (the legends in (a) also apply to (b) and (c)).

To further investigate the effect of the different milling procedures on powder mixtures, the ball-milled powder mixtures were characterized by BSEM and EDS. As shown in Figure 7.3, Ce-rich, Fe-rich and Co-rich grains represent, respectively, $\text{Ce}_{0.8}\text{Gd}_{0.2}\text{O}_{2-\delta}$, Fe_2O_3 and Co_3O_4 particles. Large Co_3O_4 and Fe_2O_3 particles or agglomerates can be seen in the powder CF-1. By contrast, Co_3O_4 and Fe_2O_3 in the powder CF-2 exhibit small and homogenous particle sizes (see Figure 7.4). Fe_2O_3 shows larger particle sizes than Co_3O_4 in the powder CF-2. No obvious agglomerates are found in the powder CF-2. The specific surface areas are $8.2 \text{ m}^2/\text{g}$ and $13.8 \text{ m}^2/\text{g}$, respectively, for the powder CF-1 and CF-2. These results suggest that agglomerates can be shattered by the two-step milling procedure for the precursor powders milled together.

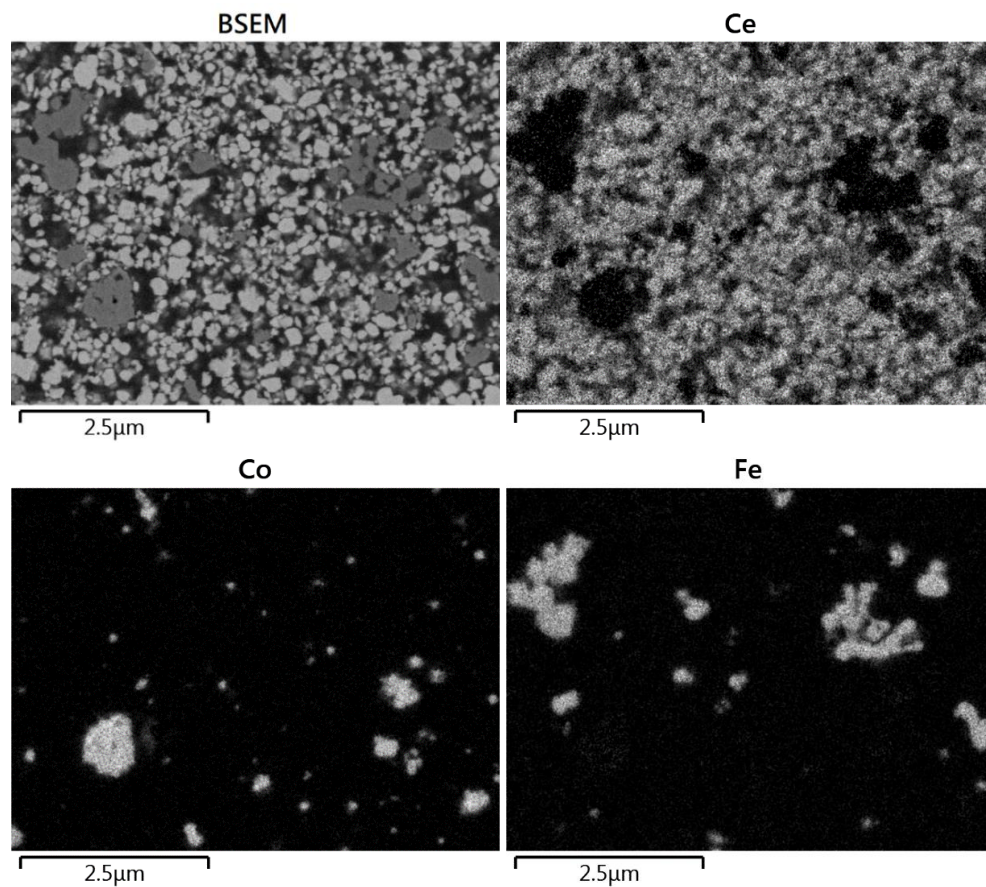


Figure 7.3 BSEM micrograph and corresponding EDS elements mapping on the powder CF-1 embedded in epoxy resin. Ce-rich, Fe-rich and Co-rich grains represent, respectively, $\text{Ce}_{0.8}\text{Gd}_{0.2}\text{O}_{2-\delta}$, Fe_2O_3 and Co_3O_4 particles.

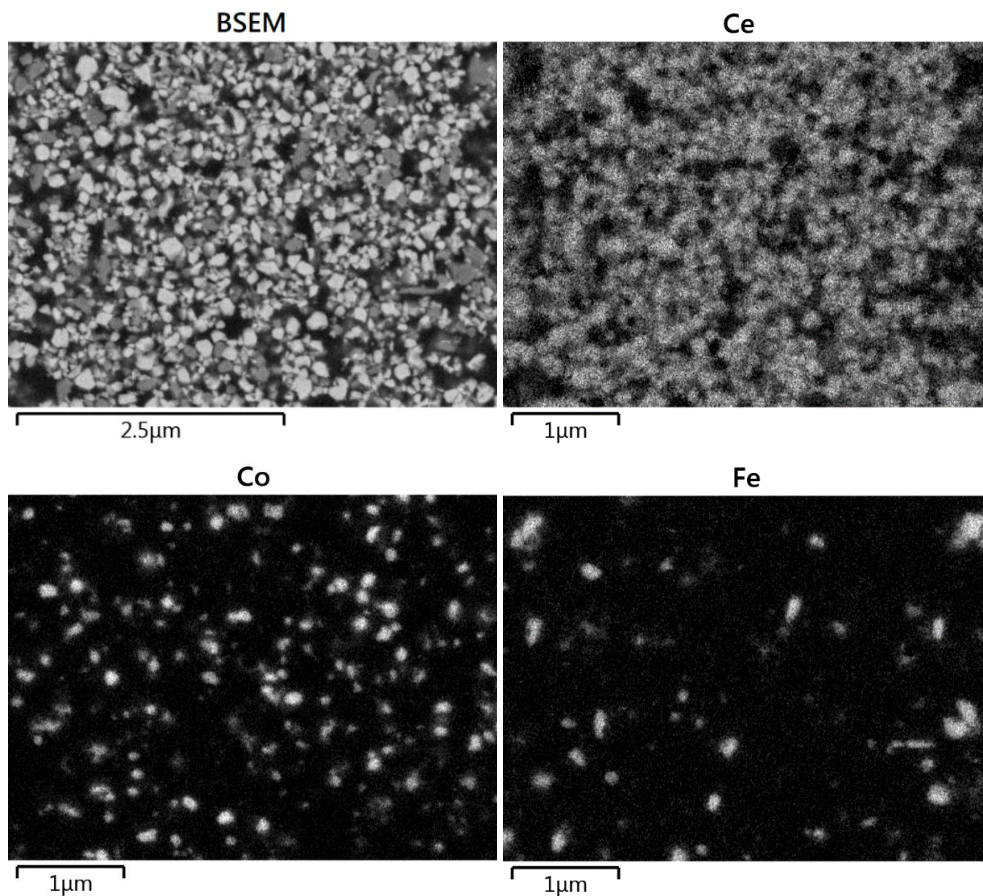


Figure 7.4 BSEM micrograph and the corresponding EDS elements mapping on the powder CF-2 embedded in epoxy resin. Ce-rich, Fe-rich and Co-rich grains represent, respectively, $\text{Ce}_{0.8}\text{Gd}_{0.2}\text{O}_{2-\delta}$, Fe_2O_3 and Co_3O_4 particles.

7.3.2 Phase and microstructure characterizations

The microstructure and phase constituent of the membranes prepared by the ball-milled powder mixtures are shown in Figure 7.5. The closed porosities of CF-1 and CF-2 are below $\sim 2\%$ (see Figure 7.5). The grains that appear black in Figure 7.5(a, c) are FCO or CoO according to the EBSD phase mapping (Figure 7.5(b, d)), while the grey and light grey grains are CGO and GCFCO, respectively. The FCO grains are well dispersed within the CGO phases. The grain size of FCO in CF-1 shows a

large variation due to the existence of a high amount of large grains (see Figure 7.5 (a,b)). The CoO phase is a residue from sintering, which should be re-oxidized to the spinel structure during cooling. The CoO phase is only detected in CF-1 (see Figure 7.5(b)). Apparently, the re-oxidation of the large grains in CF-1 would need more time and, thus, is not completed. Obviously, the one-step milling process is much less effective compared to the two-step process resulting in the coarse microstructure.

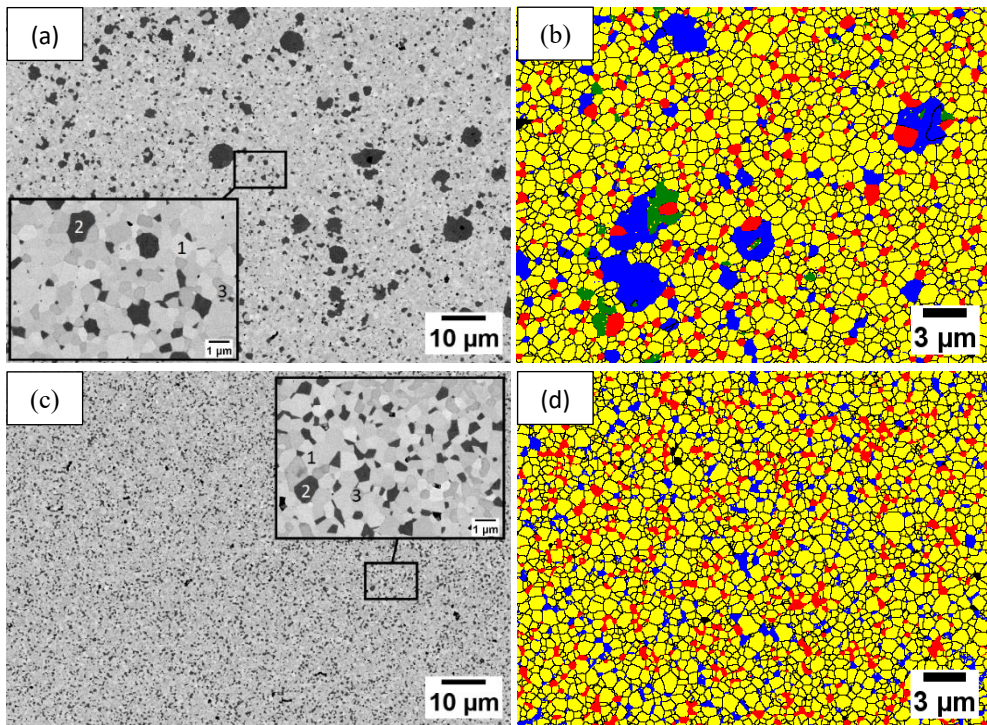


Figure 7.5 BSEM micrographs (left column: a, c) and EBSD phase mapping (right column: b,d) of (a,b) CF-1 and (c,d) CF-2. In the SEM micrographs, the grains denoted as 1, 2, 3 represent CGO, FCO (or CoO) and GCFCO grains, respectively. In the EBSD phase mapping, the yellow, blue, red and green phases are CGO, FCO, GCFCO and CoO, respectively, while the black spots and dark lines are pores and grain or phase boundaries, respectively.

Furthermore, EDS reveals the existence of Co-rich phases at the grain boundaries of CGO or GCFCO, as shown in Figure 7.6 for CF-1. The Ce-rich, Gd-rich and Co-rich

grains represent, respectively, the CGO, GCFCO and FCO (or CoO) grains, while the Fe-rich grains can be either GCFCO or FCO (or CoO) grains. The FCO grains mainly contain Co and Fe, and the GCFCO grains consist of Gd and Fe, as well as very little Ce and Co. A little amount of Co seems to segregate along the grain boundaries of CGO or GCFCO forming a grain boundary phase, which appears to create a connection between two isolated FCO grains and potentially provide paths for electronic conduction along the grain boundaries but may hinder ionic conduction across the grain boundaries [33].

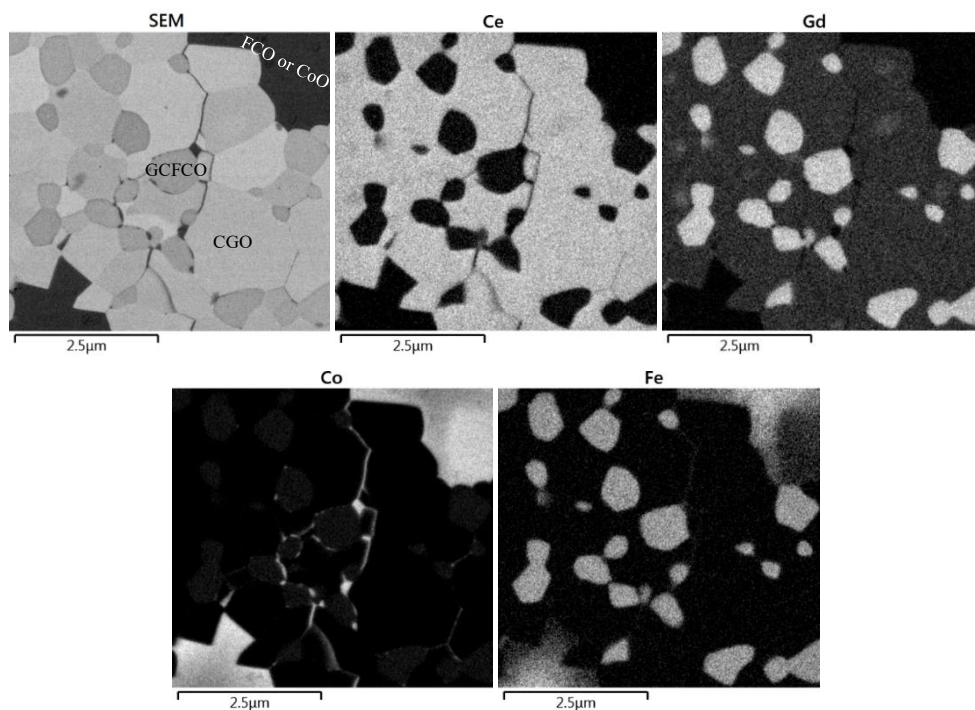


Figure 7.6 BSEM micrograph and the corresponding EDS element mapping on CF-1. The Ce-rich, Gd-rich and Co-rich grains represent, respectively, the CGO, GCFCO and FCO (or CoO) grains, while the Fe-rich grains can be either GCFCO or FCO (or CoO) grains.

By contrast, for CF-D, the FCO and CoO grains have rather small grain size variation, and are noticeably only distributed in one specific zone (see Figure 7.7(a)); phase areas in CF-D can be well distinguished as a monophasic zone and a multiphasic zone

(see Figure 7.7(b)). The different zones are well connected on the mesoscale with connections between the larger regions, rather than having connections only between distributed grains. The phase distributions are considerably homogenous in the multiphase zone in CF-D (see Figure A7.1 (a)), which is much like the one reported for 70 wt% $\text{Ce}_{0.8}\text{Gd}_{0.2}\text{O}_{2-\delta}$:30 wt% FeCo_2O_4 membrane [34]. The multiphase zone appears to have fewer pores than the monophase zone (see Figure A7.1), which benefits from the phase interactions between CGO and FCO during sintering. These phase interactions result in the formation of the GCFCO phase, and dominate the densification process [19]. The monophase zone, which mainly comprises pure $\text{Ce}_{0.8}\text{Gd}_{0.2}\text{O}_{2-\delta}$, suffers from low sintering activity leading to small but closed porosity (Figure A7.1(b)). In addition, few defects, e.g. cracks and voids (marked by arrows in Figure 7(a)), are found in the monophase zone and interfaces between different zones, but the membrane is still gastight as verified by the low helium leakage rate ($< 10^{-8} \text{ mbar}\cdot\text{L}\cdot\text{s}^{-1}$).

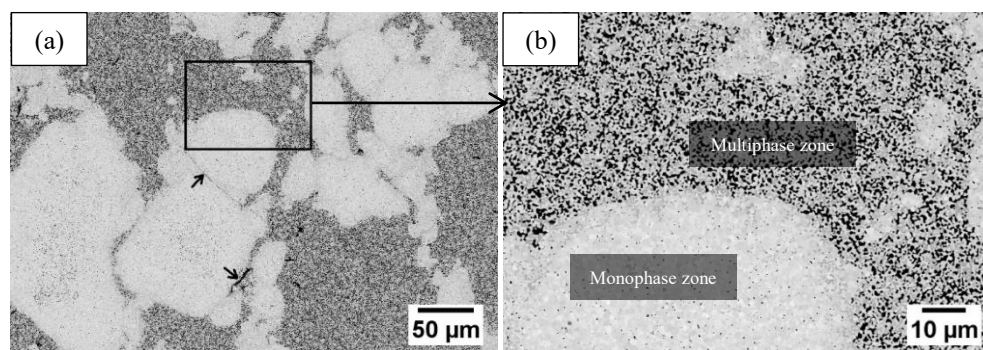


Figure 7.7 BSEM micrographs of CF-D. Only a few defects exist and are indicated by arrows in (a). Two zones consisting of a different number of phases are observed, i.e. multiphase and monophase zones, as labeled in (b).

The phase constituents in the different zones within CF-D are analyzed in detail by EBSD. As shown in Figure 7.8, CGO, FCO, GCFCO and CoO phases are observed in CF-D. Few GCFCO grains are located at the interface between the monophase zone and the multiphase zone (see Figure 7.8(a)). This is an indication of elements

diffusion and phase interactions between the different zones, which contributes to obtaining a robust interface and a dense microstructure.

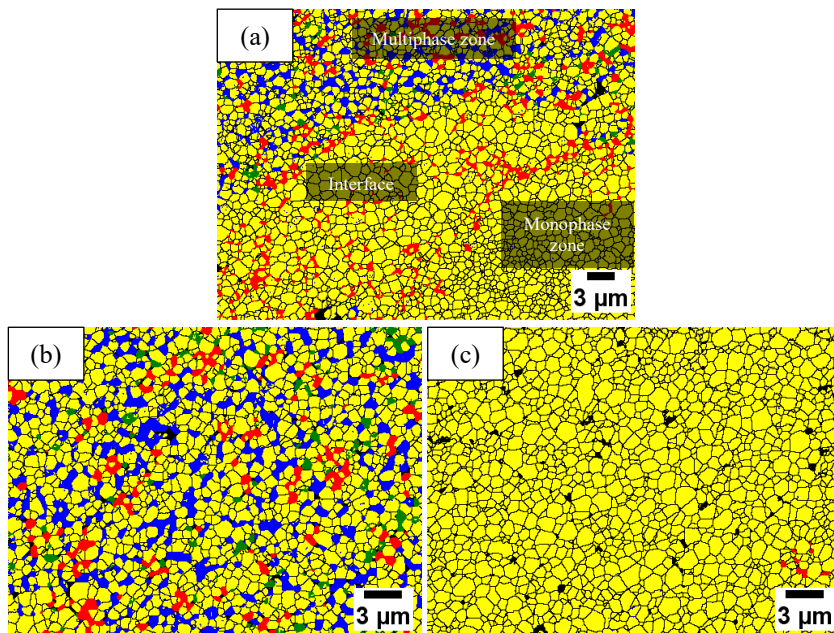


Figure 7.8 EBSD phase mapping of CF-D: (a) overview, (b) multiphase zone and (c) monophase zone: the yellow, blue, red and green phases are CGO, FCO, GCFCO and CoO, respectively, while the black spots and dark lines are pores and grain/phase boundaries, respectively.

The multiphase zone contains four different phases as expected (see Figure 7.8(b)). Microscale percolations of ion conducting phase (CGO) and electron conducting phases (FCO, CoO and GCFCO [18, 26]) can be observed (see Figure 7.8(b)). By contrast, the monophase zone mainly consists of CGO phase (see Figure 7.8(c)). The EDS point quantification results suggest that the average Ce/Gd ratio in CGO in the monophase zone is close to the one in pure $\text{Ce}_{0.8}\text{Gd}_{0.2}\text{O}_{2-\delta}$ (see Table A7.1), but higher than the one in the multiphase zone. The depletion of Gd content in CGO is caused by the formation of GCFCO [18]. It also indicates that the Gd content in the different

zones has not been homogenized through mixing or diffusion under the current sintering conditions, because the diffusion pathways might be too long.

Volumetric quantifications were determined based on the average of three different areas investigated by EBSD for each membrane and each phase zone; the sizes of the areas investigated were the same as the ones exemplarily shown in Figure 7.5(b, d) and Figure 7.8. Among these phase constituents, only CGO shows ionic conductivity, and hence, contributes to the ionic conduction during oxygen permeation, while FCO, CoO and GCFCO are good electronic conductors and responsible for electronic conduction [18, 26]. A result of a scan is shown in Table 7.1, the amount of ionic/electronic conducting phase in CF-1 and CF-2 is comparable, and electronic conducting phases are characterized to possess a minor volume.

Table 7.1 Volume fractions of individual phases in the sintered membranes.

Sample	Ionic conducting phase	Electronic conducting phase				
	CGO (vol%)	FCO (vol%)	GCFCO (vol%)	CoO (vol%)	Sum (vol%)	
CF-1	81.1	8.5	9.8	0.6	18.9	
CF-2	82.3	7.6	10.1	-	17.7	
CF-D	Monophase zone	99.7	0.1	0.1	0.1	0.3
	Multiphase zone	68.4	19.9	7.9	3.9	31.6

By contrast, phase amounts are fairly different in the two phase zones in CF-D, as shown in Table 7.1. The monophase zone in CF-D can be regarded as pure CGO phase despite the existence of a small amount of FCO and GCFCO. The amount of electron conducting phases is almost two times higher in the multiphase zone in CF-D than in either CF-1 or CF-2, representing the original 70 wt% $\text{Ce}_{0.8}\text{Gd}_{0.2}\text{O}_{2-\delta}$:30 wt% FeCo_2O_4 powder mixtures. This reveals that the concept of using a pure ion

conducting phase and a mixed ionic-electronic conducting composite with high electronic conductivity to form a novel “dual phase” works from the microstructural point of view.

7.3.3 Oxygen permeation

The helium leakage rates of all sintered membranes are determined to be below 10^{-8} mbar·L·s⁻¹, which confirms dense microstructures that are sufficient for oxygen permeation measurements.

The oxygen permeance, i.e. oxygen permeation flux (see Figure A7.3) normalized by the oxygen partial pressure gradient (see equation (7.4)) as a function of temperature [15], is provided in Figure 7.9, as determined via:

$$Permeance = \frac{J_{O_2}}{\ln \frac{P'_{O_2}}{P''_{O_2}}} \quad (7.4)$$

where J_{O_2} is the oxygen permeation flux; P'_{O_2} and P''_{O_2} are oxygen partial pressure of oxygen rich and lean side of the membrane.

For the coated membranes, the limiting effect from surface exchange is believed to be overcome by a LSCF coating so that oxygen permeation process is merely limited by bulk diffusion, the oxygen permeance can be expressed as [18, 35]:

$$Permeance = \frac{R}{16 \cdot F^2} \cdot \frac{1}{L} \cdot \sigma_{amb} \cdot T \quad (7.5)$$

where T is the temperature, R the gas constant, L the thickness of the membrane, F the Faraday constant. At a fixed temperature, σ_{amb} is a constant, hence, oxygen permeance tends to increase with decreasing thickness according to equation (7.5). The activation energy of oxygen permeance is independent of thickness but equal to the activation energy of bulk diffusion represented by $\sigma_{amb} \cdot T$, which can be described by an Arrhenius approach.

The cross section of the coated membrane is shown in Figure 7.9 for CF-D as an example. A $\sim 4 \mu\text{m}$ thick porous coating was successfully synthesized at the surface of CF-D. The coating possesses an LSCF perovskite structure as revealed by XRD (see Figure A7.2). The EDS mapping at the interface (see Figure A7.3) indicates no significant element diffusion between the coating and substrate. Similar coatings were also prepared for CF-1 and CF-2.



Figure 7.9 Cross section of the coated CF-D.

For the coated CF-D, average oxygen fluxes (see Figure A7.4) were obtained, and the experimental errors for each oxygen flux value are $\sim \pm 2\%$, the upper and lower bounds of which represent oxygen fluxes of two samples. The temperature difference between the two samples is less than 7 K, i.e. $< 0.7\%$, for each data point. For other membranes, the experimental errors of oxygen fluxes were estimated to be the same due to the same test conditions and the reproducible microstructures.

The oxygen permeances of the coated membranes increase in the order of CF-1 < CF-2 < CF-D (see Figure 7.10), which indicates that the limiting effect from bulk diffusion decreases following CF-1 > CF-2 > CF-D.

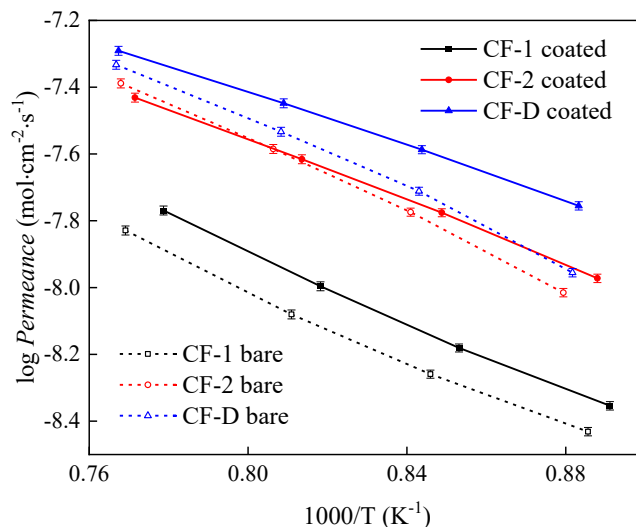


Figure 7.10 Oxygen permeances of the sintered membranes with an average thickness of $\sim 0.95 \pm 0.02$ mm.

When compared with the oxygen flux reported for the LSCF coated 85 wt% $\text{Ce}_{0.8}\text{Gd}_{0.2}\text{O}_{2-\delta}$ -15 wt% FeCo_2O_4 composite prepared by a Pechini process [15], the oxygen flux of the coated CF-D is lower as can be seen from Table 7.2. It should be noted that these results were obtained under the same test conditions and similar sample dimensions. It indicates that the microstructure obtained by the Pechini process is advantageous for preparing a better performing dual phase membrane. However, the Pechini process involves expensive raw materials, significant NO_x emissions, and is difficult to scale up. By contrast, the solid-state reactive sintering process we used contains facile treatments of commercially available precursor powders, which benefits for a feasible upscaling production. For commercialization, a balance of processing efforts and performance benefits has to be found.

Table 7.2 Comparison of oxygen fluxes of the membranes prepared by different methods.

Preparation methods	J_{O_2} (mL·cm ⁻² ·min ⁻¹)		Reference
	850 °C	900 °C	
Pechini	0.16	0.20	[15]
Solid-state reactive sintering	0.11	0.15	This work (the coated CF-D)

The activation energy (E_a) of oxygen permeance was calculated from the Arrhenius plot of oxygen permeance for each membrane, as listed in Table 7.3. In contrast to the oxygen permeance, E_a values for the coated membranes decrease in an order CF-1 > CF-2 > CF-D. The E_a value of the coated CF-D is nearly the same as the E_a value of ionic conductivity of $Ce_{0.8}Gd_{0.2}O_{2-\delta}$ (~ 79 kJ/mol [16]), which suggests that the ionic conduction within CGO is the rate-limiting steps in the coated CF-D. The E_a value of the coated CF-2 is marginally higher than the E_a value of ionic conductivity of $Ce_{0.8}Gd_{0.2}O_{2-\delta}$. Nevertheless, it can still be indicative that the ionic conduction within CGO is the permeation rate-limiting steps in the coated CF-2, but the ionic conductivity of CGO in CF-2 is lower than that of $Ce_{0.8}Gd_{0.2}O_{2-\delta}$, which can be attributed to the depletion of Gd within CGO, after phase interactions. Since such phase interactions only occur at the multiphase zone in CF-D, the composition of CGO in the monophasic zone is close to that of $Ce_{0.8}Gd_{0.2}O_{2-\delta}$, ensuring fast ionic conduction. In comparison, the E_a value of the coated CF-1 is close to the E_a value of electronic conductivity of $FeCo_2O_4$ (~ 102 kJ/mol [15]), suggesting the electronic conduction within FCO is the rate-limiting step.

Table 7.3 Activation energies of oxygen permeances of the sintered membranes.

Sample	E_a (kJ/mol)	
	bare	coated
CF-1	99 ± 5	100 ± 4
CF-2	107 ± 4	89 ± 2
CF-D	103 ± 5	77 ± 2

These results emphasize the importance of the microstructure in a composite, in particular when the phase ratio is in the range where the transition of the rate limiting mechanism from ion to electron conduction occurs. Although the volume of electronic conducting phases is almost the same in all samples, the total number of grains of the electronic conducting phases is lower in CF-1 than in CF-2 due to the existence of large FCO grains (see Figure 7.5(a)). Considering each grain of electronic conducting phases as one unit in continuous electronic conducting networks, it is harder to form long-range free paths for electronic conduction in CF-1 than in CF-2. The best percolations of ionic and electronic conducting phases are formed in CF-D through, respectively, the monophasic zone and the multiphase zone.

Possible diffusion paths through each membrane are illustrated and compared in Figure 7.11. The electronic conduction in CF-1 might partially rely on the Co-rich grain boundary phases, which bridge the neighbouring grains of electronic conducting phases, but only provides limited electronic conduction due to a bottleneck effect. As a consequence, CF-1 tends to possess the lowest performance, although the volume fraction of ionic/electronic conducting phases within CF-1 and CF-2 is similar (see Table 7.1). Such a blocking effect on electronic conduction is overcome in the CF-2 by an increased amount of robust electronic conductive paths through smaller grains (see Figure 7.11(b)), providing a higher effective electronic conductivity. Since the intrinsic electronic conductivity of FeCo_2O_4 is almost two orders higher than the intrinsic ionic conductivity of CGO [26], once there are robust

paths for conducting electrons, the bulk diffusion is limited by the ionic conductivity through the CGO.

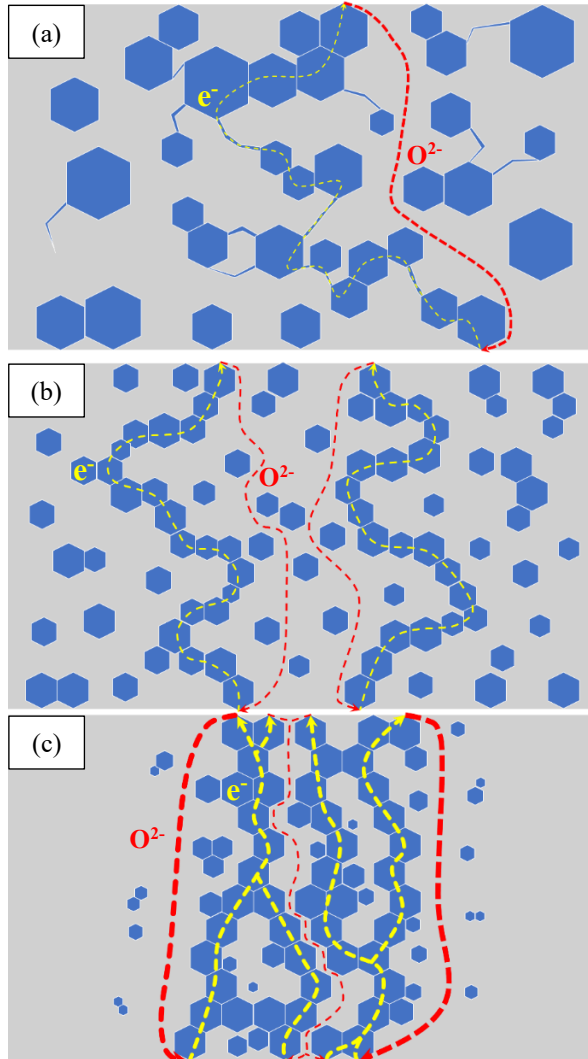


Figure 7.11 Schematic illustrating oxygen ion diffusion paths (red dashed lines) through ionic conducting phase (grey background) and electrons diffusion paths (yellow dashed lines) through electronic conducting phases (blue hexagons) in (a) CF-1, (b) CF-2 and (c) CF-D. The thicker lines represent better paths with less tortuosity.

CF-D appears to have more free paths for electronic conduction with lesser tortuosity since the small grains of electronic conducting phases are concentrated in the multiphase zone and closer to each other (see Figure 7.11(c)). More importantly, CGO within the monophase zone, which can be regarded as $\text{Ce}_{0.8}\text{Gd}_{0.2}\text{O}_{2-\delta}$ and has a somewhat higher ionic conductivity than the Gd-depleted CGO within CF-2, provides rather straight conductive paths dominating the ionic conduction within CF-D. Therefore, CF-D shows the highest performance, in particular when the porous LSCF coating distributes electrons on the surface instantaneously suppressing surface exchange limitations.

For the bare membranes, the oxygen permeance of CF-D is slightly higher than that of the CF-2 but remarkably higher than that of CF-1 (see Figure 7.10), which suggests that both surface exchange and bulk diffusion are faster during oxygen permeation in CF-2 and CF-D than in CF-1. The oxygen permeances of bare CF-1 and CF-D are lower than that of the coated CF-1 and CF-D, respectively, over the entire temperature range due to the sluggish surface exchange [22], while the oxygen permeance of bare CF-2 is marginally lower than that of the coated CF-2 below ~ 950 °C. This reflects the existence of limitations from the surface exchange during the oxygen permeation within the bare membranes. It is noteworthy that for CF-2 the improvement of oxygen permeance by LSCF coating is relatively low. This indicates that the surface exchange at the bare surface is relatively fast related to the fine and homogeneous microstructures providing long TPBs at the surface.

The bare samples share similar high E_a values (see Table 7.3), indicating the same permeation rate-limiting factors. The E_a value of bare CF-1 is comparable to that of the coated CF-1, while the E_a values of bare CF-2 and CF-D are larger than that of the coated CF-2 and CF-D, respectively, indicating different permeation rate-limiting steps, i.e. increased surface exchange influence [15].

Although the E_a values of the bare membranes are close to that of electronic conductivity of FeCo_2O_4 , it is unlikely that the electronic conductivity becomes rate-limiting. It is rather likely that the oxygen permeance is controlled by both surface

exchange and bulk diffusion, which is investigated by comparing two different membrane thicknesses.

When the limiting effects from surface exchange are not negligible, the oxygen permeance is reduced according to [35]:

$$Permeance = \frac{1}{1 + \frac{2 \cdot L_c}{L}} \cdot \frac{R}{16 \cdot F^2} \cdot \frac{1}{L} \cdot \sigma_{amb} \cdot T \quad (7.6)$$

where L_c is the characteristic thickness, defined as the thickness where oxygen permeation process experiences equal resistance from bulk diffusion and surface exchange [36]. When $L_c \ll L$, the limiting effect from surface exchange is negligible, hence, bulk diffusion is the major rate limiting factor, and equation (7.6) can be simplified leading to equation (7.5). However, when L is in the vicinity of L_c , the limiting effects from surface exchange are nonnegligible, and oxygen permeance and its activation energy are then sensitive to thickness changes [35].

Figure 7.12 compares oxygen permeances of two bare CF-2 membranes with different thicknesses. Although the thickness difference is small (~ 0.2 mm), the change of oxygen permeance, as well as its activation energy are significant. The oxygen permeance is improved when the thickness is reduced as expected according to equation (7.5), and the improvement is more significant at high temperatures, correlated with the increase of the activation energy. The bare 0.76 mm thick membrane has a higher activation energy of oxygen permeance indicating an increased limiting effect from surface exchange compared to the 0.96 mm thick membrane. For the bare 0.96 mm thick CF-2 membrane, the activation energy of oxygen permeance is smaller, but still higher than that of the coated CF-2 membrane (see Table 7.3).

It can be concluded that for the bare CF-2 the oxygen permeation is controlled by both surface exchange and bulk diffusion in the investigated region of thickness and temperature. With activation energy of oxygen permeance similar to that of the bare

CF-2, the bare CF-1 and CF-D, are expected to suffer from the same multiple bottlenecks during oxygen permeation as the bare CF-2. The surface exchange characteristics of composites need further attention because it is not only an intrinsic material property but dependent on the length of TPBs present at the surface and, thus, again microstructure dependent.

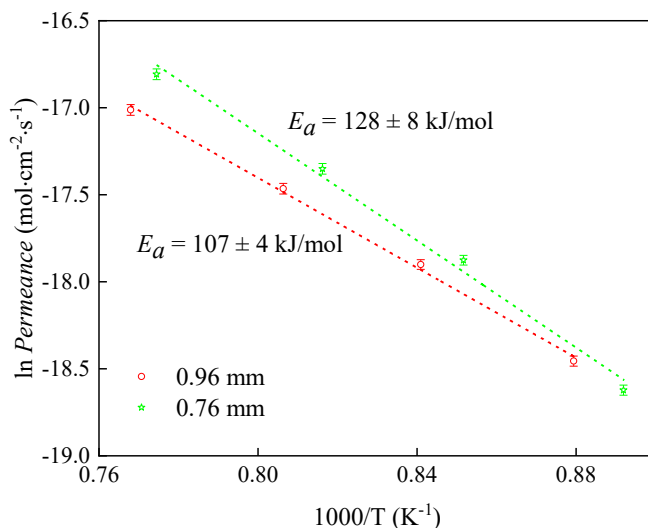


Figure 7.12 Arrhenius plot of oxygen permeance of CF-2 with different thicknesses.

Given that the coated CF-D exhibits the highest oxygen permeance, the stability of the coated CF-D was investigated. One coated CF-D sample was operated for ~ 335 h at $\sim 863 \pm 1$ °C using the same test conditions as described in the experimental section; the gas analysis was stopped twice for recalibration of the mass spectrometer. As presented in Figure 7.13, the oxygen permeation flux of the coated CF-D first experiences a slight decrease of ~ 4 % from the initial state or from the initial state after each recalibration within a relatively short time (less than 40 h), then remained constant at ~ 96 % of the initial value.

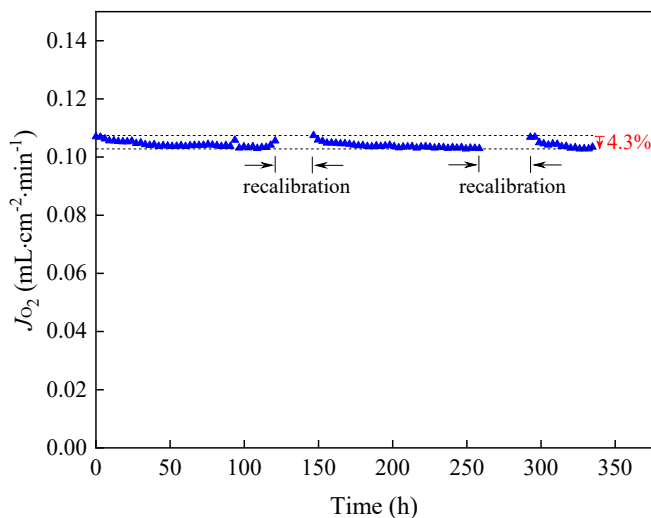


Figure 7.13 Oxygen permeation flux of the coated CF-D at $\sim 863 \pm 1$ °C as a function of time.

After operation for this long-term oxygen permeation test, the sample was fractured to reveal the cross section for further investigations. When compared with the cross section of the fresh sample, the cross section at the argon side of the measured sample shows no significant difference in microstructure (as can be seen by comparing Figure 7.14(a) and Figure 7.9) or elemental distribution (see Figure A7.3 and Figure A7.5). However, the cross section at the air side of the measured sample (see Figure 7.14(b)) exhibits different characteristics: several grains segregate out of the multiphase zone at the interface between membrane and activation layer. These grains appear to be FCO grains since they mainly contain Fe and Co (as revealed by EDS mapping shown in Figure A7.6). Such phase segregation was also observed for the same composite prepared by a Pechini process [15], and was reported to have a limited influence on oxygen permeation in the measured time frame [15]. Similarly, the segregated FCO grains at the air side shown here have not caused a significant decrease in oxygen permeation flux over 335 h as shown in Figure 7.13.

Therefore, considering the fact that the oxygen permeation flux of the coated CF-D stabilizes at around 96 % of the initial value after an operation time > 300 h despite

the phase segregation, a rather stable performance regarding oxygen permeation can be concluded for the CF-D.

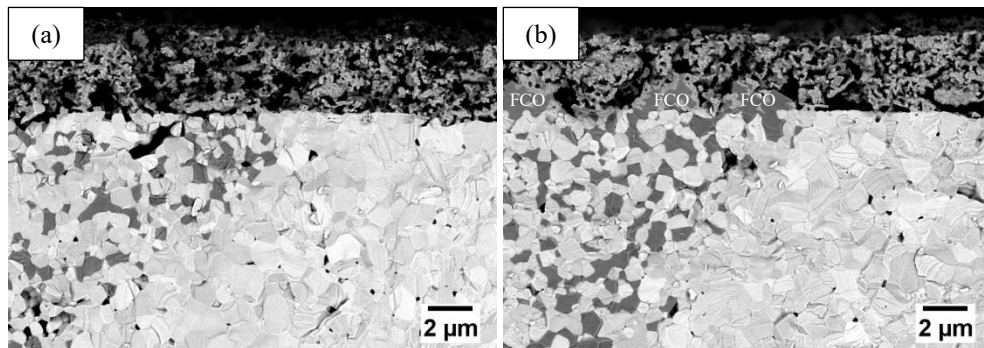


Figure 7.14 Cross sections at the (a) argon and the (b) air sides of the coated CF-D after a long-term (over 300 h) permeation test.

7.4 Conclusions

85 wt% $\text{Ce}_{0.8}\text{Gd}_{0.2}\text{O}_{2-\delta}$ -15 wt% FeCo_2O_4 composites were prepared by solid-state reactive sintering using powder mixtures containing $\text{Ce}_{0.8}\text{Gd}_{0.2}\text{O}_{2-\delta}$, Co_3O_4 and Fe_2O_3 as precursor powders. Different powder preparation methods were used to synthesize membranes with varied microstructural characteristics.

The results reveal that homogenous microstructures were obtained using the powder mixtures prepared by the traditional ball milling method. The particle sizes of powder mixtures are reduced gradually with increasing milling time and reduction of the ball size due to the improved crushing effect on agglomerates. The reduced particle sizes of powder mixtures contribute to sintering a membrane with a fine and homogeneous microstructure, which exhibits higher oxygen permeance than the membrane with large grains due to good connections between ionic/electronic conducting phase and long TPBs at the surfaces. In comparison, a rather inhomogeneous microstructure with fine grains was sintered using inhomogeneous powder mixtures, which were prepared by dry mixing of $\text{Ce}_{0.8}\text{Gd}_{0.2}\text{O}_{2-\delta}$ powders with 70 wt% $\text{Ce}_{0.8}\text{Gd}_{0.2}\text{O}_{2-\delta}$:30 wt% FeCo_2O_4 powders resulting in the same nominal

weight ratio 85:15 of $\text{Ce}_{0.8}\text{Gd}_{0.2}\text{O}_{2-\delta}$ and FeCo_2O_4 . The fine but inhomogeneous microstructure exhibits two clearly distinguishable and percolating phase zones: one monophase zone mainly consisting of $\text{Ce}_{0.8}\text{Gd}_{0.2}\text{O}_{2-\delta}$, permitting fast ionic conduction through relatively straight paths, and a multiphase zone containing both ionic and electronic conducting phases, providing mixed ionic-electronic conductivity with high electronic conduction through robust paths. Such a novel microstructure results in the highest oxygen permeance.

We present the successful synthesis of such a novel “dual phase” membrane containing a pure ionic conducting phase and a mixed ionic-electronic conducting composite with high electronic conductivity, which demonstrates how the limiting effect on bulk diffusion caused by unfavorable microstructural characteristics can be overcome. Further improvements are expected by using alternative ionic conducting compounds with high intrinsic ionic conductivity.

References

- [1] X. Bi, X. Meng, P. Liu, N. Yang, Z. Zhu, R. Ran, S. Liu, A novel CO_2 -resistant ceramic dual-phase hollow fiber membrane for oxygen separation, *Journal of Membrane Science* 522 (2017) 91-99.
- [2] C. Li, W. Li, J.J. Chew, S. Liu, X. Zhu, J. Sunarso, Oxygen permeation through single-phase perovskite membrane: Modeling study and comparison with the dual-phase membrane, *Separation and Purification Technology* 235 (2020) 116224.
- [3] M. Czaperek, P. Zapp, H.J.M. Bouwmeester, M. Modigell, K.V. Peinemann, I. Voigt, W.A. Meulenber, L. Singheiser, D. Stöver, MEM-BRAIN gas separation membranes for zero-emission fossil power plants, *Energy Procedia* 1(1) (2009) 303-310.
- [4] M. Czaperek, P. Zapp, H.J.M. Bouwmeester, M. Modigell, K. Ebert, I. Voigt, W.A. Meulenber, L. Singheiser, D. Stöver, Gas separation membranes for zero-emission fossil power plants: MEM-BRAIN, *Journal of Membrane Science* 359(1-2) (2010) 149-159.
- [5] J. Garcia-Fayos, J.M. Serra, M.W.J. Luiten-Olieman, W.A. Meulenber, 8-Gas separation ceramic membranes, in: O. Guillon (Ed.), *Advanced Ceramics for Energy Conversion and Storage*, Elsevier2020, pp. 321-385.

- [6] J. Garcia-Fayos, M. Balaguer, J.M. Serra, Dual-Phase Oxygen Transport Membranes for Stable Operation in Environments Containing Carbon Dioxide and Sulfur Dioxide, *ChemSusChem* 8(24) (2015) 4242-4249.
- [7] S. Baumann, J. Serra, M. Lobera, S. Escolástico, F. Schulze-Küppers, W.A. Meulenber, Ultrahigh oxygen permeation flux through supported $\text{Ba}_{0.5}\text{Sr}_{0.5}\text{Co}_{0.8}\text{Fe}_{0.2}\text{O}_{3-\delta}$ membranes, *Journal of Membrane Science* 377(1-2) (2011) 198-205.
- [8] J.M. Serra, J. Garcia-Fayos, S. Baumann, F. Schulze-Küppers, W.A. Meulenber, Oxygen permeation through tape-cast asymmetric all- $\text{La}_{0.6}\text{Sr}_{0.4}\text{Co}_{0.2}\text{Fe}_{0.8}\text{O}_{3-\delta}$ membranes, *Journal of Membrane Science* 447 (2013) 297-305.
- [9] B. Wei, Z. Lü, S. Li, Y. Liu, K. Liu, W. Su, Thermal and electrical properties of new cathode material $\text{Ba}_{0.5}\text{Sr}_{0.5}\text{Co}_{0.8}\text{Fe}_{0.2}\text{O}_{3-\delta}$ for solid oxide fuel cells, *Electrochemical and Solid-State Letters* 8(8) (2005) A428-A431.
- [10] S.R. Bishop, K.L. Duncan, E.D. Wachsman, Thermo-Chemical Expansion in Strontium-Doped Lanthanum Cobalt Iron Oxide, *Journal of the American Ceramic Society* 93(12) (2010) 4115-4121.
- [11] C. Zhang, J. Sunarso, S. Liu, Designing CO_2 -resistant oxygen-selective mixed ionic-electronic conducting membranes: guidelines, recent advances, and forward directions, *Chemical Society Reviews* 46(10) (2017) 2941-3005.
- [12] J.H. Joo, K.S. Yun, C.-Y. Yoo, J.H. Yu, Novel oxygen transport membranes with tunable segmented structures, *Journal of Materials Chemistry A* 2(22) (2014) 8174-8178.
- [13] K. Zhang, Z. Shao, C. Li, S. Liu, Novel CO_2 -tolerant ion-transporting ceramic membranes with an external short circuit for oxygen separation at intermediate temperatures, *Energy & Environmental Science* 5(1) (2012) 5257-5264.
- [14] K.S. Yun, C.-Y. Yoo, S.-G. Yoon, J.H. Yu, J.H. Joo, Chemically and thermo-mechanically stable LSM-YSZ segmented oxygen permeable ceramic membrane, *Journal of Membrane Science* 486 (2015) 222-228.
- [15] M. Ramasamy, E. Persoon, S. Baumann, M. Schroeder, F. Schulze-Küppers, D. Görtz, R. Bhave, M. Bram, W.A. Meulenber, Structural and chemical stability of high performance $\text{Ce}_{0.8}\text{Gd}_{0.2}\text{O}_{2-\delta}\text{-FeCo}_2\text{O}_4$ dual phase oxygen transport membranes, *Journal of Membrane Science* 544 (2017) 278-286.
- [16] Y. Lin, S. Fang, D. Su, K.S. Brinkman, F. Chen, Enhancing grain boundary ionic conductivity in mixed ionic-electronic conductors, *Nature communications* 6 (2015) 6824.
- [17] H. Luo, H. Jiang, T. Klande, F. Liang, Z. Cao, H. Wang, J. Caro, Rapid glycine-nitrate combustion synthesis of the CO_2 -stable dual phase membrane $40\text{Mn}_{1.5}\text{Co}_{1.5}\text{O}_{4-\delta}$

- 60Ce_{0.9}Pr_{0.1}O_{2-δ} for CO₂ capture via an oxy-fuel process, *Journal of Membrane Science* 423-424 (2012) 450-458.
- [18] F. Zeng, J. Malzbender, S. Baumann, M. Krüger, L. Winnubst, O. Guillon, W.A. Meulenbergh, Phase and microstructural characterizations for Ce_{0.8}Gd_{0.2}O_{2-δ}-FeCo₂O₄ dual phase oxygen transport membranes, *Journal of the European Ceramic Society* 40(15) (2020) 5646-5652.
- [19] F. Zeng, J. Malzbender, S. Baumann, A. Nijmeijer, L. Winnubst, M. Ziegner, O. Guillon, R. Schwaiger, W.A. Meulenbergh, Optimization of sintering conditions for improved microstructural and mechanical properties of dense Ce_{0.8}Gd_{0.2}O_{2-δ}-FeCo₂O₄ oxygen transport membranes, *Journal of the European Ceramic Society* 41(1) (2021) 509-516.
- [20] F. Zeng, J. Malzbender, S. Baumann, W. Zhou, M. Ziegner, A. Nijmeijer, O. Guillon, R. Schwaiger, W.A. Meulenbergh, Mechanical reliability of Ce_{0.8}Gd_{0.2}O_{2-δ}-FeCo₂O₄ dual phase membranes synthesized by one-step solid-state reaction, *Journal of the American Ceramic Society* 00 (2020) 1-17.
- [21] X. Zhu, W. Yang, *Mixed conducting ceramic membranes*, Springer-Verlag, Berlin, Germany, 2017.
- [22] M. Ramasamy, S. Baumann, J. Palisaitis, F. Schulze-Küppers, M. Balaguer, D. Kim, W.A. Meulenbergh, J. Mayer, R. Bhave, O. Guillon, Influence of Microstructure and Surface Activation of Dual-Phase Membrane Ce_{0.8}Gd_{0.2}O_{2-δ}-FeCo₂O₄ on Oxygen Permeation, *Journal of the American Ceramic Society* 99(1) (2016) 349-355.
- [23] X. Zhu, H. Wang, W. Yang, Relationship between homogeneity and oxygen permeability of composite membranes, *Journal of Membrane Science* 309(1) (2008) 120-127.
- [24] Q. Li, X. Zhu, Y. He, Y. Cong, W. Yang, Effects of sintering temperature on properties of dual-phase oxygen permeable membranes, *Journal of Membrane Science* 367(1) (2011) 134-140.
- [25] Z. Fan, A. Miodownik, P. Tsakirooulos, Microstructural characterisation of two phase materials, *Materials science technology* 9(12) (1993) 1094-1100.
- [26] U. Pippardt, J. Boer, C. Bollert, A. Hoffmann, M. Heidenreich, R. Kriegel, M. Schulz, A. Simon, Performance and stability of mixed conducting composite membranes based on substituted ceria, *Journal of Ceramic Science and Technology* 5(04) (2014) 309-316.
- [27] M. Ramasamy, S. Baumann, A. Opitz, R. Iskandar, J. Mayer, D. Udomsilp, U. Breuer, M. Bram, Phase Interaction and Distribution in Mixed Ionic Electronic Conducting Ceria-

Spinel Composites, *Advances in Solid Oxide Fuel Cells Electronic Ceramics II: Ceramic Engineering Science Proceedings* 37(3) (2017) 99-112.

[28] H. Takamura, K. Okumura, Y. Koshino, A. Kamegawa, M. Okada, Oxygen permeation properties of ceria-ferrite-based composites, *Journal of Electroceramics* 13(1-3) (2004) 613-618.

[29] H. Li, X. Zhu, Y. Liu, W. Wang, W. Yang, Comparative investigation of dual-phase membranes containing cobalt and iron-based mixed conducting perovskite for oxygen permeation, *Journal of Membrane Science* 462 (2014) 170-177.

[30] X. Zhu, Y. Liu, Y. Cong, W. Yang, $\text{Ce}_{0.85}\text{Sm}_{0.15}\text{O}_{1.925}\text{-Sm}_{0.6}\text{Sr}_{0.4}\text{Al}_{0.3}\text{Fe}_{0.7}\text{O}_3$ dual-phase membranes: One-pot synthesis and stability in a CO_2 atmosphere, *Solid State Ionics* 253 (2013) 57-63.

[31] A.J. Schwartz, M. Kumar, B.L. Adams, D.P. Field, *Electron backscatter diffraction in materials science*, Springer, New York, USA, 2009.

[32] C.A. Schneider, W.S. Rasband, K.W. Eliceiri, NIH Image to ImageJ: 25 years of image analysis, *Nature Methods* 9(7) (2012) 671-675.

[33] C. Kleinlogel, L.J. Gauckler, Sintering and properties of nanosized ceria solid solutions, *Solid State Ionics* 135(1-4) (2000) 567-573.

[34] F. Zeng, J. Malzbender, S. Baumann, F. Schulze-Küppers, M. Krüger, A. Nijmeijer, O. Guillon, W.A. Meulenberg, Micromechanical Characterization of $\text{Ce}_{0.8}\text{Gd}_{0.2}\text{O}_{2-\delta}\text{-FeCo}_2\text{O}_4$ Dual Phase Oxygen Transport Membranes, *Advanced Engineering Materials* 22(6) (2020) 1901558.

[35] J.H. Joo, G.S. Park, C.-Y. Yoo, J.H. Yu, Contribution of the surface exchange kinetics to the oxygen transport properties in $\text{Gd}_{0.1}\text{Ce}_{0.9}\text{O}_{2-\delta}\text{-La}_{0.6}\text{Sr}_{0.4}\text{Co}_{0.2}\text{Fe}_{0.8}\text{O}_{3-\delta}$ dual-phase membrane, *Solid State Ionics* 253 (2013) 64-69.

[36] C. Li, W. Li, J.J. Chew, S. Liu, X. Zhu, J. Sunarso, Rate determining step in SDC-SSAF dual-phase oxygen permeation membrane, *Journal of Membrane Science* 573 (2019) 628-638.

Appendix A7

Table A7.1 Atomic fractions of Ce and Gd in CGO in CF-D.

Phase zone	Ce	Gd	Ce/Gd
Monophase zone	79.8	20.2	3.9
Multiphase zone	82.4	17.6	4.7

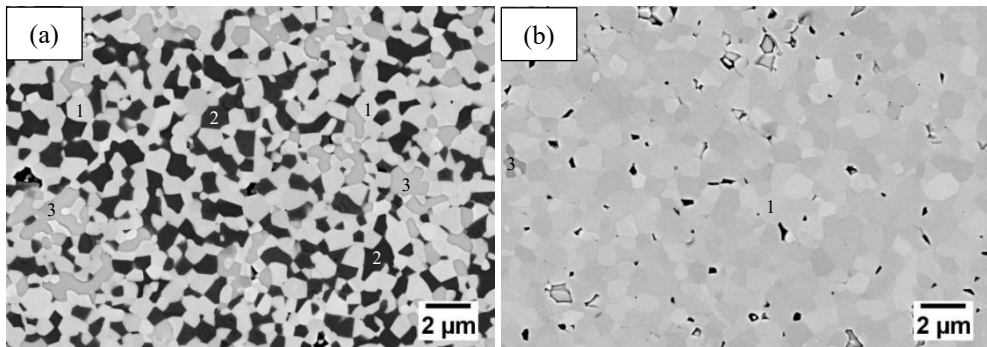


Figure A7.1 Microstructural comparison of (a) the multiphase zone and (b) the monophase zone in CF-D. Several grains are marked as 1, 2 and 3 as examples representing for CGO, FCO (or CoO) and GCFCO grains, respectively.

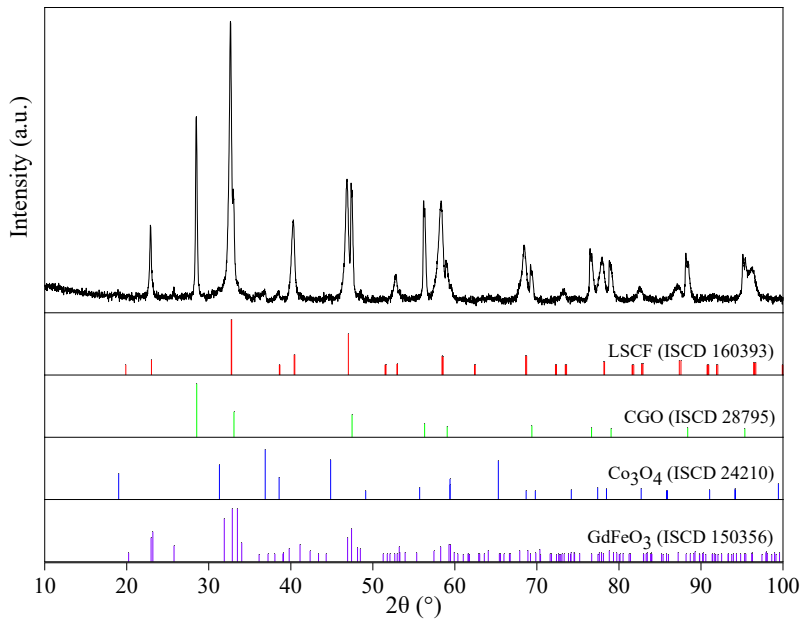


Figure A7.2 XRD patterns investigated at the surface of CF-D membrane coated with LSCF. Crystal structures of both coating and substrate materials were detected because the penetration depth of the X-Rays is larger compared to the coating thickness.

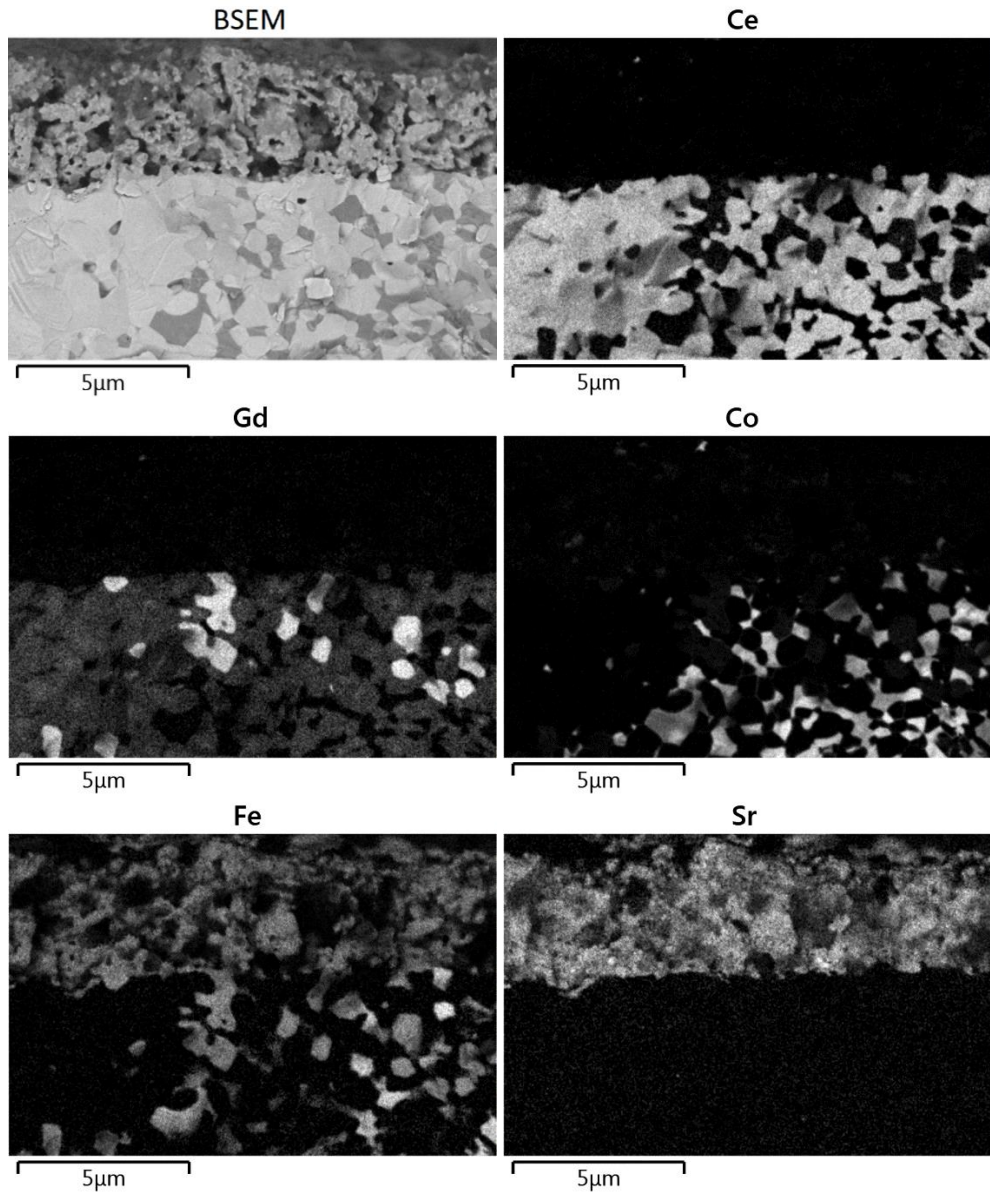


Figure A7.3 BSEM micrograph and corresponding EDS elements mapping on the cross-section of the coated CF-D. The La mapping is not shown since the La signal overlaps with Fe and/or Co signal creating artefacts in mappings.

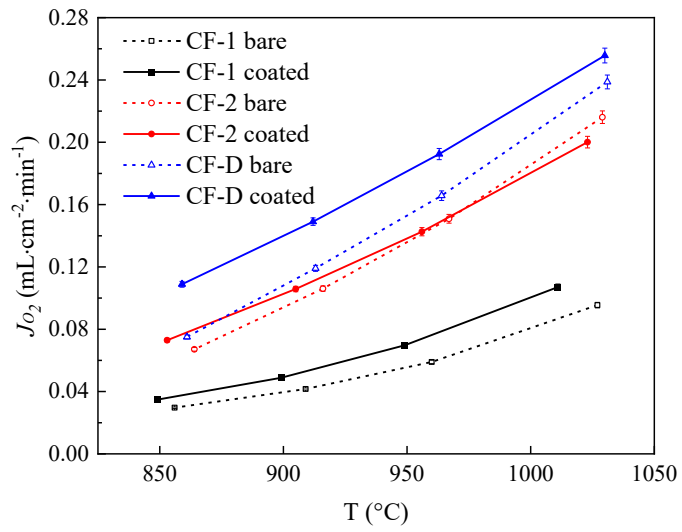


Figure A7.4 Oxygen permeation fluxes of the sintered membranes.

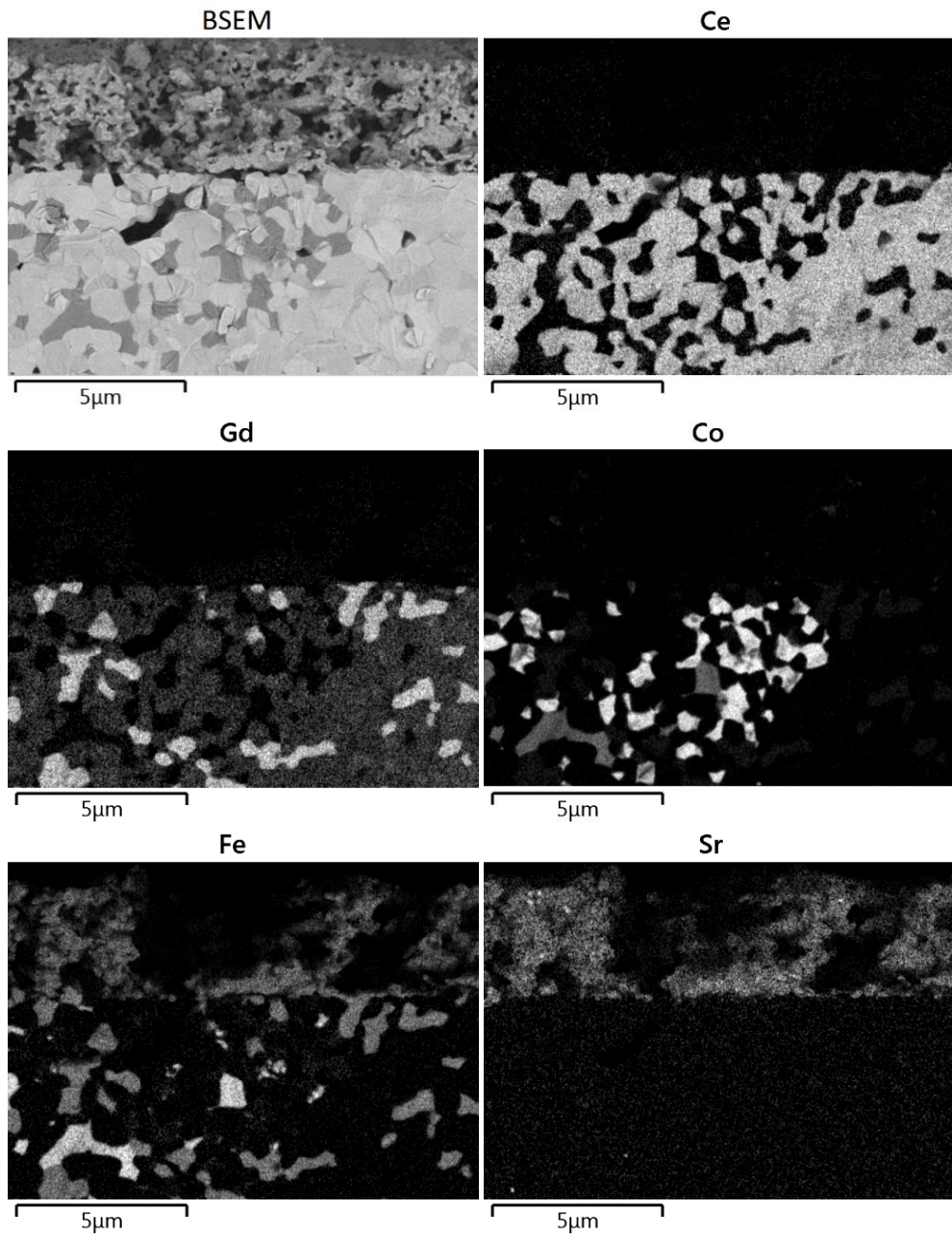


Figure A7.5 BSEM micrograph and corresponding EDS elements mapping on the cross-section at the argon side of the coated CF-D after long term permeation test.

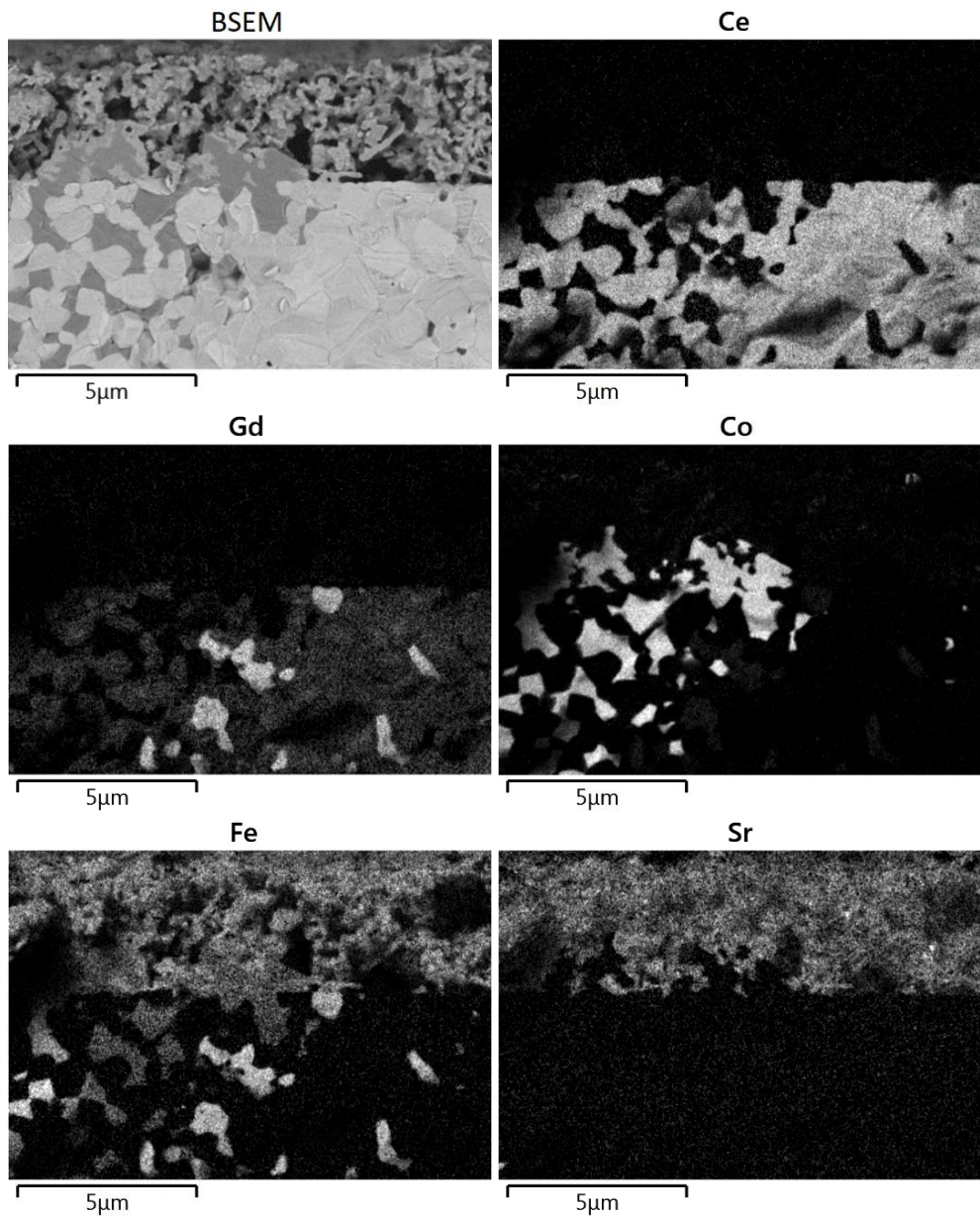


Figure A7.6 BSEM micrograph and corresponding EDS elements mapping on the cross-section at the air side of the coated CF-D after long term permeation test.

CHAPTER 8

Reflections and perspectives

8.1 Introduction

This chapter reflects the significances of the overall findings with regard to the influence of powder preparation and sintering profile on mechanical reliability, oxygen permeation and associated microstructural characteristics of $\text{Ce}_{0.8}\text{Gd}_{0.2}\text{O}_{2-\delta}$ - FeCo_2O_4 dual phase membranes, and provides recommendations for further improvement on the oxygen permeation of the very promising membrane material - 85 wt% $\text{Ce}_{0.8}\text{Gd}_{0.2}\text{O}_{2-\delta}$ -15 wt% FeCo_2O_4 [1-2]. In addition, several aspects that may impact the long-term reliable operation of the membrane are suggested for research in future studies.

8.2 Powder preparation

8.2.1 Powder composition

As shown in **Chapter 2**, the sintered nominal $\text{Ce}_{0.8}\text{Gd}_{0.2}\text{O}_{2-\delta}$ - FeCo_2O_4 dual phase membranes contain a $\text{Ce}_{0.9}\text{Gd}_{0.1}\text{O}_{2-\delta}$ phase instead of the expected $\text{Ce}_{0.8}\text{Gd}_{0.2}\text{O}_{2-\delta}$ phase since the formation of the $\text{Gd}_{0.85}\text{Ce}_{0.15}\text{Fe}_{0.75}\text{Co}_{0.25}\text{O}_3$ perovskite phase consumes Gd from the raw material - $\text{Ce}_{0.8}\text{Gd}_{0.2}\text{O}_{2-\delta}$ [3]. Since the ionic conductivity of $\text{Ce}_{0.9}\text{Gd}_{0.1}\text{O}_{2-\delta}$ is lower than that of $\text{Ce}_{0.8}\text{Gd}_{0.2}\text{O}_{2-\delta}$ [4], adding additional Gd to the membrane material during processing is expected to improve the ionic conductivity of the membrane and enhance the ambipolar conductivity. The Gd content within the membrane can be increased by adding Gd_2O_3 into the raw material to obtain $\text{Ce}_{0.8}\text{Gd}_{0.2}\text{O}_{2-\delta}$ in the sintered membrane. It is not necessary to obtain $\text{Ce}_{1-x}\text{Gd}_x\text{O}_{2-\delta}$ ($x > 0.2$), since doping 20 mol% Gd into CeO_2 has shown to increase the ionic conductivity to the maximum value [5]. All the Gd from Gd_2O_3 is anticipated to contribute to forming the $\text{Gd}_{0.85}\text{Ce}_{0.15}\text{Fe}_{0.75}\text{Co}_{0.25}\text{O}_3$ or $\text{Ce}_{0.8}\text{Gd}_{0.2}\text{O}_{2-\delta}$ phase.

An initial trial is conducted to form $\text{Ce}_{0.8}\text{Gd}_{0.2}\text{O}_{2-\delta}$ in the membrane. To 100 g “standard” powder mixtures of 85 wt% $\text{Ce}_{0.8}\text{Gd}_{0.2}\text{O}_{2-\delta}$ -15 wt% FeCo_2O_4 , around 8.85 g Gd_2O_3 was added to form nominal $\text{Ce}_{0.7}\text{Gd}_{0.3}\text{O}_{2-\delta}$, which was expected to result in the $\text{Ce}_{0.8}\text{Gd}_{0.2}\text{O}_{2-\delta}$ phase after sintering at 1200 °C.

As shown in Figure 8.1(a), the membrane sintered at 1200 °C and made with the powder mixture of $\text{Ce}_{0.7}\text{Gd}_{0.3}\text{O}_{2-\delta}$ and FeCo_2O_4 consists of CGO, GCFCO, CoO and FCO phase, but contains no Gd_2O_3 phase, which indicates that the Gd_2O_3 is consumed. However, the Ce to Gd ratio within the formed CGO needs further confirmation to verify that the desired $\text{Ce}_{0.8}\text{Gd}_{0.2}\text{O}_{2-\delta}$ is formed. Moreover, the grain sizes shown in Figure 8.1(a) are smaller than the grain sizes shown in Figure 7.5(d) for the membrane sintered at 1200 °C using the standard powder mixtures. The reduced grain size will furthermore contribute to a higher oxygen permeance.

Besides, no obvious pore agglomerates or microcracks could be found (see Figure 8.1(b)), which indicates a well-densified microstructure, being a potential basis of a high mechanical strength.

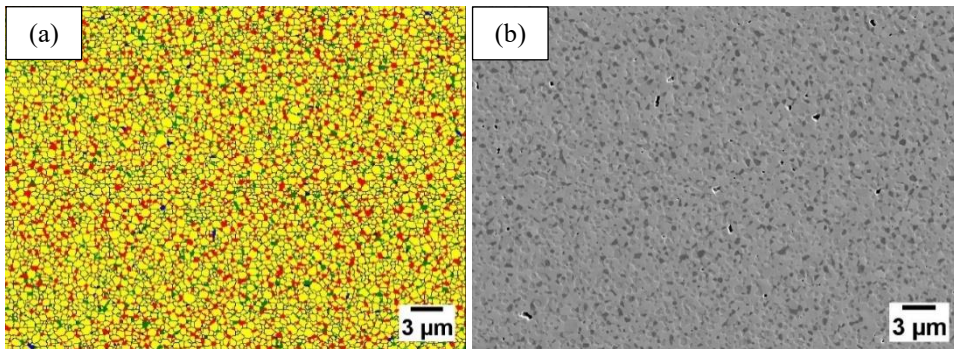


Figure 8.1 EBSD phase mapping (a) and SEM micrograph (b) of the membrane sintered at 1200 °C using a powder mixture of $\text{Ce}_{0.7}\text{Gd}_{0.3}\text{O}_{2-\delta}$ and FeCo_2O_4 . In the EBSD phase mapping, the yellow, blue, red and green phases are CGO, FCO, GCFCO and CoO phases, respectively, while the black spots and dark lines are pores and grain or phase boundaries, respectively.

8.2.2 Powder synthesis methods

For the 85 wt% $\text{Ce}_{0.8}\text{Gd}_{0.2}\text{O}_{2-\delta}$ -15 wt% FeCo_2O_4 membrane, reducing grain sizes of individual phases was shown to improve not only the mechanical reliability but also the oxygen permeance. When the solid-state reactive sintering process is used to prepare the membrane, reducing grain sizes of individual phases mainly relies on the

breaking of agglomerates in the powder mixtures by the two-step ball milling procedure. It is shown that among different wet ball milling procedures, the optimized procedure (i.e. the two-step ball milling procedure) realize the smallest particle size of the powder mixtures, resulting in the smallest grain sizes for the membrane. Further attempts to reduce the grain sizes of the individual phases can be realized by using high energy ball milling to obtain nano-sized particles or using alternative powder synthesis methods to obtain powder mixtures with smaller crystallite sizes.

A spray pyrolysis method was used as an alternative method to synthesise a 85 wt% $\text{Ce}_{0.8}\text{Gd}_{0.2}\text{O}_{2-\delta}$ -15 wt% FeCo_2O_4 powder. Here, an aqueous solution of $\text{Ce}(\text{NO}_3)_3 \cdot 6\text{H}_2\text{O}$, $\text{Gd}(\text{NO}_3)_3 \cdot 6\text{H}_2\text{O}$, $\text{Fe}(\text{NO}_3)_3 \cdot 9\text{H}_2\text{O}$ and $\text{Co}(\text{NO}_3)_2 \cdot 6\text{H}_2\text{O}$ was dissolved in distilled water. After stirring to obtain a homogenous solution, the mixture was sprayed by a nozzle in a drying chamber. The inlet and outlet temperatures during spray drying were $\sim 300\text{ }^\circ\text{C}$ and $\sim 180\text{ }^\circ\text{C}$, respectively. The ejected fine droplets were solidified in hot air from the air disperser. The spray-dried powders were then calcined at $700\text{ }^\circ\text{C}$ for 15 h.

The obtained powders contain a large amount of hollow sphere-shaped particles with relatively large sizes (see Figure 8.2(a)). After experiencing a two-step ball milling procedure (as described in experimental section of **Chapter 4**), the sphere-shaped particles are effectively shattered into nano-sized particles (see Figure 8.2(b)). Further experiments are not done yet, but it is promising to sinter membranes using these nano-sized powders and such sintered membranes are expected to exhibit significantly improved oxygen permeances.

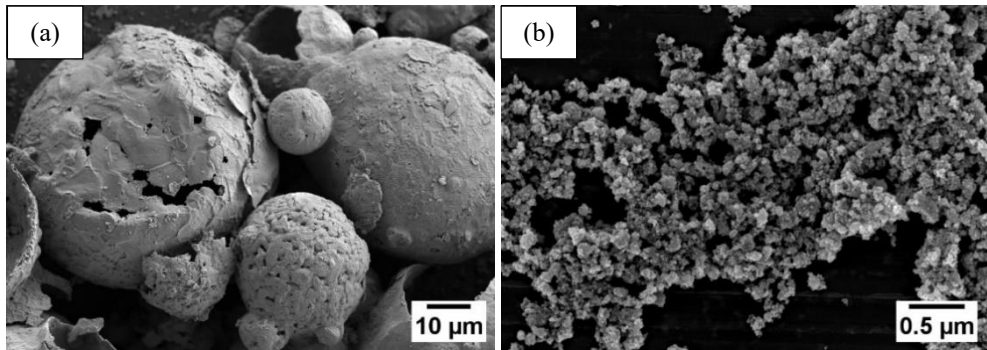


Figure 8.2 Morphologies of the spray pyrolysis synthesized 85 wt% $\text{Ce}_{0.8}\text{Gd}_{0.2}\text{O}_{2-\delta}$ -15 wt% FeCo_2O_4 powders: (a) in the as-prepared state and (b) after a two-step ball milling.

8.3 Sintering profiles

As indicated in **Chapter 4**, the grain size of an 85 wt% $\text{Ce}_{0.8}\text{Gd}_{0.2}\text{O}_{2-\delta}$ -15 wt% FeCo_2O_4 membrane is increasing with varying sintering temperature. The lowest sintering temperature to obtain a dense membrane was $\sim 1050^\circ\text{C}$, where a relatively fine microstructure has been obtained for the membrane. Hence, an improvement in oxygen permeance can be expected from this membrane due to the relative small grain size. However, the rather low sintering temperature also leads to the formation of pore agglomerates, which decreases the mechanical strength. So, to enhance oxygen permeation without sacrificing mechanical strength, it is necessary to develop sintering profiles that result in a well-densified microstructure with suppressed grain growth and pore agglomerate formations.

Here, a two-step sintering profile, in comparison with the one-step sintering profile used in **Chapters 2-7**, is proposed and has already been tested. The temperature was first increased to 1200°C at a rate of 3 K/min, then reduced to 1050°C as fast as possible (e.g. 50 K/min), and held at 1050°C for a limited time (e.g. 2 h) before cooling to room temperature. The microstructure of the two-step sintered 85 wt% $\text{Ce}_{0.8}\text{Gd}_{0.2}\text{O}_{2-\delta}$ -15 wt% FeCo_2O_4 membrane is presented in Figure 8.3. Grain sizes are relatively small, and comparable with the grain sizes of 85 wt% $\text{Ce}_{0.8}\text{Gd}_{0.2}\text{O}_{2-\delta}$ -15 wt% FeCo_2O_4 membrane sintered at 1050°C (see **Chapter 4**, Figure 4.2(e)). Most

importantly, no pore agglomerates are found (see Figure 8.3), indicating that the membrane is well densified. The fine-grained and well-densified membrane is promising to deliver not only high oxygen permanence but also high mechanical strength.

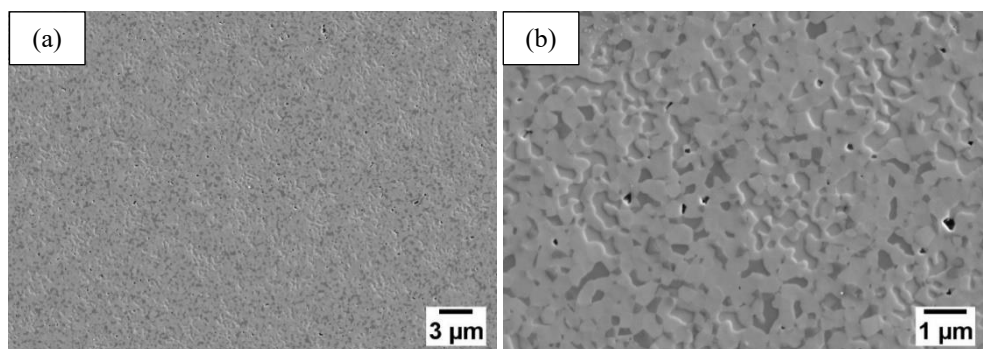


Figure 8.3 Micrographs of the two-step sintered 85 wt% $\text{Ce}_{0.8}\text{Gd}_{0.2}\text{O}_{2-\delta}$ -15 wt% FeCo_2O_4 membrane at (a) smaller and (b) larger magnification.

8.4 Mechanical stability after long-term operation

The two sides of the membrane are working under different atmospheres with varied oxygen partial pressure during oxygen permeation. It was reported for the 85 wt% $\text{Ce}_{0.8}\text{Gd}_{0.2}\text{O}_{2-\delta}$ -15 wt% FeCo_2O_4 membrane that, after oxygen permeation tests, the oxygen-rich side (air side) is enriched with iron cobalt spinel phase, while the oxygen-lean side is short of iron cobalt spinel [1]. The FCO spinel at the oxygen-lean side can possibly be reduced into the rock salt phase. Although no significant degeneration of the oxygen permeance is observed after a 300 h oxygen permeation test [1], the mechanical stability of the membrane operated for an even longer time might be challenging, because of the compositional variations at the two sides of the membrane, which can be expected to induce different stress states at the two sides and possibly induce microcracks. Accordingly, the following aspects that might influence the mechanical stability are recommended to be characterized for the membrane after long term operation:

1. Crystal structures and microstructural defects (e.g. microcracks and voids) of both cross-sections and two sides;
2. Phase transformation (i.e. reduction of spinel phase into rock salt phase) induced volume change under different oxygen partial pressures;
3. Stress states at two sides and stress gradient across the membrane;
4. Fracture behaviours (e.g. defect origins, fracture stresses and subcritical crack growth) associated with the two sides.

8.5 Conclusions

In this thesis, dense $\text{Ce}_{0.8}\text{Gd}_{0.2}\text{O}_{2-\delta}$ - FeCo_2O_4 dual phase membranes are synthesized by solid-state reactive sintering with one-step thermal processing using $\text{Ce}_{0.8}\text{Gd}_{0.2}\text{O}_{2-\delta}$, Co_3O_4 and Fe_2O_3 as raw materials.

It is reflected that the mechanical reliability and oxygen permeation of $\text{Ce}_{0.8}\text{Gd}_{0.2}\text{O}_{2-\delta}$ - FeCo_2O_4 dual phase membranes can be effectively enhanced by adapting the powder preparation procedure and sintering profile to obtain crack-free microstructures with reduced grain sizes. When a long-duration ball milling procedure (i.e. the two-step ball milling procedure) is applied on raw materials and a sintering temperature of 1200 °C is used, the membrane with a nominal composition of 85 wt% $\text{Ce}_{0.8}\text{Gd}_{0.2}\text{O}_{2-\delta}$ -15 wt% FeCo_2O_4 is mechanically more reliable for applications due to its relatively high mechanical strength (~ 266 MPa). This membrane also exhibits significantly improved oxygen permeance due to the enhanced bulk diffusion and surface exchange.

However, for potential industrial applications, further improvements in oxygen permeation are needed without compromising mechanical stability. These improvements can be promisingly realized using nano-sized powder mixtures prepared by spray pyrolysis method and/or applying a two-step sintering profile. Besides, it is necessary to investigate the mechanical stability of the membrane after

a long-term operation under an oxygen partial pressure gradient, since potential compositional gradient and stress gradient can be incurred across the membrane.

References

- [1] M. Ramasamy, E. Persoon, S. Baumann, M. Schroeder, F. Schulze-Küppers, D. Görtz, R. Bhave, M. Bram, W.A. Meulenber, Structural and chemical stability of high performance $\text{Ce}_{0.8}\text{Gd}_{0.2}\text{O}_{2-\delta}\text{-FeCo}_2\text{O}_4$ dual phase oxygen transport membranes, *Journal of Membrane Science* 544 (2017) 278-286.
- [2] M. Ramasamy, S. Baumann, J. Palisaitis, F. Schulze-Küppers, M. Balaguer, D. Kim, W.A. Meulenber, J. Mayer, R. Bhave, O. Guillon, Influence of Microstructure and Surface Activation of Dual-Phase Membrane $\text{Ce}_{0.8}\text{Gd}_{0.2}\text{O}_{2-\delta}\text{-FeCo}_2\text{O}_4$ on Oxygen Permeation, *Journal of the American Ceramic Society* 99(1) (2016) 349-355.
- [3] M. Ramasamy, S. Baumann, A. Opitz, R. Iskandar, J. Mayer, D. Udomsilp, U. Breuer, M. Bram, Phase Interaction and Distribution in Mixed Ionic Electronic Conducting Ceria-Spinel Composites, *Advances in Solid Oxide Fuel Cells Electronic Ceramics II: Ceramic Engineering Science Proceedings* 37(3) (2017) 99-112.
- [4] S. Wang, T. Kobayashi, M. Dokiya, T. Hashimoto, Electrical and ionic conductivity of Gd-doped ceria, *Journal of The Electrochemical Society* 147(10) (2000) 3606-3609.
- [5] Z. Tianshu, P. Hing, H. Huang, J. Kilner, Ionic conductivity in the $\text{CeO}_2\text{-Gd}_2\text{O}_3$ system ($0.05 \leq \text{Gd/Ce} \leq 0.4$) prepared by oxalate coprecipitation, *Solid State Ionics* 148(3-4) (2002) 567-573.

Acknowledgements

This work was accomplished at the Institute of Energy and Climate Research, Materials Synthesis and Processing (IEK-1) and Microstructure and Properties (IEK-2), at the Forschungszentrum Jülich GmbH. I would like to express my gratitude to everyone who was involved and contributed to this work directly or indirectly.

To start with, I would like to thank Prof. Dr. W. A. Meulenber, Prof. Dr. L. Singheiser and Dr. J. Malzbender for providing the opportunity to work on this PhD project and supporting my application for PhD funding.

Prof. Dr. W. A. Meulenber as my supervisor guided me to go through all the administrative, scientific and personal barriers during my stay as a PhD student, which I highly appreciated.

I gratefully acknowledge my daily advisor in IEK-2 - Dr. J. Malzbender, who supported me significantly with ideas and valued advice regarding the PhD project and the related activities.

I am very thankful to have Dr. S. Baumann being my advisor in IEK-1. He provided meaningful scientific contributions to this work, especially on aspects such as sample preparation and oxygen permeation.

I especially have to thank my promoters at Twente - Prof. Dr. A. Nijmeijer and Prof. Dr. L. Winnubst. We had many meetings for project administration requirements. And we had meaningful discussions on scientific fields that helped me to refine basic scientific ideas.

Obviously, I would like to express my gratitude also to the institute directors at Jülich - Prof. Dr. R. Schwaiger and Prof. Dr. O. Guillon. They supported my attendances at conferences and gave a lot of suggestions on scientific aspects, which aided the achievements of this work.

My great gratitude is also expressed to Ms. T. Osipova, and Mr. M. Turiaux for supporting the thermo-mechanical testing, Mr. S. Heinz for the assistances in lab works, sample preparations and permeation measurements, Dr. E. Wessel and Dr. D. Grüner for SEM, BSEM, EBSD and EDS investigations, Mr. M. Ziegner for XRD measurements, Ms. S. Schwartz-Lückge and Ms. A. Hilgers for particle morphology measurements, Ms. M. Gerhards for thermal analysis, Mr. V. Gutzeit, Mr. J. Bartsch and Mr. M. Kappertz for sample preparation assistance and Mr. V. Bader for thermal treatments. Without these experimental supports an acquisition of all these meaningful results would not have been possible.

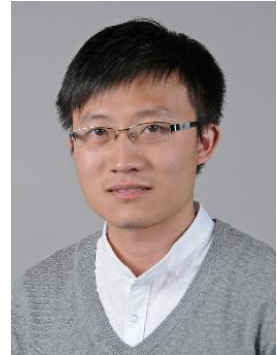
Many thanks also to Prof. Dr. M. Krüger and Dr. F. Schulze-Küppers for their supports and contributions to publications during their stay in my first two year as a PhD student.

My acknowledgements would be incomplete without thanking my families. Many thanks to my parents, my sister and my grandmother for understanding and supporting my decision to study abroad. I would like to thank especially my wife - Ms. M. Hu, who came to join me in Germany at my third year as a PhD student. The work would have been impossible to start or complete without her continuous support.

Finally, I would like to acknowledge the funding for my study by China Scholarship Council (CSC) which I highly appreciated.

About the author

Fanlin Zeng was born on 24th August, 1990, in Ganzhou, China. After finishing his high school (Ganxian High School) in the same city, he went to Jiangxi University of Science and Technology (Ganzhou, China) to study in Metallurgy Engineering, where he obtained his bachelor degree. Afterwards, he joined Shanghai University (Shanghai, China), where he finished his Master degree in Materials Machining Engineering. His master thesis, under the supervision of Prof. Dr. Y. Zhang, covered thermo-mechanical properties investigations and fabrications of sealing joint for $\text{BaCo}_{0.7}\text{Fe}_{0.2}\text{Nb}_{0.1}\text{O}_{3-\delta}$ oxygen transport membranes.



After a two-year stay in the industry, he decided to start a new science career. His scientific interests drove him to Europe, where he deepend studies as a jointed PhD student of Forschungszentrum Jülich GmbH (Jülich, Germany) and University of Twente (Enschede, the Netherlands). His PhD project, under the supervision of Prof. Dr. W. A. Meulenber, which was financially supported by Chinese Scholarship Council (CSC), focused on dual phase oxygen transport membranes. During his study as a PhD, he was the first author of six manuscripts for publications in high ranking peer reviewed journals (e.g. Journal of the European Ceramic Society, Journal of the American Ceramic Society and Journal of Membrane Science), and presented lectures in several conferences including DKG2019, ECERS2019 and MSE2020.

Band / Volume 515

Modeling and validation of chemical vapor deposition for tungsten fiber reinforced tungsten

L. Raumann (2020), X, 98, XXXVIII pp

ISBN: 978-3-95806-507-9

Band / Volume 516

Zinc Oxide / Nanocrystalline Silicon Contacts for Silicon Heterojunction Solar Cells

H. Li (2020), VIII, 135 pp

ISBN: 978-3-95806-508-6

Band / Volume 517

Iron isotope fractionation in arable soil and graminaceous crops

Y. Xing (2020), X, 111 pp

ISBN: 978-3-95806-509-3

Band / Volume 518

Geophysics-based soil mapping for improved modelling of spatial variability in crop growth and yield

C. Brogi (2020), xxi, 127 pp

ISBN: 978-3-95806-510-9

Band / Volume 519

Measuring and modelling spatiotemporal changes in hydrological response after partial deforestation

I. Wiekenkamp (2020), xxxvii, 276 pp

ISBN: 978-3-95806-512-3

Band / Volume 520

Characterization of Root System Architectures from Field Root Sampling Methods

S. Morandage (2020), xxii, 157 pp

ISBN: 978-3-95806-511-6

Band / Volume 521

Generation Lulls from the Future Potential of Wind and Solar Energy in Europe

D. S. Ryberg (2020), xxvii, 398 pp

ISBN: 978-3-95806-513-0

Band / Volume 522

Towards a Generalized Framework for the Analysis of Solar Cell Performance based on the Principle of Detailed Balance

B. J. Blank (2020), iv, 142 pp

ISBN: 978-3-95806-514-7

Band / Volume 523

A Robust Design of a Renewable European Energy System Encompassing a Hydrogen Infrastructure

D. G. Çağlayan (2020), xxii, 312 pp

ISBN: 978-3-95806-516-1

Band / Volume 524

Control and Optimization of a Lorentz Force Based Actuator System for External Flow

M. F. Seidler (2020), xii, 136 pp

ISBN: 978-3-95806-518-5

Band / Volume 525

ETV Online Tagung 2020

Industrielle Groß- und Hochtemperaturwärmepumpen im Energiesystem

D. Stolten, G. Markowz (Hrsg.) (2020), ca. 71 pp

ISBN: 978-3-95806-519-2

Band / Volume 526

Atmospheric Trace Gas Measurements Using Chemical Ionisation Time-of-Flight Mass Spectrometry

Y. Li (2020), xi, 110 pp

ISBN: 978-3-95806-520-8

Band / Volume 527

Uranium accumulation in agricultural soils as derived from long-term phosphorus fertilizer applications

Y. Sun (2020), XII, 136 pp

ISBN: 978-3-95806-521-5

Band / Volume 528

Entwicklung von Schutzschichten für nicht-oxidische Faserverbundwerkstoffe

M. D. Wolf (2021), VI, 150, 2 pp

ISBN: 978-3-95806-524-6

Band / Volume 529

Mechanical reliability and oxygen permeation of $\text{Ce}_{0.8}\text{Gd}_{0.2}\text{O}_{2-\delta}$ - FeCo_2O_4 dual phase membranes

F. Zeng (2021), IV, VI, 222 pp

ISBN: 978-3-95806-527-7

Energie & Umwelt / Energy & Environment
Band / Volume 529
ISBN 978-3-95806-527-7

Mitglied der Helmholtz-Gemeinschaft

